

Complex Self-assembly of Liquid Crystal Compounds of Different Shapes



Yaxin LI

Supervised by Dr. Xiangbing Zeng and Prof. Goran Ungar

A thesis submitted for the degree of Doctor of Philosophy in the

Department of Materials Science and Engineering

The University of Sheffield

June 2020

Acknowledgments

I am most grateful to Dr. Xiangbing Zeng and Prof. Goran Ungar for giving me the opportunity to carry out this challenging research work in their research group. Their strict attitude toward science, careful guidance and great encouragement has been the strongest support of my study and life in the UK. What I learned from them will be definitely helpful in my future adventure. I am also grateful for the help from previous and current members in our group, especially Dr. Huanjun Lu, Dr. Ruibin Zhang, Dr. Warren Stevenson and Dr. Shugui Yang.

I am also grateful for the help and suggestions I got from my examiners, Dr. Chirs Holland in our department and Prof. Georg Mehl in the University of Hull, for making this thesis to be better.

For synthesizing compounds and carrying out initial measurement, my special thanks go to Prof. Xiaohong Chen and the members of her group in Yunnan University, Fangfang Fan and Jie Wang in Zhejiang Sci-Tech University, Lilina Cseh and Daniela Haidu in Xi'an Jiaotong University and "Coriolan Dragulescu" Institute of Chemistry in Romania.

For help with synchrotron experiments, I thank Prof. N. Terrill and Dr. O. Shebanova, beamline I22, Dr. Gareth Nisbet, beamline I16, Dr. Tamas Javorfi and Dr. Rohanah Hussain, beamline B23 at Diamond Light Source. I also thank Drs. O. Bikondoa, S. Brown and P. Thompson of beamline BM28 at ESRF.

I am grateful for the help I got from the staff in our department, especially Dr. Oday Hussein and Dr. Nicola Green for the characterization. I am also thankful for the help from Dr. Barbara Ciani, Prof. Julia A. Weistein, Mr Robert Hanson in the Department of Chemistry, Dr. Nic Mullin in the Department of Physics and Dr. Patrick Baker in the Department of Molecular Biology and Biotechnology.

I would like to thank the China Scholarship Council for the stipend and our university for waiving tuition fee. My thanks also go to our department and British Liquid Crystal Society for the guidance of my Ph.D. study and the financial support to attend conferences.

I've been also fortunate to meet Dr. Dawei Wang, Dr. Zhilun Lu, Dr. Shikuan Sun, Dr. Mingwen Bai and some visiting teachers and students in our department. Lunchtime is always the happy time of the day. And also to my friends, Dr. Zhenglin Li and Dr. Ke Sun in the Department of Automatic Control and Systems Engineering for keeping my spirits up through low points.

Finally, I would like to thank my family for their support. My grandfather would definitely be glad to see my graduation in heaven. Also, I would give my special thanks to my dear boyfriend Xu Wen. Thanks for being there for me no matter what in the past 12 years. Without their unwavering love, understanding and encouragement, I would never be able to overcome the difficulties.

Abstract

Liquid crystal materials have been widely used in nano-devices and nano-patterning because of their small molecular size and self-assembly abilities. To obtain designed application properties, it is important to understand the way to control their phase behaviour. External factors, such as temperature and solvents, and internal factors, such as molecular shape and the interactions between molecules, all contribute to formation of different liquid crystalline phases.

A series of complex self-assembling liquid crystal compounds have been investigated in this project, in particular how self-assembled structures of low symmetry, e.g. chiral, non-centrosymmetric and superlattices, with important implications for applications can be manipulated by molecular design. The liquid crystal phase structures are mainly characterized by polarized optical microscopy, differential scanning calorimetry, small angle X-ray scattering and grazing incident X-ray scattering. Second harmonic generation has also been used to distinguish centrosymmetric and non-centrosymmetric structures.

In straight- and bent-core polycatenars, we have studied their 2D columnar phases and more importantly, the 3D orthorhombic *Fddd* phases. The structure is related but distinctively different from the single-network *Fddd* structures formed by block copolymers. The basic units of molecules in the *Fddd* phase are discovered to be helical columns, both left- and right-handed, similar to that found in bicontinuous cubic phases. The findings point the way to manipulate self-assembled 3D helical structures.

In bent-core bolaamphiphiles, we have discovered how the functional groups outside of the bend and inner chains can be used to control the formation of different types of honeycomb liquid crystal phases, from random hexagonal to trigonal and superlattice honeycombs.

In double-tapered molecules, we have widened the range and complexity of liquid crystal phases formed by taper-shaped molecules. The coexistence of the ionic and non-

ionic cylinders in the columnar phase formed by such double-tapered molecules gives promising applications on semiconducting nanowires or electronic conductors.

In a polymerizable ionic liquid crystal compound, we have studied double gyroid cubic phases in the form of a polymerized self-standing film. The film can be greatly swollen by absorption of water but the double gyroid network structure is found to be still intact, and shows promising ionic conductivity for applications in e.g. fuel cells.

Publications

H. F. Cheng*, **Y. X. Li***, X. B. Zeng, H. F. Gao, X. H. Cheng, G. Ungar, Trigonal columnar self-assembly of bent phasid mesogens, *Chemical Communications* 2018, 54, 156-159. doi: 10.1039/c7cc06714c. (* first co-authors).

Y. X. Li, H. F. Cheng, X. B. Zeng, Y. Tao, X. H. Cheng, G. Ungar, Tailoring liquid crystal honeycombs by head-group choice in bird-like bent-core mesogens, *Journal of Materials Chemistry C* 2020, 8, 8069-8076. doi: 10.1039/D0TC01879A.

Y. X. Li*, F. F. Fan*, J. Wang, L. Cseh, M. Xue, X. B. Zeng, G. Ungar, New type of columnar liquid crystal superlattice in double-taper ionic minidendrons, *Chemistry-a European Journal* 2019, 25, 13739-13747. doi: 10.1002/chem.201902639. (* first co-authors).

T. Kobayashi, **Y. X. Li**, A. Ono, X. B. Zeng, T. Ichikawa, Gyroid structured aqua-sheet with sub-nanometer thickness enabling 3D fast proton relay conduction, *Chemical Science* 2019, 10, 6245-6253. doi: 10.1039/c9sc00131j.

Conference Presentations

The British Liquid Crystal Society Annual Conference (BLCS), Manchester, UK, April 2018. Trigonal columnar self-assembly of bent phasid mesogens (Poster presentation)

The 11th Edition of Symposium with International Participation “New trends and strategies in the chemistry of advanced materials with relevance in biological systems, technique and environmental protection” conference, Timisoara, Romania, June 2018. Trigonal columnar self-assembly of bent phasid mesogens (poster presentation)

The 15th European Liquid Crystal Conference (ELCC), Wroclaw, Poland, July 2019. New Type of Columnar Liquid Crystal Superlattice in Double-Taper Ionic Minidendrons (Oral presentation)

Contents

Abstract	III
Publications.....	V
Conference Presentations.....	VI
Chapter 1 Introduction	1
1.1 General concepts and classification of liquid crystals	2
1.2 LC phases formed by molecules of different shapes.....	3
1.2.1 Straight Polycatenars	6
1.2.2 T-shaped and X-shaped molecules	16
1.2.3 Bent-core molecules.....	24
1.3 Aims and objectives	30
References.....	33
Chapter 2 Experimental Methods and Analysis.....	44
2.1 X-ray diffraction.....	44
2.1.1 Basic crystallography concepts.....	44
2.1.2 The principle of X-ray diffraction.....	47
2.1.3 Basic experimental setups: simultaneous SAXS/WAXS	54
2.1.4 Grazing incidence small/wide angle X-ray scattering (GISAXS/GIWAXS)	55
2.1.5 Laboratory beamline	57
2.1.6 Synchrotron radiation.....	58
2.1.7 Determination of lattice parameters and symmetry groups	60

2.2	Optical Spectroscopy.....	61
2.1.1	UV-Vis and fluorescence spectroscopy.....	62
2.1.2	Infrared spectroscopy.....	64
2.2	Other Analytical Procedures.....	65
2.2.1	Microscopy.....	65
2.2.2	Differential Scanning Calorimetry (DSC).....	70
2.2.3	Molecular modelling and dynamic simulation.....	70
	References.....	72
Chapter 3 Published paper: Trigonal columnar self-assembly of bent phasid mesogens		
	74
3.1	Abstract.....	75
3.2	Introduction.....	75
3.3	Results and discussion.....	76
3.4	Conclusion.....	84
3.5	Supporting Information.....	85
3.5.1	Characterization and Modelling Techniques.....	85
3.5.2	DSC Results.....	87
3.5.3	Additional Optical Micrographs.....	88
3.5.4	Additional X-ray Diffraction Data.....	89
3.5.5	Estimate of the number of molecules per column stratum.....	92
3.5.6	Arrangement of columns on substrate surface.....	93
3.5.7	Additional second harmonic generation data.....	93
	Acknowledgement.....	94

References.....	94
Chapter 4 A new liquid crystal phase of counter-rotating staircases.....	97
4.1 Abstract	97
4.2 Introduction	98
4.3 Results and Discussion.....	99
4.4 Methods.....	109
4.5 Supporting Information	111
4.5.1 DSC thermograms.....	111
4.5.2 Polarized Optical Microscopy (POM)	112
4.5.3 X-ray Diffraction Data	113
4.5.4 Reconstruction of Electron Density Maps	123
4.5.5 Estimate of the number of molecules per column stratum	124
4.5.6 Additional schematic models with ED maps	126
4.5.7 Additional AFM.....	129
4.5.8 UV-vis and fluorescence emission spectroscopy.....	131
4.5.9 HOMO/LUMO energy.....	131
4.5.10 Description of the video.....	131
Acknowledgements.....	132
References.....	132
Chapter 5 Published paper: Tailoring liquid crystal honeycombs by head-group choice in bird-like bent-core mesogens.....	135
5.1 Abstract	136
5.2 Introduction	136

5.3	Results and Discussion.....	138
5.4	Conclusion.....	151
5.5	Supporting Information.....	151
5.5.1	Experimental methods	151
5.5.2	DSC results	153
5.5.3	Additional POM images	155
5.5.4	Additional X-ray diffraction, SHG and molecular modelling/simulation results on individual compounds	155
5.5.5	Estimation of number of molecules per columnar stratum.....	161
5.5.6	Electron densities of functional groups involved, non-bonded interaction energies and dipole moments of headgroups	163
	Acknowledgements.....	164
	References.....	164
Chapter 6 Published paper: New Type of Columnar Liquid Crystal Superlattice in Double-Taper Ionic Minidendrons		
6.1	Abstract	169
6.2	Introduction	169
6.3	Results	173
6.4	Discussion	183
6.5	Conclusion.....	188
6.6	Supporting Information.....	189
6.6.1	Materials	189
6.6.2	Analytical Techniques	189

6.6.3	DSC.....	190
6.6.4	X-ray Diffraction	191
6.6.5	Molecular Simulation.....	198
	Acknowledgements.....	199
	References.....	199
Chapter 7 Published paper: Gyroid structured aqua-sheets with sub-nanometer thickness enabling 3D fast proton relay conduction		
		205
7.1	Abstract	206
7.2	Introduction	206
7.3	Results and discussion.....	208
7.4	Conclusion.....	223
7.5	Experimental section	223
7.6	Supporting Information	224
7.6.1	Synthesis of Diene-GZI	224
7.6.2	Thermal behavior of Diene-GZI	225
7.6.3	Thermal behavior of MX	226
7.6.4	A molecular structure of N-MZI and its liquid-crystalline behaviour	226
7.6.5	Microscopic structure in Film-Cub _{bi}	227
7.6.6	IR spectra of Film-Cub _{bi}	227
7.6.7	Relative humidity dependence of the cubic lattice length in Film-Cub _{bi}	228
7.6.8	Gravimetric analysis for Film-Cub _{bi} under humidity-controlled condition	228

7.6.9	Synchrotron X-ray diffraction patterns of Film-Cub _{bi}	229
7.6.10	Material density measurement for Film-Cub _{bi}	230
7.6.11	Preparation of samples with various water contents for synchrotron X-ray diffraction measurements	231
7.6.12	Reconstruction of electron density maps	232
7.6.13	Calculation of the surface area of a gyroid minimal surface	236
7.6.14	Characterization of Film-Meso	237
7.6.15	Synthetic scheme for GZI	238
7.6.16	Self-organization behavior of GZI and the GZI/HTf ₂ N mixtures	238
	Acknowledgements.....	239
	References.....	240
	Summary and future work	247

Chapter 1 Introduction

Liquid Crystals (LCs) have been widely studied in recent decades for their technological importance and industrial applications. The most well-known applications of LCs are in display technology, such as liquid crystal displays (LCD) [1-5]. Moreover, a variety of LC structures can be formed from molecules of different shapes, in a process called self-assembly through non-covalent interactions between molecules [6]. Thus, nano-objects and nano-structures can be created by this “bottom-up” self-assembly approach for fabrication of functional materials and devices. This “bottom-up” approach has been used in nanoscale patterning such as in nanolithography [7, 8], and for fabrication of selective nanoporous membranes [9-11], field effect transistors (FETs) [12, 13], photovoltaic solar cell [14-17] and so on.

The scope of this chapter is to provide an overview of the variety of LC phases formed by molecules of different shapes, and our current understanding of how the self-assembly process can be controlled by interactions between molecules and other parameters such as relative volumes of different moieties of the molecules. This would guide the way to design new LC molecules and to manipulate LC structures with promising applications.

1.1 General concepts and classification of liquid crystals

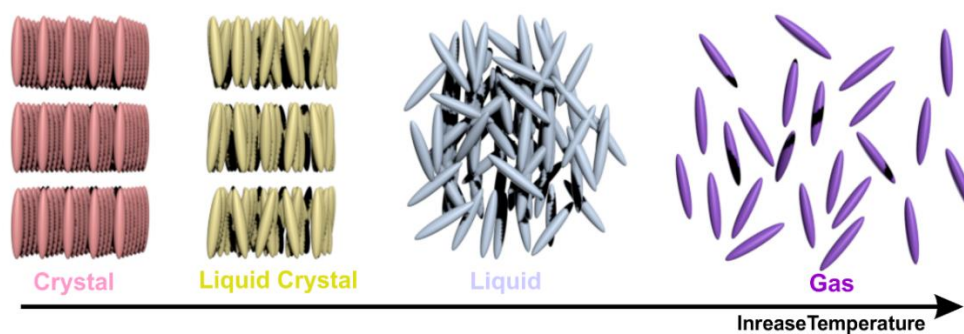


Figure 1.1 The four states of matter and their sequence with the increasing of temperatures.

Table 1.1 The classification of LC phases by symmetry [1].

Phase		Dimensionality of Positional long-range order	Dimensionality of orientational long-range order
Isotropic liquid		0	0
Nematic	uniaxial	0	1
	(biaxial)		3
Smectic	A	1	1
	C		3
	B (Hexatic)		1
	F, I (Hexatic)		3
Columnar	hexagonal	2	1
	rectangular		1, 3
	oblique		1, 3
3-D	cubic	3	3
	hexagonal		
	tetragonal		
Crystal		3	3

Gas, liquid and crystal are the three well-known states of matter. However, there is also a ‘fourth state of matter’, LC, as shown in Figure 1.1. LCs are different from solid and

liquid. They can be regarded as an ordered fluid, representing a unique combination of crystal-like order and liquid-like fluidity.

To be more specific, a crystal has both positional and orientational long-range order in three dimensions. This means that center of gravity of each and every molecule in the crystal has a preferred position as well as orientation. At the same time, a liquid only has short-range order but no long-range order in any dimension [1]. The states between the two, where some but not all long-range orders have been lost, are LCs. The classifications of the different LC phases by symmetry are displayed in Table 1.1. It is worth noting that there are also LC phases with full 3D long-range positional and orientational orders. The key difference between such 3D LC phases and crystals is that in LCs long range orders are kept for the aggregate of molecules, but not for individual molecules.

There are two classes of LCs: lyotropic and thermotropic LCs. Lyotropic LCs are usually formed by the disruptive effect on crystals of a solvent (often water). It has mainly three different types, surfactant (amphiphilic), chromonic and polymeric LCs [18]. Thermotropic LCs contain no solvent and form by melting crystal or cooling from isotropic liquid phase. Most compounds studied in this project are thermotropic LCs. In the next section, thermotropic LC phases will be discussed according to the shapes of the molecules that form them.

1.2 LC phases formed by molecules of different shapes

Considering the geometrical shape of molecules forming them, LCs can be grouped into some types such as rod-like, disk-like, cone-shaped, star-shaped, etc. Two classic

types: the “calamitic” LCs from rod-like molecules and the “discotic” LCs from disk-like molecules, are discussed here as shown in Figure 1.2.

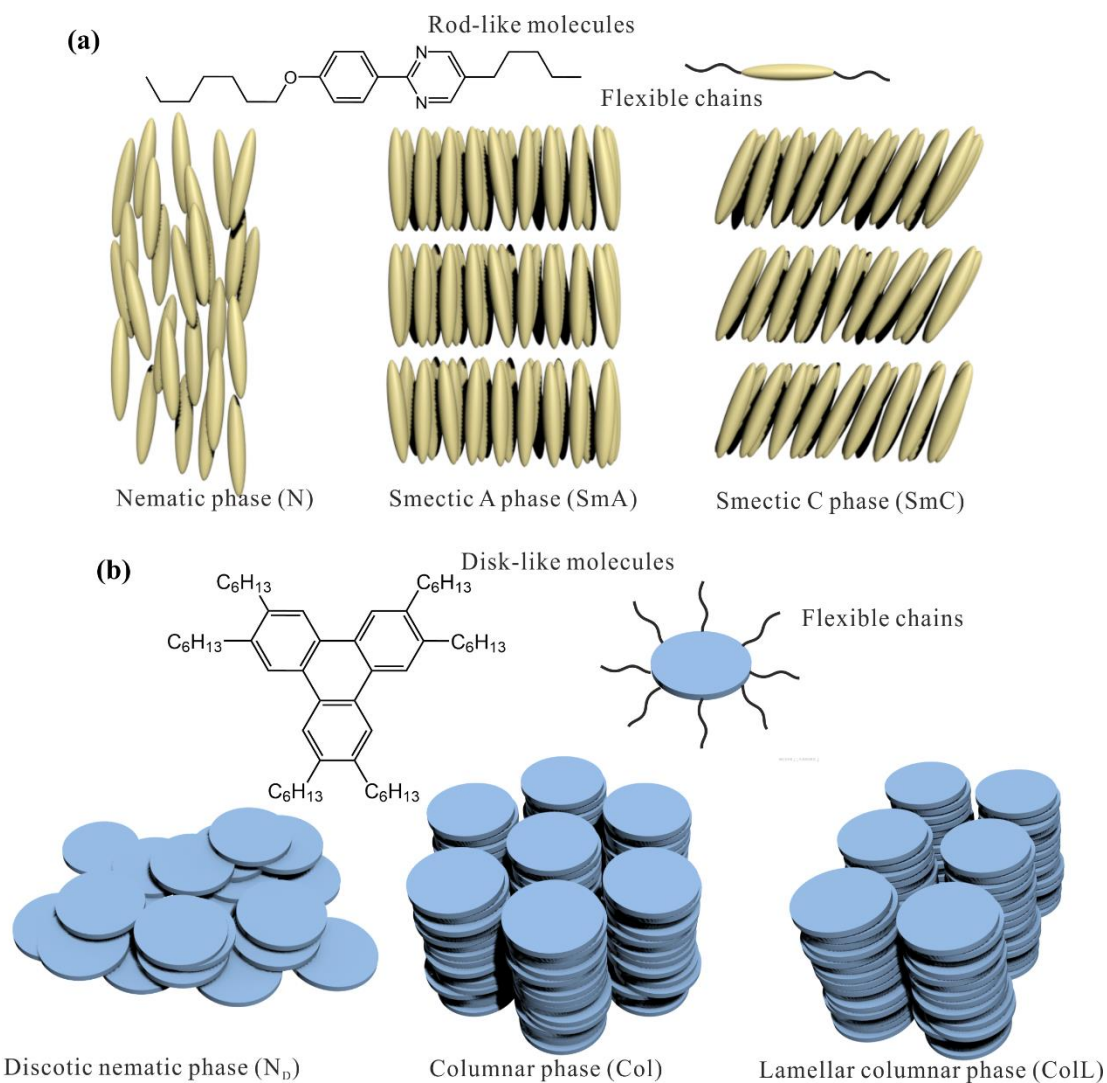


Figure 1.2 Examples of rod-like and disk-like molecules and phases they form. (a) Calamitic nematic and smectic phases formed by rod-like molecules. (b) Discotic nematic phase, columnar phase and lamellar columnar phase formed by disk-like molecules.

The most common LC phases formed by rod-like molecules are nematic (N) and smectic phases (Sm), as shown in Figure 1.2a. The principal architecture of the rod-like molecule generally includes a rigid core and flexible chains which attached to one

terminal end or each terminal end of the rigid core. The rigid core almost always possesses a large shape-anisotropy. Nematic phase (N) is the simplest LC phase, and molecules maintain on a preferred direction without any long range positional order. When the LCs possess also 1D long range positional order, they form smectic phases where molecules lie in layers. If the long axes of the molecules (on average) are parallel to the layer normal, it is called a Smectic A phase (SmA). If the director tilts away from the layer normal, it is called a Smectic C phase (SmC) [19-21].

Disk-like (discotic) molecules can form N, columnar (Col), and lamellar columnar (ColL) phases, as shown in Figure 1.2b. Col phases are a class of LCs that molecules assemble into cylindrical structures. ColL phases are a combination of lamellar and Col phases in which molecules not only form cylindrical structures but also layered structures. Most disk-like molecules consist of an aromatic core and attached aliphatic tails. The tails are liquid-like. Like the N phase formed by rod-like molecules, discotic N phase only possesses orientational long-range order without any positional long-range order. Col and ColL phases are composed of columns, however the periodicity is only in two dimensions. Thus they possess 2D positional long-range order and also orientational long-range order, as also concluded in Table 1.1 [22, 23].

As a large extent of types of LCs are determined by molecular shapes, then the understanding of the self-assembled LC structures is fundamental and it leads the way to tailor molecules with desirable phases and physical properties. The rod-like molecules are widely used in FETs [13] and LCDs, such as twist nematic (TN) LCDs, in-plane switching (IPS) LCDs and vertically aligned (VA) LCDs [1-5]. In LCD cells, the orientation of the molecules can be controlled by electric field, switching between bright and dark states. Chiral nematic phases formed by rod-like molecules with chiral centre(s) are of interest for their optical properties. For example, they are widely used

in LC thermometers as their colours change with temperature, due to the change of their chiral pitch (the distance between layers that molecules undergo a 360° twist) [24]. The disk-like molecules are also used as organic semiconductors in FETs, photovoltaic devices, VA LCD and so on [6, 12, 22]. Further modifications on rod-like molecules are discussed in the next sections.

1.2.1 Straight Polycatenars

Molecule shapes are important in determining the mode of self-assembly, the structures and order of LCs. Thus the modifications on rod-like molecules have been studied by adding flexible chains at the end(s) of the rod-like aromatic core. These compounds are called polycatenars. Strong π - π interactions between rigid aromatic cores often lead to conductive properties of such LCs, that can be used in molecular electronics, optical and photovoltaic devices [52-53]. Polycatenar molecules can be further modified by introducing thiophenes, oxadiazoles or fluorenones with high electron densities for better conductive properties [54-60]. Some of such molecules will be studied in this project.

The classification of polycatenars according to the arrangement of the attached chains could be taper/wedge-shaped, dumbbell-shaped molecules and so on [25]. More details are discussed in the next sections.

1.2.1.1 *Taper-shaped Polycatenars*

Taper-shaped molecules, also called wedge-shaped molecules, have two or three aliphatic chains at the broader molecular end and one or no chain at the other end. Here we use symbols 2-1- or 3-1- to represent such taper-shaped molecules.

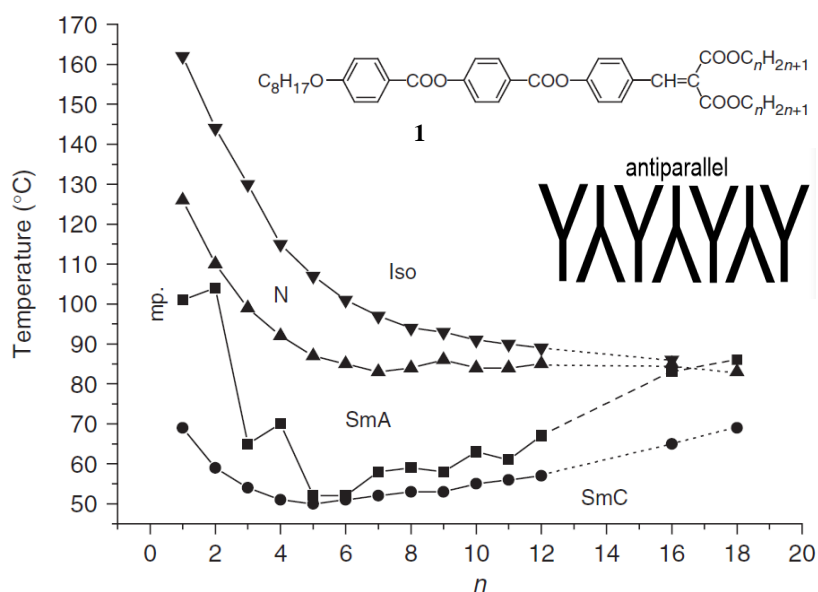


Figure 1.3 Phase temperatures of 2-1-taper-shaped molecules vs. the length of attached chains [25, 26]. Reproduced with permission from ref [25].

An example phase diagram of 2-1-taper-shaped molecules is shown in Figure 1.3 [25, 26]. All members in this homologous series show N, SmA and SmC phases. The trend of the change of transition temperatures with the enlargement of end chains is similar. The layer thickness is close to the length of molecules in smectic phase and molecules pack antiparallel with each other in the layer, as shown in the inset of Figure 1.3. There is small free volume in the antiparallel arrangement. The polar interactions, which are electrostatic interactions and exist in molecules that have permanent dipoles, stabilize the smectic layers [26]. However, when $C_8H_{17}O-$ is replaced by $CN-$, the new homologous series molecules prefer to form only N phases because of the strong competition between polar and steric interactions [25, 27].

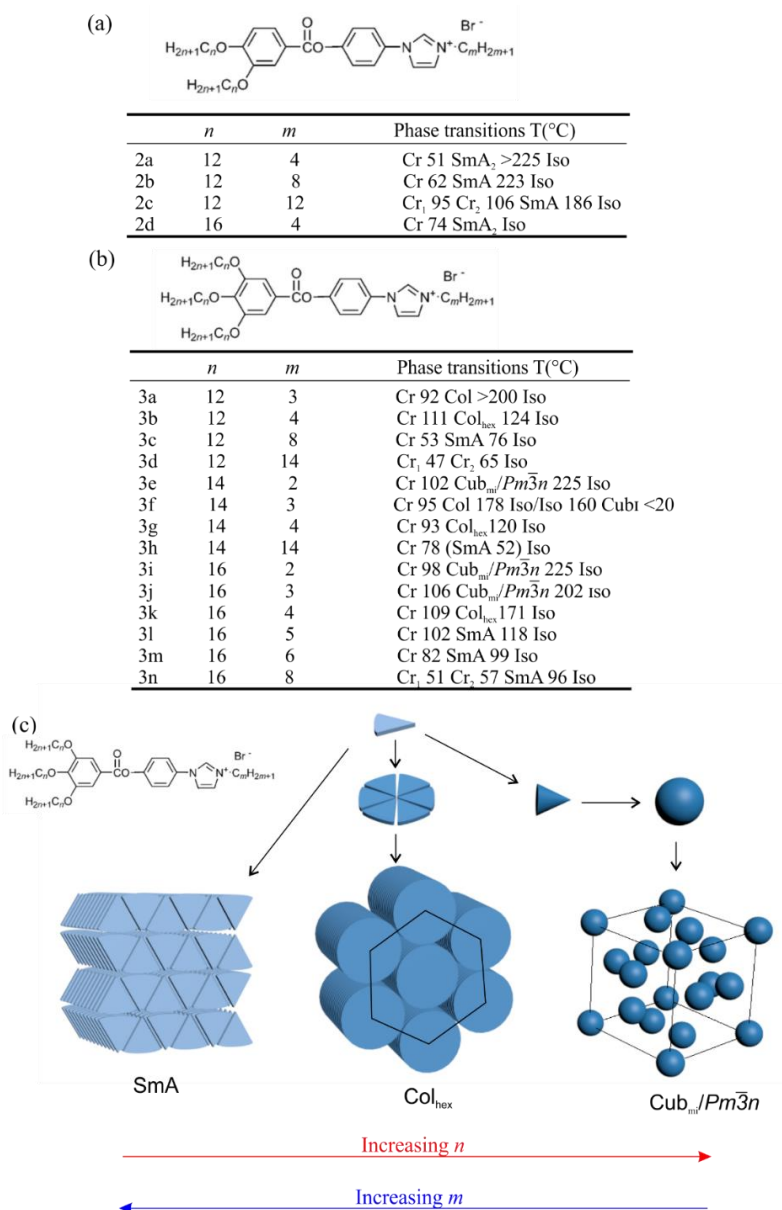


Figure 1.4 Transition temperatures of (a) 2-1- and (b) 3-1-taper-shaped molecules [25, 28, 29] and (c) the development of phases according to the length of end chains. Figures (a, b) are reproduced with permission from ref [28].

When another chain is added on the rigid core, some more phases can be formed. As shown in Figure 1.4, SmA phase is formed by 2-1 polycatenar compound 2a, while hexagonal columnar (Col_{hex}) phase is formed by adding the third alkyl chain onto the core (compound 3a). With increasing chain length at the broader (3-chain) molecular

end, micellar cubic (Cub_{mi}) phases are observed. The $\text{Cub}_{\text{mi}}/Pm\bar{3}n$ phases were first determined by U. Goran's group (collaborated with V. Percec's group) [29] and C. Tschierske's group [30] simultaneously in 1997.

The phase sequence is from SmA with 1D positional long-range order to Col with 2D positional long-range order, and to Cub_{mi} phase with 3D positional long-range order, as shown in Figure 1.4c. The opposite phase sequence is observed with the enlargement of the narrower (1-chain) molecular end.

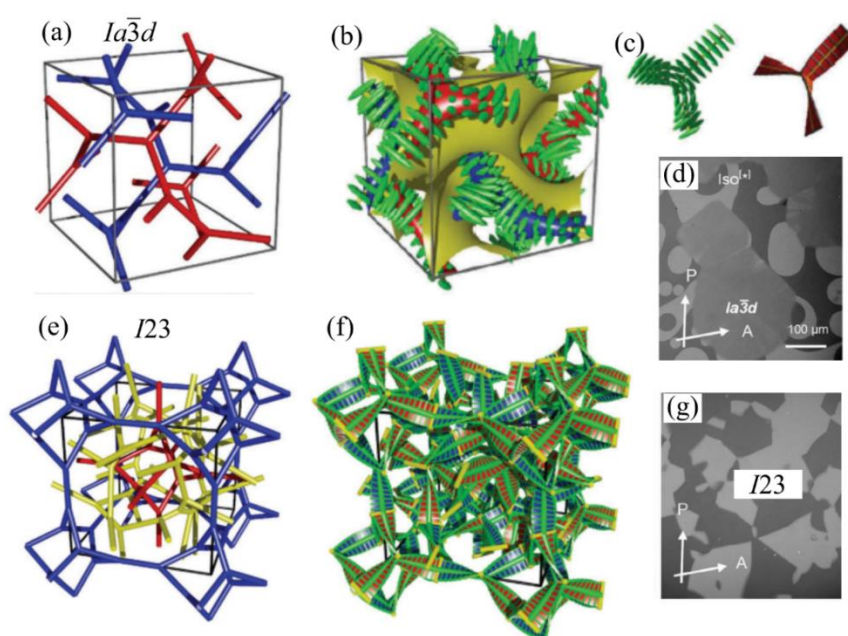


Figure 1.5 The comparison of achiral double network ($Ia\bar{3}d$) and chiral triple network ($I23$) cubic phases [31, 32]; (a, e) the networks of the cubic phases; (b) the arrangement of $Ia\bar{3}d$ of the rigid cores coloured in green with the minimum surface coloured in yellow; (c) the network junctions of $Ia\bar{3}d$ represented by rigid cores and twisted ribbons; (f) The networks of $I23$ represented by twisted ribbons; (d, g) optical textures of $Ia\bar{3}d$, $I23$ and iso^* under slightly uncrossed polarizers. Figures (a-c, d, g) are reproduced with permission from ref [32]. For reproduction of Figures (e, f) from CC: Reproduced from ref [32] with permission from The Royal Society of Chemistry.

Moreover, other different cubic phases are observed in 3-1-taper-shaped molecules, and they are called bicontinuous cubic phases [21, 33-35]. Different from the Cub_{mi} that are

found above Col phases with increasing volume of the end chains at the broader side, the bicontinuous cubic (Cub_{bi}) phases are found in between Sm and Col phases [35]. In the bicontinuous structures, the sub-spaces occupied by the two moieties of the molecules, typically rigid aromatic cores and flexible end groups respectively, are all 3D continuous (e.g. Figure 1.5b) [32, 36-41], while in comparison in the Cub_{mi} , Col and Sm phases there are discrete finite domains such as layers, columns and micelles (e.g. Figure 1.4c). The most commonly observed Cub_{bi} $Ia\bar{3}d$ phases were determined by A.M. Levelut's group in 1998 [42]. The $Ia\bar{3}d$ structure is the "double gyroid", as shown in Figure 1.5a-b. It consists of two interpenetrating infinite 3D networks (coloured blue and red in Figure 1.5b) of columnar segments, typically formed by the rigid aromatic cores oriented perpendicular or slightly tilted to the axis of the column segment (green rods, Figure 1.5b). All network segments have the same length and there are always three network segments joining at each network junction. The two networks are separated by an infinitely periodic minimum surface (IPMS, yellow surface, Figure 1.5b) in between, with the flexible end groups occupy the region around it.

Furthermore, there is often another Cub_{bi} phase found near $Ia\bar{3}d$, and was initially assigned to be a triple network $Im\bar{3}m$ phase, where there are three instead of two interpenetrating networks of columnar segments formed by rigid cores of the molecules [34]. Another model of $Im\bar{3}m$ proposed by S. Kutsumizu's group consists of spherical shells and one network [43]. However, more recently this phase has been found to be always chiral by polarized optical microscopy (POM) and circular dichroism (CD) spectroscopy, even though the compounds themselves are achiral [32]. The chirality of this cubic phase is shown clearly in Figure 1.5g, where optically active left- and right-handed domains can be observed under slightly uncrossed polarizers. The chirality

observed is incompatible with the initial $Im\bar{3}m$ space group assignment, which has mirror symmetries. The true space group of this phase has been revealed recently by X. Zeng's group to be a non-centrosymmetric space group $I23$, as shown in Figure 1.5e-f [31] (before this clarification, sometimes this phase was assigned to $I432$ in literature). Similar to the $Ia\bar{3}d$ phase, the $I23$ phase has only 3-way junctions, but with three different lengths of the columnar segments.

The origin of the chirality in $I23$ phase has been attributed to the chirality of the columnar segments of the networks. Firstly, three to four molecules parallel with each other form a raft, then the rafts stack on top of each other, with molecular direction in successive rafts rotated by $\sim 8-10^\circ$ to form the helical columns (Figure 1.5b,f). In order to minimize the clash at the junctions, the segments joining at each junction should be coplanar, and the converging columns should possess the same handedness (Figure 1.5c). This leads to the homochirality of each network. Such chiral network segments by rotation of molecular direction, and homochirality of each network, in fact also apply to the $Ia\bar{3}d$ phase. Even though the $Ia\bar{3}d$ phase is achiral, the two networks of the $Ia\bar{3}d$ phase are both chiral but are mirror images of each other with opposite handedness, resulting in zero overall chirality of the phase. In the triple network of the $I23$ phase however, it is most likely that the chirality of all three networks are the same, even if they are not the same, the chirality of three networks added together do not cancel out.

Another phase worth mentioning is the chiral isotropic (iso*) phase observed between isotropic and $I23/Ia\bar{3}d$ or other phases (Figure 1.5d, black and white domains with curved interfaces). It is a true liquid phase and lacks any long-range order, neither positional nor orientational. However, the mirror symmetry is still broken. It has been suggested that there are short range networks in the chiral domains that are enantiopure

in the iso* phase, similar to that in the $I23$ phase. More work still need to be done to lift the veil on this fascinating phase. Chemical formulae of some of the achiral molecules that form chiral $I23$ and iso* phases are listed in Figure 1.6.

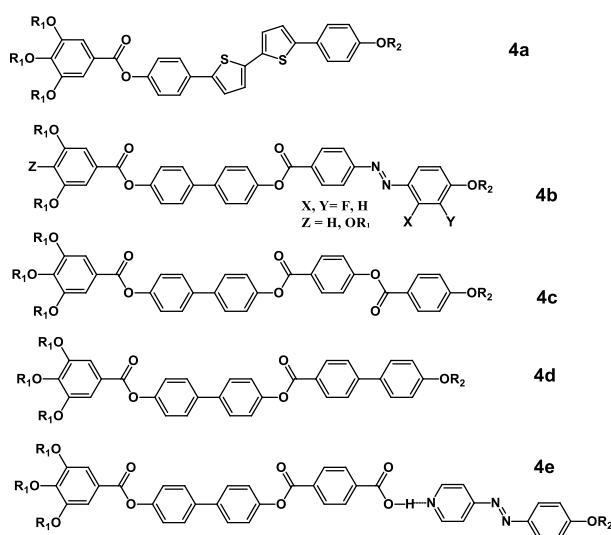


Figure 1.6 3-1-Taper-shaped molecules forming triple network cubic ($I23$) and chiral isotropic phases (iso*). Reproduced with permission from ref [40].

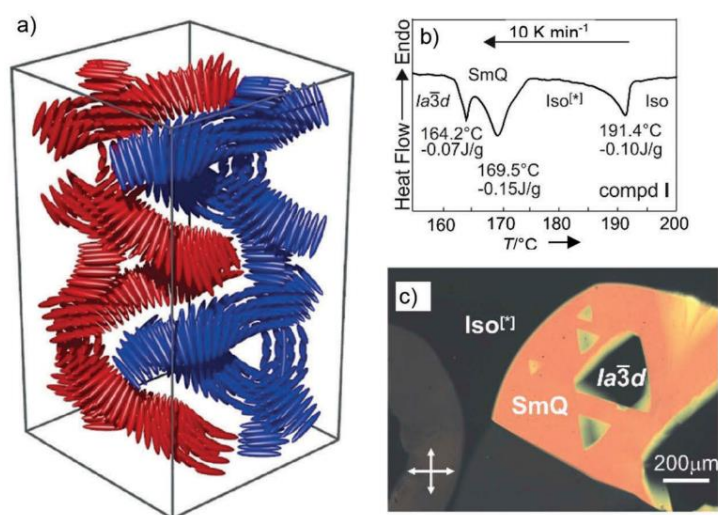


Figure 1.7 (a) Schematic model of SmQ phase showing two uniformly twisted networks; (b) phase transitions; (c) the growth of triangular domains of $Ia\bar{3}d$ phase from SmQ phase. Reproduced with permission from ref [39, 40].

A tetragonal phase called SmQ phase with space group $I4_122$, was only found in chiral compounds previously, often replacing the $Ia\bar{3}d$ phase found in their racemic equivalents [44-46]. Recently it has been also found in achiral 3-1-taper-shaped compound, and its structure turned out to be bicontinuous too. The structure is made up of orthogonal twisted columns with four-way junctions [39], as shown in Figure 1.7a. The SmQ phase is chiral due to the identical helical sense in the two networks. This confirms again that the bicontinuous phases, formed by polycatenar molecules, consist of homochiral networks of helical columnar segments, and long range homochirality is sustained by the matched handedness at network junctions. Because of the birefringence of SmQ, even though weak, it is difficult to observe directly its chirality by CD and under de-crossed POM as in other Cub_{bi} phases. However, its lack of mirror symmetry can be inferred from the observed triangular shaped $Ia\bar{3}d$ domains grown inside the birefringent SmQ domains, as shown in Figure 1.7b, c [39].

Overall, these phases mentioned above have contributed significantly to the understanding of dynamic mirror symmetry breaking. Coordinated helicity, previously unrecognized, is a key driving force to the formation of these and other chiral and achiral bicontinuous phases [31].

1.2.1.2 Dumbbell-shaped Polycatenars

The outer parts of the molecules are broader than the rigid core when two or three aliphatic chains are attached on both sides of the core. The aliphatic chains can be symmetrically or non-symmetrically arranged on the rigid core. This kind of molecules do not prefer to form SmA phase due to the insufficient packing density. The symmetric compounds with four and six aliphatic chains will be discussed in this section.

Table 1.2 The phase behaviour of compound 5 with different central part A. Reproduced with permission from ref [25].

No.	-A-	Phase transitions
5a		Cr 96 Col _{ob} 106 SmC 147 N 171 Iso
5b		Cr 111 Col _{ob} 206 Iso
5c		Cr 124 Col _{ob} 209 Col _h 314 Iso
5d		Cr 95 SmC _{re} 117 Col _{ob} 154 SmC 187 N 209 Iso
5e		Cr 133 SmC 165 Col _{ob} 181 Col _h 188 M _x 243 Iso

The dumbbell-shaped polycatenars such as compound 5 in Table 1.2 with two aliphatic chains attached at each end symmetrically, are also called double-swallow-tailed or biforked molecules. They were first introduced and studied by W. Weissflog's group [26] and A. M. Levelut's group in 1980s [47]. Comparing compound 5a, b and c, the stability of LC phases is higher with more phenyl rings and columnar phases are more favourable. Compounds 5d and 5e with central ethylene or amide-linking groups, could form more LC phases.

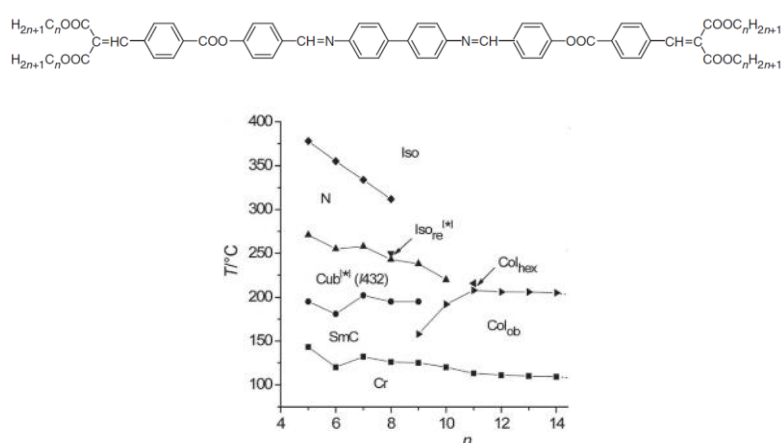


Figure 1.8 Phase diagram of a series of double-swallow-tailed compound 5b. The compound exhibits a re-entrant isotropic phase (iso*) when n is 8 [25, 48-50]. For reproduction of the figure from CC: [48]-Published by The Royal Society of Chemistry.

The phase diagram of the homologous series compound 5b is shown in Figure 1.8. Compounds with shorter chains form N, bicontinuous cubic and SmC phases; however, compounds with longer chains form columnar oblique (Col_{ob}) and Col_{hex} phases. For octyloxy derivative ($n = 8$), the rare re-entrant isotropic phase observed between Cub_{bi} (marked $I432$, later proved to be $I23$ [31]) and N phases is confirmed to be the chiral isotropic phase (iso^*) by later optical studies [48].

Table 1.3 The phase behaviour of phasimidic compound 6 with different central part A. Reproduced with permission from ref [25].

No.	n	-A-	Transition temperatures
6a	6		Col 49 Iso
6b	6		Col 107 Iso
6c	6		Col 163 Iso
6d	8		Cr 67 Col _L 84 Iso
6e	12		Cr 77 Col 82 Iso
6f	12		Cr 70 Col 117 Iso
6g	14		Cr 91 M 109 Col _h 116 Iso
6h	14		Cr 111 Col _{int} 137 Cub 152 Iso

The polycatenars with three aliphatic chains attached at each end of the core are also called phasmids due to its similar shape to insects. Typically, phasmids form Col phases, as listed in Table 1.3 for phasmids with different central cores. Comparing compounds 6a-c, the isotropic temperatures increase by 60 °C with the increase of each phenyl ring. No LC phase is observed in their terphenyl derivatives. For compounds 6a-c, the number of phenyl rings does not affect the phases they form [51]. Thiophenes and

oxadiazoles are introduced in the rigid core due to their application in molecular electronics [52-60]. Compound 6d and e show fluorescence properties in solvent, but the nitrogen atoms in aromatic rings does not affect the phases they form [51, 58]. Compound 6f has an additional methylene unit on each side of the central aromatic rings and still forms Col phase. Compounds 6g and h have different phase behaviour with the different spacers in the rigid core. Apart from the Col phase, a Cub_{mi} phase ($Pm\bar{3}n$) is also found in 6h, which is a rare finding [54, 61]. This might be due to the increase of flexibility of the core.

1.2.2 T-shaped and X-shaped molecules

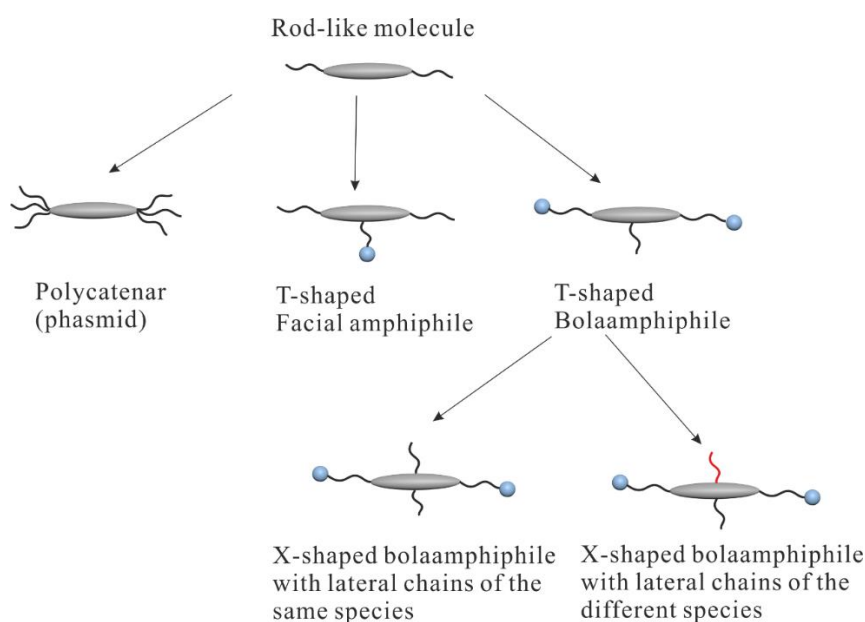


Figure 1.9 T-shaped and X-shaped amphiphile/bolaamphiphile made by rod-like molecules.

In order to further increase the complexity of the mode of self-assembly, the structure and order of LCs, modifications of the shape of rod-like molecule have been carried out by attaching polar groups and aliphatic chains to the side as well as the ends of the core. Molecules of different shapes, such as T-shaped and X-shaped molecules, are obtained

as shown in Figure 1.9. There are two types of T-shaped molecules, bolaamphiphiles and facial amphiphiles. In T-shaped bolaamphiphiles, two polar terminal groups (typically glycerol units) are added at each end of the rod-like core and an alkyl chain is added as a side group. In facial amphiphiles, there are two apolar end groups and a polar side group. X-shaped molecules have two lateral chains on each side of the rigid core and the two chains can be same or different in length or chemical structure. Apart from the linear alkyl chains, the attached side- and end-chains could also be siloxane, semi-fluoroalkyl, perfluoroalkyl, carbosilane, other bulky lipophilic groups or branched chains. A variety of different LCs phases/structures have resulted from this combination of increased complexity in both molecular shapes and chemistry in T- and X-shaped molecules.

Both ionic and non-ionic groups can be introduced in T- and X-shaped molecules, generating different conducting channels for applications as conducting, semiconducting, photoluminescent, photovoltaic materials etc.[62] The soft square and rectangular sub-5 nm LC tiling patterns formed by these molecules are of interest for the application on nanolithography [8]. These nanoscale tiling patterns also have potential applications on selective membranes and drug delivery [10, 63]. Moreover, the polar and unpolar groups on the ends and the sides of the core could also play an important role in generating different functions. For example, X-shaped molecules with different side chains could form multicolour tiling patterns, which can be used not only on nanolithography but also as multi-block LC organic semiconductors [64, 65].

1.2.2.1 T-shaped molecules

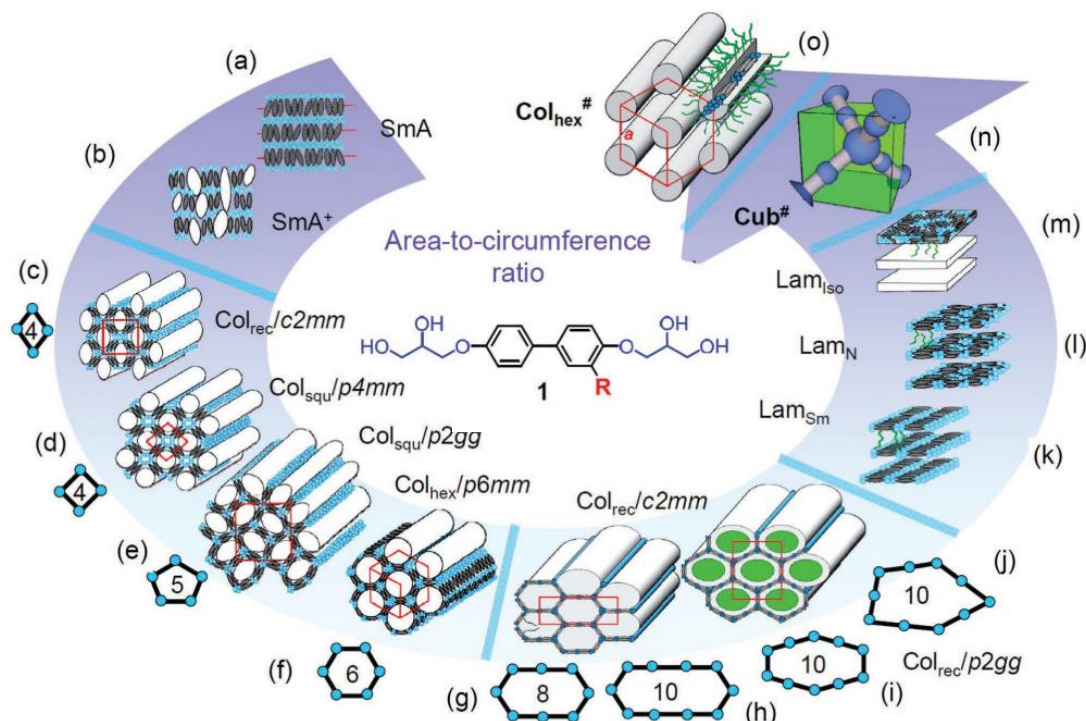


Figure 1.10 Self-assembled liquid crystalline structures formed by T-shaped bolaamphiphile with the increase of chain length. Reproduced with permission from ref [8].

For bolaamphiphiles, two types of smectic phases, SmA and SmA⁺ can be formed when the length of the lateral chains is very short, as shown in **Error! Reference source not found.a-b** [66, 67]. The SmA⁺ phase has typical SmA texture, but segregated side chains are randomly distributed, showing an additional diffuse small angle X-ray scattering [66, 68-70].

A series of more complex and interesting honeycomb 2D columnar phases are formed with longer lateral chains. As shown in **Error! Reference source not found.c-f**, the terminal glycerol groups (coloured blue) act like ‘seams’ that connect the cell walls, aromatic cores (grey) with each other by hydrogen bondings. The space inside of the cell walls of the polygonal cells are filled by side

aliphatic chains (white). Rectangular, square and hexagonal columnar phases with well-defined polygonal shapes (number of sides 4-6) are formed by increasing the lateral chain length [66, 68, 71-73]. Apart from the square columnar phase with $p4mm$ symmetry shown in **Error! Reference source not found.**d, a new rectangular columnar phase with $p2mm$ symmetry composed of four molecules in each unit cell has also been reported recently [8].

Giant cylinder phases are formed by further extending the lateral chain. The excess of the chain length that allowing the formation of regular polygonal shapes lead to the increase of the number of polygonal sides, in the range of 8 to 10, as shown in **Error! Reference source not found.**g-j [66, 72, 74, 75]. Here it is worth comparing the Col phases in Section 1.2.1.1 formed by taper-shaped polycatenars with these honeycomb Col phases. The self-assembling of T-shaped bolaamphiphiles is driven by hydrogen bondings, while it is driven by the incompatibility of aliphatic chains and aromatic cores in taper-shaped polycatenars. The aromatic cores of T-shaped bolaamphiphiles form the cylinder walls and aliphatic chains fill the space inside. However, the inside part of the cylinders formed by taper-shaped polycatenars is aromatic cores, surrounded by the aliphatic chains on the outside.

Further enlargement of the chain leads to the merge of cylinders and the formation of Lam (lamella) phases [66, 68, 76-80]. The rigid cores are π -conjugated and parallel to the layer plane in Lam phases, unlike in Sm phases. When the relative volume of flexible lateral chain can increase either by chemistry (longer lateral chains) or by increasing of temperature, the phase sequence follows the anticlockwise direction around the **Error! Reference source not found.** [62].

In Error! Reference source not found.n and o, a co-axial rod-bundle double diamond cubic phase ($Pn\bar{3}m$, also in Figure 1.11b) and a co-axial rod-bundle hexagonal columnar phase are formed by molecules with branched lateral chains [82-85]. This kind of molecules can also form a 3D honeycomb hexagonal columnar phase ($P6/mmm$), a double gyroid cubic phase ($Ia\bar{3}d$, Figure 1.11a), and a single diamond cubic phase ($Fd\bar{3}m$, Figure 1.11e) [8, 84, 86]. A single-network ‘plumber’s nightmare’ ($Pm\bar{3}m$, Figure 1.11f) cubic phase has also been reported to be formed by T-shaped bolaamphiphiles with two lateral chains recently [81].

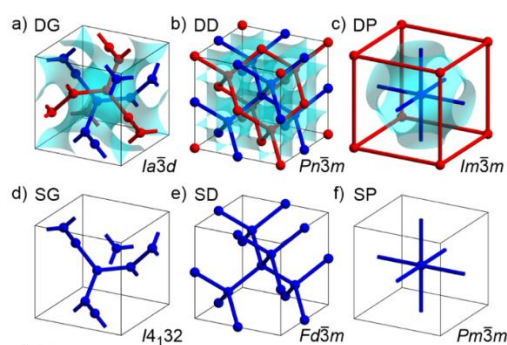


Figure 1.11 (a-c) Double-network with infinite minimal surfaces and (d-f) single-network cubic phases. DG: double gyroid, DD: double diamond, DP: double-network ‘plumber’s nightmare’ structures; SG: single gyroid, SD: single diamond, SP: single-network ‘plumber’s nightmare’ structures. Reproduced with permission from ref [81].

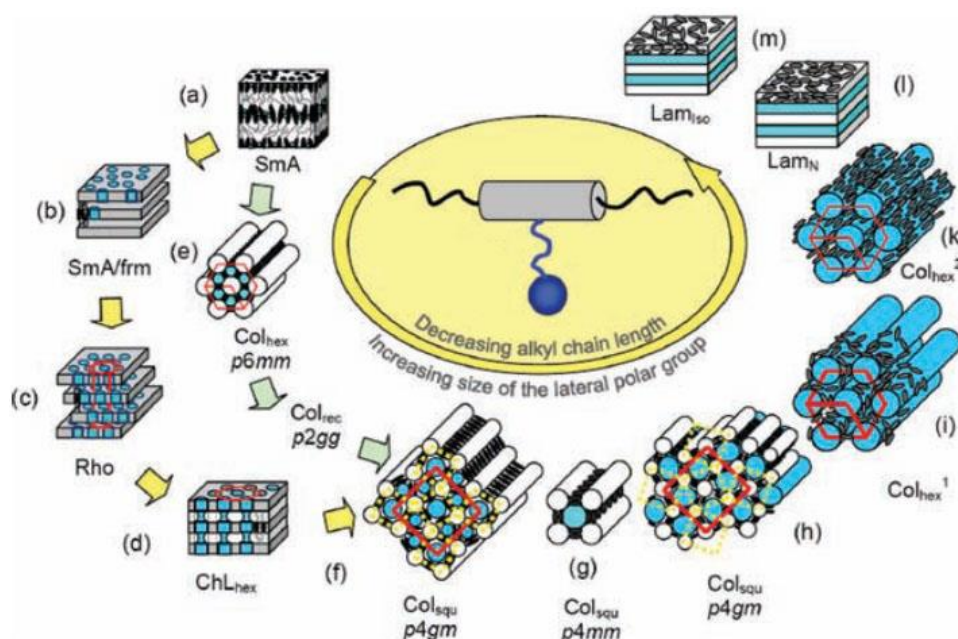


Figure 1.12 Self-assembled liquid crystalline structures formed by T-shaped facial amphiphiles [62, 71]. Reproduced with permission from ref [62].

For facial amphiphiles, the positions of polar and lipophilic groups are reversed comparing with bolaamphiphiles. The sequence of LC phases starts from a conventional SmA phase, with shortest lateral groups, as shown in Figure 1.12 [87, 88]. This is followed by the honeycomb phases with increasing lateral chain length/volume. They are phases with hexagonal ($p6mm$), rectangular ($p2gg$) and square ($p4gm$ and $p4mm$) lattices respectively. In the $p4gm$ phase as shown in Figure 1.12f and h, the cylinders are trapezoidal formed by pentagons (5 molecules) or triangles and squares (3 and 4 molecules) [89, 90]. In addition to the 2D columnar phases, different types of filled mesh phases (SmA/frm (filled random mesh), Rho (3D rhobohedral, $R\bar{3}m$) in Figure 1.12b-c and channelled layer phases (ChL_{hex}, 3D hexagonal lattice, $P6/mmm$) in Figure 1.12d are also found [91]. The aromatic cores are not necessarily confined to lie perpendicular to the column axis, but instead they can be inclined at a high angle or even be close to parallel to the column axis, forming non-honeycomb hexagonal

columnar phase shown in Figure 1.12i, k [62, 92]. Lamellar phases form with further increase of lateral polar groups.

1.2.2.2 X-shaped molecules

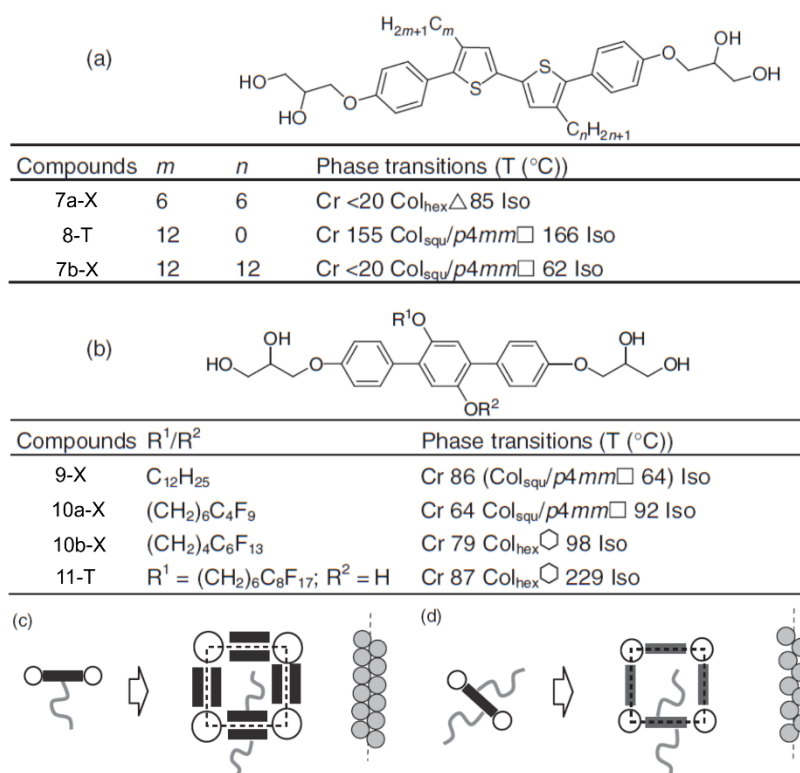


Figure 1.13 (a, b) Comparison of X-shaped (same lateral chains) with T-shaped amphiphilics. (c, d) double-wall and single-wall square cylinders formed by T-shaped and X-shaped amphiphilics, respectively [73, 93, 94]. Reproduced with permission from ref [94].

X-shaped molecules are designed by introducing another side chain in an originally T-shaped molecule, as shown in Figure 1.9. They also form honeycomb phases, but unlike in T-shaped molecules where cylinder walls contain two rigid cores that arrange back to back (Figure 1.13c), the honeycomb wall is only one molecule thick due to the added chain (Figure 1.13d). In fact, the wall thickness is thicker than one molecule as

molecules stagger to improve packing. Thinner walls leave more space for the lateral chains to fill and because of this smaller lattices could be formed. For the X-shaped molecule with the same side chains in Figure 1.13, compound 7a-X forms smaller triangular cylinder compared to square cylinder formed by compound 8-T. However, the LC stability is highly reduced in X-shaped molecules (7a-X vs. 8-T, 9-X or 10-X vs. 11-T) and due to this reason, longer aromatic cores are required for X-shaped molecules [55, 65, 95-102].

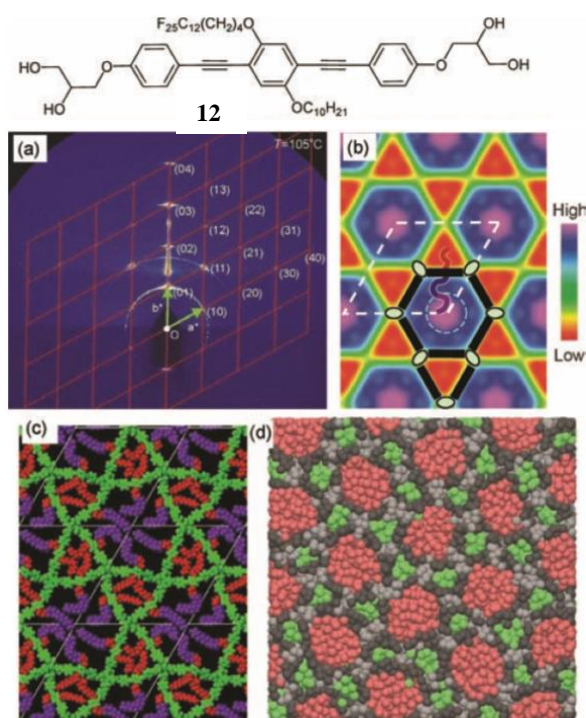


Figure 1.14 Self-assembled liquid crystalline structures formed by X-shaped bolaamphiphiles. Reproduced with permission from ref [103].

In another kind of X-shaped molecules the attached lateral chains are different and incompatible. This makes that the LC honeycomb cells are filled by different lateral chains, increasing the complexity of the LC structure. For example, compound 12 in Figure 1.14 with a alkyl chain and a semiperfluorinated chain on the two sides of the

rigid core, was designed and studied [103]. As these two different lateral chains have different volumes, they need different sizes of columns to fill in. Consequently, hexagonal and triangular columns are formed periodically. The triangles are filled by alkyl chains and the hexagons are filled by semiperfluorinated chains. Molecules connect through hydrogen bondings between glycerol end groups.

In addition, a range of X-shaped molecules were studied and they can form honeycombs of highly complex tiling patterns and polygonal shapes. The achiral double gyroid cubic phase ($Ia\bar{3}d$, Figure 1.11a) and chiral ‘single gyroid’ cubic phase with two chemically non-equal networks ($I4_132$, Figure 1.11b) were also found to be formed by this kind of X-shaped molecules [55, 64, 95, 104-109].

Overall, the studies on T-shaped and X-shaped molecules have contributed significantly to the understanding of complexity of the mode of self-assembly, LC structures and phase sequences, pointing the way to manipulate the designed LC structures for applications.

1.2.3 Bent-core molecules

The above sections mainly describe the modification of molecular shapes on straight rigid cores. However, the LC phases formed by the bent-core molecules, become more complicated because of the reduced symmetry of the molecules. For example, the Col_{hex} phases formed by T-shaped molecules are centrosymmetric with 6-fold symmetry, however, the trigonal columnar phases formed by bent-core molecules are noncentrosymmetric with 3-fold symmetry. These structures formed by bent-core molecules are attractive for their ferroelectric, pyroelectric and nonlinear optical properties. The reduced symmetry of the molecules could also form some other LC

phases (N, Sm) with similar properties. More details will be discussed on simple bent-core molecules and special cases such as bent-core T-shaped bolaamphiphiles and bent-core phasmids in this section.

Bent-core molecules, also called banana-shaped molecules, could form a range of ‘banana phases’, which are different from conventional phases formed by rod-like molecules. The bent-shaped molecules with rigid core can form different kinds of N, Sm and Col phases [110-112]. While in the flexible core bent-shaped molecules, N, chiral N and twist-bend N phases can be formed [113], we will focus on the Sm and Col phases formed by rigid core bent-shaped molecules.

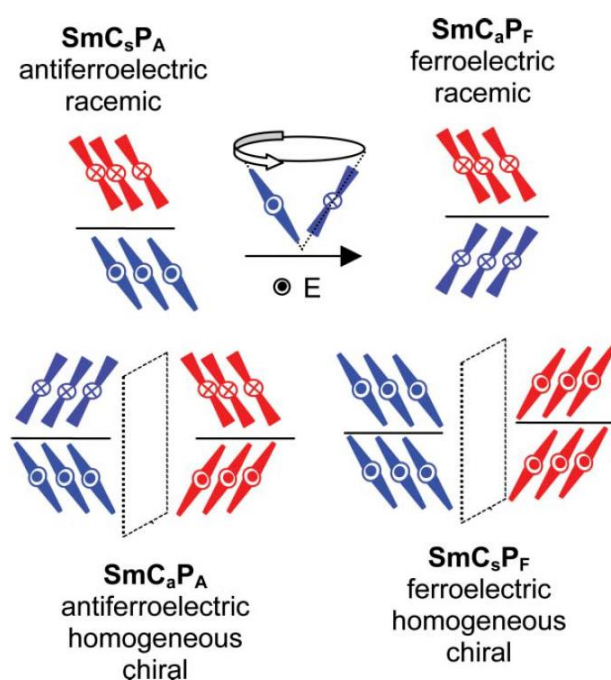


Figure 1.15 The four arrangements of B2 phases. For the abbreviations: C_s = synclitic tilt, C_a = anticlinal tilt, PF = ferroelectric polar order, PA = antiferroelectric polar order. For reproduction of the figure from JMC: Reproduced from ref [114] with permission from The Royal Society of Chemistry.

The ‘banana phases’ are abbreviated as B_n (B1-B7), where n is the sequence of LC discovery. The B2 phase has been extensively studied in banana phases. Its structure is

related to SmC phase formed by rod-like molecules (Figure 1.2a). However, due to the bent core of the molecule, four different arrangements instead of one are formed [115-117], as shown in Figure 1.15. New notations are adopted to describe the four subphases according to their clinicity (S: synclitic tilt, a: anticlinic tilt) and ferroelectricity (PF: ferroelectric polar order, PA: antiferroelectric polar order). From the structures in Figure 1.15, we know that the SmC_sP_a and SmC_aP_F phases are racemic and the SmC_aP_A and SmC_sP_F phases are chiral.

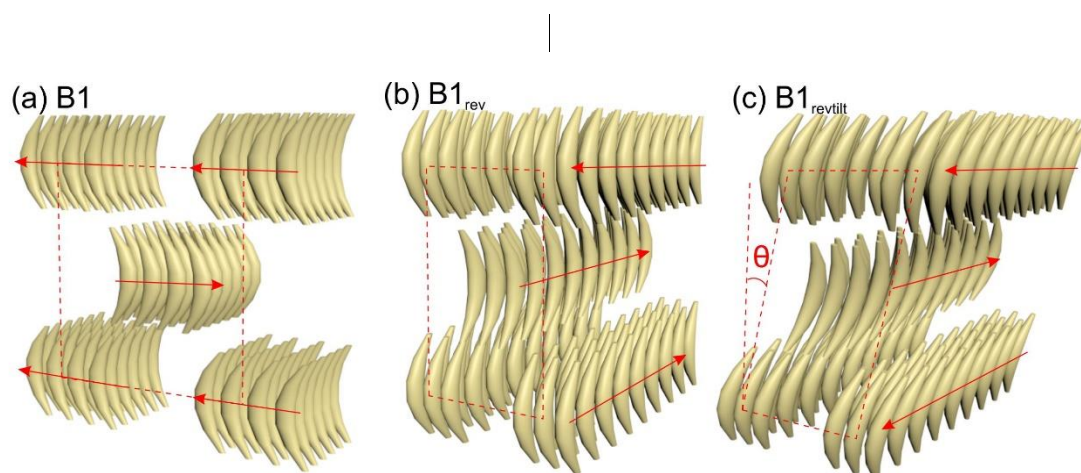


Figure 1.16 The structures of (a) B1 , (b) B1_{rev} and (c) $\text{B1}_{\text{revtilt}}$. The polar direction is indicated by red arrows.

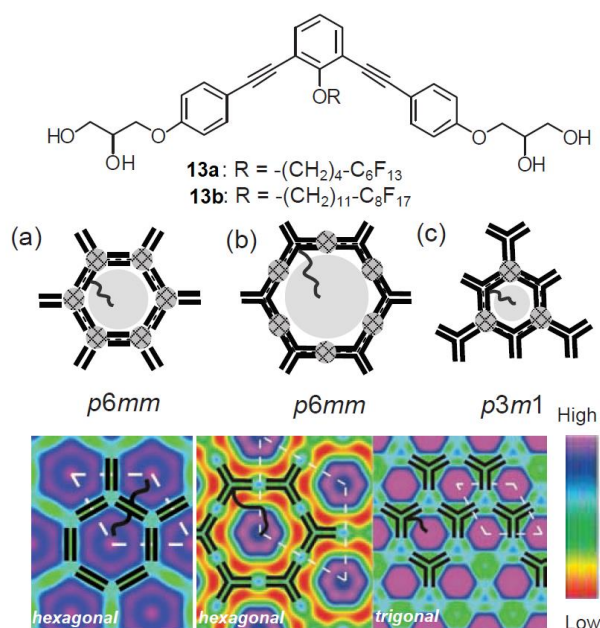


Figure 1.17 Examples of simple bent-core bolaamphiphiles 13a and 13b, and a comparison of the hexagonal honeycombs formed by T-shaped bolaamphiphiles. Reproduced with permission from ref [119].

For the columnar phases, there are two categories. One is formed by frustrated layer fragments, the other is formed by columns composed of disk-shaped assemblies of bent-core molecules [113]. The B1 phase is a frustrated layer structure, forming a 2D Col phase with a rectangular unit cell [118]. There are three variations of the B1 phase, as shown in Figure 1.16. Due to the reversed molecular bend direction between columns, the structures do not possess a polar order in B1 phases. They also do not possess overall chirality even in the tilted case because of the equal number of left- and right-handed columns.

A special series of T-shaped bolaamphiphiles which replace the rigid aromatic core by a bent one is designed to obtain more structures. Compound 13 as shown in Figure 1.17, has an aromatic core with a bend of 120° , form Col_{hex} phases [114]. Compared with the T-shaped bolaamphiphiles, the hydrogen bonding networks in $\text{Col}_{\text{hex}}/p6mm$ phase formed by compound 13b (long side chains) are located in the middle of the walls

instead of in the corners. In the columnar phase with $p3m1$ symmetry formed by compound 13a (short side chain), only every other node contains glycerol groups. However, no method was used to prove trigonal symmetry. In Chapter 3, the trigonal symmetry was confirmed by using second harmonic generation. With the decrease of the volume of the lateral chain, the formed honeycombs change from larger hexagons containing 6 molecules to smaller hexagons containing 3 molecules.

Another kind of bent-core compounds, phasmidic, with three alkyl chains at each ends, were also reported to form Col_{hex} phase. A series of compounds were synthesized and the model proposed for the Col_{hex} phase is an overall flat discoid assembly at higher temperature, as shown in Figure 1.18a. Some voids are shown between the molecular branches. At lower temperatures, a phase transition to a conical-shape phase (Col_{hPA} phase) take place (Figure 1.18b). The voids are filled up by bringing the branches together, which is achieved by the deformation of the flat discs into supermolecular cones. The changes of birefringence and light transmission of the two phases are observed. However, more methods need to be used such as electric properties to prove the arrangements. Also, the voids in the arrangement of Col_{hex} is doubtful as there are flexible linkages between aromatic rings. The three molecules should be able to pack back by back and fill the space well with the aliphatic chains. The bent-core compound in Figure 1.18c, with a dicyanothiophene bend group, was also reported to form a Col_{hex} phase. However, the packing mode proposed was not star-like and was based on antiparallel stacking of overlapping bent cores as for the highly dipolar nature of the core. On the basis of X-ray diffraction, other methods such as computation, UV-vis and fluorescence emission spectroscopy were used to confirm the antiparallel arrangements.

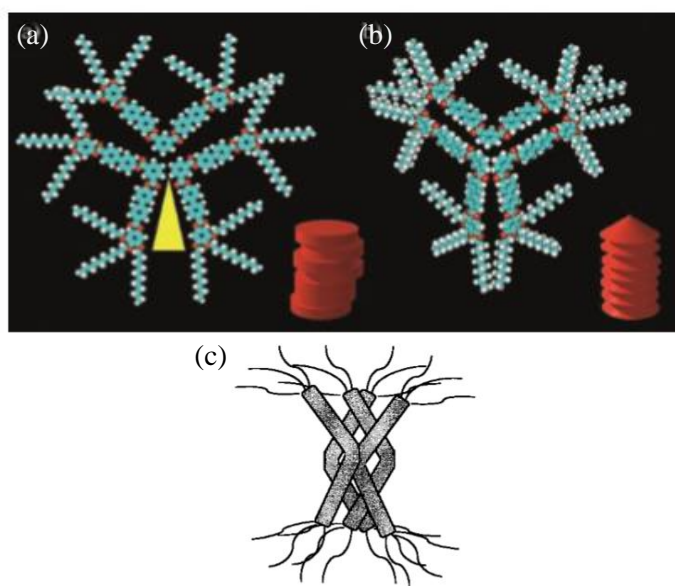
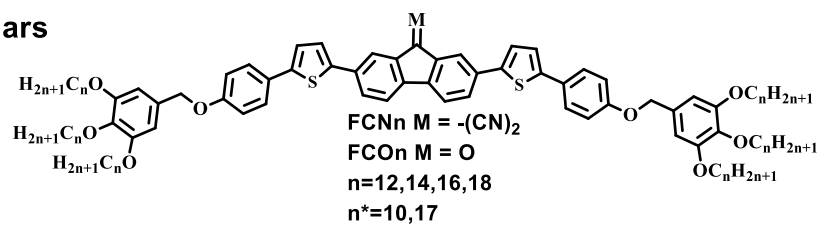


Figure 1.18 Examples of molecular arrangement of phasid bent-core molecules (a) Col_{hex} phase, (b) Col_{hPA} phase and (c) antiparallel bent-core structure. Reproduced with permission from ref [120] and [121].

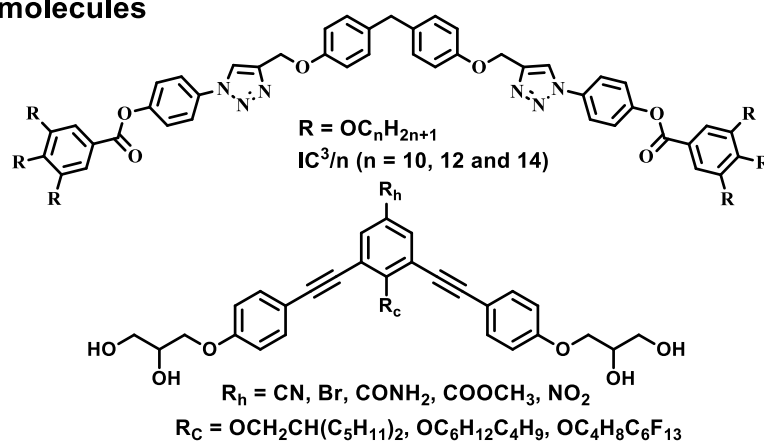
These findings on bent-core molecules indicate that there are still a lot of possibilities to explore, to realize different complex LC phases and structures by modifying the molecular shapes with promising properties for applications.

1.3 Aims and objectives

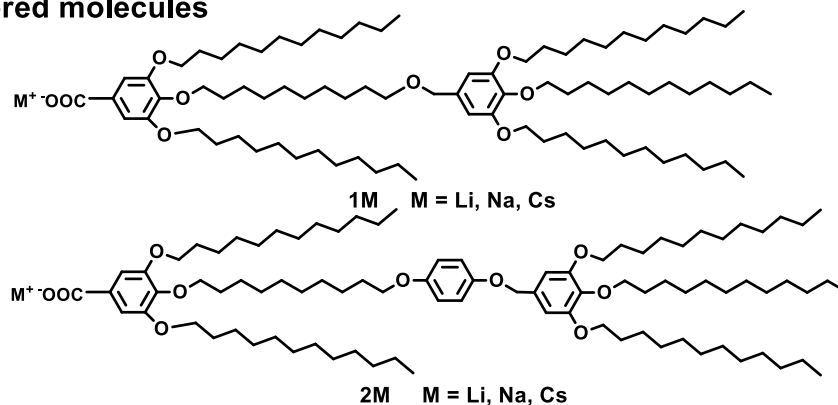
Polycatenars



Bent-core molecules



Double-tapered molecules



Gemini-type amphiphile and bis(trifluoromethanesulfonyl)imide

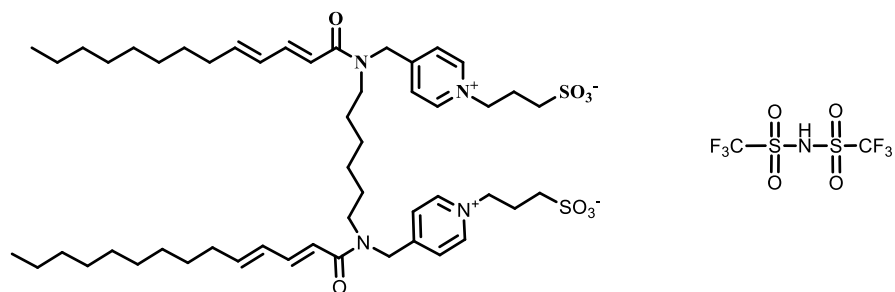


Figure 1.19 The list of compounds of different shapes studied in the thesis.

In this project, our aim is to investigate a series of LC compounds capable of complex, low symmetry self-assembly, study their LC phase behaviours as well as physical properties. These include straight polycatenars (chiral or non-chiral), bent-core polycatenars, simple bent-core bolaamphiphiles, double-tapered molecules and polymerizable gemini-type amphiphile with acid (Figure 1.19). While X-ray diffraction is the main method used to study the structures of the complex LC phases, other spectroscopy and microscopy methods have been used extensively to characterize other physical e.g. optical properties of the compounds, which are important for their potential applications and closely linked to their deliberately introduced low symmetry. More importantly, we aim to understand how such properties could be controlled through self-assembly and from the level of molecular design. More details of experimental methods and analysis are given in Chapter 2.

The higher temperature phase, trigonal columnar phase, formed by bent-core phasimid molecules (IC^3/n) is described in Chapter 3. Second harmonic generation was used to prove the non-centrosymmetric structure rather than centrosymmetric structure.

The lower temperature phase of bent-core phasimids, with an orthorhombic lattice and $Fddd$ space group is investigated in Chapter 4. Interestingly, the same phase is also found to form from straight polycatenars (FCN16 and FCO16), and results are presented in Chapter 4 too.

In Chapter 5, bent-core bolaamphiphiles with different functional groups on the outer side of the bend and a chain on the inner side were investigated. Four types of honeycombs are formed by these compounds and the way to tailor hexagonal, trigonal and superlattice honeycombs in such systems is demonstrated.

In order to widen the range and complexity of LC phases formed by taper-shaped molecules, we have designed double-tapered ionic compounds and studied their phase behaviour as described in Chapter 6.

In Chapter 7, we investigated a gemini-type amphiphile composed of two zwitterionic head groups and polymerized it with bis(trifluoromethanesulfonyl)imide. A self-standing double gyroid cubic phase ($Ia\bar{3}d$) is formed with the ability to absorb water and shows good ionic conductivity, with potential applications in fuel cells.

References

- [1] P.J. Collings, *Liquid crystals: nature's delicate phase of matter*, Princeton University Press, 2002.
- [2] G.W. Gray, S.M. Kelly, *Liquid crystals for twisted nematic display devices*, *J. Mater. Chem.*, **9** (1999) 2037-2050.
- [3] P. Raynes, TN, STN, and Guest–Host Liquid Crystal Display Devices, Chap. 1, in: J.W. Goodby, P.J. Collings, T. Kato, C. Tschierske, H.F. Gleeson, P. Raynes (Eds.) *Handbook of Liquid Crystals*, Wiley-VCH, Weinheim, Germany, Vol. **8**, 2014.
- [4] H. Hong, In-Plane Switching Display Devices, Chap. 2, in: J.W. Goodby, P.J. Collings, T. Kato, C. Tschierske, H.F. Gleeson, P. Raynes (Eds.) *Handbook of Liquid Crystals*, Wiley-VCH, Weinheim, Germany, Vol. **8**, 2014.
- [5] S.T. Lagerwall, *Ferroelectric Liquid Crystal Displays and Devices*, Chap. 7, in: J.W. Goodby, P.J. Collings, T. Kato, C. Tschierske, H.F. Gleeson, P. Raynes (Eds.) *Handbook of Liquid Crystals*, Wiley-VCH, Weinheim, Germany, Vol. **8**, 2014.
- [6] T. Kato, N. Mizoshita, *Self-assembly and phase segregation in functional liquid crystals*, *Curr. Opin. Solid State Mater. Sci.*, **6** (2002) 579-587.
- [7] K. Nickmans, A. Schenning, *Directed Self-Assembly of Liquid-Crystalline Molecular Building Blocks for Sub-5 nm Nanopatterning*, *Adv. Mater.*, **30** (2018).
- [8] A. Lehmann, A. Scholte, M. Prehm, F. Liu, X.B. Zeng, G. Ungar, C. Tschierske, *Soft Rectangular Sub-5 nm Tiling Patterns by Liquid Crystalline Self-Assembly of T-Shaped Bolapolyphiles*, *Adv. Funct. Mater.*, **28** (2018) 1804162.

- [9] M. Gupta, Y. Suzuki, T. Sakamoto, M. Yoshio, S. Torii, H. Katayama, T. Kato, Polymerizable Photocleavable Columnar Liquid Crystals for Nanoporous Water Treatment Membranes, *ACS Macro Lett.*, **8** (2019) 1303-1308.
- [10] K. Hamaguchi, D. Kuo, M. Liu, T. Sakamoto, M. Yoshio, H. Katayama, T. Kato, Nanostructured Virus Filtration Membranes Based on Two-Component Columnar Liquid Crystals, *ACS Macro Lett.*, **8** (2019) 24-30.
- [11] T. Sakamoto, T. Ogawa, H. Nada, K. Nakatsuji, M. Mitani, B. Soberats, K. Kawata, M. Yoshio, H. Tomioka, T. Sasaki, M. Kimura, M. Henmi, T. Kato, Development of Nanostructured Water Treatment Membranes Based on Thermotropic Liquid Crystals: Molecular Design of Sub-Nanoporous Materials, *Adv. Sci.*, **5** (2018).
- [12] Y. Shimizu, K. Oikawa, K.I. Nakayama, D. Guillon, Mesophase semiconductors in field effect transistors, *J. Mater. Chem.*, **17** (2007) 4223-4229.
- [13] H. Iino, T. Usui, J. Hanna, Liquid crystals for organic thin-film transistors, *Nat. Comm.*, **6** (2015).
- [14] J.H. Lee, S.Y. Jeong, G. Kim, B. Park, J. Kim, S. Kee, B. Kim, K. Lee, Reinforcing the Built-In Field for Efficient Charge Collection in Polymer Solar Cells, *Adv. Funct. Mater.*, **28** (2018).
- [15] J. Zhang, Q. Sun, Q.Y. Chen, Y.K. Wang, Y. Zhou, B. Song, N.Y. Yuan, J.N. Ding, Y.F. Li, High Efficiency Planar p-i-n Perovskite Solar Cells Using Low-Cost Fluorene-Based Hole Transporting Material, *Adv. Funct. Mater.*, **29** (2019).
- [16] S. Daskeviciute, N. Sakai, M. Franckevicius, M. Daskeviciene, A. Magomedov, V. Jankauskas, H.J. Snaith, V. Getautis, Nonspiro, Fluorene-Based, Amorphous Hole Transporting Materials for Efficient and Stable Perovskite Solar Cells, *Adv. Sci.*, **5** (2018).
- [17] Suman, A. Bagui, A. Garg, B. Tyagi, V. Gupta, S.P. Singh, A fluorene-core-based electron acceptor for fullerene-free BHJ organic solar cells-towards power conversion efficiencies over 10%, *Chem. Commun.*, **54** (2018) 4001-4004.
- [18] D. Demus, J.W. Goodby, G.W. Gray, H.W. Spiess, V. Vill, *Handbook of Liquid Crystals*, Wiley-VCH, Weinheim, Germany, 1998.
- [19] C. Tschierske, 6 Non-conventional soft matter, *Annual Reports Section "C" (Phys. Chem.)*, **97** (2001) 191-267.
- [20] J.W. Goodby, G.H. Mehl, I.M. Saez, R.P. Tuffin, G. Mackenzie, R. Auzély-Velty, T. Benvegnu, D. Plusquellec, Liquid crystals with restricted molecular topologies: supermolecules and supramolecular assemblies, *Chem. Commun.*, (1998) 2057-2070.

- [21] C. Tschierske, Micro-segregation, molecular shape and molecular topology—partners for the design of liquid crystalline materials with complex mesophase morphologies Basis of a presentation given at Materials Discussion No. 4, 11–14 September 2001, Grasmere, UK, *J. Mater. Chem.*, **11** (2001) 2647-2671.
- [22] S. Sergeev, W. Pisula, Y.H. Geerts, Discotic liquid crystals: a new generation of organic semiconductors, *Chem. Soc. Rev.*, **36** (2007) 1902-1929.
- [23] K. Binnemans, Ionic liquid crystals, *Chem. Rev.*, **105** (2005) 4148-4204.
- [24] P.J. Jessy, S. Radha, N. Patel, Morphological, optical and dielectric behavior of chiral nematic liquid crystal mixture: Study on effect of different amount of chirality, *J. Mol. Liq.*, **255** (2018) 215-223.
- [25] W. Weissflog, Laterally Alkyl- and Aryl-Substituted, Swallow-Tailed, and Polycatenar Mesogens: Structural Features and Functionalities, Chap. 3, in: J.W. Goodby, P.J. Collings, T. Kato, C. Tschierske, H.F. Gleeson, P. Raynes (Eds.) *Handbook of Liquid Crystals*, Wiley-VCH, Weinheim, Germany, Vol. **5**, 2014, pp. 89-154.
- [26] W. Weissflog, A. Wiegeleben, S. Diele, D. Demus, Liquid-crystalline swallow-tailed compounds 1, *Cryst. Res. Technol.*, **19** (1984) 583-591.
- [27] W. Weissflog, G. Pelzl, H. Kresse, D. Demus, LIQUID-CRYSTALLINE SWALLOW-TAILED COMPOUNDS .3. SWALLOW-TAILED COMPOUNDS WITH TERMINAL CYANO GROUPS, *Cryst. Res. Technol.*, **23** (1988) 1259-1265.
- [28] X.H. Cheng, X.Q. Bai, S. Jing, H. Ebert, M. Prehm, C. Tschierske, Self-Assembly of Imidazolium-Based Rodlike Ionic Liquid Crystals: Transition from Lamellar to Micellar Organization, *Chem. Eur. J.*, **16** (2010) 4588-4601.
- [29] V.S.K. Balagurusamy, G. Ungar, V. Percec, G. Johansson, Rational design of the first spherical supramolecular dendrimers self-organized in a novel thermotropic cubic liquid-crystalline phase and the determination of their shape by X-ray analysis, *J. Am. Chem. Soc.*, **119** (1997) 1539-1555.
- [30] K. Borisch, S. Diele, P. Goring, H. Muller, C. Tschierske, Amphiphilic N-benzoyl-1-amino-1-deoxy-D-glucitol derivatives forming thermotropic lamellar, columnar and different types of cubic mesophases, *Liq. Cryst.*, **22** (1997) 427-443.
- [31] X. Zeng, G. Ungar, Spontaneously chiral cubic liquid crystal: three interpenetrating networks with a twist, *J. Mater. Chem. C*, (2020).
- [32] C. Dressel, F. Liu, M. Prehm, X. Zeng, G. Ungar, C. Tschierske, Dynamic mirror-symmetry breaking in bicontinuous cubic phases, *Angew. Chem. Int. Ed.*, **53** (2014) 13115-13120.

- [33] X. Zeng, L. Cseh, G.H. Mehl, G. Ungar, Testing the triple network structure of the cubic $Im\bar{3}m$ (I) phase by isomorphous replacement and model refinement, *J. Mater. Chem.*, **18** (2008) 2953.
- [34] X. Zeng, G. Ungar, M. Imperor-Clerc, A triple-network tricontinuous cubic liquid crystal, *Nat. Mater.*, **4** (2005) 562-567.
- [35] G. Ungar, F. Liu, X. Zeng, Cubic and other Thermotropic Liquid Crystal Phases and Quasicrystals, Chap. 7, in: J.W. Goodby, P.J. Collings, T. Kato, C. Tschierske, H.F. Gleeson, P. Raynes (Eds.) *Handbook of Liquid Crystals*, Wiley-VCH, Weinheim, Germany, Vol. **5**, 2014.
- [36] C. Dressel, T. Reppe, M. Prehm, M. Brautzsch, C. Tschierske, Chiral self-sorting and amplification in isotropic liquids of achiral molecules, *Nat. Chem.*, **6** (2014) 971-977.
- [37] M. Alaasar, S. Poppe, Q.S. Dong, F. Liu, C. Tschierske, Mirror symmetry breaking in cubic phases and isotropic liquids driven by hydrogen bonding, *Chem. Commun.*, **52** (2016) 13869-13872.
- [38] M. Alaasar, M. Prehm, Y. Cao, F. Liu, C. Tschierske, Spontaneous Mirror-Symmetry Breaking in Isotropic Liquid Phases of Photoisomerizable Achiral Molecules, *Angew. Chem. Int. Ed.*, **55** (2016) 312-316.
- [39] H.J. Lu, X.B. Zeng, G. Ungar, C. Dressel, C. Tschierske, The Solution of the Puzzle of Smectic-Q: The Phase Structure and the Origin of Spontaneous Chirality, *Angew. Chem. Int. Ed.*, **57** (2018) 2835-2840.
- [40] C. Tschierske, Mirror symmetry breaking in liquids and liquid crystals, *Liq. Cryst.*, **45** (2018) 2221-2252.
- [41] Tino Reppe, Christian Dressel, Silvio Poppe, C. Tschierske, Controlling spontaneous mirror symmetry breaking in cubic liquid crystalline phases by the cycloaliphatic ring size, *Chem. Commun.*, **56** (2020) 711-714.
- [42] A.M. Levelut, M. Clerc, Structural investigations on 'smectic D' and related mesophases, *Liq. Cryst.*, **24** (1998) 105-115.
- [43] K. Saito, Y. Yamamura, Y. Miwa, S. Kutsumizu, A structural model of the chiral " $Im\bar{3}m$ " cubic phase, *PCCP*, **18** (2016) 3280-3284.
- [44] M. Vogrin, N. Vaupotic, M.M. Wojcik, J. Mieczkowski, K. Madrak, D. Pocięcha, E. Gorecka, Thermotropic cubic and tetragonal phases made of rod-like molecules, *PCCP*, **16** (2014) 16067-16074.

- [45] T. Yamamoto, I. Nishiyama, M. Yoneya, H. Yokoyama, Novel Chiral Effect That Produces the Anisotropy in 3D Structured Soft Material: Chirality-Driven Cubic-Tetragonal Liquid Crystal Phase Transition, *J. Phys. Chem. B*, **113** (2009) 11564-11567.
- [46] B. Pansu, Y. Nastishin, M. Imperor-Clerc, M. Veber, H.T. Nguyen, New investigation on the tetragonal liquid-crystalline phase or SmQ, *Eur. Phys. J. E*, **15** (2004) 225-230.
- [47] N.H. Tinh, C. Destrade, A.M. Levelut, J. Malthete, Biforked mesogens - A new type of thermotropic liquid crystals, *Journal De Physique*, **47** (1986) 553-557.
- [48] C. Dressel, W. Weissflog, C. Tschierske, Spontaneous mirror symmetry breaking in a re-entrant isotropic liquid, *Chem. Commun.*, **51** (2015) 15850-15853.
- [49] W. Weissflog, I. Letko, G. Pelzl, S. Diele, Reentrant isotropic behavior of a pure double-swallow-tailed compound, *Liq. Cryst.*, **18** (1995) 867-870.
- [50] W. Weissflog, M. Rogunova, I. Letko, S. Diele, G. Pelzl, A reentrant smectic-C phase in a sequence smectic-C oblique-columnar smectic-C nematic, *Liq. Cryst.*, **19** (1995) 541-544.
- [51] N.H. Sultana, S.M. Kelly, B. Mansoor, M. O'Neill, Polycatenar oligophenylene liquid crystals, *Liq. Cryst.*, **34** (2007) 1307-1316.
- [52] Y.L. Xiao, R.L. Zhang, H.F. Gao, H.M. Zhao, X.H. Cheng, Benzothiadiazole-based bolaamphiphiles: synthesis, self-assembly and white-light emissive properties, *J. Mater. Chem. C*, **7** (2019) 1237-1245.
- [53] L.M. Popescu, P. van 't Hof, A.B. Sieval, H.T. Jonkman, J.C. Hummelen, Thienyl analog of 1-(3-methoxycarbonyl)propyl-1-phenyl-[6,6]-methanofullerene for bulk heterojunction photovoltaic devices in combination with polythiophenes, *Appl. Phys. Lett.*, **89** (2006) 213507.
- [54] T. Yasuda, H. Ooi, J. Morita, Y. Akama, K. Minoura, M. Funahashi, T. Shimomuro, T. Kato, pi-Conjugated Oligothiophene-Based Polycatenar Liquid Crystals: Self-Organization and Photoconductive, Luminescent, and Redox Properties, *Adv. Funct. Mater.*, **19** (2009) 411-419.
- [55] H.F. Gao, Y.F. Ye, L.Y. Kong, X.H. Cheng, M. Prehm, H. Ebert, C. Tschierske, Dithiophene based X-shaped bolaamphiphiles: liquid crystals with single wall honeycombs and geometric frustration, *Soft Matter*, **8** (2012) 10921-10931.
- [56] W. Bu, H.F. Gao, X.P. Tan, X. Dong, X.H. Cheng, M. Prehm, C. Tschierske, A bolaamphiphilic sexithiophene with liquid crystalline triangular honeycomb phase, *Chem. Commun.*, **49** (2013) 1756-1758.

- [57] H.F. Gao, H.F. Cheng, Z.H. Yang, M. Prehm, X.H. Cheng, C. Tschierske, Synthesis and self-assembly of 5,5'-bis(phenylethynyl)-2,2'-bithiophene-based bolapolyphiles in triangular and square LC honeycombs, *J. Mater. Chem. C*, **3** (2015) 1301-1308.
- [58] H.T. Wang, F.L. Zhang, B.L. Bai, P. Zhang, J.H. Shi, D.Y. Yu, Y.F. Zhao, Y. Wang, M. Li, Synthesis, liquid crystalline properties and fluorescence of polycatenar 1,3,4-oxadiazole derivatives, *Liq. Cryst.*, **35** (2008) 905-912.
- [59] E. Westphal, M. Prehm, I.H. Bechtold, C. Tschierske, H. Gallardo, Room temperature columnar liquid crystalline phases of luminescent non-symmetric star-shaped molecules containing two 1,3,4-oxadiazole units, *J. Mater. Chem. C*, **1** (2013) 8011-8022.
- [60] D. Chen, M. Nakata, R. Shao, M.R. Tuchband, M. Shuai, U. Baumeister, W. Weissflog, D.M. Walba, M.A. Glaser, J.E. MacLennan, N.A. Clark, Twist-bend heliconical chiral nematic liquid crystal phase of an achiral rigid bent-core mesogen, *Phys. Rev. E*, **89** (2014) 022506.
- [61] T. Yasuda, K. Kishimoto, T. Kato, Columnar liquid crystalline pi-conjugated oligothiophenes, *Chem. Commun.*, (2006) 3399-3401.
- [62] G. Ungar, C. Tschierske, V. Abetz, R. Holyst, M.A. Bates, F. Liu, M. Prehm, R. Kieffer, X. Zeng, M. Walker, B. Glettner, A. Zywockinski, Self-Assembly at Different Length Scales: Polyphilic Star-Branched Liquid Crystals and Mikroarm Star Copolymers, *Adv. Funct. Mater.*, **21** (2011) 1296-1323.
- [63] R.K. Thapa, R. Baskaran, T. Madheswaran, J.Y. Rhyu, J.O. Kim, C.S. Yong, B.K. Yoo, Effect of saturated fatty acids on tacrolimus-loaded liquid crystalline nanoparticles, *J. Drug Deliv. Sci. Technol.*, **23** (2013) 137-141.
- [64] X. Zeng, R. Kieffer, B. Glettner, C. Nürnberger, F. Liu, K. Pelz, M. Prehm, U. Baumeister, H. Hahn, H. Lang, Complex multicolor tilings and critical phenomena in tetraphilic liquid crystals, *Science*, **331** (2011) 1302-1306.
- [65] C. Nurnberger, H.J. Lu, X.B. Zeng, F. Liu, G. Ungar, H. Hahn, H. Lang, M. Prehm, C. Tschierske, Soft self-assembled sub-5 nm scale chessboard and snub-square tilings with oligo(paraphenyleneethynylene) rods, *Chem. Commun.*, **55** (2019) 4154-4157.
- [66] X. Cheng, M. Prehm, M.K. Das, J. Kain, U. Baumeister, S. Diele, D. Leine, A. Blume, C. Tschierske, Calamitic bolaamphiphiles with (semi) perfluorinated lateral chains: polyphilic block molecules with new liquid crystalline phase structures, *J. Am. Chem. Soc.*, **125** (2003) 10977-10996.

- [67] A. Lehmann, M. Prehm, C.L. Chen, F. Liu, X.B. Zeng, G. Ungar, C. Tschierske, Transition between tangential and co-axial liquid crystalline honeycombs in the self-assembly of Y-shaped bolaamphiphiles, *Chem. Commun.*, **54** (2018).
- [68] X.H. Cheng, M.K. Das, U. Baumeister, S. Diele, C. Tschierske, Liquid crystalline bolaamphiphiles with semiperfluorinated lateral chains: Competition between layerlike and honeycomb-like organization, *J. Am. Chem. Soc.*, **126** (2004) 12930-12940.
- [69] X.H. Cheng, X. Dong, R. Huang, X.B. Zeng, G. Ungar, M. Prehm, C. Tschierske, Polygonal cylinder phases of 3-alkyl-2,5-diphenylthiophene-based bolaamphiphiles: Changing symmetry by retaining net topology, *Chem. Mater.*, **20** (2008) 4729-4738.
- [70] M. Kolbel, T. Beyersdorff, X.H. Cheng, C. Tschierske, J. Kain, S. Diele, Design of liquid crystalline block molecules with nonconventional mesophase morphologies: Calamitic bolaamphiphiles with lateral alkyl chains, *J. Am. Chem. Soc.*, **123** (2001) 6809-6818.
- [71] C. Tschierske, Liquid crystal engineering--new complex mesophase structures and their relations to polymer morphologies, nanoscale patterning and crystal engineering, *Chem. Soc. Rev.*, **36** (2007) 1930-1970.
- [72] M. Prehm, F. Liu, U. Baumeister, X. Zeng, G. Ungar, C. Tschierske, The giant-hexagon cylinder network--a liquid-crystalline organization formed by a T-shaped quaternary amphiphile, *Angew. Chem. Int. Ed.*, **46** (2007) 7972-7975.
- [73] X.H. Cheng, X. Dong, G.H. Wei, M. Prehm, C. Tschierske, Liquid-Crystalline Triangle Honeycomb Formed by a Dithiophene-Based X-Shaped Bolaamphiphile, *Angew. Chem. Int. Ed.*, **48** (2009) 8014-8017.
- [74] A. Scholte, S. Hauche, M. Wagner, M. Prehm, S. Poppe, C.L. Chen, F. Liu, X.B. Zeng, G. Ungar, C. Tschierske, A self-assembled liquid crystal honeycomb of highly stretched (3-1-1)-hexagons, *Chem. Commun.*, **56** (2020) 62-65.
- [75] M. Prehm, C. Enders, M.Y. Anzahae, B. Glettner, U. Baumeister, C. Tschierske, Distinct columnar and lamellar liquid crystalline phases formed by new bolaamphiphiles with linear and branched lateral hydrocarbon chains, *Chem. Eur. J.*, **14** (2008) 6352-6368.
- [76] M. Prehm, C. Enders, X. Mang, X. Zeng, F. Liu, G. Ungar, U. Baumeister, C. Tschierske, Lamellar Liquid Crystals of In-Plane Lying Rod-Like Mesogens with Designer Side-Chains: The Case of Sliding versus Locked Layers, *Chemistry*, **24** (2018) 16072-16084.
- [77] X.H. Cheng, M.K. Das, S. Diele, C. Tschierske, Novel liquid-crystalline phases with layerlike organization, *Angew. Chem. Int. Ed.*, **41** (2002) 4031-4035.

- [78] M. Prehm, X.H. Cheng, S. Diele, M.K. Das, C. Tschierske, New liquid crystalline phases with layerlike organization, *J. Am. Chem. Soc.*, **124** (2002) 12072-12073.
- [79] N.M. Patel, M.R. Dodge, M.H. Zhu, R.G. Petschek, C. Rosenblatt, M. Prehm, C. Tschierske, Twist elasticity and anchoring in a lamellar nematic phase, *Phys. Rev. Lett.*, **92** (2004).
- [80] N.M. Patel, I.M. Syed, C. Rosenblatt, M. Prehm, C. Tschierske, Possible structures for the lamellar-isotropic (Lam-I) and lamellar-nematic (Lam-N) liquid crystalline phases, *Liq. Cryst.*, **32** (2005) 55-61.
- [81] P. Silvio, C. Xiaohong, C. Changlong, Z. Xiangbing, Z. Rui-bin, L. Feng, U. Goran, T. Carsten, Liquid Organic Frameworks: The Single Network “Plumber's Nightmare” Bicontinuous Cubic Liquid Crystal, *J. Am. Chem. Soc.*, **142** (2020) 3296-3300.
- [82] M. Prehm, F. Liu, X. Zeng, G. Ungar, C. Tschierske, 2D and 3D Ordered Columnar Liquid Crystal Phases by Bundles of Bolaamphiphiles with Swallow-Tail Side Chains, *J. Am. Chem. Soc.*, **130** (2008) 14922-14923.
- [83] C. Tschierske, Development of Structural Complexity by Liquid-Crystal Self-assembly, *Angew. Chem. Int. Ed.*, **52** (2013) 8828-8878.
- [84] X.B. Zeng, S. Poppe, A. Lehmann, M. Prehm, C.L. Chen, F. Liu, H.J. Lu, G. Ungar, C. Tschierske, A Self-Assembled Bicontinuous Cubic Phase with a Single-Diamond Network, *Angew. Chem. Int. Ed.*, **58** (2019) 7375-7379.
- [85] X. Zeng, M. Prehm, G. Ungar, C. Tschierske, F. Liu, Formation of a Double Diamond Cubic Phase by Thermotropic Liquid Crystalline Self-Assembly of Bundled Bolaamphiphiles, *Angew. Chem. Int. Ed.*, **55** (2016) 8324-8327.
- [86] S. Poppe, C.L. Chen, F. Liu, C. Tschierske, A skeletal double gyroid formed by single coaxial bundles of catechol based bolapolyphiles, *Chem. Commun.*, **54** (2018) 11196-11199.
- [87] B. Chen, U. Baumeister, S. Diele, M.K. Das, X.B. Zeng, G. Ungar, C. Tschierske, A new type of square columnar liquid crystalline phases formed by facial amphiphilic triblock molecules, *J. Am. Chem. Soc.*, **126** (2004) 8608-8609.
- [88] B. Chen, U. Baumeister, G. Pelzl, M.K. Das, X.B. Zeng, G. Ungar, C. Tschierske, Carbohydrate rod conjugates: Ternary rod-coil molecules forming complex liquid crystal structures, *Journal of the American Chemical Society*, **127** (2005) 16578-16591.
- [89] B. Chen, X.B. Zeng, U. Baumeister, G. Ungar, C. Tschierske, Liquid crystalline networks composed of pentagonal, square, and triangular cylinders, *Science*, **307** (2005) 96-99.

- [90] F. Liu, B. Chen, B. Glettner, M. Prehm, M.K. Das, U. Baumeister, X. Zeng, G. Ungar, C. Tschierske, The trapezoidal cylinder phase: A new mode of self-assembly in liquid-crystalline soft matter, *J. Am. Chem. Soc.*, **130** (2008) 9666-+.
- [91] B. Chen, X.B. Zeng, U. Baumeister, S. Diele, G. Ungar, C. Tschierske, Liquid crystals with complex superstructures, *Angew. Chem. Int. Ed.*, **43** (2004) 4621-4625.
- [92] B. Chen, U. Baumeister, G. Pelzl, M.K. Das, X. Zeng, G. Ungar, C. Tschierske, Carbohydrate Rod Conjugates: Ternary Rod–Coil Molecules Forming Complex Liquid Crystal Structures, *J. Am. Chem. Soc.*, **127** (2005) 16578-16591.
- [93] R. Kieffer, M. Prehm, B. Glettner, K. Pelz, U. Baumeister, F. Liu, X.B. Zeng, G. Ungar, C. Tschierske, X-Shaped polyphilics: liquid crystal honeycombs with single-molecule walls, *Chem. Commun.*, (2008) 3861-3863.
- [94] C. Tschierske, G. Ungar, Side-Branched Polyphiles and Polygonal Cylinder Phases, Chap. 8, in: J.W. Goodby, P.J. Collings, T. Kato, C. Tschierske, H.F. Gleeson, P. Raynes (Eds.) *Handbook of Liquid Crystals*, Wiley-VCH, Weinheim, Germany, Vol. **5**, 2014, pp. 437-479.
- [95] X.H. Cheng, H.F. Gao, X.P. Tan, X.Y. Yang, M. Prehm, H. Ebert, C. Tschierske, Transition between triangular and square tiling patterns in liquid-crystalline honeycombs formed by tetrathiophene-based bolaamphiphiles, *Chem. Sci.*, **4** (2013) 3317-3331.
- [96] E. Lee, J.K. Kim, M. Lee, Reversible scrolling of two-dimensional sheets from the self-assembly of laterally grafted amphiphilic rods, *Angew. Chem. Int. Ed.*, **48** (2009) 3657-3660.
- [97] P. Niton, A. Zywockinski, R. Holyst, R. Kieffer, C. Tschierske, J. Paczesny, D. Pocięcha, E. Gorecka, Reversible aggregation of X-Shaped bolaamphiphiles with partially fluorinated lateral chains at the air/water interface, *Chem. Commun.*, **46** (2010) 1896-1898.
- [98] P. Niton, A. Zywockinski, J. Paczesny, M. Fialkowski, R. Holyst, B. Glettner, R. Kieffer, C. Tschierske, D. Pocięcha, E. Gorecka, Aggregation and Layering Transitions in Thin Films of X-, T-, and Anchor-Shaped Bolaamphiphiles at the Air-Water Interface, *Chem. Eur. J.*, **17** (2011) 5861-5873.
- [99] S. Poppe, M. Poppe, H. Ebert, M. Prehm, C.L. Chen, F. Liu, S. Werner, K. Bacia, C. Tschierske, Effects of Lateral and Terminal Chains of X-Shaped Bolapolyphiles with Oligo(phenylene ethynylene) Cores on Self-Assembly Behaviour. Part 1: Transition between Amphiphilic and Polyphilic Self-Assembly in the Bulk, *Polymers*, **9** (2017).

- [100] W.S. Fall, C. Nurnberger, X.B. Zeng, F. Liu, S.J. Kearney, G.A. Gehring, C. Tschierske, G. Ungar, An Ising transition of chessboard tilings in a honeycomb liquid crystal, *Mol. Syst. Des. Eng.*, **4** (2019) 396-406.
- [101] J. Paczesny, P. Niton, A. Zywockinski, K. Sozanski, R. Holyst, M. Fialkowski, R. Kieffer, B. Glettner, C. Tschierske, D. Pocięcha, E. Gorecka, Stable, ordered multilayers of partially fluorinated bolaamphiphiles at the air-water interface, *Soft Matter*, **8** (2012) 5262-5272.
- [102] B.D. Lechner, H. Ebert, M. Prehm, S. Werner, A. Meister, G. Hause, A. Beerlink, K. Saalwachter, K. Bacia, C. Tschierske, A. Blume, Temperature-Dependent In-Plane Structure Formation of an X-Shaped Bolapolyphile within Lipid Bilayers, *Langmuir*, **31** (2015) 2839-2850.
- [103] B. Glettner, F. Liu, X. Zeng, M. Prehm, U. Baumeister, M. Walker, M.A. Bates, P. Boesecke, G. Ungar, C. Tschierske, Liquid-crystalline kagome, *Angew. Chem. Int. Ed.*, **47** (2008) 9063-9066.
- [104] F. Liu, R. Kieffer, X. Zeng, K. Pelz, M. Prehm, G. Ungar, C. Tschierske, Arrays of giant octagonal and square cylinders by liquid crystalline self-assembly of X-shaped polyphilic molecules, *Nat. Comm.*, **3** (2012) 1104.
- [105] C. Tschierske, C. Nurnberger, H. Ebert, B. Glettner, M. Prehm, F. Liu, X.B. Zeng, G. Ungar, Complex tiling patterns in liquid crystals, *Interface Focus*, **2** (2012) 669-680.
- [106] M. Poppe, C.L. Chen, H. Ebert, S. Poppe, M. Prehm, C. Kerzig, F. Liu, C. Tschierske, Transition from nematic to gyroid-type cubic soft self-assembly by side-chain engineering of pi-conjugated sticky rods, *Soft Matter*, **13** (2017) 4381-4392.
- [107] M. Poppe, C.L. Chen, F. Liu, S. Poppe, C. Tschierske, Formation of a Cubic Liquid Crystalline Nanostructure with pi-Conjugated Fluorinated Rods on the Gyroid Minimal Surface, *Chem. Eur. J.*, **23** (2017) 7196-7200.
- [108] M. Poppe, C.L. Chen, F. Liu, M. Prehm, S. Poppe, C. Tschierske, Emergence of tilt in square honeycomb liquid crystals, *Soft Matter*, **13** (2017) 4676-4680.
- [109] C.L. Chen, R. Kieffer, H. Ebert, M. Prehm, R.B. Zhang, X.B. Zeng, F. Liu, G. Ungar, C. Tschierske, Chirality Induction through Nano-Phase Separation: Alternating Network Gyroid Phase by Thermotropic Self-Assembly of X-Shaped Bolapolyphiles, *Angew. Chem. Int. Ed.*, **59** (2020) 2725-2729.
- [110] S.H. Eichhorn, A.J. Paraskos, K. Kishikawa, T.M. Swager, The interplay of bent-shape, lateral dipole and chirality in thiophene based di-, tri-, and tetracatenar liquid crystals, *J. Am. Chem. Soc.*, **124** (2002) 12742-12751.

- [111] A.J. Paraskos, T.M. Swager, Effects of desymmetrization on thiophene-based bent-rod mesogens, *Chem. Mater.*, **14** (2002) 4543-4549.
- [112] H. Gallardo, M. Ferreira, A.A. Vieira, E. Westphal, F. Molin, J. Eccher, I.H. Bechtold, Columnar mesomorphism of bent-rod mesogens containing 1,2,4-oxadiazole rings, *Tetrahedron*, **67** (2011) 9491-9499.
- [113] A. Jakli, O.D. Lavrentovich, J.V. Selinger, Physics of liquid crystals of bent-shaped molecules, *Rev. Mod. Phys.*, **90** (2018).
- [114] R.A. Reddy, C. Tschierske, Bent-core liquid crystals: polar order, superstructural chirality and spontaneous desymmetrisation in soft matter systems, *J. Mater. Chem.*, **16** (2006) 907-961.
- [115] C. Tschierske, G. Dantlgraber, From antiferroelectricity to ferroelectricity in smectic mesophases formed by bent-core molecules, *Pramana-J. Phys.*, **61** (2003) 455-481.
- [116] R.A. Reddy, C.H. Zhu, R.F. Shao, E. Korblova, T. Gong, Y.Q. Shen, E. Garcia, M.A. Glaser, J.E. MacLennan, D.M. Walba, N.A. Clark, Spontaneous Ferroelectric Order in a Bent-Core Smectic Liquid Crystal of Fluid Orthorhombic Layers, *Science*, **332** (2011) 72-77.
- [117] E. Westphal, H. Gallardo, G.F. Caramori, N. Sebastian, M.G. Tamba, A. Eremin, S. Kawauchi, M. Prehm, C. Tschierske, Polar Order and Symmetry Breaking at the Boundary between Bent-Core and Rodlike Molecular Forms: When 4-Cyanoresorcinol Meets the Carbosilane End Group, *Chem. Eur. J.*, **22** (2016) 8181-8197.
- [118] H. Takezoe, Y. Takanishi, Bent-Core Liquid Crystals: Their Mysterious and Attractive World, *Jpn. J. Appl. Phys.*, **45** (2006) 597-625.
- [119] B. Glettner, F. Liu, X. Zeng, M. Prehm, U. Baumeister, G. Ungar, C. Tschierske, Liquid-crystal engineering with anchor-shaped molecules: honeycombs with hexagonal and trigonal symmetries formed by polyphilic bent-core molecules, *Angew. Chem. Int. Ed.*, **47** (2008) 6080-6083.
- [120] J. Matraszek, J. Mieczkowski, D. Pocięcha, E. Gorecka, B. Donnio, D. Guillon, Molecular factors responsible for the formation of the axially polar columnar mesophase Col(h)P(A), *Chem. Biodivers.*, **13** (2007) 3377-3385.
- [121] I.A. Levitsky, K. Kishikawa, S.H. Eichhorn, T.M. Swager, Exciton coupling and dipolar correlations in a columnar liquid crystal: photophysics of a bent-rod hexacatenar mesogen, *J. Am. Chem. Soc.*, **122** (2000) 2474-2479.

Chapter 2 Experimental Methods and Analysis

2.1 X-ray diffraction

In our work, X-ray diffraction is the most important experimental technique used to reveal the structure of complex liquid crystalline phases. In the following, we will introduce some basic concepts of crystallography before discussing X-ray diffraction.

2.1.1 Basic crystallography concepts

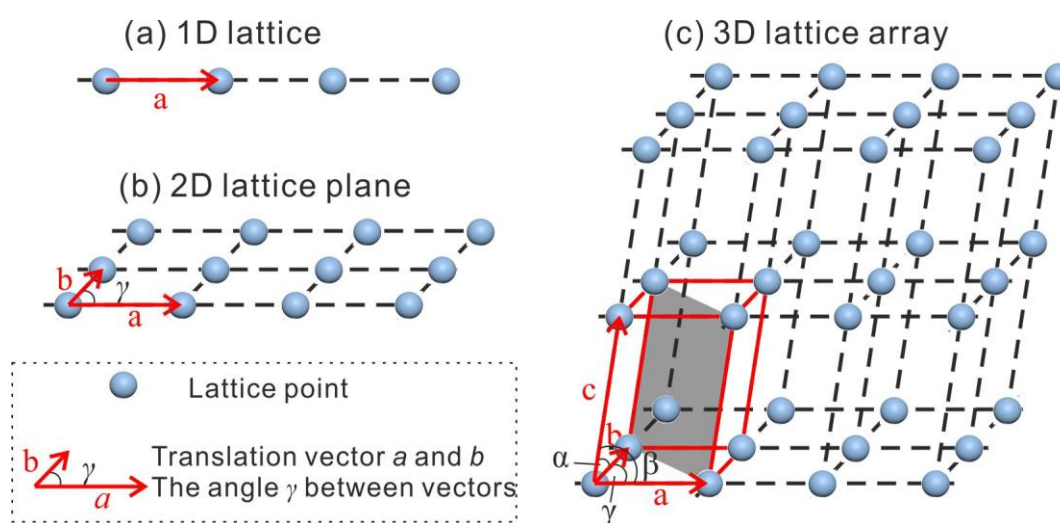


Figure 2.1 (a) 1D lattice with parameter a ; (b) 2D lattice plane with lattice translation vectors a and b and inter-axial angle γ ; (c) 3D lattice array with primitive unit cell highlighted in red. Lattice points are represented by the solid purple circles.

A crystal structure is the periodic arrangement of matter such as atoms, ions or molecules in three-dimensional space [1]. The periodicity of a structure can be mathematically represented by a lattice, which can be defined by up to 3 lattice vectors (the number depending on the dimension of the lattice). The description of the structure

can then be reduced to that in a unit cell bounded by the lattice vectors (equivalent to unit cell parameters), and that is repeated periodically in space. For a better understanding of a crystal structure, we could ignore the matter and focus on the points of the lattices. Figure 2.1a shows the simplest 1D lattice with a translation vector \vec{a} and the length of it is defined as the lattice parameter a . Any lattice point that translates $n\vec{a}$ can bring it to another equivalent lattice point (n is an integer number). The three non co-linear vectors \vec{a} , \vec{b} and \vec{c} of 3D lattices define the unit cell with three inter-axial angles α , β and γ in Figure 2.1c. The length of three vectors are a , b and c . A lattice point that translates by $n\vec{a} + p\vec{b} + q\vec{c}$ can bring it to another equivalent one. It should be noted that the smallest cell that retains the lattice symmetry is chosen as the unit cell in 3D lattices and there are an infinite number of choices for it.

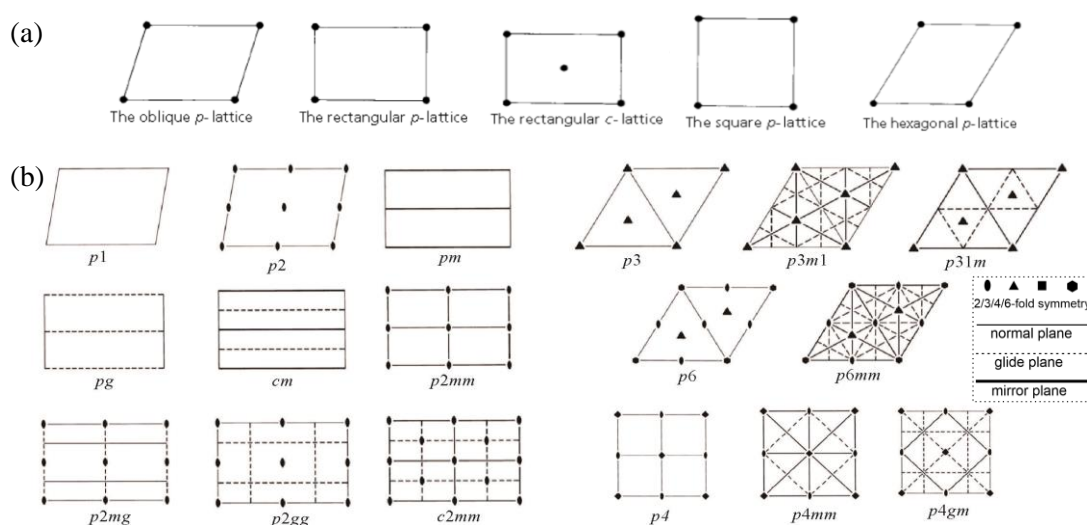


Figure 2.2 (a) Unit cells of the five basic plane lattices, showing the symmetry element (p for primitive, c for centred) (b) The symmetry elements outlined within (conventional) unit cells of the seventeen plane groups (m for mirror planes, g for glide planes, 2 for 2-fold symmetry, etc.).

The symmetry of such periodic structures, are of particular importance in X-ray crystallography, and are classified as plane groups in 2D and space groups in 3D. Plane

groups can be described as one of the five basic plane lattices (Figure 2.2a), combined with an appropriate set of points and translational symmetry elements. The seventeen plane groups are shown with the indication of the symbols of glide or mirror planes and rotation axis in Figure 2.2b. In three dimensions, there are seven crystal systems according to the relationships of the lattice parameters and angles, as shown in Table 2.1. There are four types of lattice centering, primitive (P), base-centered (A, B or C), body-centered (I) and face-centered (F). If lattice centering is considered, there are 14 Bravais Lattices which were defined by A. Bravais in 1848, as shown in Figure 2.3. Furthermore, considering the point symmetry on 14 Bravais Lattices, there are 32 point groups. The point group was named as the fact that all symmetry elements can be considered going through on point of the molecule or crystal. The application of the combination of point symmetry and translation on the 32 point groups would give rise to 230 space groups in total. These space groups indicate sets of symmetry elements that brings a periodic arrangement to its original position.

Table 2.1 The seven crystal systems and their lattice parameters and angles (P for primitive, F for face-centred C for base-centred, I for body-centred).

System (Bravais lattices*)	Lattice parameters and angles	d -spacing equations*
Cubic (<i>PIF</i>)	$a = b = c, \alpha = \beta = \gamma = 90^\circ$	$\frac{1}{d_{hkl}^2} = \frac{h^2 + k^2 + l^2}{a^2}$
Tetragonal (<i>PI</i>)	$a = b \neq c, \alpha = \beta = \gamma = 90^\circ$	$\frac{1}{d_{hkl}^2} = \frac{h^2 + k^2}{a^2} + \frac{l^2}{c^2}$
Orthorhombic (<i>PICF</i>)	$a \neq b \neq c, \alpha = \beta = \gamma = 90^\circ$	$\frac{1}{d_{hkl}^2} = \frac{h^2}{a^2} + \frac{k^2}{b^2} + \frac{l^2}{c^2}$
Rhombohedral (<i>R</i>)	$a = b = c, \alpha = \beta = \gamma \neq 90^\circ$	-
Hexagonal (<i>P</i>)	$a = b \neq c, \alpha = \beta = 90^\circ, \gamma = 120^\circ$	$\frac{1}{d_{hkl}^2} = \frac{4}{3} \left(\frac{h^2 + hk + k^2}{a^2} \right) + \frac{l^2}{c^2}$
Monoclinic (<i>PC</i>)	$a \neq b \neq c, \alpha = \gamma = 90^\circ, \beta \neq 90^\circ$	-
Triclinic(<i>P</i>)	$a \neq b \neq c, \alpha \neq \beta \neq \gamma \neq 90^\circ$	-

*More information of the d -spacing will be discussed in the next section.

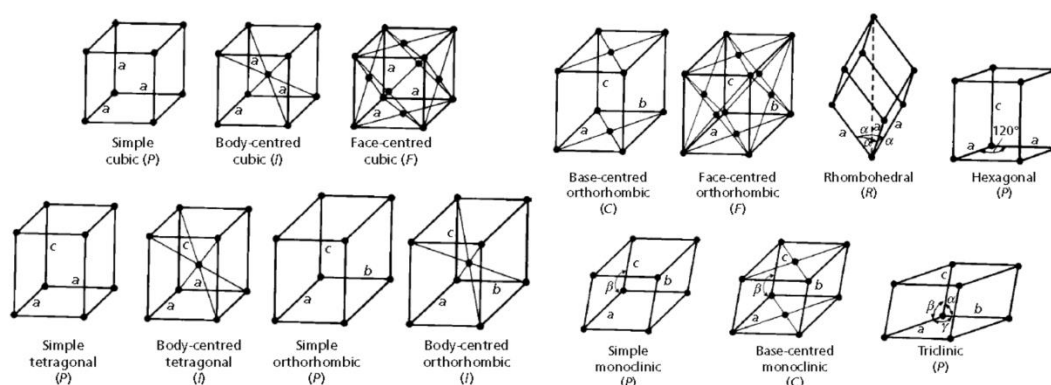


Figure 2.3 The fourteen Bravais lattices (*P* for primitive, *F* for face-centred, *C* for base-centred, *I* for body-centred).

2.1.2 The principle of X-ray diffraction

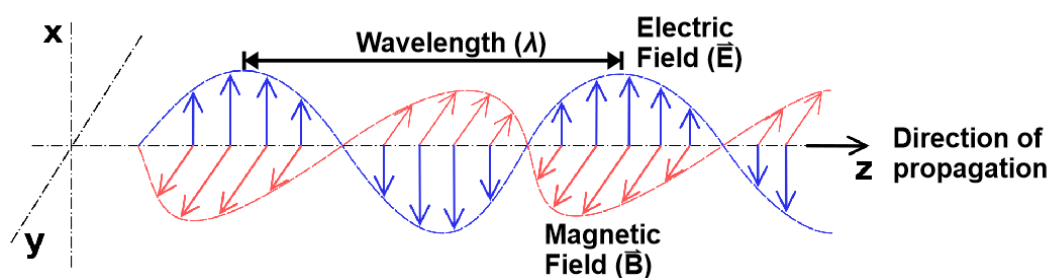


Figure 2.4 A linearly polarized sinusoidal electromagnetic wave.

Electromagnetic radiation can be described as electromagnetic waves with wavelength (λ) and vibration frequency (ν , the number of waves that pass a fixed point per unit of time), and its speed of propagation in vacuum $c = \lambda\nu$. As shown as an example in Figure 2.6, the electromagnetic wave propagates along z axis, with electric (blue) and magnetic fields (red) vibrating in directions perpendicular to the propagation direction and to each other (along x and y axes respectively). X-rays are electromagnetic waves with short wavelength (0.01-10 Å) and they are emitted or absorbed by electrons in the inner orbitals of relatively heavy atoms. X-rays are scattered by electrons in the sample, which oscillate in the oscillating electric field of the X-ray. For elastic scattering, the

wavelength and frequency of emitted electromagnetic waves from the oscillating electron and the incident beam are the same.

For an electron, Thomson equation describes the relationship between the intensity of scattered beam (I_e) and the scattering angle (2θ) as below,

$$I_e = \frac{I_0}{r^2} \left(\frac{e^2}{m_e c^2} \right)^2 \frac{(1 + \cos^2 2\theta)}{2} \quad (\text{Eq 2.1})$$

where I_0 is the intensity of the incident beam; r is the distance between the detector and the electron; e and m_e are the charge and the mass of the electron, respectively; c is the speed of propagation in vacuum; The factor $\frac{(1 + \cos^2 2\theta)}{2}$ is called the polarization factor (p).

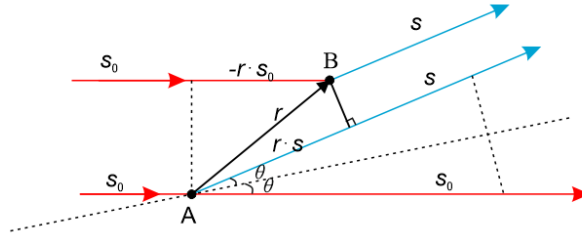


Figure 2.5 X-ray scattering from two electrons with the distance between them as vector \vec{r} .

The schematic figure of X-ray scattering from two electrons at positions A and B is shown in Figure 2.5. The unit wave vectors \vec{s}_0 and \vec{s} are indicated as the incident and scattered rays, respectively. The two electrons are separated by the vector \vec{r} . The path difference between the two waves is $\vec{r} \cdot (\vec{s} - \vec{s}_0)$ and then the phase difference is $\frac{2\pi}{\lambda} \cdot \vec{r} \cdot (\vec{s} - \vec{s}_0)$. Therefore, a scattering vector \vec{q} is defined as below.

$$\vec{q} = \frac{2\pi}{\lambda} \cdot (\vec{s} - \vec{s}_0) \quad (\text{Eq 2.2})$$

thus, the phase difference is represented as $\vec{q} \cdot \vec{r}$.

It could be seen from Figure 2.5 that $(\vec{s}-\vec{s}_0)$ lies symmetrically with reference to the incident and scattered beams, and the magnitude is $2\sin\theta$ (θ is the half of the scattering angle) [2]. Thus, the scattering vector \vec{q} has the same direction and magnitude as $\vec{s}-\vec{s}_0$, and it can be expressed as below.

$$q = |\vec{q}| = \frac{4\pi}{\lambda} \cdot \sin\theta \quad (\text{Eq 2.3})$$

The q values are used as the typical length scales examined by the scattering instrument.

The scattered intensity is expressed by,

$$I(\vec{q}) = I_e F(\vec{q}) F^*(\vec{q}) = I_e |F(\vec{q})|^2 \quad (\text{Eq 2.4})$$

where $F(\vec{q})$ is the structure factor. It is the summation of exponential functions expressing phase differences of N electrons in a system, as shown below.

$$F(\vec{q}) = \sum_1^N e^{i\vec{q}\cdot\vec{r}} \quad (\text{Eq 2.5})$$

As electrons are distributed like a cloud, the electron density (ED) at a point indicated by vector \vec{r} is denoted as $\rho(\vec{r})$. Then the equation for the whole volume can be expressed as,

$$F(\vec{q}) = \int \rho(\vec{r}) \cdot e^{i\vec{q}\cdot\vec{r}} \cdot dv \quad (\text{Eq 2.6})$$

where dv is the volume element of the electrons.

The $F(\vec{q})$ is the Fourier transform of the ED distribution in the matter, linking real and reciprocal space. The overall diffraction intensity in the whole space is expressed as below,

$$I(\vec{q}) = I_e |F(\vec{q})|^2 = I_e \left| \int \rho(\vec{r}) \cdot e^{i\vec{q}\cdot\vec{r}} \cdot dv \right|^2 \quad (\text{Eq 2.7})$$

Miller indices represent the orientation of a plane in a lattice and they are defined by the reciprocals of the fractional intercepts with the unit cell axes. A general set of Miller

indices for a plane is written as (hkl) , where the plane intercepts on the axes \vec{a} , \vec{b} and \vec{c} are a/h , b/k and c/l , respectively. For example, the Miller indices of the grey plane in Figure 2.1c are (110) . When a plane is parallel to an axis, the intercept is infinity and the reciprocal is zero. For the family of lattice planes (hkl) , the 1st plane intercepts on the axes are a/h , b/k and c/l , and the 2nd plane intercepts are $2a/h$, $2b/k$ and $2c/l$, etc. Each plane goes through infinite number of lattice points. In 3D lattices, the relation of interplanar spacing, d_{hkl} , and the lattice parameters and angles depend on the crystal system. Some equations of common crystal systems are listed in Table 2.1.

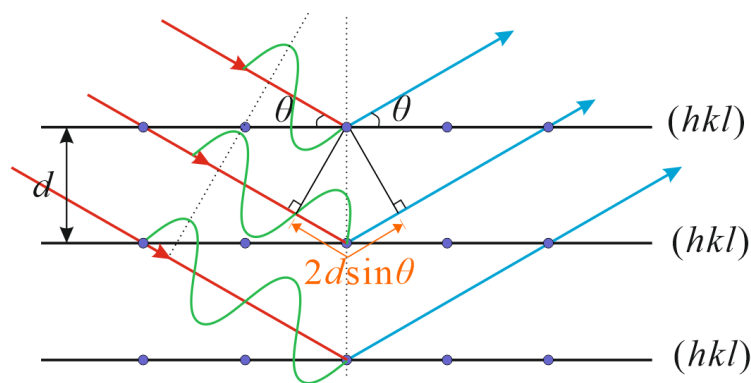


Figure 2.6 Schematic diagram of Bragg's law.

X-rays diffract when passing through a 3D-periodic crystal or a periodic LC structure (with dimensions from 1D to 3D). As shown in Figure 2.6, diffraction happens by the constructive interference of the scattered X-rays beam at a series of Miller planes with indices (hkl) of the periodic lattice. Constructive interference, meaning that the scattered waves are in phase, happens when the path difference is an integral number of wavelengths. Thus, the Bragg's Law is obtained as below:

$$n\lambda = 2d \sin \theta \quad (\text{Eq 2.8})$$

where n is the order of the diffraction, d is inter-planar spacing and θ is the incident angle. The value of n is always set to be 1 in practice, as $d_{nh, nk, nl} = d_{h, k, l}/n$. Thus, from equation 2.3, the relationship of d -spacings and q values is obtained as $q = \frac{2\pi}{d}$.

In a 3D crystal lattice, an atom or electron at position (x, y, z) with unit vectors \vec{a} , \vec{b} and \vec{c} in a unit cell, it has $N = N_1 \cdot N_2 \cdot N_3$ equivalent atoms/electrons in three dimensions. Thus the vector \vec{r} is expressed as below,

$$\vec{r} = \sum_0^{N_1} n_1 \cdot \vec{a} + \sum_0^{N_2} n_2 \cdot \vec{b} + \sum_0^{N_3} n_3 \cdot \vec{c} + x \cdot \vec{a} + y \cdot \vec{b} + z \cdot \vec{c} \quad (\text{Eq 2.9})$$

In the direction of defined vector \vec{q} , the total intensity can be expressed as,

$$I(\vec{q}) = I_e |F(\vec{q})|^2 \frac{\sin^2(N_1 \vec{q} \cdot \vec{a}/2)}{\sin^2(\vec{q} \cdot \vec{a}/2)} \frac{\sin^2(N_2 \vec{q} \cdot \vec{b}/2)}{\sin^2(\vec{q} \cdot \vec{b}/2)} \frac{\sin^2(N_3 \vec{q} \cdot \vec{c}/2)}{\sin^2(\vec{q} \cdot \vec{c}/2)} \quad (\text{Eq 2.10})$$

where $F(\vec{q})$ is calculated in the unit cell.

The values of the sine quotients in equation (2.10) increase sharply as their denominators approach zero. The values of intensity $I(q)$ will therefore increase to a sharp maximum when the following conditions are satisfied at the same time (Laue diffraction conditions), which is equivalent to the Bragg's Law.

$$\vec{q} \cdot \vec{a} = 2\pi h, \vec{q} \cdot \vec{b} = 2\pi k, \vec{q} \cdot \vec{c} = 2\pi l \quad (\text{Eq 2.11})$$

The experimentally measured intensity is proportional to N as the peak width decreases with increasing N (more details are discussed in equations 2.15-2.18). Therefore, the experimentally measured intensity

$$I_{hkl} = I_e F_{hkl}^2 N \quad (\text{Eq 2.12})$$

where the structure factor F_{hkl} of a unit cell of a crystal ($0 < x < a$, $0 < y < b$, and $0 < z < c$),

$$F_{hkl} = \int \rho(xyz) \cdot e^{[2\pi i(hx/a + ky/b + lz/c)]} \cdot dv \quad (\text{Eq 2.13})$$

The structure factor (F_{hkl}) is the Fourier transform of the ED map ($\rho(xyz)$), so $\rho(xyz)$ can be expressed as Fourier series as below,

$$\rho(xyz) = \frac{1}{abc} \sum_{hkl}^{+\infty} F_{hkl} e^{-2\pi i(hx/a+ky/b+lz/c)} \quad (\text{Eq 2.14})$$

Equation 2.14 shows the relationship between real space (electron density distribution in the liquid crystals, the left part of the equation) and the reciprocal space (diffraction images, on the right part of the equation). The ED of the crystal could be calculated when the value of F_{hkl} is determined from X-ray diffraction patterns. In equation 2.12, although I_{hkl} is related to F_{hkl} , the measured intensity from experiments is actually an integration of the diffracted intensity in a range of angular deviations from ideal Bragg angles. Thus the integrated intensity is expressed below.

$$I = K \cdot v \cdot L \cdot p |F_{hkl}|^2 \quad (\text{Eq 2.15})$$

where K is the scale factor, v is the volume of the crystal, L is the Lorentz factor,

p is the polarization factor, which for an unpolarized beam equals $\frac{(1+\cos^2 2\theta)}{2}$.

The beam used in the work presented in this thesis is highly polarized and the region used is small in angle, so p can be treated as 1. The Lorentz factor L depends on the orientation of the sample, the position and geometry of the detector. For the powder diffraction method that uses a linear detector,

$$L = \frac{1}{\sin 2\theta \sin \theta} \quad (\text{Eq 2.16})$$

In small angle X-ray diffraction, the factor $L \cdot p$ could be simplified to $1/q^2$. Thus the integrated intensity,

$$I = \frac{Kv|F_{hkl}|^2}{q^2} \quad (\text{Eq 2.17})$$

The Lorentz corrected intensity I_c is expressed as,

$$I_c = Iq^2 = Kv|F_{hkl}|^2 \quad (\text{Eq 2.18})$$

It is noticeable that all possible diffraction peaks are likely to be observed from the powder diffraction pattern. However, only one family of peaks can be observed in a single crystal diffraction pattern, and limited families of peaks can be observed in a grazing incidence diffraction pattern for a sample with preferred orientation. Consequently, the intensities observed in powder diffraction patterns are always used after Lorentz correction and the $Iq^2 - q$ plots are displayed throughout this thesis.

Structure factor F_{hkl} is a complex number, consisting of real and imaginary parts A and B respectively, as expressed below,

$$F_{hkl} = A_{hkl} + iB_{hkl} = |F_{hkl}| \cdot e^{-i\varphi_{hkl}} \quad (\text{Eq 2.19})$$

where φ_{hkl} is the phase angle. As only the absolute value of $|F_{hkl}|$ can be determined experimentally from equation 2.18, the determination of φ_{hkl} for reconstruction of the electron density map according to equation 2.14 is the “phase problem” in X-ray crystallography.

If the structure is centrosymmetric, the structure factor F_{hkl} is a real number and phase angle φ_{hkl} is either 0 or π . This would decrease the number of phase choices to a finite number of 2^n , where n is the number of reflections used in the reconstruction. This makes it possible for a “trial-and-error” approach to find the ‘correct’ phase combination. However, it would be more complicated if the structure is non-centrosymmetric as the phase φ_{hkl} of some reflections could vary from 0 to 2π . Consideration of other information about the system, for example the molecular size, electron densities of different moieties of the molecule, number of molecules in the unit cell and filling of space, will be helpful in the determination of the ‘correct’ ED map.

The intensities of diffraction peaks were measured by using Origin 9.1 (OriginLab Corp, Northampton, MA, USA) to integrate the diffraction peaks in $Iq^2 - q$ plot. The diffraction peaks are fitted by Gaussian or Lorentz functions, for accurate measurement

of peak positions and intensities, particularly for overlapping diffraction peaks. Using the information of lattice parameters, Miller indices and intensities of diffraction peaks, and plane/space group symmetry of the phase, Electron Density (ED) maps can be reconstructed according to equation 2.14.

2.1.3 Basic experimental setups: simultaneous SAXS/WAXS

As described in sections above, diffraction peaks result from constructive interference of X-rays scattered from ordered arrays of electrons, atoms and unit cell. Materials may possess ordering both at the nanoscale and at the atomic level. From the Bragg equation (Eq 2.8 $d = \lambda/2\sin\theta$) we know that the larger the periodicity, the smaller the diffraction angle. Therefore, the combination of small and wide angle X-ray scattering (SAXS/WAXS) is valuable in the investigation of phase information about the materials. The set-up of the simultaneous SAXS/WAXS experiments is schematically drawn in Figure 2.7.

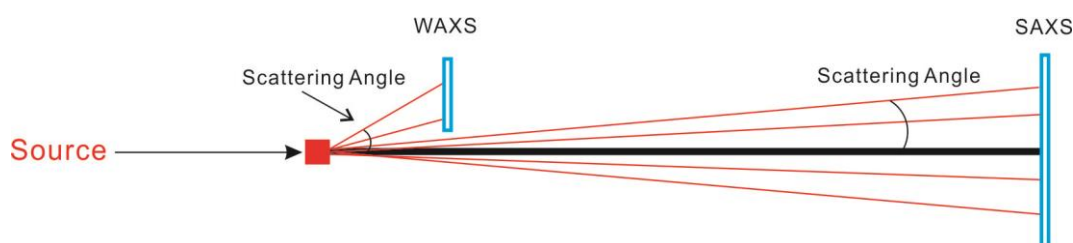


Figure 2.7 The sketched set-up of simultaneous SAXS/WAXS experiments.

In this work SAXS refers to scattering of X-rays of 2θ between 0.1° and 10° . Therefore, the scattering information enables to probe large structures according to the inverse relationship between probing size and the scattering angle. WAXS is a wide-angle scattering technique and often used to determine the crystalline structure of materials recording scattering at relatively large angles. Most useful for the study of liquid

crystals, if sharp diffraction peaks are observed in this region, it indicates ordering at the atomic level and that the sample is crystalline, instead of liquid crystalline.

2.1.4 Grazing incidence small/wide angle X-ray scattering (GISAXS/GIWAXS)

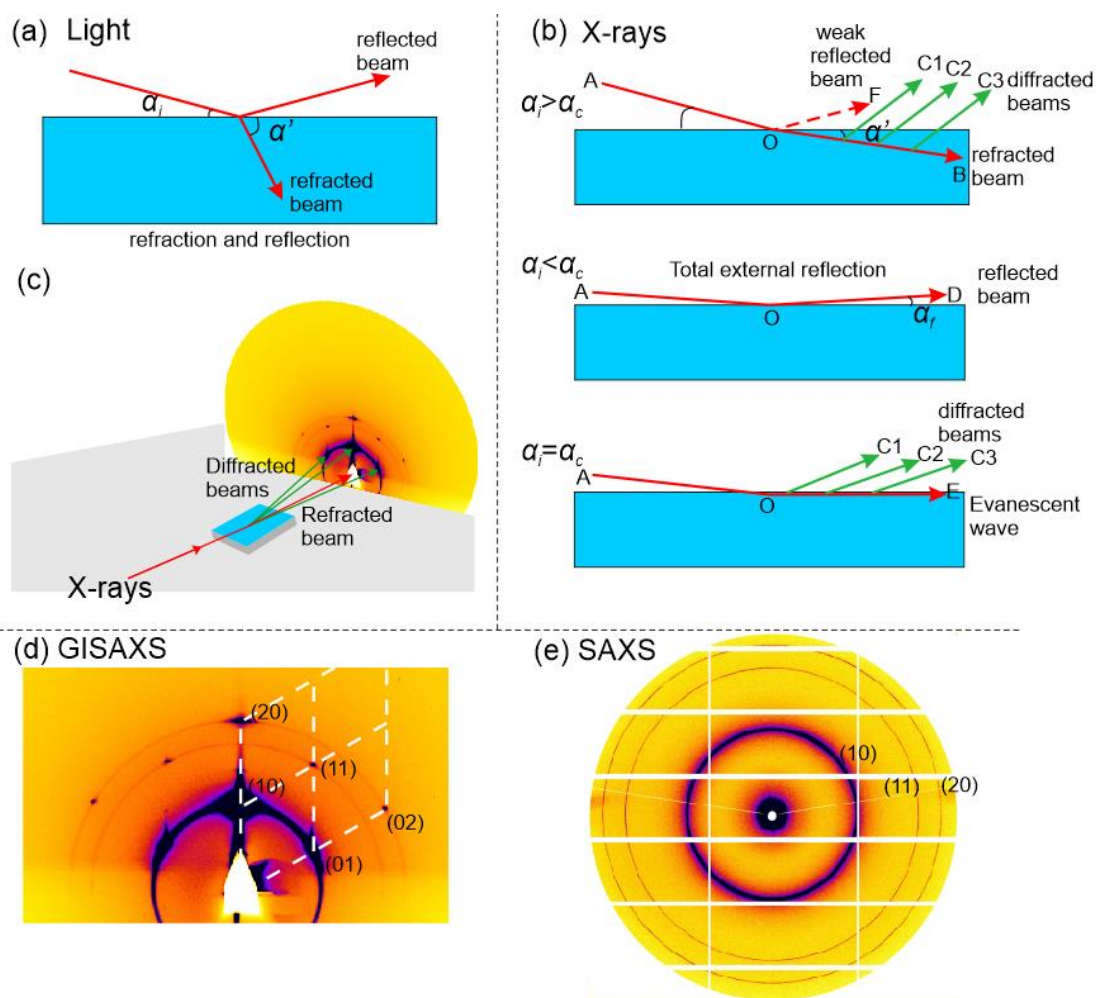


Figure 2.8 (a) The refraction and reflection of visible light in the sample, (b) the sketched figure at different conditions: the incident beam (OA), the refraction (OB), and weak reflection (OF) and diffracted beams (OC1, OC2, OC3) in the sample if $\alpha_i > \alpha_c$; the total external reflection (OD) on the surface of the sample if $\alpha_i < \alpha_c$; the diffracted beams (OC1, OC2, OC3) and the evanescent wave (OE) that penetrates the sample in the nanometer scale and travels parallel with the sample surface if $\alpha_i = \alpha_c$ [3]; (c) sketch of GISAXS/GIWAXS geometry when $\alpha_i > \alpha_c$ (green and red arrows represent the diffracted and refracted beams respectively); The comparison of (d) GISAXS and (e) powder SAXS patterns of a CoI_{hex} phase in the same scale.

Grazing incidence small/wide angle X-ray scattering (GISAXS/GIWAXS) is another X-ray scattering technique used to study nanostructures on the surfaces or thin films. It requires little amount of sample that can be easily oriented on the substrate surface and provides extra information on sample orientation for easy lattice and symmetry assignment for liquid crystalline samples. Thin film samples were prepared from melt on silicon substrates, and normally quenched to room temperature from melt to start with.

Refraction and reflection phenomena are commonly observed in visible light. For the refraction, the wave speed and the propagation direction changes when the wave passes from one medium to another. The rays of visible light are refracted from air towards the normal of the sample surface, as shown in Figure 2.8a. The common refractive indexes of light in air, water, glass are 1.0, 1.3 and 1.5, respectively. Refraction at interfaces of different media in X-rays also happens due to the fact that X-rays are electromagnetic waves. Different from visible light, X-rays coming from air are refracted away from the normal of the surface and the refractive index of X-rays is less than one [3]. The sketched refraction and weak reflection beams are shown in Figure 2.8b if the incident angle is larger than the critical angle ($\alpha_i > \alpha_c$). Also, unlike visible light which shows total internal reflection, X-rays exhibit total external reflection under a condition that the incident angle is smaller than the critical angle ($\alpha_i < \alpha_c$). When the incident and critical angles are the same, the X-ray beam penetrates the sample in the nanometer scale and travels parallel with the sample surface, and this beam is called evanescent wave [3-5].

For the thin sample, there are actually two critical angles: at air/sample interface (α_{c1}), and at sample/substrate interface (α_{c2}) [6]. When the incident angle α_i is larger than the two critical angles, the signals are mainly from the scattering of the primary beam. The path length of X-rays through the sample is sufficiently long and the volume of sample

hit by X-rays is high even for the sample in micron-scale thickness. Thus an intense diffracted pattern could be observed. If α_i is between α_{c1} and α_{c2} , the scattering comes from not only the primary beam but also the stronger reflected beam from the silicon plate, resulting in the split diffraction peaks in the perpendicular direction. If α_i is smaller than α_{c1} , total external reflection happens and beams do not go into the sample. This is the condition that we need to avoid. Occasionally, when the information in small or wide angles near the equator is needed, the incidence angle is set to be the same as (or slightly below) the critical angle α_c and X-ray beams penetrate the sample and travel parallel with the sample surface.

The GISAXS/GIWAXS patterns are typically collected by an area detector as schematically shown in Figure 2.8c. Compared to the powder SAXS/WAXS technique, smaller amount of sample is needed for the thin film and the extra orientation information of the diffraction peaks from a GISAXS pattern makes identification of lattice types and indexing of diffraction peaks much easier. An example of GISAXS and powder SAXS patterns of a $\text{Co}_{1\text{hex}}$ phase in the same scale is shown in Figure 2.8d-e.

2.1.5 Laboratory beamline

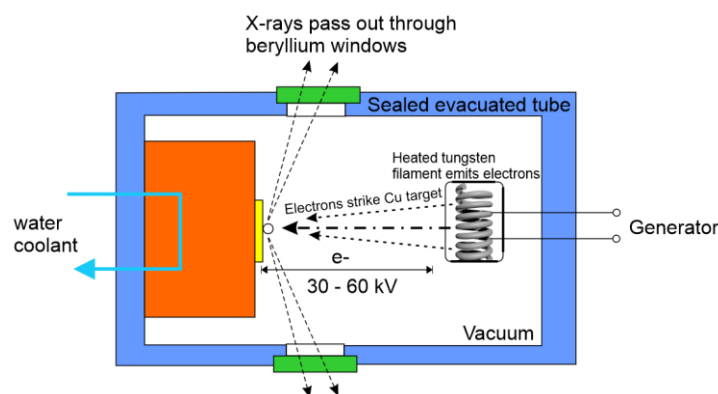


Figure 2.9 The schematic diagram of X-ray tube.

Sometimes the laboratory beamline is used for preliminary studies of samples. In the laboratory, the X-rays are generated when a Cu target is bombarded by electrons within an X-ray tube, as shown in

Figure 2.9. The generated electrons are emitted from a heated tungsten filament and accelerated by an applied potential to impact on the Cu target. The collision between electrons and atoms of the Cu target would generate heat and X-rays [7].

The setup we have used was a Xenocs GeniX microfocus Cu X-ray source. The X-ray tube is constantly being pumped during operation. It was coupled with FOX 3D Cu 12-INF infinity focus multilayer mirrors and a two scatterless slits collimator. A homebuilt furnace for capillaries connected to a Eurotherm temperature controller via a suitable transformer within ± 0.5 °C accuracies. A Bruker Vantec 500 microstrip 2D detector (68 μm pixel size) was used.

2.1.6 Synchrotron radiation

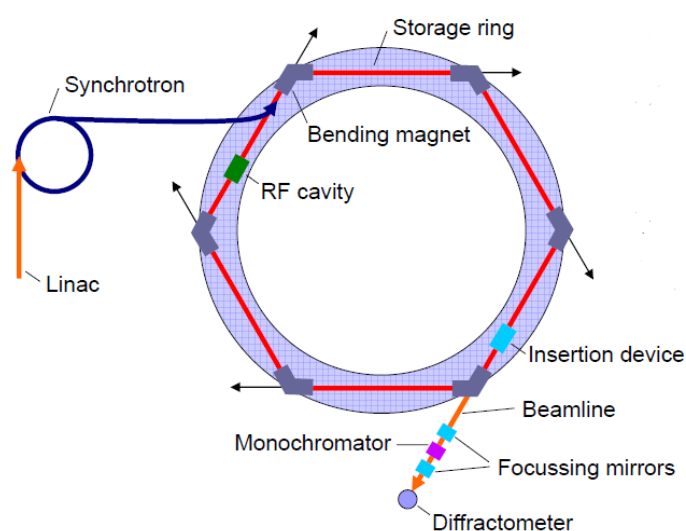


Figure 2.10 Schematic outline of a synchrotron radiation facility.

Synchrotron radiation is generated by the acceleration of charged elementary particles (typically electrons), normally by the use of magnetic fields, and maintained on a closed orbit under high vacuum in a storage ring [7], as shown in Figure 2.10. Electrons emitted by an electron gun are first accelerated in a linear accelerator (linac) and then transmitted to a circular accelerator (booster synchrotron) where they are accelerated to reach an energy level of GeV. The storage ring maintains electrons in the closed orbit by bending magnets, and the energy of electrons is restored by RF cavity. Synchrotron radiation, with a range of different wavelengths, is generated by bending magnets which bend the electron trajectory, and by insertion devices, which are also composed by magnets, but periodically arrayed, to wiggle or undulate electron trajectory. The synchrotron radiation is then guided to beamlines, which contain monochromators, focusing mirrors and diffractometers for X-ray diffraction experiments.

The radiation emitted by the orbiting electrons covers an extremely broad range of the electromagnetic spectrum, from the infrared ($\lambda \sim 10^{-2}$ cm) to the hard X-ray ($\lambda \sim 10^{-2}$ nm). The flux (i.e., intensity per unit area) of X-rays is high, enabling to shorten the required time for each measurement. Therefore, rapid time series measurements with samples undergoing dynamic evolution are allowed and high resolution diffraction results can be obtained [8]. X-ray diffraction experiments involved in this report were carried out at different beamlines of synchrotron radiation source facility, Diamond Light Source (DLS, U.K.) and European Synchrotron Radiation Facility (ESRF, France).

Powder SAXS/WAXS samples were examined at station I22 in DLS. They were prepared in glass capillaries of 1.0mm diameter and held in a modified Linkam hot stage. Pilatus detectors were used for both SAXS and WAXS. The X-ray energy was usually 12.4 keV, and the exposure time was typically in seconds.

GISAXS/GIWAXS experiments were carried out at BM28 at ESRF and I16 at DLS. The 2d diffractograms were collected using a MAR165 CCD camera at BM28, and

Pilatus 2M detector was used at I16. *n*-tetracontane (C₄₀H₈₂) was used to calibrate the distance between sample and detector in all X-ray experiments.

2.1.7 Determination of lattice parameters and symmetry groups

The *d*-spacings or *q* values ($q = \frac{d}{2\pi}$) of diffraction peaks can be measured from SAXS results, with the liquid crystalline nature of the phases confirmed by simultaneous WAXS. For simple lattice types, it is relatively easy to work out the Miller indices of diffraction peaks, from their q^2 ratios [9], as shown in Table 2.2.

Table 2.2 The q^2 ratio, Miller index and crystallographic relationships of different structures.

Phase	q^2 ratio	Miller index (<i>hk</i>)	Crystallographic relationships
Lamellar	1:4:9:16...	(10), (20), (30), (40) ...	$\frac{1}{d^2} = \frac{n^2}{a^2}$
Hexagonal (<i>p6mm</i> , <i>p31m</i> , <i>p3m1</i> ...)	1:3:4:7...	(10), (11), (20), (21) ...	$\frac{1}{d_{hkl}^2} = \frac{4}{3} \left(\frac{h^2 + hk + k^2}{a^2} \right)$
Square (<i>p4mm</i>)	1:2:4:5...	(10), (11), (20), (21) ...	$\frac{1}{d_{hkl}^2} = \frac{h^2 + k^2}{a^2}$
Square (<i>p4gm</i>)	2:4:5:8...	(11), (20), (21), (22) ...	
Cubic (<i>Ia3d</i>)	6:8:14:16...	(211), (220), (321), (400) ...	$\frac{1}{d_{hkl}^2} = \frac{h^2 + k^2 + l^2}{a^2}$

However, a lot of times, when the structure is more complex, it might not be possible to work out the lattice type simply from the q^2 ratios. In such cases examination of orientated samples, either single crystal domains (using a goniometer) or oriented thin-film samples, typically prepared on silicon substrates (using GISAXS), can help to index the observed diffraction peaks.

Using the methods mentioned above, lattice parameters and diffraction peaks of the phase can be determined and indexed. Next, it is necessary to check the general and special reflection rules observed against that listed in the International Tables for Crystallography, for determination of plane or space groups. Sometimes, the exact

plane or space group cannot be uniquely determined from XRD, for example, for plane groups $p6mm$ and $p3m1$. In such cases other characterization methods, for example, second harmonic generation (SHG, Section 2.2.1.2) which can distinguish centrosymmetric and non-centrosymmetric structures, will be used whenever necessary.

2.2 Optical Spectroscopy

Optical Spectroscopy studies the interaction between atoms or molecules and incident electromagnetic radiation as a function of its wavelength, or equivalently its frequency or photon energy [10]. Electromagnetic radiation can be described as electromagnetic waves as in Section 2.1.2. It can also be described as photons (wave-particle duality in quantum mechanics), massless particles with quantized energy.

In an entire range of the electromagnetic spectrum, from low wavelength to the higher, electromagnetic waves are called by different names, from gamma-rays, X-rays, ultraviolet, visible, infrared, microwaves to radio waves [11]. Short wavelength X-rays (1-10 Å) are emitted or absorbed by electrons in the inner orbitals of relatively heavy atoms. In the UV-vis range (Ultraviolet: 180-400 nm, visible: 400-750 nm), the electron cloud around atoms can be polarised by the electric field of the incident beam, leading to electronic transitions between ground and excited states. UV-vis spectroscopy is used on this basis to obtain the information of electronic structure of molecules. In addition, fluorescence spectroscopy records the emitted light (fluorescence) when the polarised electron cloud returns from the excited state to ground state. The energy of the emitted photon equals the energy difference between the two states (ΔE) and hence,

$$\Delta E = h\nu = hc/\lambda \quad (\text{Eq 2.20})$$

where h is Planck constant (6.6268×10^{-34} J s), ν is the frequency of absorbed

electromagnetic radiation, c is the velocity of light (2.998×10^8 m/s) and λ is the wavelength.

In most spectroscopy, the relationship of the amount of materials in the sample (l : the thickness of the sample, c : the concentration) and the absorption of light passing through (A : absorbance) is described by Lambert-Beer's Law, as shown below

$$A = \epsilon lc \quad (\text{Eq 2.21})$$

where ϵ is the molar absorptivity and its value shows how well a compound absorbs a given wavelength of light.

The detectors measure the absorbance (A) by comparing the intensity of incident light (I_0) and the intensity of transmitted light (I),

$$A = \log_{10} \frac{I_0}{I} \quad (\text{Eq 2.22})$$

At longer wavelength, in the Infrared (IR) region (700 nm - 1 mm), the incident beam frequencies are similar to that of molecular vibration, therefore IR spectroscopy is able to help identify molecules and their functional groups.

Specific spectroscopy methods used in our work will be discussed in detail in next sections.

2.1.1 UV-Vis and fluorescence spectroscopy

The energy absorbed by the molecule in UV range lead to its change of electronic energy and consequently transitions of valence electrons [11]. There are three types of electrons in organic molecules, σ -, π -, n -electrons. σ - and π -electrons are involved in saturated and unsaturated bonds, respectively. n -electrons are electrons in atoms that are not involved in saturated and unsaturated bonds, *i.e.* non-bonding electrons. When the molecule is excited by the light, electrons would move from a bonding to an

antibonding orbital. There are four different transitions and the order of energy values from low to high of them are $n \rightarrow \pi^*$, $\pi \rightarrow \pi^*$, $n \rightarrow \sigma^*$, $\sigma \rightarrow \sigma^*$ [12].

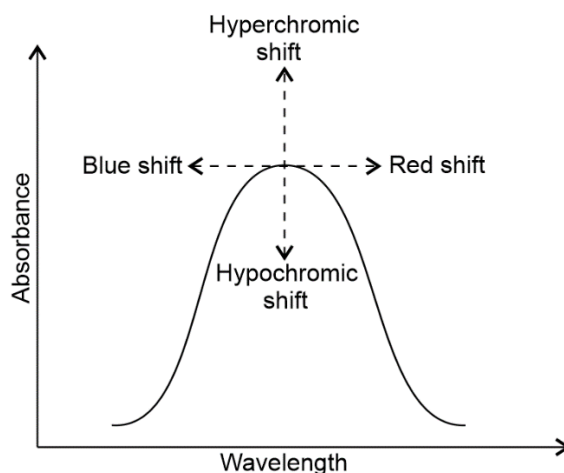


Figure 2.11 Absorbance and wavelength shifts of UV-vis spectra.

The absorbance or intensity shifts may happen when there are changes in temperature, solvent or some other conditions of the sample (Figure 2.11). Red/bathochromic shift is the shift of maximum absorption towards longer wavelength and it could be produced by changing the solvent. Additionally, when there are two or more chromophores in conjugation in a molecule, there is a red shift. In Chapter 4, compounds FCN16 and FCO16 show a red shift in the cooling process because of an increase in conjugation at the transition from one phase to another. Blue/hypsochromic shift could show due to removal of conjugation or a change of the solvent polarity. Hyperchromic and hypochromic effect is caused by the presence of an auxochrome and the distortion of the geometry of the molecules, respectively.

Fluorescence spectroscopy is complementary to UV-vis as it measures the transitions from the excited state to ground state. Fluorescence is emission of visible radiation after molecules are excited by an incident beam [11, 12].

The solid samples were prepared by melting and spreading evenly between two quartz plates. UV-vis spectra were recorded using Lambda 900 (Perkin Elmer). Fluorescence emission spectra were recorded using Fluoromax4.

2.1.2 Infrared spectroscopy

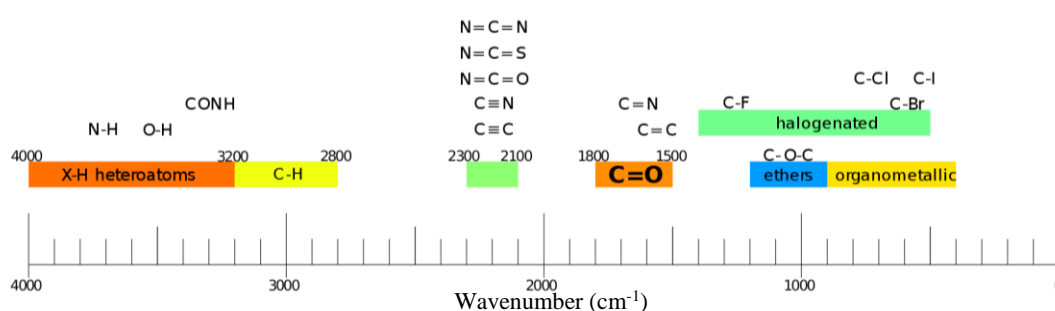


Figure 2.12 IR spectroscopy correlation table. Reproduced with permission from ref [13].

Infrared (IR) spectroscopy is a powerful technique to investigate chemical structures. It can be also used for quantitative analysis. Absorption in IR range results from transitions between vibrational energy levels of a molecule. A molecule shows absorption bands in the IR spectrum when vibrational motion is coupled with a change of the overall dipole moment [11]. IR spectrum of a molecule below 2000 cm^{-1} is also a ‘fingerprint’ for its identification, showing bands for functional groups as well as characteristic bands of the molecule. The main IR bands are summarized in Figure 2.12.

IR spectra were recorded with a Perkin-Elmer Frontier FTIR instrument. As the samples (1X and 2X in Chapter 6) may absorb water in the air, they were melted on a CsI window and dried under vacuum at 40°C for 1 day. A second CsI window was placed over the sample as cover. The sandwich was then heated into the mesophase (50 - 60 °C) under vacuum to ensure uniform film thickness before the measurement.

2.2 Other Analytical Procedures

2.2.1 Microscopy

2.2.1.1 Polarized optical microscopy

Polarized optical microscope (POM) is often used to observe the temperature range and the texture of LC phases. Some details such as the direction of aromatic cores and columns can also be obtained.

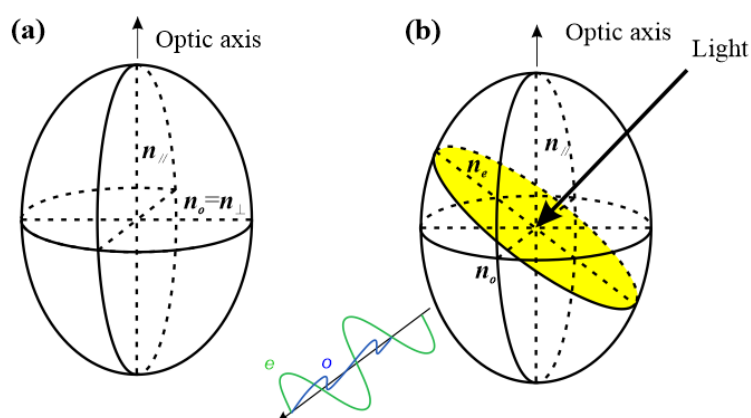


Figure 2.13 (a) Index ellipsoid (extraordinary indicatrix); (b) Determining n_e , n_o and the direction of polarization of o and e beams.

In optically isotropic media (liquids, cubic crystals), the relationship between the refractive index (n), the speed of light in vacuum and in material (c , v) can be described as $n = c/v$. In optically anisotropic (birefringent) materials light beam splits into an ordinary ray (n_o) and an extraordinary ray (n_e), see Figure 2.13. Both e and o rays are plane-polarized (linearly polarized). The planes are perpendicular to each other. The plane of e light contains the unique axis of the birefringent material [14].

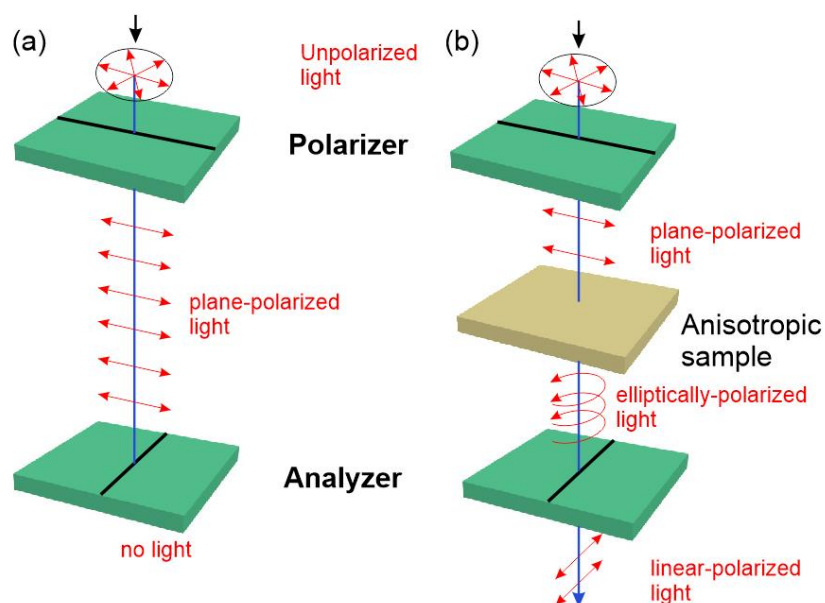


Figure 2.14 Light path through two crossed polarizers with (a) no sample or isotropic sample and (b) birefringent sample.

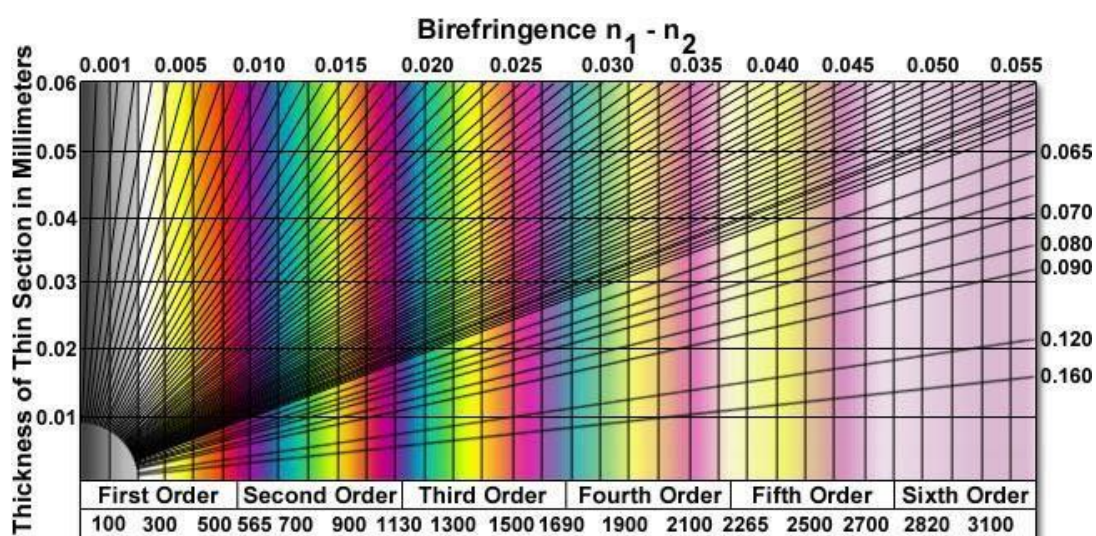


Figure 2.15 The Michel-Levy Birefringence chart.

Phase difference (Γ , in radians) between the two components at depth d is:

$$\Gamma = \frac{2\pi}{\lambda}(n_e - n_o)d$$

Note the special cases of $\Gamma = k\pi$ (k is an integer), where the light is linearly polarized. When k is an even integer, after leaving the sample the light retains the state of polarization as at the exit (i.e. generally elliptical).

Normally, the material is placed between two polarizers crossed at 90° to each other. The plane-polarized light transmitted by the 1st polarizer is not altered when there is no sample or there is an optically isotropic sample between crossed polarizers. It is hence fully absorbed by the 2nd polarizer (“analyzer”), as shown in Figure 2.14a. Elliptically polarized light is created when an anisotropic material is placed between the polarizers, as shown in Figure 2.14b. The component of the light which is parallel to the analyzer can now transmit through the analyzer. In general, an anisotropic sample is bright and coloured when viewed through crossed polarizers. The colour comes from different phase delays Γ of the components of the white light when they leave the birefringent sample. A $1-\lambda$ retardation plate (550 nm) is often used as it slows down propagation in all directions and help to understand the orientation of molecules. Northwest-southeast is normally its direction of slow axis which retards the 550 nm light by exactly $1-\lambda$. The Michel-Levy birefringence chart in Figure 2.15 shows the relationship of sample colour to its thickness, birefringence and actual retardation. If two of the three values are known, the value of the remaining one can be obtained from the lines from the bottom left corner to the upper/right boundaries.

POM were recorded using an Olympus BX50 microscope equipped with Linksys32 or Mettler HS82 hot stage and $1-\lambda$ retardation plate.

2.2.1.2 Second harmonic generation (SHG) microscopy

Second harmonic generation (SHG) is a nonlinear optical process, in which two photons with the same frequency interacting with a nonlinear material are effectively

"combined" to generate a new photon with twice the energy, and therefore twice the frequency and half the wavelength of the initial photons (Figure 2.16) [15, 16]. It is an even-order nonlinear optical effect and only noncentrosymmetric structures are capable of emitting SHG light, so SHG experiments are performed to distinguish centrosymmetric and non-centrosymmetric structures. In Chapters 3 and 5, SHG was used to distinguish the centrosymmetric symmetry $p6mm$ and non-centrosymmetric symmetry $p31m/p3m1$.

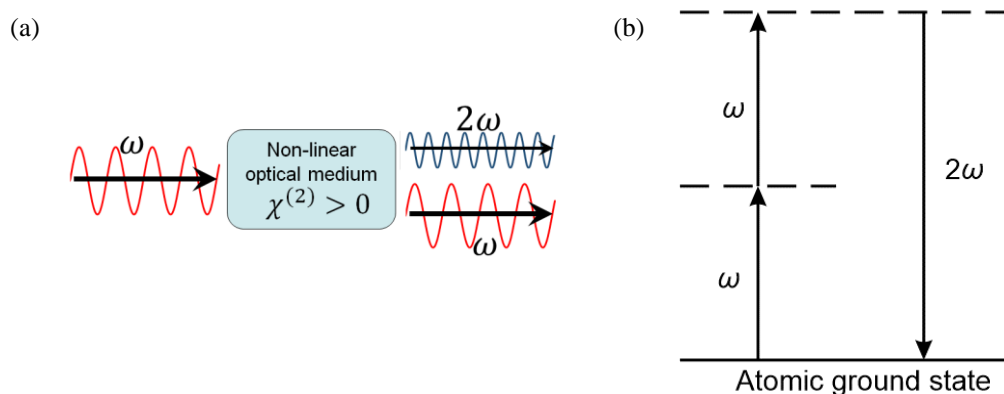


Figure 2.16 (a) Geometry of SHG and (b) energy level diagram describing SHG (ω is the wavelength, $\chi^{(2)}$ is the second-order nonlinear optical susceptibilities). Reproduced with permission from ref [15].

A Zeiss LSM 510 Meta upright laser-scanning confocal microscope (Oberkochen, Germany) with a 40X/0.75NA objective was used to examine the sample. The temperature was controlled by a Linkam or Mettler HS82 hot stage. A Chameleon Ti:Sapphire femtosecond pulsed laser (Coherent, California, USA) tuned to 800 nm, was attached to the microscope and focused onto the sample resulting in a SHG signal detectable at 400 nm. Samples of about 50 μm thickness for SHG measurements were prepared on the rough side of a silicon wafer. In order to exclude possible surface effects, the beam was first focused at the bottom of the LC film in contact with the Si substrate,

then at 10 μm , 20 μm and sometimes 30 μm height above it. The SHG ratio was calculated by dividing the intensities at 400 nm by the averaged background around the peak.

2.2.1.3 Atomic force microscopy

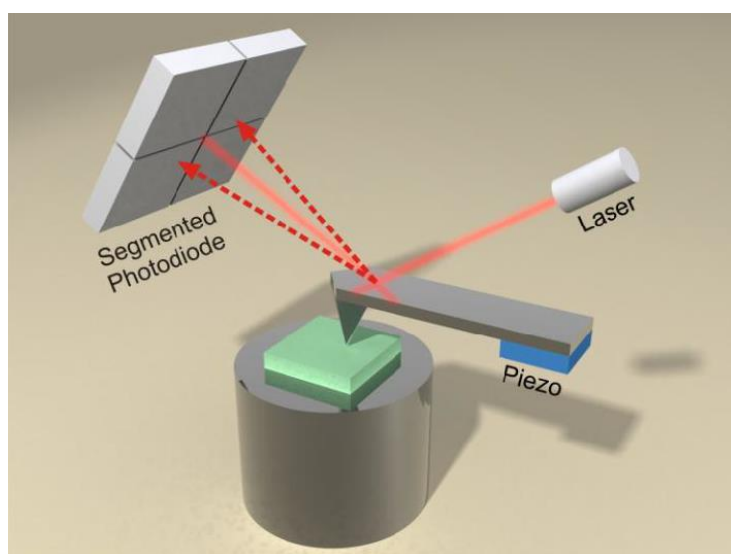


Figure 2.17 Schematic setup of AFM. Reproduced with permission from ref [17].

Scanning probe microscopes which use a physical probe to record the interactions between the probe and the surfaces of the sample, are a family including scanning tunnelling microscope, scanning probe electrochemistry, atomic force microscopy (AFM) etc [18, 19].

AFM records the repulsive and attractive forces between the probe and the surfaces and produces high resolution images in nanometres. A typical setup of AFM is shown in Figure 2.17. The reflected beam on the photodetector monitors the change of the position which is caused by the force of bending or twisting applied on the tip of the cantilever. Tapping mode AFM is used as it is non-destructive, particularly important to soft liquid crystalline materials, has high spatial resolution and can record

simultaneously sample topography. In this mode, a piezoelectric element is used to excite the cantilever with a certain vibration amplitude and frequency. The arrangement of the molecules in the LC phase could be observed by AFM [20-23]. A Veeco Multimode instrument with a Nanoscope IIIa controller and OTESPA probes (Bruker) was used in our work.

2.2.2 Differential Scanning Calorimetry (DSC)

Differential scanning calorimetry (DSC) is a standard technique used to measure phase transition temperatures and enthalpy changes at the transitions [24]. The sample (2 - 5 mg) is sealed in an aluminium pan with known weight and a reference pan that does not show any phase transition in the temperature range. They are heated or cooled simultaneously at a constant rate. When the sample shows a phase transition, its temperature will deviate from that of the reference due to positive or negative transition enthalpy. The temperature difference should be compensated by heating or cooling, and dH/dT (the changes of enthalpy with temperature) can be measured according to the required electrical power. Phase transitions, for example, from crystal to LC or from LC to isotropic, which require the input of additional energy, show endothermic peaks in the heating. Commonly, the peak positions shift downwards in the cooling (thermal hysteresis) and exothermic peaks are shown because of the output of energy. The energy of transition can often be used to provide an idea of the transition type. However, it is always necessary to combine DSC with other techniques like POM and X-ray diffraction to determine the existence and nature of a transition.

2.2.3 Molecular modelling and dynamic simulation

Molecular modelling and dynamic simulation is used to study the microscopic behaviour of matter resulting from the interaction between atoms and molecules [25]. In such simulation, a trajectory that includes position, velocity and acceleration with the time of all atoms in the simulated system can be calculated and saved at regular intervals, providing information for investigations of the dynamic and static phenomena of the simulated system.

The static picture of molecular structure provided by molecular mechanics is not realistic because molecules are dynamic, undergoing vibrations and rotations continuously [26]. Consequently, molecular dynamics must be used to analyse models by calculating the motion of atoms in the molecules, thus more realistic information about possible conformations, thermodynamic properties, and dynamic behaviour of molecules can be reached. Molecular dynamics can also be used to evaluate and compare different models proposed on the base of reconstructed ED maps.

Materials Studio (Accelrys) was used to visualize the model. The methods of modelling and simulation follow the procedures below,

- (1) Structural visualization: Build a crystal with the determined unit cell parameters by experiment. Construct molecules according to their chemical structure and arrange them within the unit cell, taking into consideration of their symmetry.
- (2) Geometry minimization: The forcite module and the universal forcefield is used.
- (3) Dynamic simulation: Annealing dynamics is used. The process of annealing can reduce stress on molecules, take high-energy conformational states towards stable conformation, overcome potential energy barriers and force molecules toward the lower energy conformation. Universal Force-field is selected and NVT (constant volume/constant temperature) is used as dynamics ensemble. The convergence tolerances for geometry optimization were 0.001 kcal/mol for energy and 0.5

kcal/mol/Å for force. Typically, thirty temperature cycles of NVT dynamics are run between 300 and 600K, with a total annealing time of 30 ps.

References

- [1] C. Hammond, *The Basics of Crystallography and Diffraction*, Oxford, 2001.
- [2] G. O., K. O., *Small Angle X-ray Scattering*, A Subsidiary of Harcourt Brace Jovanovich, 1982.
- [3] J. Als-Nielsen, *Elements of modern X-ray physics [electronic resource]*, 2nd ed. ed., Chichester, West Sussex : John Wiley, 2011, Chichester, West Sussex, 2011.
- [4] O. Sakata, M. Nakamura, *Grazing Incidence X-Ray Diffraction*, in: G. Bracco, B. Holst (Eds.) *Surface Science Techniques*, Springer Berlin Heidelberg, Berlin, Heidelberg, Vol., 2013, pp. 165-190.
- [5] M. Birkholz, M. Birkholz, *Grazing Incidence Configurations*, 2006.
- [6] D. J., G. A., *X-ray and Neutron Reflectivity: Principles and Applications*, Springer, Berlin Heidelberg, 2009.
- [7] B.D.C.S.R. Stock, *Elements of X-Ray Diffraction*, Prentice Hall, 2001.
- [8] R.-J. Roe, *Methods of X-ray and neutron scattering in polymer science*, Oxford University Press on Demand, 2000.
- [9] U. Müller, *Symmetry Relationships between Crystal Structures*, Oxford University Press, U.K., 2013.
- [10] A.M. Nagao Kobayashi, John Mack, *Circular Dichroism and Magnetic Circular Dichroism Spectroscopy for Organic Chemists*, The Royal Society of Chemistry, UK, 2011.
- [11] G.R. Chatwal, S.K. Anand, *Spectroscopy: Atomic and Molecular*, Global Media, 2008.
- [12] J. Jerry Workman, *The Handbook of Organic Compounds*, Elsevier, U.S.A., 2001.
- [13] G. Socrates, *Infrared and Raman Characteristic Group Frequencies: Tables and Charts*, John Wiley & Sons, 2012.
- [14] P.J. Collings, *Liquid crystals: nature's delicate phase of matter*, Princeton University Press, 2002.
- [15] R. Boyd, *The Nonlinear Optical Susceptibility*, 2008.

- [16] E. Garmire, Nonlinear optics in daily life, *Opt. Express*, **21** (2013) 30532.
- [17] R. Zhang, *Complex Liquid Crystal Phases in Cylindrical Confinement*, in: Department of Material Science and Engineering, The University of Sheffield, Sheffield, 2012.
- [18] S.H. Cohen, M.I. Lightbody, *Atomic Force Microscopy/Scanning Tunneling Microscopy 3*, Kluwer Academic Publishers, New York, Boston, London, Moscow, 2002.
- [19] S. Morita, F.J. Giessbl, E. Meyer, R. Wiesendanger, *Noncontact Atomic Force Microscopy*, Springer, Berlin, London, 2015.
- [20] L. Gross, F. Mohn, N. Moll, P. Liljeroth, G. Meyer, The Chemical Structure of a Molecule Resolved by Atomic Force Microscopy, *Science*, **325** (2009) 1110-1114.
- [21] R.B. Zhang, X.B. Zeng, B. Kim, R.J. Bushby, K. Shin, P.J. Baker, V. Percec, P. Leowanawat, G. Ungar, Columnar Liquid Crystals in Cylindrical Nanoconfinement, *Acs Nano*, **9** (2015) 1759-1766.
- [22] R.B. Zhang, X.B. Zeng, M. Prehm, F. Liu, S. Grimm, M. Geuss, M. Steinhart, C. Tschierske, G. Ungar, Honeycombs in Honeycombs: Complex Liquid Crystal Alumina Composite Mesostructures, *Acs Nano*, **8** (2014) 4500-4509.
- [23] R.B. Zhang, X.B. Zeng, G. Ungar, Direct AFM observation of individual micelles, tile decorations and tiling rules of a dodecagonal liquid quasicrystal, *J. Phys. Condens. Matter*, **29** (2017).
- [24] P. Gabbott, *Principles and Applications of Thermal Analysis*, Blackwell Publishing Ltd, 2008.
- [25] J.-R. Hill, L. Subramanian, A. Maiti, *Molecular modeling techniques in material sciences*, CRC press, 2005.
- [26] C.S. Tsai, *An introduction to computational biochemistry*, John Wiley & Sons, 2003.

Chapter 3 Published paper: Trigonal columnar self-assembly of bent phasid mesogens

Chemical Communication, 2018, 54, 156-159

Huifang Cheng,^{a‡} Ya-xin Li,^{b‡} Xiang-bing Zeng,^b Hongfei Gao,^a Xiaohong Cheng,^{a*}
Goran Ungar^{b,c*}

a. Key Laboratory of Medicinal Chemistry for Natural Resources, Chemistry Department, Yunnan University, Yunnan 650091, P. R. China, E-mail: xhcheng@ynu.edu.cn

b. Department of Materials Science and Engineering, University of Sheffield, Sheffield S1 3JD, U.K. E-mail: g.ungar@sheffield.ac.uk

c. Department of Physics, Zhejiang Sci-Tech University, Xiasha College Park, Zhejiang 310018, China

‡ Both authors contributed equally to this work.

This Chapter was published as an article in Chemical Communication. I have carried out the experiments and data analysis by POM, X-ray diffraction, SHG, molecular modelling and dynamic simulation, and written the corresponding parts in the article. Huifang Cheng, Hongfei Gao and Prof. Xiaohong Cheng from Yunnan University synthesized the compounds. They confirmed the chemical structures by NMR and examined the compounds by DSC.

The article is reproduced in its Open Access under a CC BY 3.0 license, with minor adaptations on the figures and section numbering, and correction of some typos. The details of the synthesis part in the supporting information are not included here and the references in the manuscript and supporting information have been combined for clarity.

3.1 Abstract

Three compounds with a bent rod-like aromatic core and with three alkoxy chains at each end were synthesised by click reaction. The compounds form a columnar liquid crystal phase with noncentrosymmetric trigonal $p31m$ symmetry, the columns having a 3-arm star-like cross-section.

3.2 Introduction

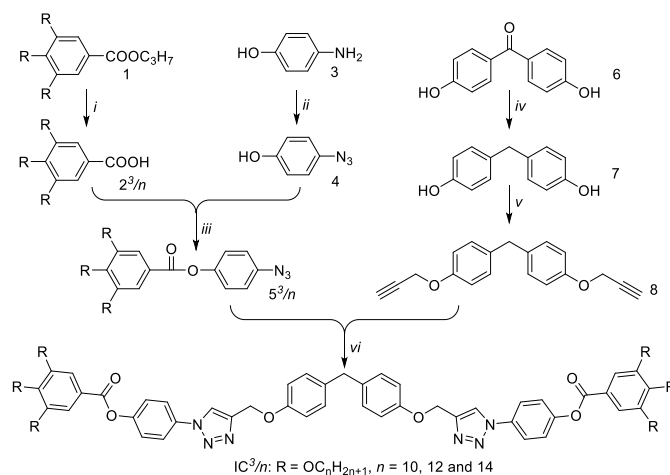
The term “phasmid” mesogen is used to describe rod-like molecules with three flexible chains, usually alkyl, at each end, and the name refers to the similarity with insects known by the same name [1]. Usually such mesogens form the hexagonal columnar liquid crystal (LC) phase, where typically three aromatic rods lie parallel to each other and perpendicular to the column axis, forming a stratum of the column; the alkyls fill the space between the columns [2]. Phasmids are a subclass of a wider class of rod-like molecules with more than one chain at each end, known as polycatenar mesogens. Columnar phases, particularly the most commonly observed hexagonal phase, are normally assembled from disk-like or fan-shaped molecules [3-7]. Alternatively a variety of “honeycomb” columnar phases are seen in rod-like amphiphiles with flexible side-chains [8, 9]. One may ask why phasmidic columns, with elongated rods lying normal to the column axis, pack on a lattice with hexagonal symmetry, when such packing is normally reserved for round cylinders or hexagonal prisms. The answer may be in that the successive strata in a column are rotated, forming a helix, making the averaged cross-section circular. Such helical twist of polycatenar strata has recently been suggested by the observation of chirality in non-chiral polycatenar compounds in the triple-network cubic phase, where the networks are also made up of short column segments [10]. Columns made up of more circular strata, containing discotic or fan-

shaped mesogens, are also understood to feature helical twist [11-14]. The question we address here is whether a trigonal columnar LC phase can be formed, with three-fold rather than six-fold symmetry and with non-cylindrical columns. In honeycomb-like inverted columnar phases of side-chain-containing rod-like amphiphiles, in some cases the cross-section of the prismatic channels with aromatic walls is hexagonal; thus although the columns are not circular, naturally the symmetry is still hexagonal, plane group $p6mm$ [8, 9]. However, in two cases amphiphiles of that kind were reported to form honeycombs with only three-fold symmetry (see below) [15, 16]. Such non-centrosymmetric structures are rare in liquid crystals but are of interest for their potential ferroelectric, pyroelectric or nonlinear optical properties. The question remains whether such three-fold symmetry is possible in the more conventional columnar phases where the hard aromatic moieties occupy the centre, rather than the periphery of the column. Here we show that columns with a three-arm star cross-section and trigonal symmetry can form from bent-core, or banana-shaped phasids. While the crystallographic plane group belongs to the hexagonal system, the phase symmetry is actually trigonal.

3.3 Results and discussion

The aromatic rod-like core in the compounds described here have a bend of 109° in the centre due to the sp^3 -hybridized methylene group – see Scheme 3.1. The compounds are labelled IC^3/n , with $n = 10, 12, 14$ the number of carbon atoms in each of the six terminal alkoxy chains. They were synthesized by a Cu(I)-catalyzed click reaction [17]. All three compounds display a liquid crystal phase, with the texture recorded by polarized optical microscopy (POM) featuring clear developable domains (“spherulites”) [18], typical of a columnar LC phase – see Figure 3.1. The transition

temperatures and heats of transition on 1st heating, cooling and 2nd heating, determined by DSC in combination with X-ray diffraction and nonlinear optical studies, are listed in Table 1. The DSC traces are shown in Figure S3.1 and S3.2 of Electronic Supporting Information (SI).



Scheme 3.1. Synthesis of compounds **IC³/*n***. Reagents and conditions: (i) KOH, CH₃CH₂OH, reflux, overnight; (ii) a) NaNO₂/HCl, 0 °C, 1 h; b) NaN₃, 0-5 °C, 5 h; (iii) dicyclohexylcarbodiimide, 4-dimethylaminopyridine, CH₂Cl₂, 0-5 °C, 18 h; (iv) LiAlH₄, AlCl₃, THF, 65 °C, 48 h; (v) KOH, propargyl bromide, acetone, reflux; (vi) tert-butanol, THF, H₂O, sodium ascorbate, CuSO₄·5H₂O, 25 °C, 20 h.

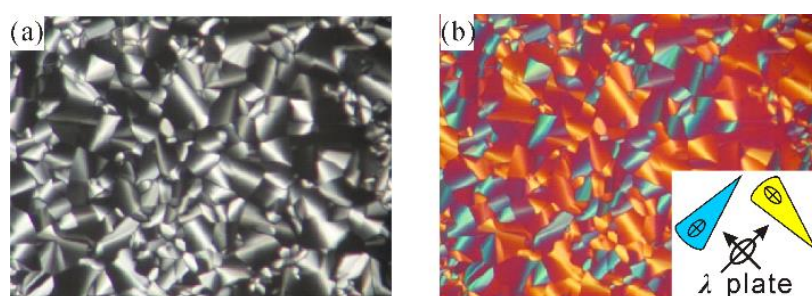
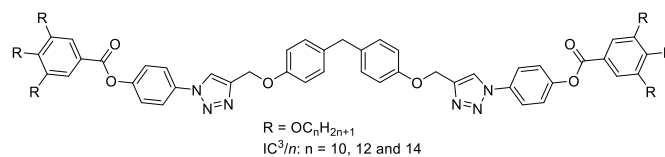


Figure 3.1 Polarized optical microscopy textures of **IC³/14** at 70 °C. (b) is recorded with a full-wave (λ) plate. For explanation of colours see SI.

Table 3.1 The phase transition temperatures of compounds **IC³/*n****

Compd	<i>n</i>	<i>T</i> /°C [ΔH /kJ mol ⁻¹]
IC³/10	10	↑Cr ₁ 69.6 [17.3] Cr ₂ 107.0 [33.3] Iso ↓ 87.4 [1.2] <i>p31m</i> 52.8 [12.0] M ↑ 56.5 [12.3] <i>p3</i> +Cr ₁ 65.4 [2.4] <i>p31m</i> 90.3 [1.2] Iso+Cr ₂ 108.6 [3.3] Iso
IC³/12	12	↑ Cr ₁ 86 [21.1] Cr ₂ 110.2 [41.5] Iso ↓ 88.6 [0.7] <i>p31m</i> 58.3 [11.5] M ↑ 62.1 [11.6] <i>p31m</i> 89 Cr ₂ 110.3 [35.7] Iso
IC³/14	14	↑Cr ₁ 38.7 [30.5] Cr ₂ 73 [23.1] <i>p31m</i> 82.7 [0.8] Iso ↓ 76.2 [0.3] <i>p31m</i> 58.5 [14.6] M ↑ 62.5 [14.7] <i>p31m</i> +Cr ₂ 68.2 [1.0] <i>p31m</i> 83.9 [0.6] Iso

*Peak DSC transition temperatures [and enthalpies] on 1st heating (↑), followed by cooling (↓), followed by 2nd heating (↑), all at 5 K min⁻¹. Cr₁, Cr₂=crystal, *p31m* = hexagonal columnar phase with three-fold symmetry, Iso = isotropic melt, and M is a complex metastable unidentified LC phase.

All of the target compounds **IC³/*n*** were synthesized by click reaction between the bisacetylene **8** and the appropriate substituted aromatic azides **5³/*n*** (Scheme 3.1). Reduction of commercially available 4,4'-dihydroxybenzophenone **6** with LiAlH₄/AlCl₃ [19] yielded 4,4'-dihydroxydiphenylmethane **7**, which was etherified with propargyl bromide to yield bisacetylene **8**. 4-Azidophenol **4** was synthesized from commercially available 4-aminophenol **3** by formation of the diazonium salt and subsequent substitution with sodium azide. **4** was esterified with the appropriate 3,4,5-trialkoxybenzoic acids **2³/*n*** to 4-azidophenyl-3,4,5-trialkoxybenzoates **5³/*n*** [20]. Finally click reaction between bisacetylene **8** and aromatic azides **5³/*n*** produced the target compounds **IC³/*n***. All of the target compounds were purified by column chromatography. For more details, see SI.

X-ray scattering at small and wide angles (SAXS and WAXS) experiments were performed to characterize the LC phases. Grazing incidence SAXS (GISAXS) on thin films on silicon substrate was also employed in order to facilitate indexing of X-ray reflections.

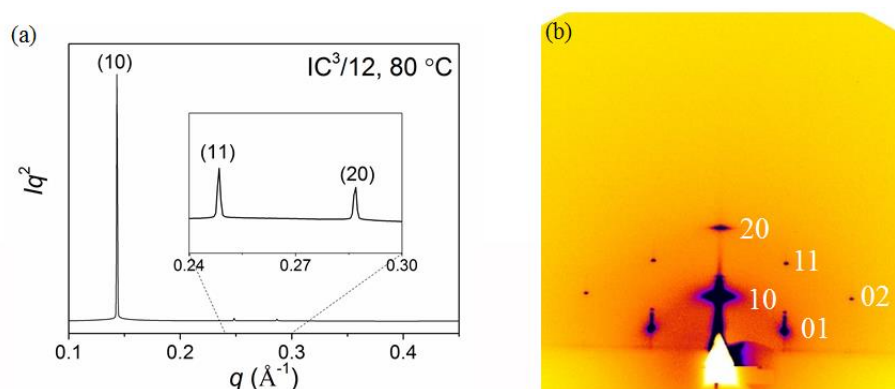


Figure 3.2 (a) Powder SAXS curve of **IC³/12** recorded at 80 °C at station I22 at Diamond. (b)GISAXS diffraction pattern of **IC³/12** recorded at 80 °C on beamline B28 at ESRF.

Furthermore, for any potential future application of such materials in electronic or optical devices, orientation in thin film needs to be understood. Figure 3.2 shows a transmission powder SAXS and a GISAXS pattern of the main liquid crystal phase, on the example of **IC³/12**. Equivalent patterns for compounds **IC³/10** and **IC³/14** are shown in SI, Figure S3.4-3.6. The measured and calculated d -spacings for all three compounds are listed in Tables S1-S3 in SI. The d^2 values of the three peaks in the SAXS pattern are in the ratio 1 : 3 : 4, which is typical of a two-dimensional hexagonal lattice, with the respective Miller indices (10), (11) and (20). The GISAXS patterns confirm this indexing, as seen in Figure 3.2b and Figure S3.4a and S3.5a (SI). The fact that the reflections are not confined to the equatorial plane means that the columns are oriented parallel to the substrate surface (planar anchoring), rather than perpendicular to it. This is consistent with the appearance of the optical micrographs in Figure 3.1 and Figure S3.3 (SI). As the real space unit cell is related to the reciprocal cell by 90° rotation, the fact that reflections (10) and (20) are on the meridian means that the real hexagonal cell lies on one of its sides on the substrate. That implies that the (10) plane is parallel to the substrate, suggesting in turn that it is the most densely packed plane (See Figure S3.9, SI) [21]. In compounds **IC³/12** and **IC³/14** another metastable

mesophase has been observed in rapidly cooled samples. The GISAXS pattern is presented in Fig. S3.7 (SI). The structure of this phase is not clear at present, and is the subject of further investigations. (This lower temperature phase is indexed as a 3D orthorhombic *Fddd* phase and the details can be seen in Chapter 4).

Table 3.2 Comparison of the values of lattice parameter (in nm) of the hexagonal columnar phase in the three compounds at different temperatures

Compound	60°C	70°C	80°C	90°C
IC³/10	5.03	4.98	4.94	4.89
IC³/12	5.23	5.18	5.13	
IC³/14	5.41	5.35	5.28	

The lattice parameters of **IC³/10**, **IC³/12** and **IC³/14** at different temperatures are listed in Table 3.2. As expected, the value of lattice parameter *a* is seen to increase with increasing end-chain length. The continuous trend suggests that the basic phase structure is the same in all three compounds. It is also seen in Table 3.2 that the *a* decreases with increasing temperature, a common trend observed in columnar phases, particularly those containing a large aliphatic fraction [12].

In order to determine the molecular arrangement in the columnar phase, we first need to establish the orientation of the molecular cores relative to the column axis and then determine the number of molecules in the unit cell. Using the λ retardation plate (Figure 3.1b, S3.3d, f) we confirm that the slow axis, hence the long axis of the aromatic core, is perpendicular to the column axis. For the calculation of the number of molecules refer to Table S4 in SI. To estimate molecular volume in the LC phase the molecule is split in two parts. The volume of the rigid aromatic part is estimated using the methods of crystalline volume increments [22]. For the aliphatic part the density of 0.8 g cm⁻³ is assumed, being in between the values for liquid *n*-alkanes and amorphous polyethylene. From the measured area of the unit cell and an assumed intermolecular spacing along the column axis *c* in the usual range between 0.4 and 0.45 nm, we obtain close to 3 as the number of molecules per unit cell. As we don't know the actual value of *c*, in Table

S4 we give the calculated value of c assuming that the number of molecules, which must be an integer, is exactly 3. As can be seen, the value of c is in the range between 0.407 and 0.433, increasing slightly with the length of the terminal chains.

With the above in mind, we consider two alternative models of molecular packing. In both models three molecules cluster together in one stratum, with their aromatic cores back-to-back, forming a three-arm star. The models differ in the arrangement of the star-profiled columns. In model A the centres of the stars are situated at apices of hexagons, producing a hexagonal honeycomb with aromatic walls where the central methylene groups occupy alternative corners of the hexagon. This packing mode resembles that found in anchor-shaped mesogens consisting of a bent-rod aromatic core with a flexible chain attached to the inside of the bend point [15]. However, while in the case of anchor mesogens the ends of the aromatic arms were linked via hydrogen-bonding terminal groups, and had the inward-facing flexible chains filling the inside of the hexagon, neither of these features apply to the present compounds. In fact the bulky end-chains on adjacent molecules would face each other and clash, having to bend sharply in order to fill the interior of the hexagonal channel. Even rotating the star-like columns by 60° about their axis does not solve the packing problem as tested by molecular simulation.

In the alternative model (B) the self-assembled stars are located on a triangular lattice all with the same orientation – see the models in Figure 3.3b-d. This arrangement is favoured for steric reasons, as the bunch of six alkyls emanating from the end of a star arm faces the empty concave “armpit” of the adjacent column. To test the viability of the two arrangements and their variants, molecular models of crystals were built with the experimental unit cell parameter a and with c from Table S4. These were then subjected to molecular dynamics annealing. Space could not be filled uniformly with model A, while a very satisfactory density distribution was achieved with model B –

see snapshot in Figure 3.3b. A short video of the dynamics of model B is available from <http://www.rsc.org/suppdata/c7/cc/c7cc06714c/c7cc06714c1.mp4>.

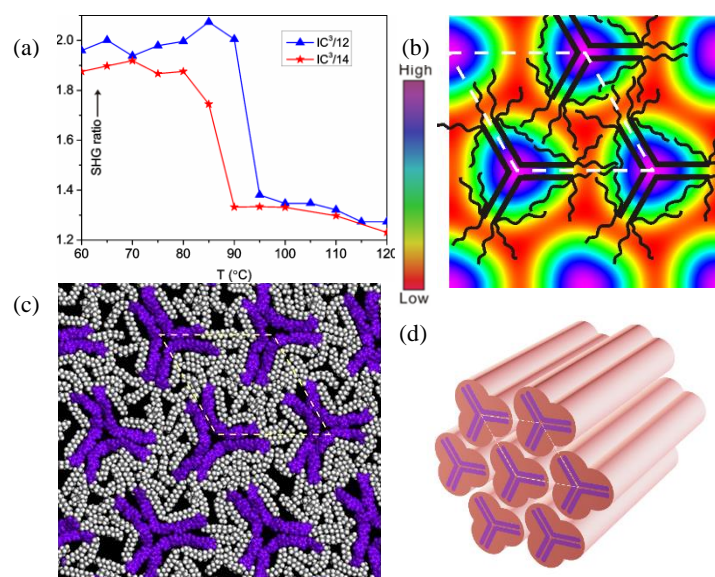


Figure 3.3 The $\text{Col}_{\text{hex}}/p31m$ phase: (a) temperature dependent intensity of the second harmonic (400 nm) vs background for 800 nm excitation, generated 20 μm above the substrate surface in $\text{IC}^3/12$ and $\text{IC}^3/14$; (b) electron density map, with schematic molecules overlaid; (c) snapshot of molecular dynamic simulation: purple = aromatic, grey and white = aliphatic chains (see video in SI); (d) schematic of the $\text{Col}/p31m$ phase. In (b,c) the view is down the columns. Note that according to the GISAXS pattern in Figures 3.2b, S3.4a and S3.5a the column orientation in this figure is as in a film on a horizontal substrate viewed along the substrate surface (see Figure S3.9 in SI).

The columnar structure in Figure 3.3 has 3-fold rather than 6-fold symmetry, and the plane group is $p31m$ rather than the usual $p6mm$ symmetry of the Col_{hex} phase. While the $p6mm$ plane group has a centre of inversion, $p31m$ has not. To distinguish between them, we performed second harmonic generation (SHG) experiments. Figure 3.3a shows a large increase in SHG signal above the background level on cooling from Iso to Col_{hex} phase, showing clearly that the latter phase lacks centre of symmetry and is thus a trigonal phase (see also SI).

This lack of centre of symmetry causes a problem when reconstructing the electron density (ED) map from X-ray diffraction intensities. That is, the phase ϕ of the structure factor of one of the three reflections, the (11), is not limited to 0° or 180° , a condition that applies to all reflections in centrosymmetric space groups. A value of ϕ different from 0° or 180° breaks the hexagonal symmetry. Choosing an arbitrary angle $\phi = 120^\circ$ we obtain the ED map in Figure 3.3a, onto which the schematic molecules of an \mathbf{IC}^3/n compound are superimposed. The high density regions (purple) represent the aromatic moieties, and the blur comes from the time and space averaging in the liquid crystal. We note that choosing a different value of ϕ merely changes the extent of deviation from circularity of the high-density maxima – see Figure S3.8.

We consider that the efficient back-to-back packing of the three bent cores in this structure is facilitated by a degree of flexibility in the core, particularly around the oxymethylene linkage. The long-range polarity, on the other hand, is believed to be secured by the high barrier for uncorrelated rotation around the column axis.

It is interesting to compare the present structure with that of a bent-core phasid compound also having six terminal $\text{C}_{14}\text{H}_{29}$ chains but with longer arms and a pyridine ring as the bend point [23]. The model proposed for the hexagonal columnar phase of that compound was one in which four rather than three molecules assemble in a stratum resulting in a 4-arm star. $p6mm$ symmetry was assumed. Interestingly, at lower temperatures a phase transition to a polar columnar phase took place but unlike in the current case, the poling was parallel rather than perpendicular to the column axis. Longitudinal poling was explained by an out-of-plane distortion of the stars.

It is also appropriate to compare the present structure with those of a number of mesogens with 3-fold (C_3) symmetry in their chemical structure. In the columnar phase of the 3-arm star molecules by Lehmann *et al.*[24] the molecules are actually thought to be distorted into an E-shaped conformation, making their effectively fan-shaped and

thus assembling as other fan-shaped mesogens such as dendrons. In other cases the fact that the non-centrosymmetric 3-arm star molecules of C_3 symmetry formed the hexagonal columnar phases was thought to be the result of rotational averaging [25]. However, even though the diffraction pattern has hexagonal symmetry, this does not preclude the real structure having only trigonal symmetry. One has to remember that the Laue symmetry (i.e. the symmetry of the diffraction pattern) is hexagonal even if the crystal symmetry is trigonal. Indeed the columnar phase of compounds described in ref. [26] showed strong second harmonic generation (SHG), characteristic of non-centrosymmetric structures. In other reported cases of C_3 star-like mesogens only 6-fold symmetry was reported for the columnar LC phase [26-28].

As hinted in the introduction, beside the already mentioned trigonal columnar phase in anchor-shaped compounds [15], there has been another case of triangular honeycomb LC of straight rod amphiphiles, where two incompatible side-chains, a carbosilane and a perfluoroalkane, were attached at each side of the aromatic rod [16]. While at higher temperatures the two chain types were mixed in the triangular channels, a second-order Curie-type phase transition on cooling brought about a trigonal $p31m$ columnar phase in which the two side-chain types were separated in triangles on two separate sublattices. A recent Monte Carlo simulation helps understand such $p6mm-p31m$ transitions [29].

3.4 Conclusion

In summary, we have synthesised a series of bent-core phasid compounds and found that they form a trigonal columnar phase, where the aromatic columns adopt a 3-armed star-shaped cross-section. This finding indicates a potential new path to creating non-

centrosymmetric selfassemblies that could, with suitable substituents, be used in ferroelectric, pyroelectric or frequency-doubling optical devices.

3.5 Supporting Information

3.5.1 Characterization and Modelling Techniques

DSC thermograms were recorded on a DSC 200 F3 Maia calorimeter (NETZSCH) instrument with heating/cooling rates as specified. **Optical micrographs** with crossed polarizers were recorded using an Olympus BX1 microscope equipped with Mettler HS82 hot stage.

GISAXS experiments were carried out at BM28 at European Synchrotron Radiation Facility, France. The X-ray energy was 12.0 keV, and the 2d diffractograms were collected using a MAR165 CCD camera. Thin film samples were prepared from melt on silicon substrate. *n*-tetracontane was used to calibrate the sample to detector distance. **Powder SAXS and WAXS** experiments were done at station I22 of Diamond Light Source, U.K. Powder samples were prepared in 1 mm glass capillaries and held in a modified Linkam hot stage. Pilatus 2M detector (Dectris) at a distance of 2.2 m from the sample was used. The X-ray energy was 12.4 keV. **Preliminary SAXS** patterns were recorded on a Xenocs system based at Zhejiang Sci-Tech University consisting of a microspot Cu-K α X-ray generator, an infinity focusing multilayer 3D-curved mirror, scatterless slits collimator, and a MAR Research 345 image plate detector. **Electron density maps** were calculated by inverse Fourier transformation using the standard procedure as described in International Tables for Crystallography. The choice of phase is discussed in the text.

Samples of ca. 50 μm thickness for frequency-doubled light emission, or **second harmonic generation** (SHG) measurements were prepared on the rough side of silicon

wafer and examined using a Zeiss LSM 510 Meta upright laser-scanning confocal microscope (Oberkochen, Germany) with a 40X/0.75NA objective. Temperature was controlled by a Linkam hot stage. A Chameleon Ti:Sapphire femtosecond pulsed laser (Coherent, California, USA) tuned to 800 nm, was attached to the microscope and focused onto the sample resulting in a SHG signal detectable at 400 nm. In order to exclude possible surface effects, first the beam was focused at the bottom of the LC film in contact with the Si substrate, then at 10 μm , 20 μm and sometimes 30 μm height. The SHG ratio was calculated by dividing the intensities at 400 nm by the averaged background around the peak. The normalized 400 nm signal for **IC³/12** and **IC³/14**, collected 20 μm above the substrate, is shown as a function of temperature in Figure 3a. Measurements are made on very slow cooling from the isotropic phase. The sharp increase in the signal below the isotropization temperature confirms that the columnar LC phase that forms at that temperature lacks centre of inversion. Diagrams that also include the measurements at 0 and 10 μm height are shown in Figure S3.10.

Molecular models were built using Materials Studio (Accelrys). Geometry optimization and molecular dynamic simulation were performed using the Forcite Plus module with Universal Force Field. The experimental value for a -parameter and the value for c from Table S4 were used. The convergence tolerances for geometry optimization were 0.001 kcal/mol for energy and 0.5 kcal/mol/Å for force. NVT annealing dynamics was performed through 30 cycles between 300 and 600 K. with a total annealing time of 30 ps. The MD annealing was performed in a “supercell” box with periodic boundary conditions containing 9 unit cells.

3.5.2 DSC Results

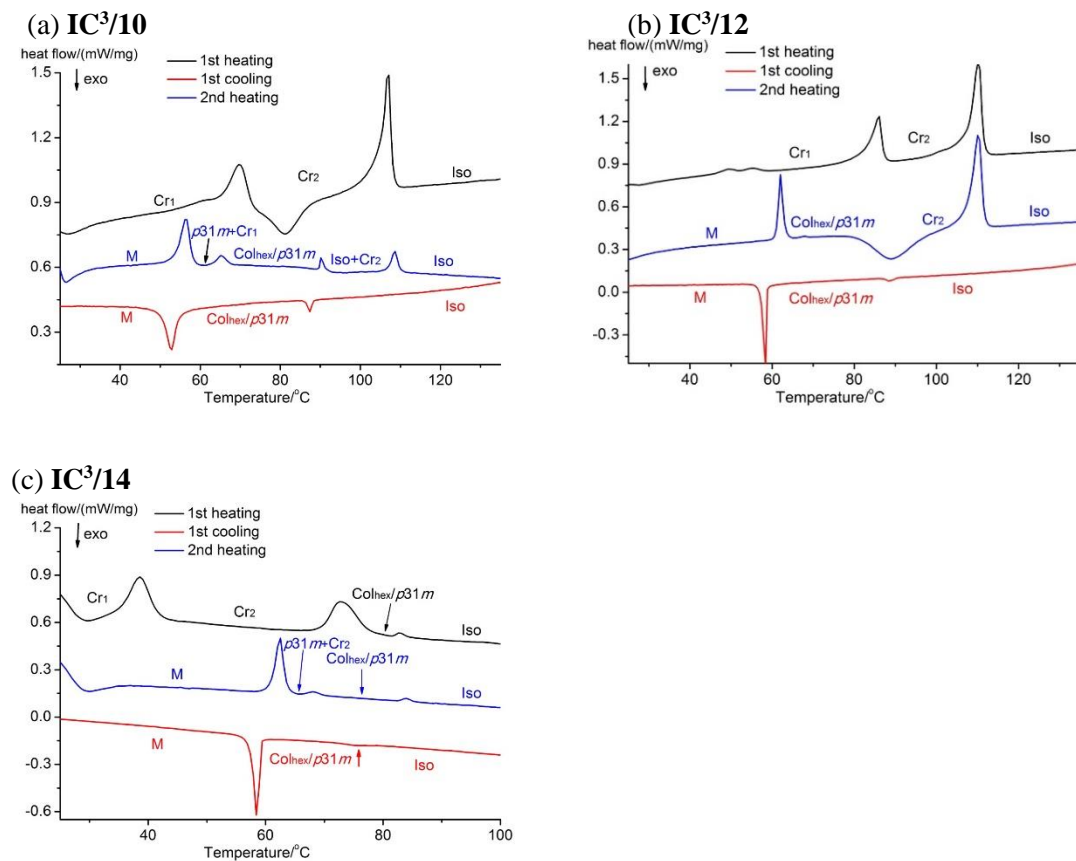


Figure S3.1 DSC thermograms of compounds IC^3/n at heating and cooling scan rate of 5 K min^{-1} .

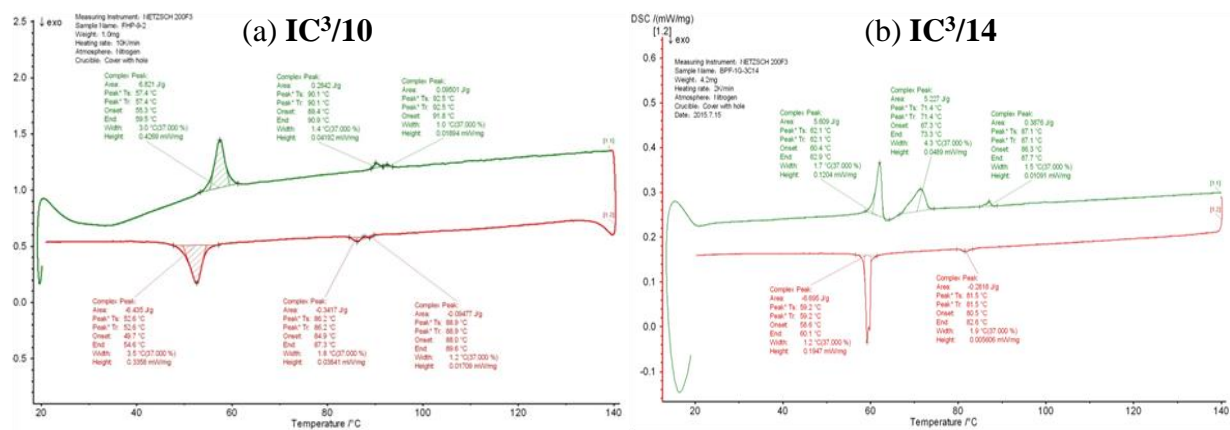


Figure S3.2 DSC cooling and 2nd heating scans of (a) $IC^3/10$ at 10 K min^{-1} , and (b) $IC^3/14$ at 2 K min^{-1} .

3.5.3 Additional Optical Micrographs

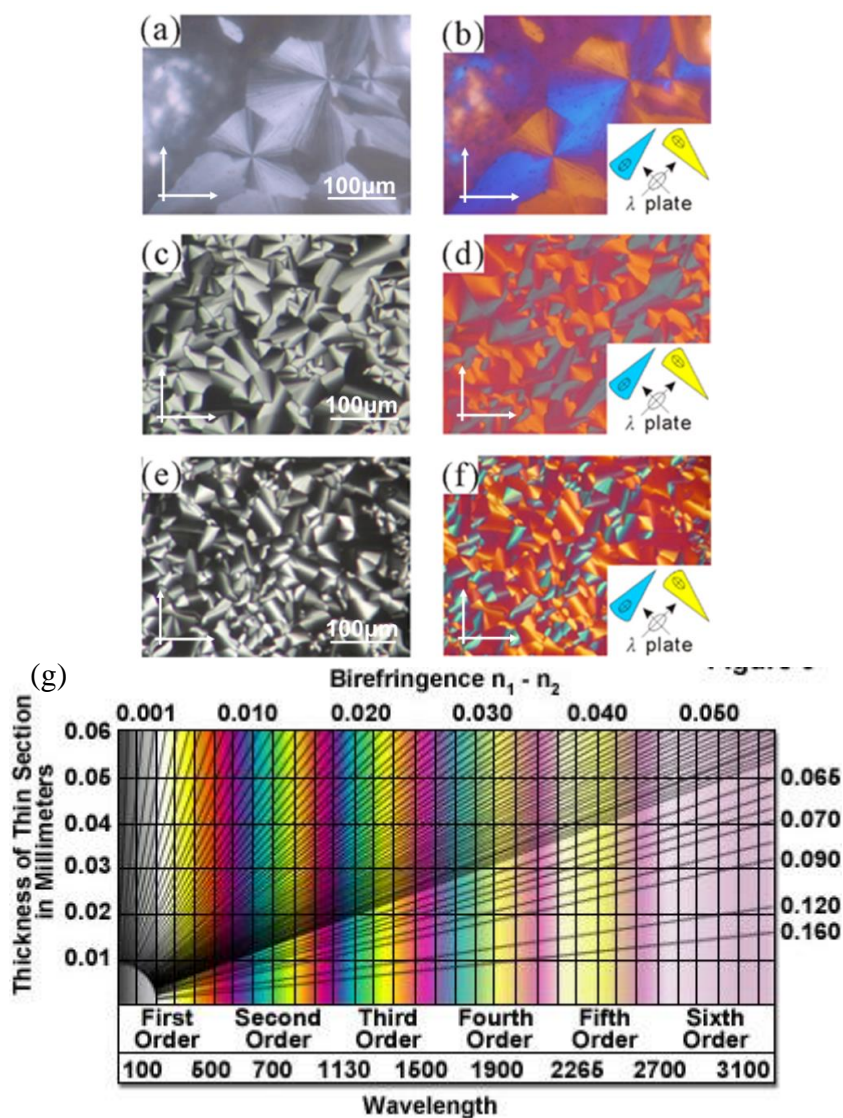


Figure S3.3 Polarized optical microscopy textures of (a, b) IC³/10 at 90 °C, (c, d) IC³/12 at 77 °C and (e, f) IC³/14 at 70 °C. (b,d,f) are recorded with a full-wave (λ) plate. (g) Michel-Levy colour chart (<http://www.olympusmicro.com/primer/techniques/polarized/michel.html>).

Determination of the direction of the slow (high refractive index) axis was based on the fact that by adding a fixed retardation to the whole image using a λ -plate, positive and negative phase shifts $+\Delta\Gamma$ and $-\Delta\Gamma$ between the ordinary and extraordinary rays could be distinguished. The λ -plate we used added a retardation of exactly 2π in the green (530 nm), so what appears black without the plate becomes magenta (white minus green

– see the Michel-Levy chart in Figure S3.3g). In areas with positive retardation parallel to the slow axis of the λ -plate the retardation is added, making the colour blue (phase difference $2\pi+\Delta\Gamma$), while in areas where retardation was subtracted the colour is yellow (phase difference $2\pi-\Delta\Gamma$). Thus e.g. in the blue sectors of the “spherulites” the slow axis of the LC is southwest-to-northeast, while the column direction is southeast-to-northwest (columns circle around the “spherulite”). Thus the slow axis, i.e. the long axis of the aromatic core of the molecules, is perpendicular to the columns.

3.5.4 Additional X-ray Diffraction Data

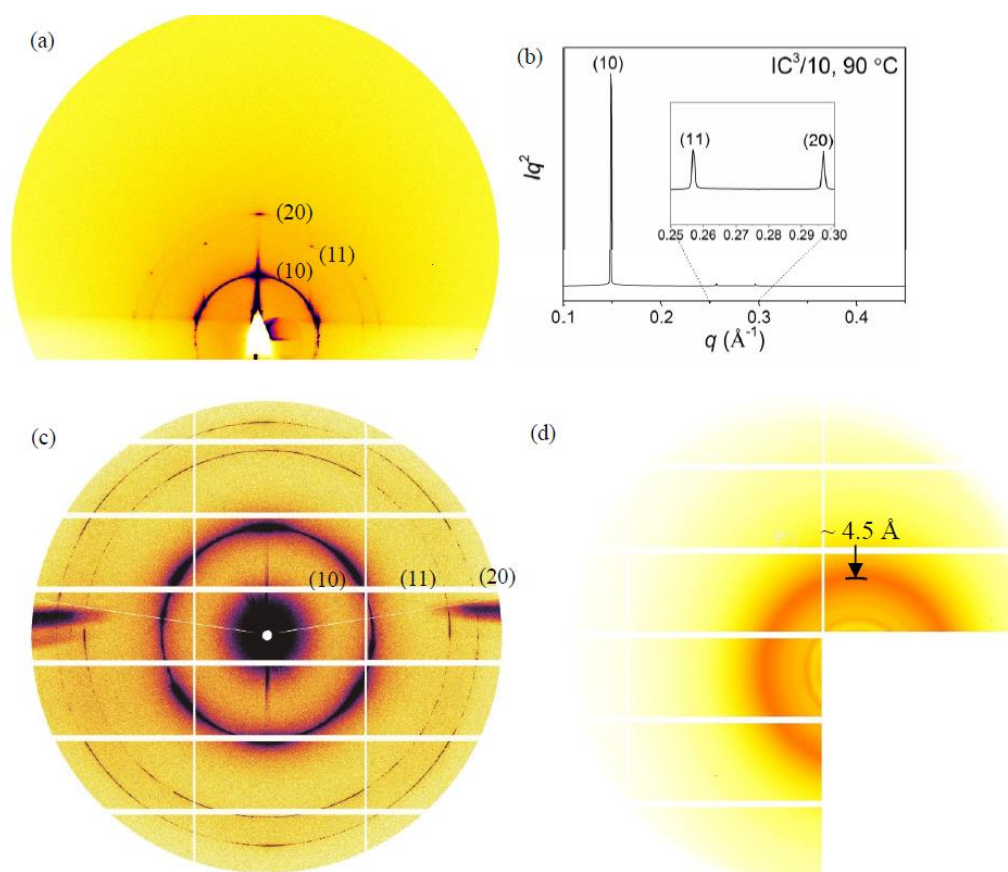


Figure S3.4 GISAXS diffraction pattern of IC³/10 recorded at 90 °C (a), transmission powder SAXS 2D profile and 1D curve recorded at 90 °C (b, c) and transmission powder WAXS 2D profile (d).

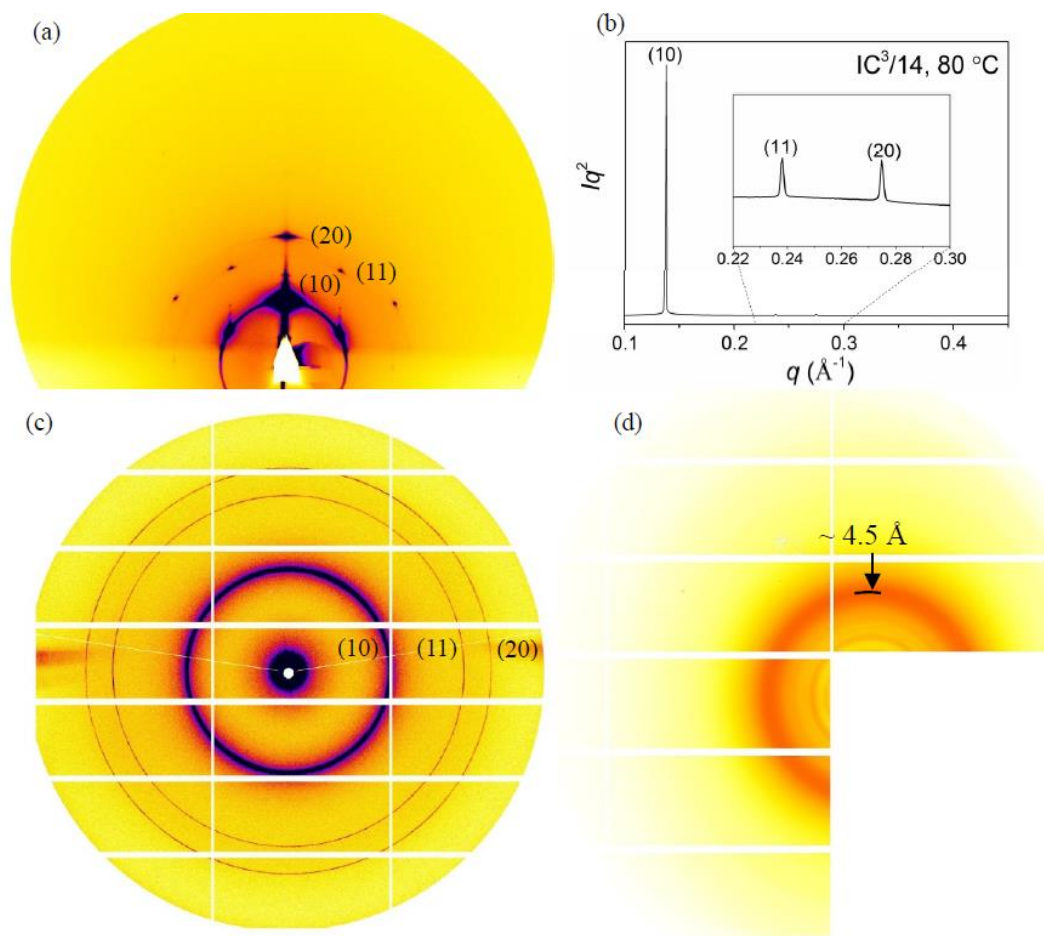


Figure S3.5 GISAXS diffraction pattern of **IC³/14** recorded at 80 °C (a), transmission powder SAXS 2D profile and 1D curve recorded at 80 °C (b, c) and transmission powder WAXS 2D profile (d).

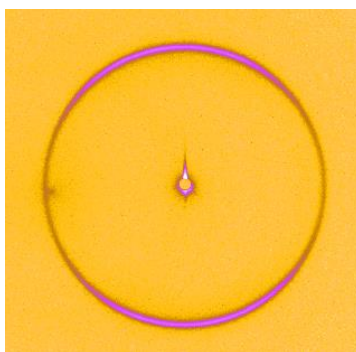


Figure S3.6 Transmission SAXS pattern of **IC³/14** held in glass capillary recorded at 90 °C. Capillary axis is horizontal. Only the inner ring (10) is shown. Preferred orientation of the columns parallel to the capillary axis is visible.

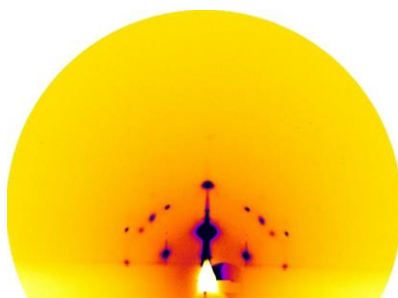


Figure S3.7 GISAXS pattern of the M-phase in IC³/12 cooled from the isotropic liquid to 50 °C.

Table S3.1 The indices, experimental, calculated d -spacings, intensities and lattice parameter of IC³/10 obtained from SAXS at 90 °C. All intensity values are Lorentz and multiplicity corrected.

(hk)	d -spacing (nm) experimental	d -spacing (nm) calculated	<i>Intensity</i>
(10)	4.25	4.24	23.7
(11)	2.44	2.45	0.148
(20)	2.12	2.12	0.0791
$a = 4.89$ nm			

Table S3.2 The indices, observed, calculated d -spacings, intensities and lattice parameter of IC³/12 obtained from SAXS at 80 °C. All intensity values are Lorentz and multiplicity corrected.

(hk)	d -spacing (nm) experimental	d -spacing (nm) calculated	<i>Intensity</i>	<i>Phase angle</i> (°)
(10)	4.46	4.45	27.7	0
(11)	2.56	2.57	0.272	120
(20)	2.22	2.22	0.217	180
$a = 5.13$ nm				

Table S3.3 The indices, experimental, calculated d -spacings, intensities and lattice parameter of IC³/14 obtained from SAXS at 80 °C. All intensity values are Lorentz and multiplicity corrected.

(hk)	d -spacing (nm) experimental	d -spacing (nm) calculated	<i>Intensity</i>
(10)	4.59	4.58	14.6
(11)	2.64	2.64	0.0655
(20)	2.29	2.29	0.0672
$a = 5.28$ nm			

Electron density maps as a function of the phase angle ϕ of reflection (11)

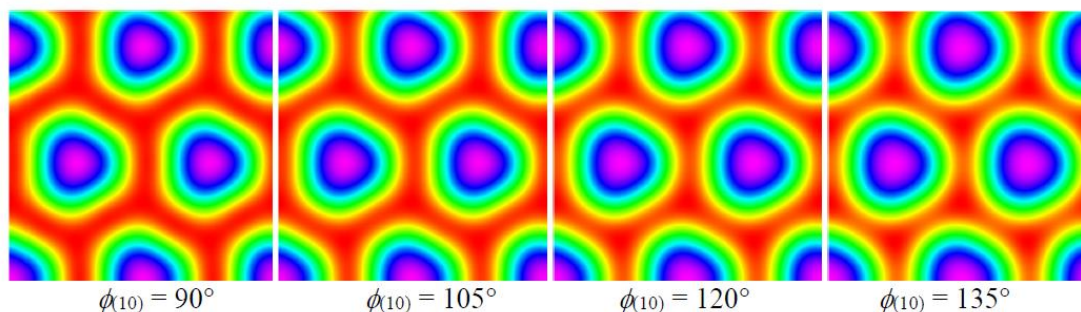


Figure S3.8 Electron density maps of the $p31m$ columnar phase of compound **IC³/12** using different values of $\phi_{(10)}$.

3.5.5 Estimate of the number of molecules per column stratum

Table S3.4 Estimation of the height of a stratum c assuming $n = 3$ molecules per unit cell (column stratum)

Compound	V_{arom} (nm ³) ^a	V_{aliph} (nm ³) ^b	V_{mol} (nm ³) ^c	V_{cell} (nm ³) ($n = 3$)	A (nm ²) ^d	c (nm) ($n = 3$)
IC³/10	0.98	2.01	2.99	8.99	20.7	0.434
IC³/12	0.98	2.40	3.38	10.14	22.8	0.445
IC³/14	0.98	2.80	3.78	11.34	24.1	0.471

a: V_{arom} = Volume of aromatic part of the molecule calculated using the crystal volume increments. [22]

b: V_{aliph} = Volume of aliphatic part of the molecule assuming a density of 0.8 g/cm³.

c: Volume of molecule (V_{mol}) = $V_{\text{arom}} + V_{\text{aliph}}$;

d: Cross section area of a unit cell of hexagonal phase $A = a^2 * 3^{1/2}/2$

e: $c = V_{\text{cell}}/A$

3.5.6 Arrangement of columns on substrate surface

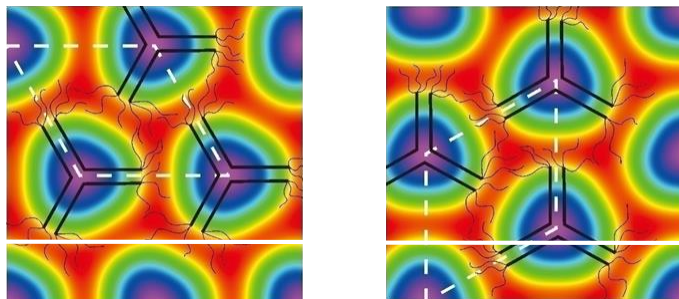


Figure S3.9 Two possible orientations of the hexagonal lattice of columns on a horizontal silicon substrate surface – view along column axis. The GISAXS patterns in Figures 2b, S3.4a and S3.5a all show that the $\text{Col}_{\text{hex}}/p31m$ phase in IC^3/n compounds faces the substrate with its (100) face (figure on the left) rather than its (110) face (figure on the right). This is the usual case in columnar phases with planar anchoring (ref 21). The horizontal white line suggests how the column array might face the substrate, showing that the columns would have to be cut through in the (110) arrangement (right). It should also be noted that the columns are surrounded by flexible alkyl chains, which reduces the effect of the shape of the column core, as the cores are not in direct contact with the substrate. Even so, there is bound to be a degree of surface reconstruction in the layer in direct contact with the substrate.

3.5.7 Additional second harmonic generation data

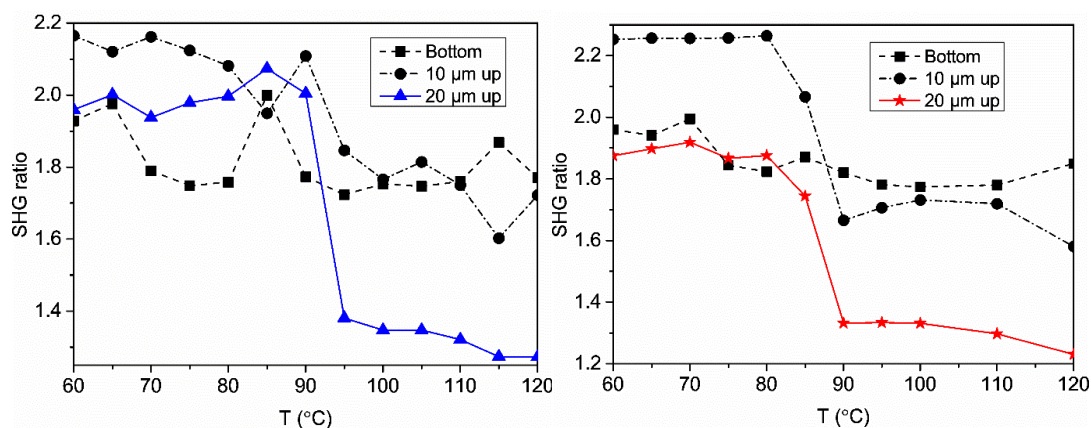


Figure S3.10 Normalized second harmonic (400 nm) intensity as a function of temperature for $\text{IC}^3/12$ (left) and $\text{IC}^3/14$ (right) sampled at the LC-Si interface (squares), 10 μm above it (circles) and 20 μm above it (blue triangles for $\text{IC}^3/12$ and red stars for $\text{IC}^3/14$). The large

step-up in SHG signal for the bulk LC coincides with the transition from isotropic liquid to the trigonal phase $\text{Col}_{\text{hex}}/p31m$.

Acknowledgement

The authors acknowledge funding for this work from EPSRC (EP-K034308, EP-P002250), NSFC (No. 21664015, 21364017, 21602195) and YEDF (ZD2015001). Y.X. L. thanks CSC for stipend and UoS for waiving the tuition fee of Y.X. L. For help with synchrotron experiments we thank Prof. N. Terrill and Dr. O. Shebanova, beamline I22, Diamond Light Source, and Drs. O. Bikondoa, S. Brown and P. Thompson of beamline BM28 at the ESRF.

References

- [1] D. Demus, J.W. Goodby, G.W. Gray, H.W. Spiess, V. Vill, Handbook of Liquid Crystals, Wiley-VCH, Weinheim, Germany, 1998.
- [2] D. Fazio, C. Mongin, B. Donnio, Y. Galerne, D. Guillon, D.W. Bruce, Bending and shaping: cubics, calamitics and columnars Basis of a presentation given at Materials Discussion, J. Mater. Chem., **11** (2001) 2852-2863.
- [3] W. Pisula, M. Zorn, J.Y. Chang, K. Mullen, R. Zentel, Liquid Crystalline Ordering and Charge Transport in Semiconducting Materials, Macromol. Rapid Commun., **30** (2009) 1179-1202.
- [4] M. O'Neill, S.M. Kelly, Ordered Materials for Organic Electronics and Photonics, Adv. Mater., **23** (2011) 566-584.
- [5] M. Funahashi, Nanostructured liquid-crystalline semiconductors - a new approach to soft matter electronics, J. Mater. Chem. C, **2** (2014) 7451-7459.
- [6] T. Wohrle, I. Wurzbach, J. Kirres, A. Kostidou, N. Kapernaum, J. Litterscheidt, J.C. Haenle, P. Staffeld, A. Baro, F. Giesselmann, S. Laschat, Discotic Liquid Crystals, Chem. Rev., **116** (2016) 1139-1241.
- [7] T. Kato, M. Yoshio, T. Ichikawa, B. Soberats, H. Ohno, M. Funahashi, Transport of ions and electrons in nanostructured liquid crystals, Nature Reviews Materials, **2** (2017).

- [8] C. Tschierske, Development of Structural Complexity by Liquid-Crystal Self-assembly, *Angew. Chem. Int. Ed.*, **52** (2013) 8828-8878.
- [9] G. Ungar, C. Tschierske, V. Abetz, R. Holyst, M.A. Bates, F. Liu, M. Prehm, R. Kieffer, X. Zeng, M. Walker, B. Glettner, A. Zywockinski, Self-Assembly at Different Length Scales: Polyphilic Star-Branched Liquid Crystals and Miktoarm Star Copolymers, *Adv. Funct. Mater.*, **21** (2011) 1296-1323.
- [10] C. Dressel, F. Liu, M. Prehm, X. Zeng, G. Ungar, C. Tschierske, Dynamic mirror-symmetry breaking in bicontinuous cubic phases, *Angew. Chem. Int. Ed.*, **53** (2014) 13115-13120.
- [11] E. Fontes, P.A. Heiney, W.H. Dejeu, Liquid-crystalline and helical order in a discotic mesophase, *Phys. Rev. Lett.*, **61** (1988) 1202-1205.
- [12] Y.K. Kwon, S.N. Chvalun, J. Blackwell, V. Percec, J.A. Heck, Effect of temperature on the supramolecular tubular structure in oriented fibers of a poly (methacrylate) with tapered side groups, *Macromolecules*, **28** (1995) 1552-1558.
- [13] M.A. Shcherbina, X.B. Zeng, T. Tadjiev, G. Ungar, S.H. Eichhorn, K.E.S. Phillips, T.J. Katz, Hollow Six-Stranded Helical Columns of a Helicene, *Angew. Chem. Int. Ed.*, **48** (2009) 7837-7840.
- [14] V. Percec, M. Peterca, T. Tadjiev, X.B. Zeng, G. Ungar, P. Leowanawat, E. Aqad, M.R. Imam, B.M. Rosen, U. Akbey, R. Graf, S. Sekharan, D. Sebastiani, H.W. Spiess, P.A. Heiney, S.D. Hudson, Self-Assembly of Dendronized Perylene Bisimides into Complex Helical Columns, *J. Am. Chem. Soc.*, **133** (2011) 12197-12219.
- [15] B. Glettner, F. Liu, X. Zeng, M. Prehm, U. Baumeister, M. Walker, M.A. Bates, P. Boesecke, G. Ungar, C. Tschierske, Liquid-crystalline kagome, *Angew. Chem. Int. Ed.*, **47** (2008) 9063-9066.
- [16] X. Zeng, R. Kieffer, B. Glettner, C. Nürnberger, F. Liu, K. Pelz, M. Prehm, U. Baumeister, H. Hahn, H. Lang, Complex multicolor tilings and critical phenomena in tetraphilic liquid crystals, *Science*, **331** (2011) 1302-1306.
- [17] H.C. Kolb, M.G. Finn, K.B. Sharpless, Click chemistry: Diverse chemical function from a few good reactions, *Angew. Chem. Int. Ed.*, **40** (2001) 2004-2021.
- [18] Y. Bouligand, Defects and textures of hexagonal discotics, *Journal de Physique*, **41** (1980) 1307-1315.
- [19] A.K. Boal, V.M. Rotello, Radial control of recognition and redox processes with multivalent nanoparticle hosts, *J. Am. Chem. Soc.*, **124** (2002) 5019-5024.
- [20] X.P. Tan, L.Y. Kong, H. Dai, X.H. Cheng, F. Liu, C. Tschierske, Triblock Polyphiles through Click Chemistry: Self-Assembled Thermotropic Cubic Phases

Formed by Micellar and Monolayer Vesicular Aggregates, *Chem. Eur. J.*, **19** (2013) 16303-16313.

[21] G. Ungar, F. Liu, X.B. Zeng, B. Glettner, M. Prehm, R. Kieffer, C. Tschierske, GISAXS in the study of supramolecular and hybrid liquid crystals, *Journal of Physics: Conference Series*, **247** (2010) 012032.

[22] A. Immirzi, B. Perini, Prediction of density in organic crystals, *Acta Crystallogr. A*, **33** (1977) 216-218.

[23] J. Matraszek, J. Mieczkowski, D. Pocięcha, E. Gorecka, B. Donnio, D. Guillon, Molecular factors responsible for the formation of the axially polar columnar mesophase Col(h)P(A), *Chem. Biodivers.*, **13** (2007) 3377-3385.

[24] M. Lehmann, M. Jahr, Programming star-mesogens toward the formation of columnar or cubic phases, *Chem. Mater.*, **20** (2008) 5453-5456.

[25] G. Hennrich, A. Omenat, I. Asselberghs, S. Foerier, K. Clays, T. Verbiest, J.L. Serrano, Liquid crystals from C-3-symmetric mesogens for second-order nonlinear optics, *Angew. Chem. Int. Ed.*, **45** (2006) 4203-4206.

[26] E. Beltrán, J.L. Serrano, T. Sierra, R. Giménez, Functional star-shaped tris(triazolyl)triazines: columnar liquid crystal, fluorescent, solvatochromic and electrochemical properties, *J. Mater. Chem.*, **22** (2012) 7797.

[27] S.K. Pathak, R.K. Gupta, S. Nath, D.S. Rao, S.K. Prasad, A.S. Achalkumar, Columnar self-assembly of star-shaped luminescent oxadiazole and thiadiazole derivatives, *J. Mater. Chem. C*, **3** (2015) 2940-2952.

[28] E. Westphal, M. Prehm, I.H. Bechtold, C. Tschierske, H. Gallardo, Room temperature columnar liquid crystalline phases of luminescent non-symmetric star-shaped molecules containing two 1,3,4-oxadiazole units, *J. Mater. Chem. C*, **1** (2013) 8011-8022.

[29] S. George, C. Bentham, X. Zeng, G. Ungar, G.A. Gehring, Monte Carlo study of the ordering in a strongly frustrated liquid crystal, *Phys. Rev. E*, **95** (2017) 062126.

[30] X.H. Cheng, X.Q. Bai, S. Jing, H. Ebert, M. Prehm, C. Tschierske, Self-Assembly of Imidazolium-Based Rodlike Ionic Liquid Crystals: Transition from Lamellar to Micellar Organization, *Chem. Eur. J.*, **16** (2010) 4588-4601.

Chapter 4 A new liquid crystal phase of counter-rotating staircases

This Chapter is a manuscript in preparation. I have carried out the experiments and data analysis by POM, X-ray diffraction, UV-vis, fluorescence emission spectroscopy, molecular modelling and dynamic simulation, and written the corresponding parts in the article. Prof. Xiaohong Cheng and her students from Yunnan University synthesized the compounds.

The references in the manuscript and supporting information have been combined for clarity.

4.1 Abstract

The recent discovery of spontaneous macroscopic chirality in some bicontinuous cubic and tetragonal liquid crystal (LC) phases of achiral compounds has revealed that fact that the ribbon-like columnar segments constituting their 3D networks are highly twisted around the columnar axis. Here we report the first example of 3D *columnar* LC phases formed by such twisted ribbons, discovered in two types of phasmids with bent or straight core. The phase has an orthorhombic lattice with space group *Fddd*, consisting of parallel twisted ribbons, both left- and right-handed in equal numbers. Each layer of the ribbon is formed by 2-3 molecules, either arranged parallel to each other in straight core phasmids, or back to back forming a three-arm star in bent core ones. The structure is related to, but distinct from, the *Fddd* phase previously found in block copolymers. The findings point the way to manipulating 3D helical self-assembled structures, with promising optical properties for applications.

4.2 Introduction

Soft matter such as block copolymers and liquid crystal (LC) materials, through self-assembly, has produced a variety of complex 2D and 3D nano-structures. In LCs, columnar phases are best known in compounds with discotic or wedge-shaped molecules [1-3], and more recently in rod-like amphiphiles with side-chains, forming various honeycomb structures [4-6]. Since 1980s rod-like molecules with more than one chain at each end (polycatenar mesogens, including “phasmids” with three chains at each end), have been known to form columnar phases, mainly the hexagonal columnar (Col_h), as well as cubic phases [7, 8]. Since then the progress in this area has been relatively limited.

In recent years such polycatenar compounds have been shown to form twisted ribbon-like segments of bicontinuous cubic, triple-network cubic and non-cubic 3D liquid crystals, with spontaneous chirality propagated by homochiral network junctions [8-10]. In the absence of such junctions, columnar phases of similar polycatenars have not been found to sustain uniform twist sense. Even if twist exists locally, helix reversals cannot be prevented in a 1D column. However, increasing evidence shows that even in columnar phases of polycatenars, twist sense can be maintained over macroscopic distances, propagated by intercolumnar steric interactions [11].

Here we report a new complex 3D LC phase formed by counter-rotating ribbons. It has an orthorhombic lattice and space group $Fddd$, with long range order between helical columns, but without positional correlation between individual molecules. The phase is found in two types of phasmidic compounds, one with a straight core, and the other with a 120° bent core, below the Col_h or trigonal columnar (Col_{tri}) phases [12]. Fluorene based fluorescent groups have been introduced to the cores of such compounds, and

their optical properties were studied, to investigate their application potentials in solar cells [13-15] and organic light-emitting diodes [16, 17].

It is worth noting that an *Fddd* phase, albeit with a distinctively different structure, has been reported previously in block copolymers [18-21]. Unlike our phase which is essentially columnar, this *Fddd* phase in block copolymers is a single network bicontinuous structure, even though both are closely linked to the bicontinuous cubic double gyroid structure, as will be discussed in more detail later.

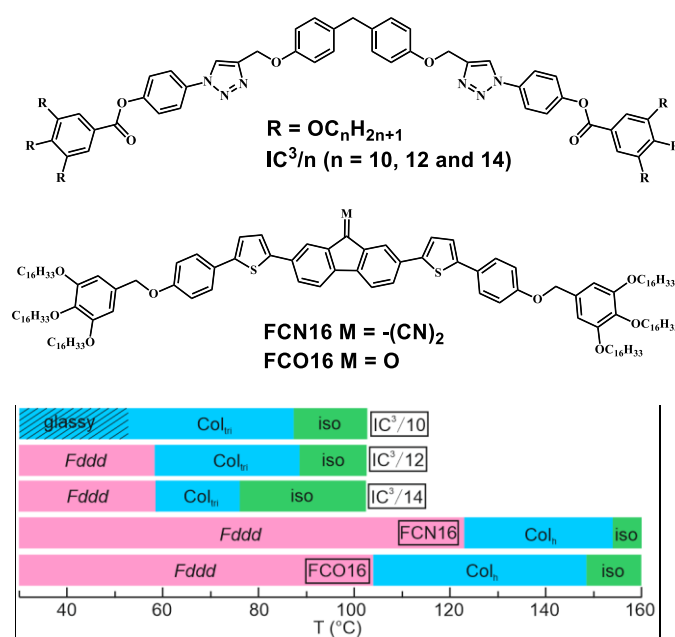
4.3 Results and Discussion

The chemical formulae of the LC compounds studied, bent-core phasmids IC^3/n and straight core phasmids FCN16 and FCO16, are shown in Table 1. All compounds form columnar phases at higher temperatures (

Table 4.1 and Figure S4.1, Supplementary Information, (SI)), with their lower temperature 3D LC phase the main focus of study of this work. Spherulitic textures, typical of LC columnar phases, are observed for all compounds below the isotropic temperature using polarized optical microscopy (POM) (Figure S4.2-4). No obvious change in optical texture can be observed on transition to the lower temperature phase, except the edges of spherulitic domains in FCN16 become blurry (Figure S4.3). This indicates that there are probably only minor changes to the molecular arrangement from the high-T columnar phase to the low-T phase. Only diffuse wide angle X-ray scattering (WAXS) is observed for IC^3/n ($n = 12$ and 14) in the low-T phase, with the intensity maximum corresponding to a d -spacing of 4.5 \AA (Figure S4.6). This confirms the LC nature of the phase. In addition to the peak at 4.5 \AA in WAXS, the low-T phase of FCN16 and FCO16 has an additional diffuse peak at 3.4 \AA (Figure S4.8-4.9, 4.12-4.13). The 3.4 \AA peak is observed on the horizon, for thin film samples where columns are

aligned parallel to the substrate surface, using grazing incidence WAXS (GIWAXS). This indicates a close 3.4 Å average intermolecular distance along the column, a sign of strong π - π interaction and potentially superior electroptical properties [3].

Table 4.1 The phase transition temperatures of compounds



Name	a, b, c (Å)	$T/^\circ\text{C}$ [$\Delta H/\text{kJ mol}^{-1}$]
$\text{IC}^3/10$	-	Iso 87.4 [1.2] Col _h 52.8 [12.0] glassy
$\text{IC}^3/12$	173.5, 106.1, 40.8	Iso 88.6 [0.7] Col _{tri} 58.3 [11.5] Fddd
$\text{IC}^3/14$	186.8, 107.8, 40.8	Iso 76.2 [0.3] Col _{tri} 58.5 [14.6] Fddd
FCN16	186.9, 107.9, 34.9	Iso 154.4 [1.8] Col _h 123.2 [37.4] Fddd 27.9 [103.0] Cr
FCO16	186.0, 107.4, 32.5	Iso 148.3 [0.7] Col _h 103.8 [8.3] Fddd 29.0 [10.5] Cr

*Peak DSC transition temperatures [and enthalpies] on cooling, at 5 K min⁻¹ for IC³/n and 10 K min⁻¹ for FCN16 and FCO16. Cr = crystal, Col_h = hexagonal columnar phase, Col_{tri} = trigonal columnar phase, Iso = isotropic melt. For more information of DSC, please see ref [12]/Chapter 3 and SI.

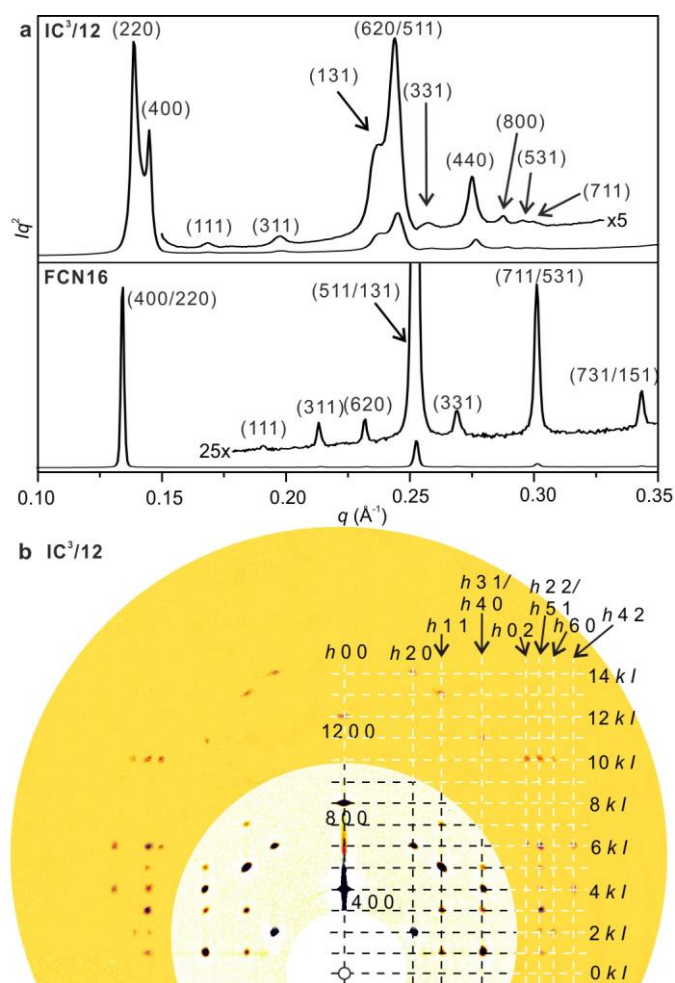


Figure 4.1 X-ray diffraction patterns. a, Transmission powder SAXS curve of IC³/12 recorded at 60 °C and FCN16 recorded at 120 °C in the cooling process; b, GISAXS diffractogram of IC³/12 recorded at 60 °C.

The transmission powder small angle X-ray scattering (SAXS) patterns of the compounds are rather complex (Figure a, S4.7a, S4.15a and Tables S4.1,4.3,4.5,4.7). The observed diffraction peaks can be indexed to an orthorhombic lattice ($a \sim 190 \text{ \AA}$, $b \sim 110 \text{ \AA}$ and $c \sim 40 \text{ \AA}$, Table 1) with the help of grazing incidence SAXS (GISAXS) diffraction patterns on surface oriented thin film samples of the phase (IC³/12, Figure b; IC³/14, Figure S4.7b; FCN16, Figure S4.11a-b; and FCN16, Figure S4.15b). The indices of peaks confirm the reflection conditions $h + k$, $h + l$, $k + l$ even, and $h + l$, $h +$

k equals $4n$ for $(h0l)$ and $(hk0)$ respectively. This narrows down the choice of space groups to either $F2dd$ or $Fddd$ (Table S2). The difference between the two rests on $(0kl)$, i.e. whether there is an additional condition that $k + l$ equals $4n$ ($Fddd$) or not ($F2dd$). However, no $(0kl)$ peaks were observed experimentally (Figure 4.1), and the higher symmetry $Fddd$ is considered first.

Starting with $IC^3/12$, its three strongest peaks (220), (400) and (511) (Table S1) are used to reconstruct the ED maps of the low-T phase on the assumption of an $Fddd$ space group. As $Fddd$ is centrosymmetric, there are eight different possible phase combinations as the phase of each peak can be only 0 or π . Many of these phase combinations are equivalent to one another by a simple shift of origin or inversion of electron density. This has made the selection of the phase combination $(0\pi0)$ very easy, bearing in mind that the structure should be closely related to the high-T Col_{tri} phase of IC^3/n , judging by the little change in the texture observed under POM upon transition to the low-T phase. Previously it has been found that the high-T Col_{tri} phase, with non-cylindrical columns, each stratum of which consists of three molecules packed back-to-back like a three-arm star (Chapter 3/[12]).

In the selected ED maps of the low-T phase of $IC^3/12$ as shown in Figures 4.2a,c, there are eight columns in the unit cell, and the number of molecules in each stratum of the column is calculated to be three as expected (Table S4.8 in SI). The cross-sections of columns look triangular, similar to that of the high-T phase. However, different to the high-T phase, the orientation of the triangles changes with increasing z elevation, creating four left- and four right-handed helical columns. The same three-arm molecular star based model can be constructed of the $Fddd$ phase, as shown in Figures 4.2b,d, with each three-arm star stratum of a column rotated by 13.3° around the column axis with respect to the previous one.

The reconstructed ED maps of the *Fddd* phase of FCN16 (Figures 4.2e,g) show the same eight twisted ribbons in the unit cell. Here the cross-section of each column is oval, hence the twisted columns have two grooves here instead of three as in $IC^3/12$. The number of molecules in each layer of a column is calculated to be about two (Table S4.8), and they are parallel to each other. The twist of molecular orientation in successive layers is calculated to be $\sim 18^\circ$, larger than that in IC^3/n compounds. The schematic model of the phase is shown in Figures 4.2f and h.

The two adjacent columns along *b*-axis rotate in the same direction, either clockwise or anticlockwise. However, along *a*-axis the column rotating direction alternates. View of single layers at different elevations (Figures 4.3 and S4.18-4.19) shows that molecules try to avoid clashing with each other for better packing. Molecular dynamic simulation results are also shown in Figures 4.4c-d to demonstrate how efficient molecular packing can be achieved in single layers. The mixing of left- and right-handed twisted columns, along with their neighbour avoiding mode at each and every level, are believed to have led to the formation of this complex phase. Such alternating helical columns in the *Fddd* phase, has also been directly observed by atomic force microscopy (AFM) on sample FCN16 (see Figure 4.2k, S4.22 and S4.23). The measured distance between the helical columns of $\sim 53 \text{ \AA}$, and helical pitch of $\sim 35 \text{ \AA}$, matches almost exactly our ED map and the proposed structural model. Edge dislocations and stacking faults of mismatching chiral columns have also been observed in Figure 4.2k1 and k2, respectively.

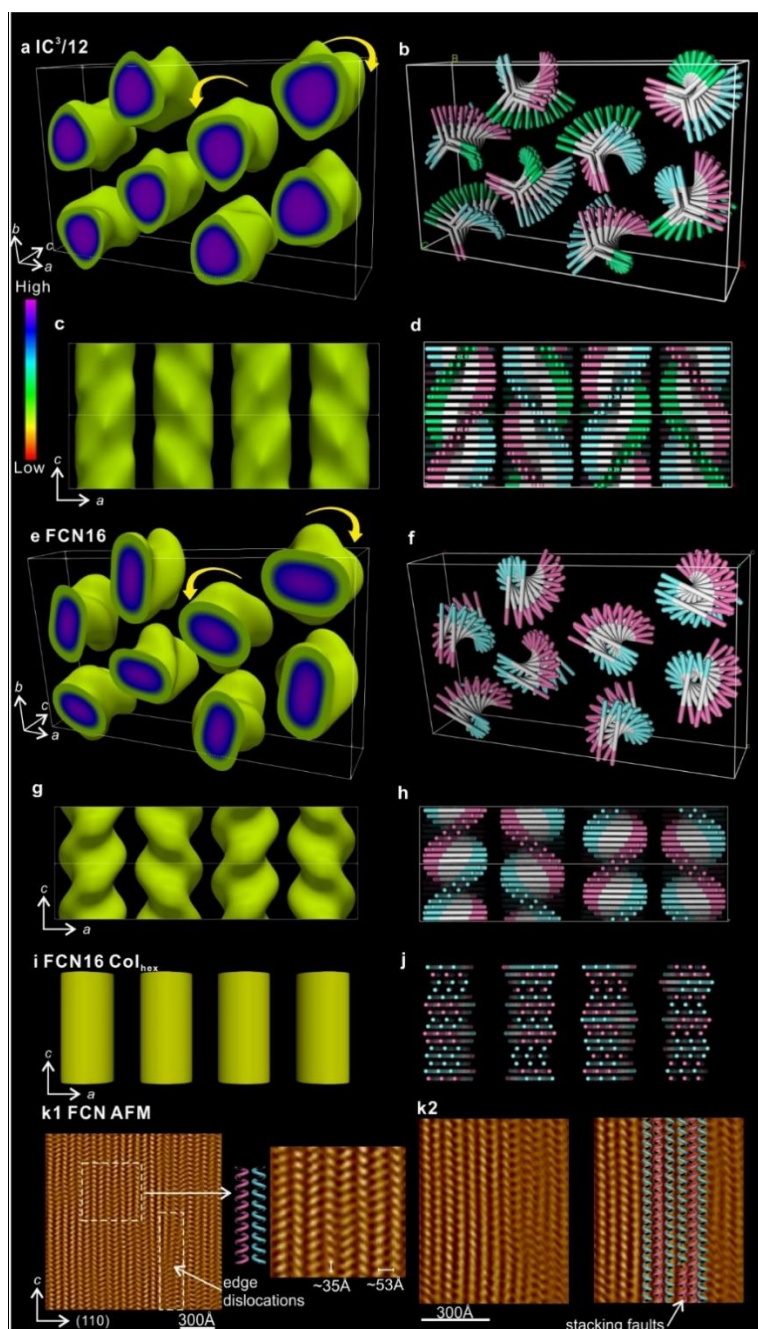


Figure 4.2 ED maps, sketched models and AFM images (a-d $IC^3/12$, e-k FCN16). a, c, e, g and i The ED maps showing high ED region. b, d, f, h and j Sketched models relevant to the ED maps. The two or three ends of molecules are showed by different colours for clarity. In c, d, four columns on a, c plane are displayed to observe the rotation direction. k1 and k2 are AFM of $Fddd$ of FCN16 recorded at 50 °C. The enlarged area shows the alternating left- and right-handed columns and also edge dislocations. And k2 shows stacking faults of mismatching chiral columns.

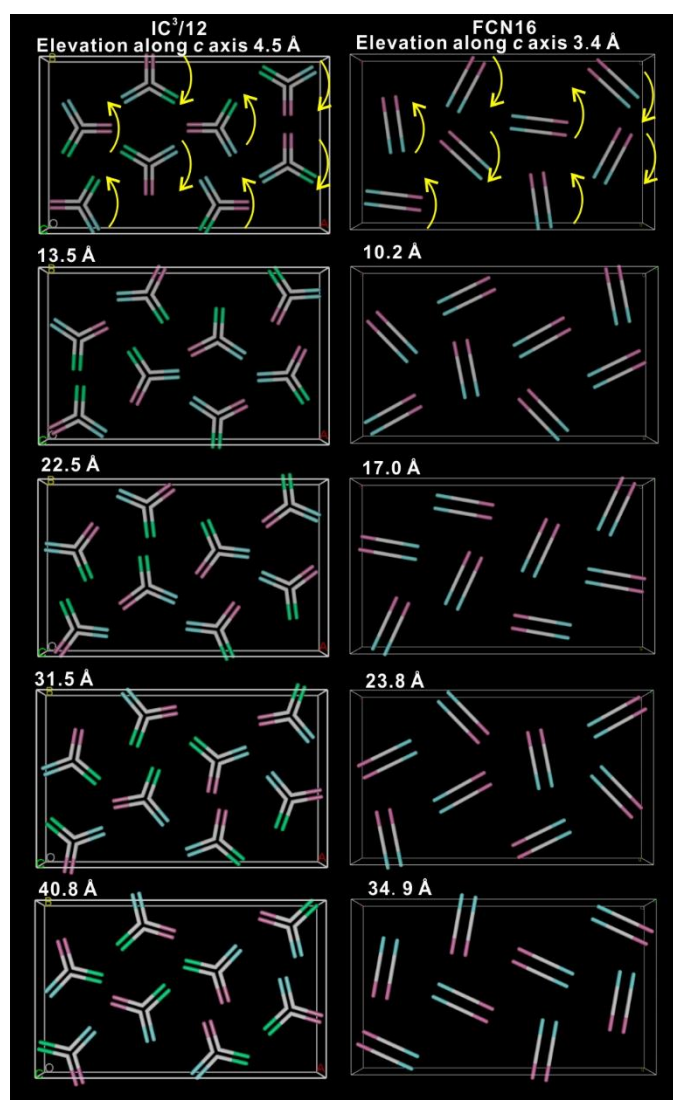


Figure 4.3 The layers at different elevation of the $Fddd$ model of $IC^3/12$ and FCN16.

Considering the transition between the low-T $Fddd$ phase and the high-T Col_{tri} phase, in IC^3/n compounds both consist of columns formed by layers of three-arm stars, with a triangular aromatic core surrounded by flexible alkoxy chains. While all the three-arm stars would (on average) point to the same direction in Col_{tri} phase, at lower temperatures the columns become helical, either left- or right-handed. Eight of such columns, are symmetrically related to each other, forming the unit cell of the $Fddd$ phase, for a more efficient packing of space. In FCN16 and FCO16, molecules in the

higher temperature Col_h phase orient randomly, with three molecules in each layer of a column and intermolecular distance of 4.5 Å (Figure 4.2i, j). The number of molecules in each layer of a column decreases to about two (Table S4.8, S4.10) and at the same time intermolecular distance decreases to 3.4 Å in the $Fddd$ phase (Figure S4.8,S4.9,S4.12,S4.13).

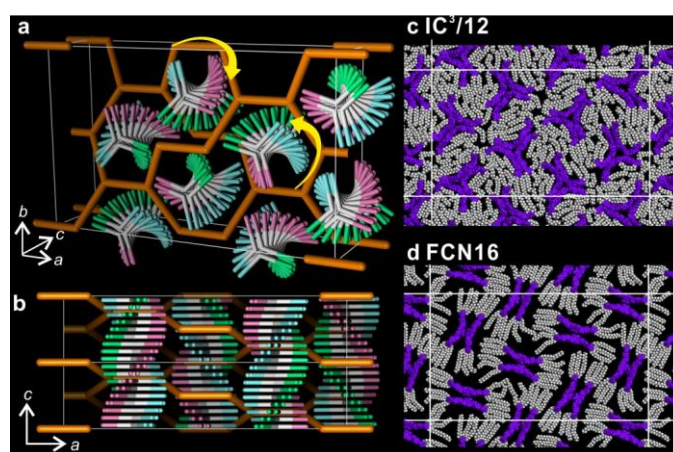


Figure 4.4 Sketched $Fddd$ models and snapshots of dynamic simulation. a, b Comparison of the single network model of copolymers (eg. poly(styrene-*block*-polyisoprene) and poly(isoprene-*b*-styrene-*b*-ethylene oxide) with the model of IC^3/n . The yellow arrows indicate the rotation direction of the columns and networks. The columns in the unit cell has been moved in a and b plane for better comparison with copolymers. Snapshot of dynamic simulation of c $\text{IC}^3/12$ and d FCN16: purple = aromatic, grey and white = aliphatic chains.

It is also interesting to compare our $Fddd$ structure with that formed by diblock (poly(styrene-*block*-polyisoprene)) or triblock copolymers (Poly(isoprene-*b*-styrene-*b*-ethylene oxide))[18-22]. Of course, the lattice parameters of the latter are much larger, for example, a values vary from 750 to 2125 Å[21, 23, 24] (a is defined as the largest lattice parameter as used in this paper, and in the following parameters from literature have been changed accordingly for easier comparison). However, the $a:b$ ratio is similar, about $\sqrt{3}:1$ in both copolymers and in LCs (Table S4.9). The $Fddd$ phase in copolymers has been determined to be a single network bicontinuous phase with 3-fold

junctions, and we have shown the network (in orange) in Figure 4.4a-b (after scaling) together with our $IC^3/12$ model for comparison. For copolymer, poly(styrene-block-polyisoprene), polystyrene forms the single network and the centre space is filled by polyisoprene [20]. While in our model, the aromatic cores are in the centre space and aliphatic chains fill the other space. It is obvious that our helical columns fill nicely the spaces between the network segments, with the twist sense of each column matching that of the network segments surrounding it. The $Fddd$ phase formed by copolymers is found to locate between lamellar and cubic phases ($Ia\bar{3}d$ or $I4_132$)[24, 25]. In contrast, our $Fddd$ phase is found at temperatures below the columnar phase.

The chiral columns in $Fddd$ phase remind us of the similar helical segments in the bicontinuous double gyroid cubic $Ia\bar{3}d$ phase, triple-network cubic $I23$ phase and non-cubic SmQ ($I4_122$) phase [9, 10]. The two networks in $Ia\bar{3}d$ phase possess opposite handedness, resulting in no overall chirality. The twist angle between successive layers is about 8° . The triple network $I23$ phase is chiral, but with similar twist angle, $7.5-9^\circ$. SmQ phase is also chiral as the two networks have the same chirality, and with twist angle $\sim 9^\circ-10^\circ$. Successive layers keep lying parallel to maximize the π - π interactions, and also have to rotate to minimize the steric clash in such bicontinuous phases, especially at network junctions. In the $Fddd$ phase, there is no junction. Columns are parallel with each other and molecular layers twist $\sim 13^\circ$ in IC^3/n and $\sim 18^\circ$ in FCN16 and FCO16. From the bicontinuous phases formed by polycatenars to the $Fddd$ phases formed by phasmids, the number of alkyl chains increases from 4 to 6, and thus molecules have to twist by higher degrees to avoid clashing. The aliphatic chains of the two parallel FCN16 molecules with straight cores have higher limitation of flexibility to fill the space than the aliphatic chains of the three-arm star formed by bent-core $IC^3/12$ molecules (see the cross sections of ED map in Figure 4.2a,e). Due to this, the twist angle of FCN16 and FCO16 with straight cores is higher than that of IC^3/n

with bent cores. There is no net chirality as there is an equal number of left- and right-handed helical columns. It is expected that other complex columnar LC phases with helical columns and overall chirality could also exist in similar compounds.

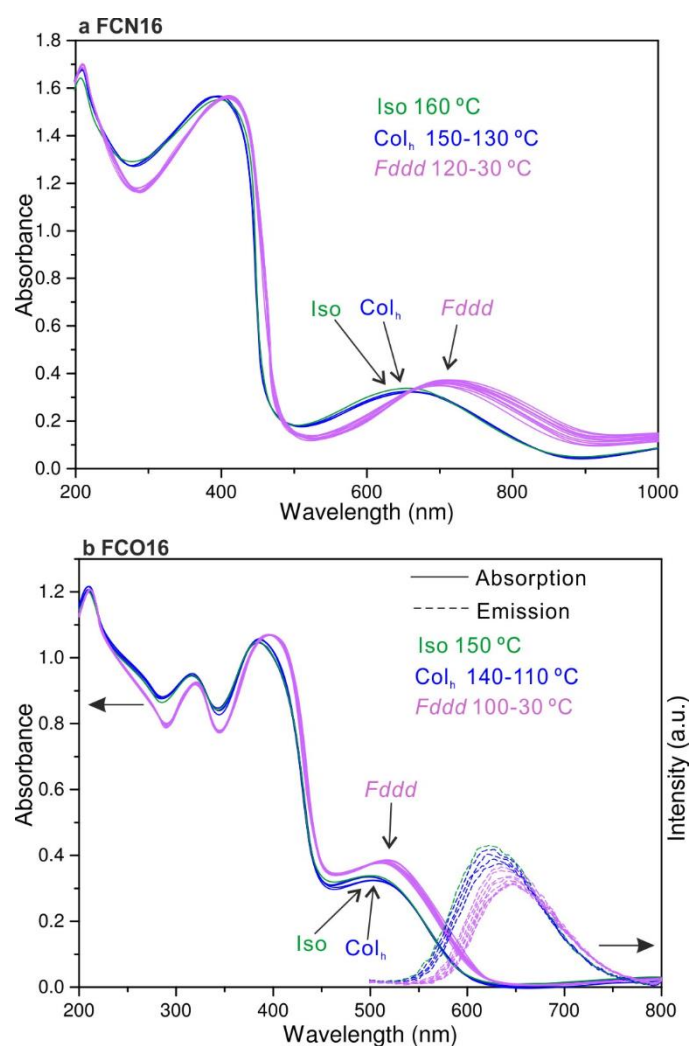


Figure 4.5 UV-vis spectra of FCN16 and FCO16, and fluorescence emission spectra of FCO16 excited at 420 nm. The spectra are recorded from isotropic phase to *Fddd* phase in the cooling process.

With fluorescently conjugated cores, FCN16 and FCO16 are potential materials for electrooptical applications. The UV-vis spectra of FCN16 and FCO16 (Figure 4.5) show the bathochromic/red shift at the transition from Col_h to *Fddd* phase, suggesting an

increase of conjugation between molecules in the cooling process. This also relates to the change of intermolecular distance from 4.5 (Col_h) to 3.4 Å (*Fddd*) observed in WAXS and GIWAXS (Figure S4.8, S4.9, S4.12, S4.13). The band gaps of FCN16 and FCO16 in *Fddd* phase can be determined to be ~1.39 and ~2.12 eV respectively (Table S11). This corresponds well with the HOMO/LUMO energy of FCO16, calculated by Density Functional Theory, of -5.02/-2.25 eV (Figure S4.24) [26]. The fluorescence emission signal is observed in FCO16 at ~644 nm in *Fddd* phase with a 130 nm Stokes shift.

In summary, a new complex 3D orthorhombic *Fddd* phase, consisting of counter-rotating helical columns, has been discovered in bent and straight core phasmidic LC compounds. The discovery of this first confirmed example of columnar LC phase with long range ordered chiral columns in non-chiral compounds, shows the underlying universality of polycatenar compounds to form columns with twisting molecular strata. It points to the possibility of even more complex 3D columnar structures in similar compounds with potential spontaneous formation of macroscopic chirality. This, coupled with incorporation of fluorescent rigid cores in such molecules as demonstrated in this paper, could lead the way to the design of a new generation of organic semiconductor devices, e.g. OLEDs that emit circularly polarized light.

4.4 Methods

X-ray diffraction

Transmission powder SAXS/WAXS experiments were carried out at station I22 of Diamond Light Source, U.K. Powder samples were prepared in 1 mm glass capillaries and held in a modified Linkam hot stage. Pilatus 2M detector (Dectris) was used and the X-ray energy was 12.4 keV. GISAXS/GIWAXS experiments were carried out at

BM28 of European Synchrotron Radiation Facility, France and I16 of Diamond Light Source, U.K. The 2d diffractograms were collected using a MAR165 CCD camera at BM28 and Pilatus 2M detector (Dectris) at I16. Thin film samples were prepared from melt on silicon substrate. *n*-tetracontane was used to calibrate the sample to detector distance.

Reconstruction of ED map

Electron density maps were calculated by inverse Fourier transformation using the standard procedure as described in International Tables for Crystallography [27]. All the peaks were fitted by Gaussian functions and the intensities can be obtained by the value of the fitted peak area. For the peaks which contribute to the intensity of the same peak that cannot be resolved in the powder diffraction pattern, the relative intensities of the peaks can be measured from the GISAXS diffraction pattern. More details can be found in SI.

Sketched models and molecular models

Sketched models and molecular models were built using Materials Studio (Accelrys). For molecular models, geometry optimization and molecular dynamic simulation were performed using the Forcite Plus module with Universal Force Field. The convergence tolerances for geometry optimization were 0.001 kcal/mol for energy and 0.5 kcal/mol/Å for force. NVT annealing dynamics was performed through 30 cycles between 300 and 600 K, with a total annealing time of 30 ps.

AFM

AFM was recorded by Bruker Multimode 8 with Nanoscope V controller. The sample was dissolved in toluene and spin coated on a highly oriented pyrolytic graphite substrate.

UV-vis and fluorescence emission spectroscopy

The solid samples were melt and spread evenly between quartz plates (1 mm thickness). UV-vis spectra were recorded by Lambda 900 (Perkin Elmer). Fluorescence emission spectra of FCO16 were excited at 420 nm and recorded by the instrument Fluoromax4. The sample (2-5 mg) was sealed between two aluminium pans and another two blank pans were used as a reference. Differential scanning calorimetry (DSC) thermograms were recorded on a DSC 200 F3 Maia calorimeter (NETZSCH) instrument with heating/cooling rates as specified.

Polarized Optical Microscopy (POM) figures were recorded using an Olympus BX-50 which is equipped with a 1- λ retardation plate, 40 times lens and Mettler HS82 hot stage.

4.5 Supporting Information

4.5.1 DSC thermograms

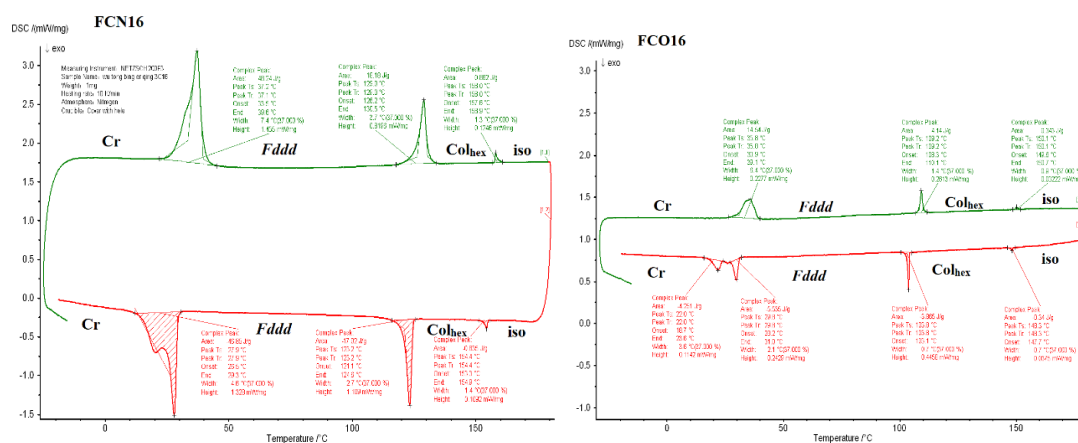


Figure S4.1 DSC thermograms of compounds **FCN16** and **FCO16** at heating and cooling scan rate of 10 K min⁻¹.

4.5.2 Polarized Optical Microscopy (POM)

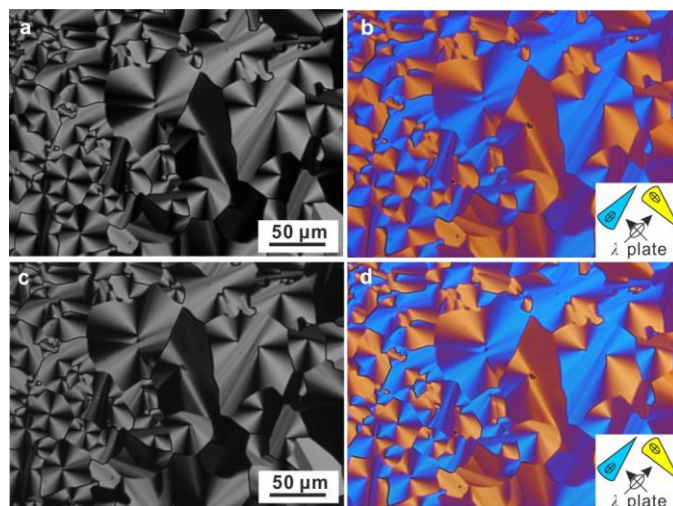


Figure S4.2 POM of IC³/14 examined at (a,b) 70 °C and (c, d) 40 °C, at which temperatures the sample was in Col_{tri} and *Fddd* phases, respectively.

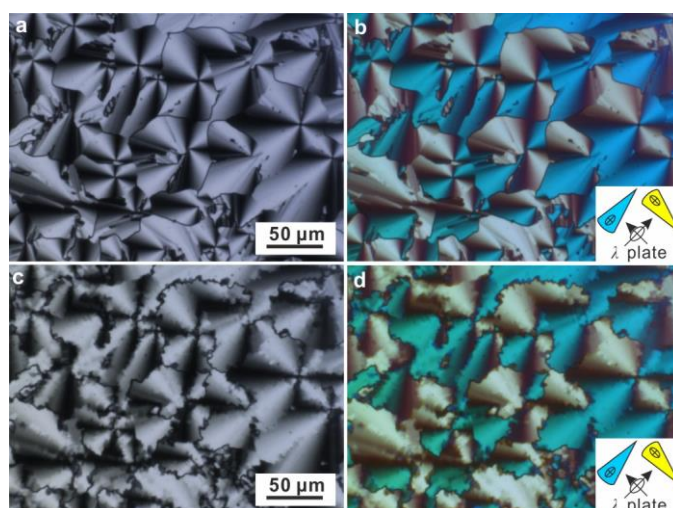


Figure S4.3 POM of FCN16 examined at (a,b) 140 °C and (c, d) 100 °C, at which temperatures the sample was in Col_h and *Fddd* phases, respectively.

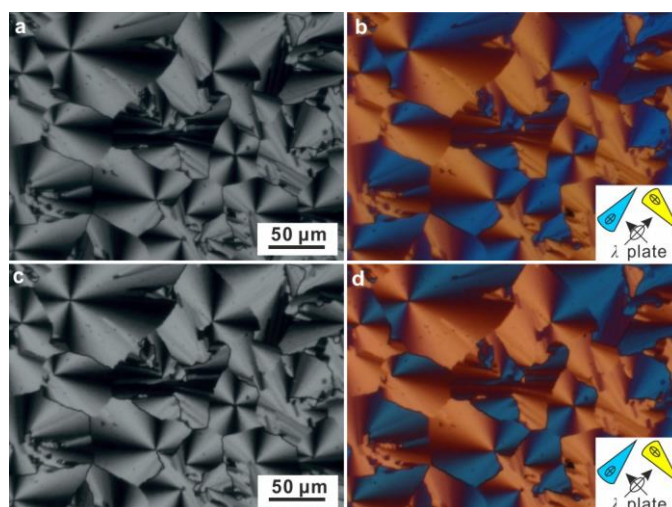


Figure S4.4 POM of FCO16 examined at (a,b) 140 °C and (c, d) 90 °C, at which temperatures the sample was in Col_h and $Fddd$ phases, respectively.

4.5.3 X-ray Diffraction Data

IC³/10

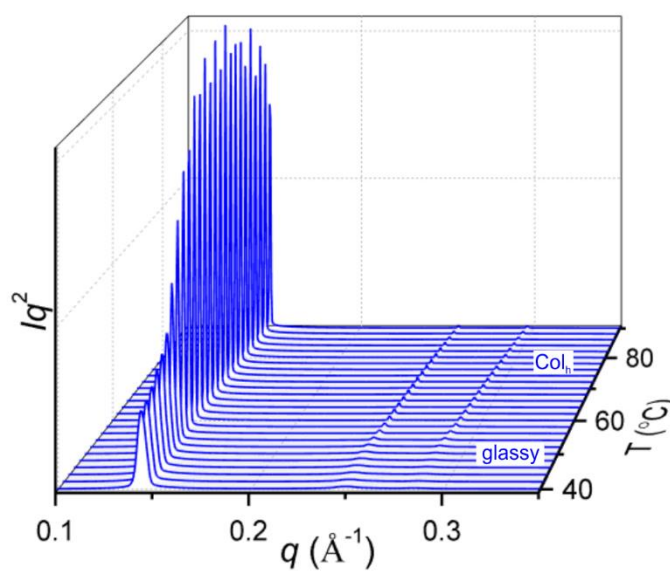


Figure S4.5 SAXS cooling scans of IC³/10.

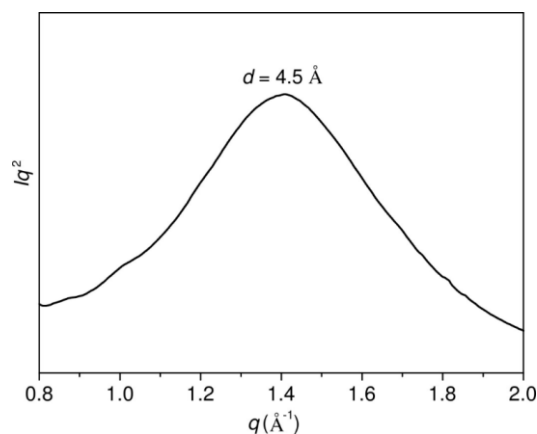
IC³/12

Figure S4.6 Transmission powder WAXS diffractogram of *Fddd* phase of **IC³/12** recorded at 60 °C.

Table S4.1 Indices, experimental, calculated *d*-spacings, intensities, phases and lattice parameters of diffraction peaks of **IC³/12** recorded by transmission powder SAXS in the *Fddd* phase at 60 °C. All intensities are Lorentz and multiplicity corrected.

<i>(hkl)</i>	experimental <i>d</i> -spacings (Å)	calculated <i>d</i> -spacings (Å)	<i>Intensity</i>	<i>Phase</i>
(220)	45.2	45.3	93.0	0
(400)	43.3	43.4	100.0	π
(111)	37.2	37.2	0.4	-
(311)	31.7	31.8	0.4	-
(131)	26.4	26.4	4.0	-
(511) ^a	25.6	25.6	6.4	0
(620)			3.8	-
(331)	24.3	24.3	0.2	-
(440)	26.8	26.3	3.9	-
(800)	21.7	21.7	1.2	-
(531)	21.2	21.2	0.1	-
(711)	20.8	20.8	0.1	-
a = 173.5 Å, b = 106.1 Å and c = 40.8 Å				

a: (511) and (620) diffraction peaks are overlapping in the powder diffraction pattern. While their total intensity is taken from the powder diffraction results, the intensity ratio between the two has been determined from the GISAXS pattern. An azimuthal scan through the (511) and (620) diffraction peaks in the 2D GISAXS pattern is obtained first, and the intensities of the two diffraction peaks are measured from the areas of the diffraction peaks in the scan by fitting

each peak to a Gaussian function. Due to the sample geometry (multiple domains sharing the same a -axis), measured intensities need to be multiplied by the corresponding q_{bc} , i.e. q vector component which is perpendicular to the common a -axis of domains, for (511) and (620) these are $q_{(011)}$ and $q_{(020)}$ respectively. Further correction by diffraction peak multiplicity leads to an intensity ratio $I_{(511)}:I_{(620)}$ of 0.63:0.37.

Table S4.2 Reflection conditions and space groups.

Reflection conditions							Space group
hkl	$h0l$	$hk0$	$0kl$	$h00$	$0k0$	$00l$	
	$h+l$	$h+k$	$k+l$	h	k	l	$F222$, $Fmm2$, $Fm2m$, $F2mm$, $Fmmm$,
$h+k, h+l, k+l$	h, l	$h+k=4n; h, k$	$k+l=4n; k, l$	$h=4n$	$k=4n$	$l=4n$	$Fd2d$
	$h+l=4n; h, l$	h, k	$k+l=4n; k, l$	$h=4n$	$k=4n$	$l=4n$	$Fdd2$
	$h+l=4n; h, l$	$h+k=4n; h, k$	k, l	$h=4n$	$k=4n$	$l=4n$	$F2dd$
	$h+l=4n; h, l$	$h+k=4n; h, k$	$k+l=4n; k, l$	$h=4n$	$k=4n$	$l=4n$	$Fddd$

* $h+k$ means the value of h plus k is even; h, k and l means the values are even.

IC³/14

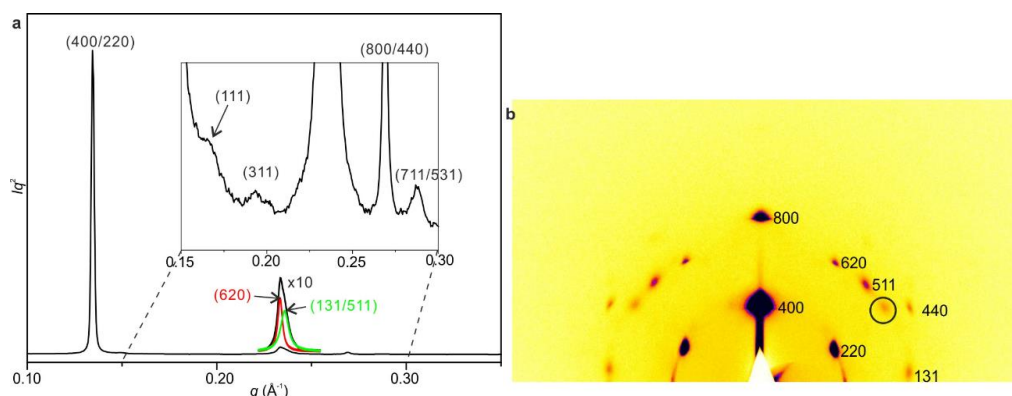


Figure S4.7 The powder SAXS curve and GISAXS pattern of $Fddd$ phase of $IC^3/14$ recorded at 60 °C (cooled from 80 °C). The black circled spots are (511) from the other orientation. More details of the other orientation can be seen in Figure S10. As the d -spacings of (620) and

(511/131) are close with each other, it is shown in one peak in powder SAXS. The separated and fitted peaks are displayed in the figure.

Table S4.3 Indices, experimental, calculated d -spacings, intensities, phases and lattice parameters of diffraction peaks of **IC³/14** recorded by transmission powder SAXS in the $Fddd$ phase at 60 °C (cooled from 80 °C). All the intensities are Lorentz and multiplicity corrected.

(hkl)	experimental d - spacings (Å)	calculated d - spacings (Å)	<i>Intensity</i>
(400) ^a	46.7	46.7	100.0
(220)			93.0
(111)	37.4	37.4	0.3
(311)	32.5	32.5	0.5
(620)	27.0	27.0	1.4
(511) ^b	26.8	26.7	0.8
(131)		26.7	0.1
(800)	23.4	23.4	1.1
(440)		23.3	1.0
(711) ^c	21.9	21.9	0.3
(531)			0.3
$a = 186.8 \text{ \AA}$, $b = 107.8 \text{ \AA}$ and $c = 40.8 \text{ \AA}$			

a: As (400) is on the meridian of the GISAXS pattern, its intensity cannot be accurately determined (sensitive to incident beam angle and distribution of domain orientations), consequently it is not possible to determine the (400) and (220) intensity ratio in the same way as described before for (511) and (620) peaks of IC³/12. It is assumed that the ratio of the two is the same as that of two in powder SAXS of IC³/12. Similar treatment is used to calculate the intensities of (800) and (440).

b: The ratio of the intensities of (511) and (131) from the GISAXS pattern can be calculated to be 0.85:0.15.

c: As the intensities of (711) and (531) are too weak to be observed in GISAXS pattern, the contribution of them in powder SAXS is assumed to be the same as in IC³/12.

FCN16

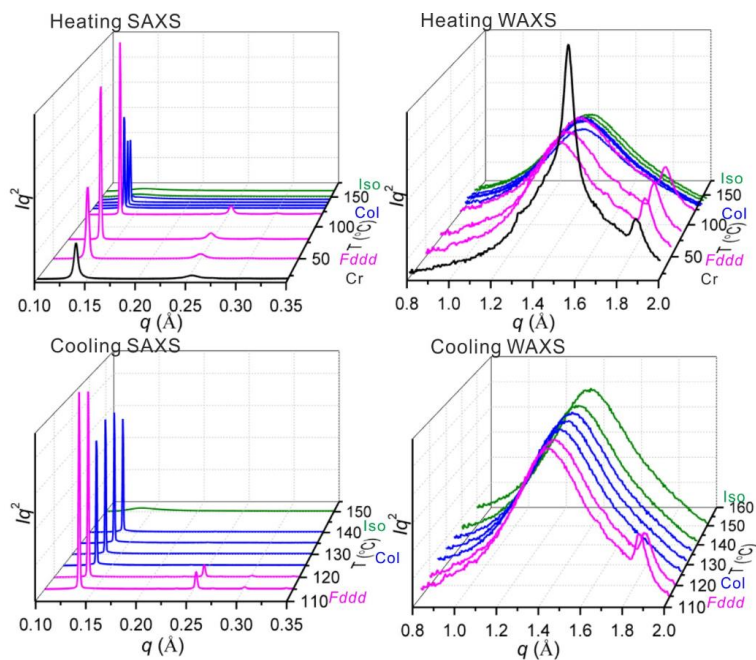


Figure S4.8 SAXS/WAXS heating and cooling scans of **FCN16**.

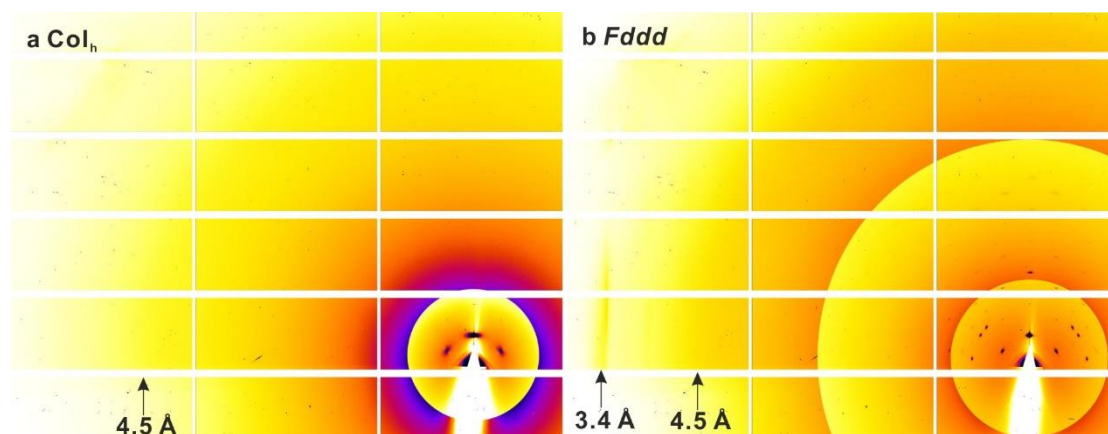


Figure S4.9 The GIWAXS/GISAXS patterns of (a) Col_h and (b) $Fddd$ of **FCN16** recorded at 130 °C and 100 °C, respectively.

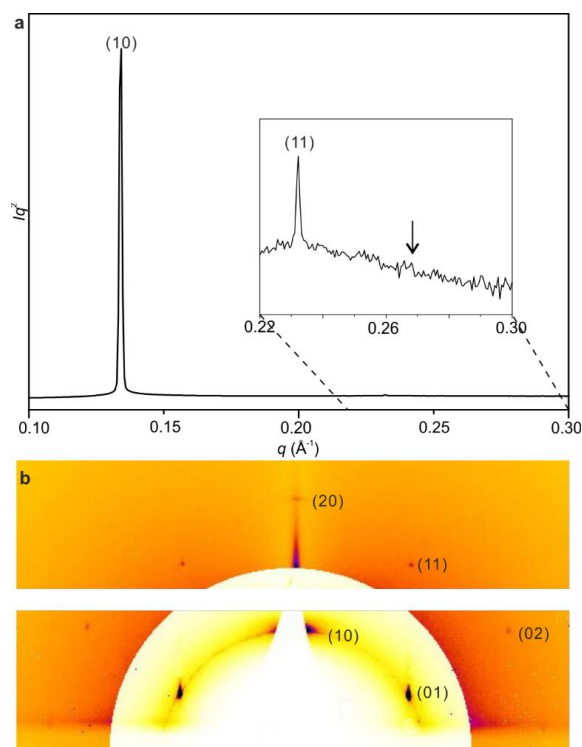


Figure S4.10 The powder SAXS curve and GISAXS pattern of Col_h phase of **FCN16** recorded at 130 °C (cooled from 150 °C). In SAXS curve, the intensity of (20) is too weak to be observed, as indicated by the arrow.

Table S4.4 Indices, experimental, calculated d -spacings, intensities, phases and lattice parameters of diffraction peaks of **FCN16** recorded by transmission powder SAXS in the Col_h phase at 130 °C (cooled from 150 °C). All the intensities are Lorentz and multiplicity corrected.

(hk)	experimental d -spacings (Å)	calculated d -spacings (Å)	<i>Intensity</i>	<i>Phase</i>
(10)	46.9	46.9	100.0	0
(11)	27.1	27.1	0.03	0
(20)	-	23.4	-	-
$a = 54.1 \text{ \AA}$				

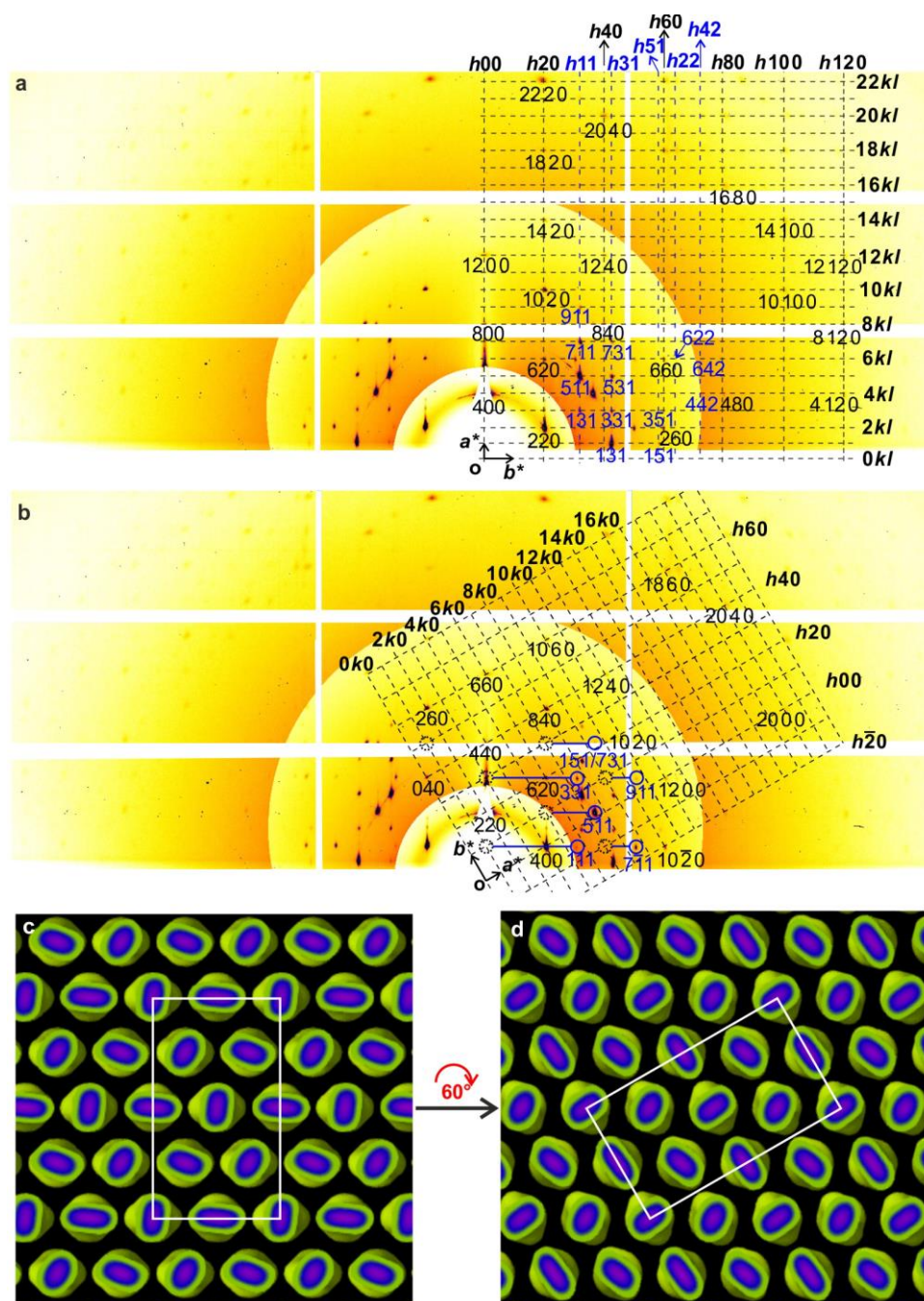


Figure S4.11 a, b The GISAXS pattern of *Fddd* phase of FCN16 recoded at 120 °C (cooled from 150 °C); c, the two orientations on ED maps, matched with the lattices on the GISAXS pattern. In b, the full line of circles are the projections of relevant reflections in dashed circles. The position of the projection of reflection (*hkl*) rotating along (110) on the 2D plane is

$$\text{calculated by } \left(\sqrt{\frac{h^2}{a^2} + \frac{l^2}{b^2} + \frac{l^2}{c^2} - \frac{(\frac{h}{a^2} + \frac{k}{b^2})^2}{\frac{1}{a^2} + \frac{1}{b^2}}}, \frac{\frac{h}{a^2} + \frac{k}{b^2}}{\sqrt{\frac{1}{a^2} + \frac{1}{b^2}}} \right).$$

Table S4.5 Indices, experimental, calculated d -spacings, intensities, phases and lattice parameters of diffraction peaks of FCN16 recorded by transmission powder SAXS in the $Fddd$ phase at 120 °C (cooled from 160 °C). All the intensities are Lorentz and multiplicity corrected.

$(hkl)^a$	experimental d -spacings (Å)	calculated d -spacings (Å)	Intensity	Phase
(400)	46.7	46.7	100.0	π
(220)			93.0	π
(111)	32.7	32.7	0.1	-
(311)	29.2	29.3	0.2	-
(620)	27.0	27.0	0.4	-
(511)	24.8	24.8	8.4	π
(131)			1.5	π
(331)	23.3	23.2	0.2	-
(711)	20.8	20.8	0.6	π
(531)			0.6	0
(731)	18.3	18.3	0.2	-
(151)			0.2	-
$a = 186.9 \text{ \AA}$, $b = 107.9 \text{ \AA}$ and $c = 34.9 \text{ \AA}$				

a: The calculation of the contribution of each reflection (hkl) to overlapped peaks in powder diffraction pattern is the same as in IC³/12 and IC³/14.

FCO16

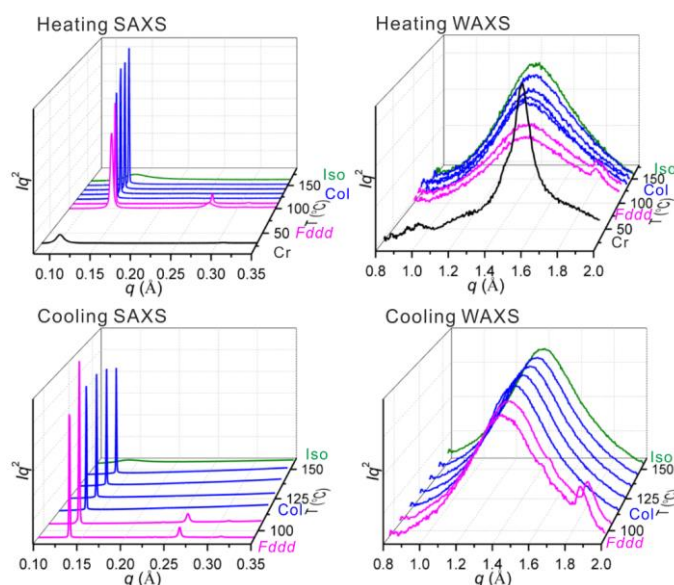


Figure S4.12 SAXS/WAXS heating and cooling scans of FCO16.

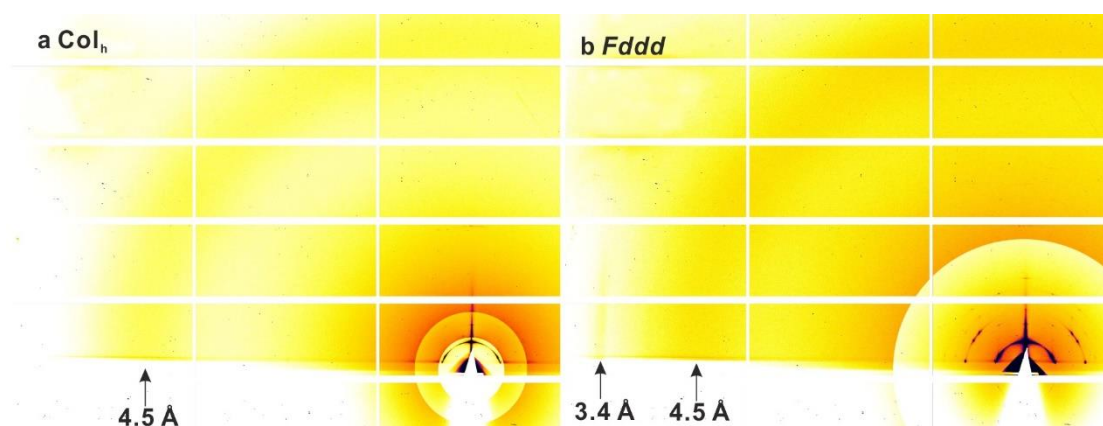


Figure S4.13 The GIWAXS/GISAXS patterns of (a) Col_h and (b) $Fddd$ of **FCO16** recorded at 115 °C and 90 °C, respectively.

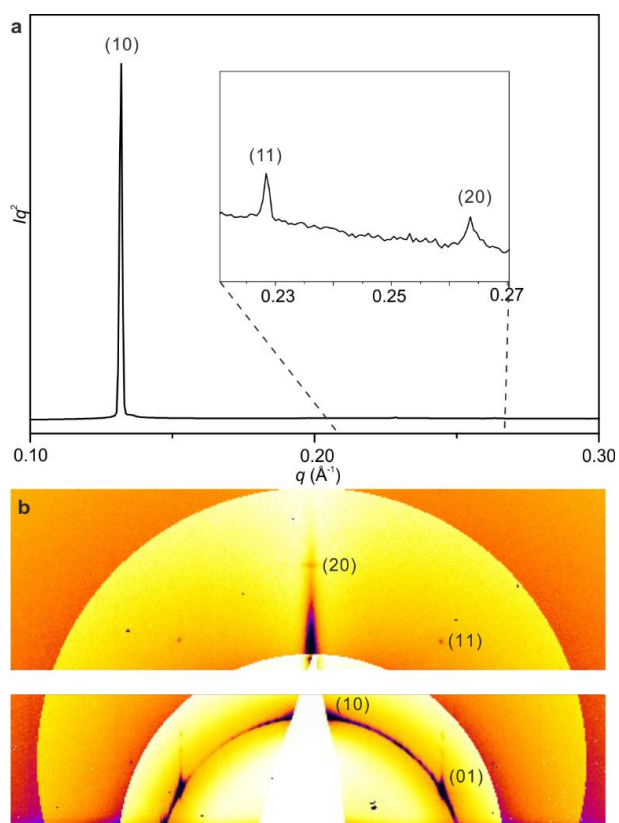


Figure S4.14 The powder SAXS curve and GISAXS pattern of Col_h phase of **FCO16** recorded at 115 °C (cooled from 150 °C).

Table S4.6 Indices, experimental, calculated d -spacings, intensities, phases and lattice parameters of diffraction peaks of **FCO16** recorded by transmission powder SAXS in the Col_h phase at 130 °C (cooled from 150 °C). All the intensities are Lorentz and multiplicity corrected.

(hk)	experimental d -spacings (Å)	calculated d -spacings (Å)	Intensity	Phase
(10)	47.6	47.6	100	0
(11)	27.4	27.5	0.2	0
(20)	23.8	23.8	0.1	π
$a = 55.0 \text{ \AA}$				

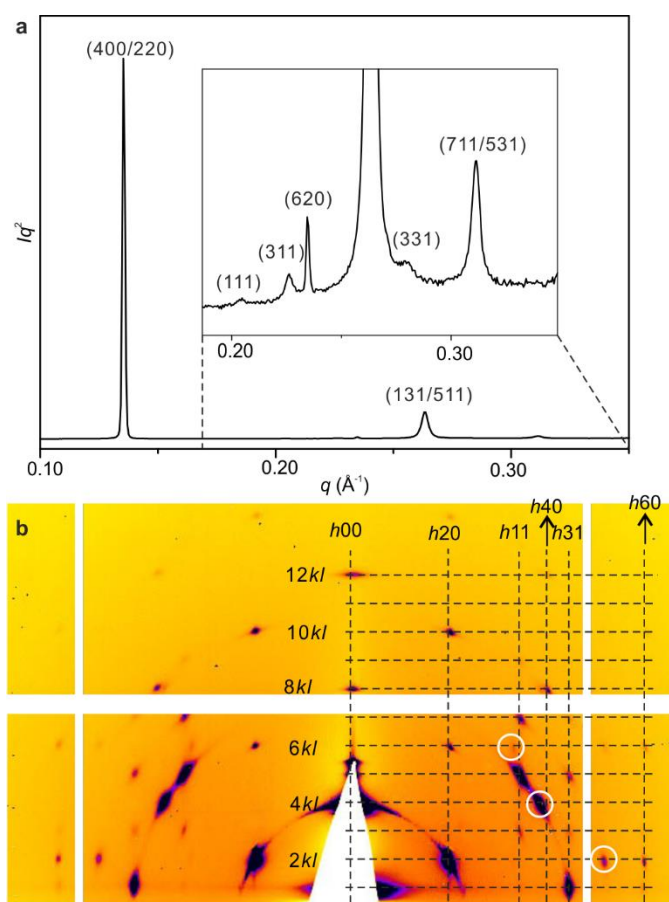


Figure S4.15 The powder SAXS curve and GISAXS pattern of $Fddd$ phase of **FCO16** recorded at 105 °C (cooled from 150 °C). The white circled spots are (511), (331) and $(7\bar{1}1)$ from the other orientation.

Supplementary Table S4.7 Indices, experimental, calculated d -spacings, intensities, phases and lattice parameters of diffraction peaks of **FCO16** recorded by transmission powder SAXS in the $Fddd$ phase at 105 °C (cooled from 160 °C). All the intensities are Lorentz and multiplicity corrected.

$(hkl)^a$	experimental d -spacings (Å)	calculated d -spacings (Å)	Intensity
(400)	46.5	46.5	100.0
(220)			93.0
(111)	30.7	30.7	0.3
(311)	27.8	27.8	0.07
(620)	26.7	26.7	0.5
(511)	23.9	23.9	4.0
(131)			0.7
(331)	22.4	22.4	0.4
(711)	20.2	20.2	0.1
(531)			0.1
$a = 186.0 \text{ \AA}$, $b = 107.4 \text{ \AA}$ and $c = 32.5 \text{ \AA}$			

a: The calculation of the contribution of each reflection (hkl) to overlapped peaks in the powder diffraction pattern is the same as in IC³/12 and IC³/14.

4.5.4 Reconstruction of Electron Density Maps

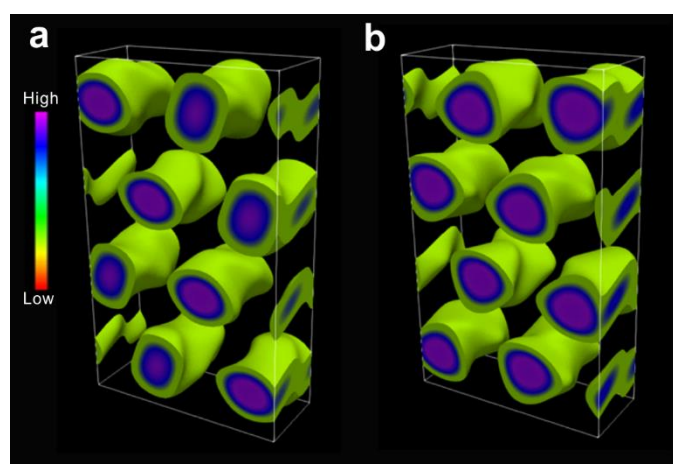


Figure S4.16. The different phase combinations of IC³/12 of (220), (400) and (511): (a) $\pi\pi 0$ and (b) $0\pi 0$.

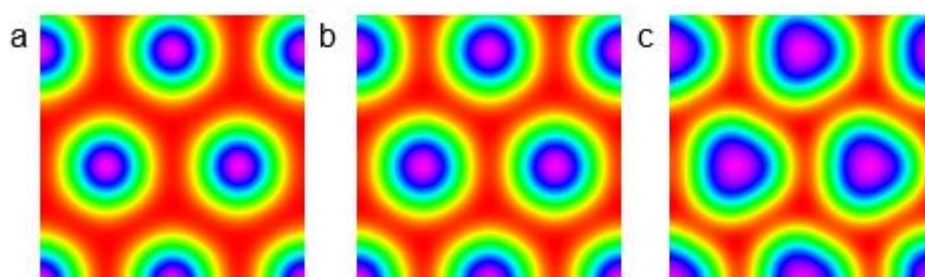


Figure S4.17 The ED maps of columnar phases of (a) **FCN16**, (b) **FCO16** and (c) **IC³/12**.

4.5.5 Estimate of the number of molecules per column stratum

Table S4.8 Calculation of number of molecules per column stratum.

Compound	Lattice parameters Å	V_{cell} (Å ³ *10 ⁴) ^a	V_{mol} (Å ³ *10 ³) ^b	n_1 ^c	n_2 ^d	n_3 ^e	n_4 ^f	α ^g
IC³/12	$a = 173.5$ $b = 106.1$ $c = 40.8$	75.11	3.38	222.2	27.8	9.1	3.1	13.3
IC³/14	$a = 186.8$ $b = 107.8$ $c = 40.8$	82.16	3.78	217.4	27.2	9.1	3.0	13.3
FCN16	$a = 186.9$ $b = 107.9$ $c = 34.9$	70.37	3.82	184.3	23.0	10.3	2.2	17.5
FCO16	$a = 186.0$ $b = 107.4$ $c = 32.5$	64.92	3.76	172.8	21.6	9.6	2.3	18.8

a: $V_{\text{cell}} = a*b*c$;

b: Volume of molecule ($V_{\text{mol}} = V_{\text{arom}} + V_{\text{aliph}}$);

V_{arom} = Volume of aromatic part of the molecule calculated using the crystal volume increments [28];

V_{aliph} = Volume of aliphatic part of the molecule assuming a density of 0.8 g/cm³;

c: Number of molecules in each unit cell $n_1 = V_{\text{cell}} / V_{\text{mol}}$;

d: Number of molecules per column $n_2 = n_1 / 8$;

e: Number of stratum $n_3 = c / 4.5$ or 3.4 (intermolecular distance of IC³/n is estimated to be 4.5 Å; intermolecular distance of FCN16 and FCO16 is 3.4 Å, as indicated by the peak in WAXS and GIWAXS).

f: Number of molecules per column stratum $n_4 = n_2 / n_3$.

g: twist angles α between stratum. For IC³/n, $\alpha = 120^\circ / n_4$; For FCN16 and FCO16, $\alpha = 180^\circ / n_4$.

Table S4.9 Lattice parameters ratio comparison.

Compound	$c:b:a$	$b:a$
Block copolymers* [22]	1:2:3.5	1:1.732
IC³/12	1:2.6:4.3	1:1.635
IC³/14	1:2.6:4.6	1:1.733
FCN16	1:3.1:5.4	1:1.732
FCO16	1:3.3:5.7	1:1.732

*The lattice parameter a is defined as the largest one.

Table S4.10 Calculation of number of molecules in a unit cell in Col_h phase.

Compound	a (Å)	V_{cell} (Å ³ ·10 ¹) ^a	n^b
FCN16	54.1	114.1	3.0
FCO16	55.0	117.9	3.1

a: $V_{\text{cell}} = a^2 c \sin 60^\circ$ (c is estimated to be 4.5 Å);

b: $n = V_{\text{cell}} / V_{\text{mol}}$.

4.5.6 Additional schematic models with ED maps

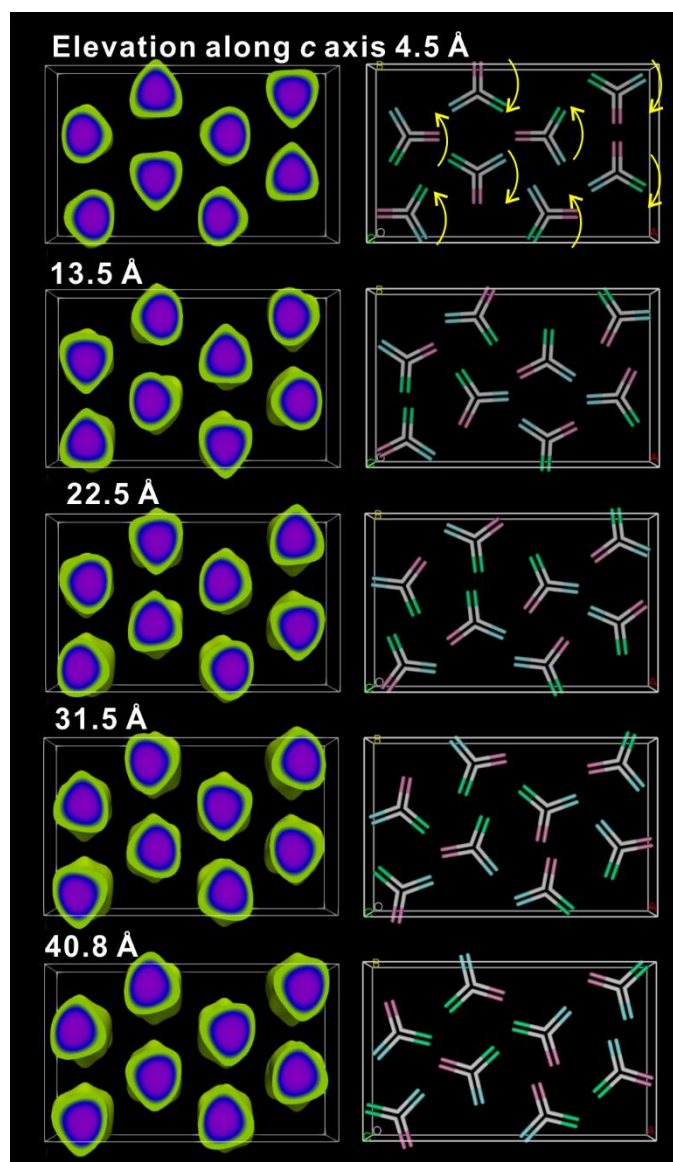


Figure S4.18 Detailed ED maps (high ED region) and sketched models viewing along *c*-axis with different layers of IC³/12.

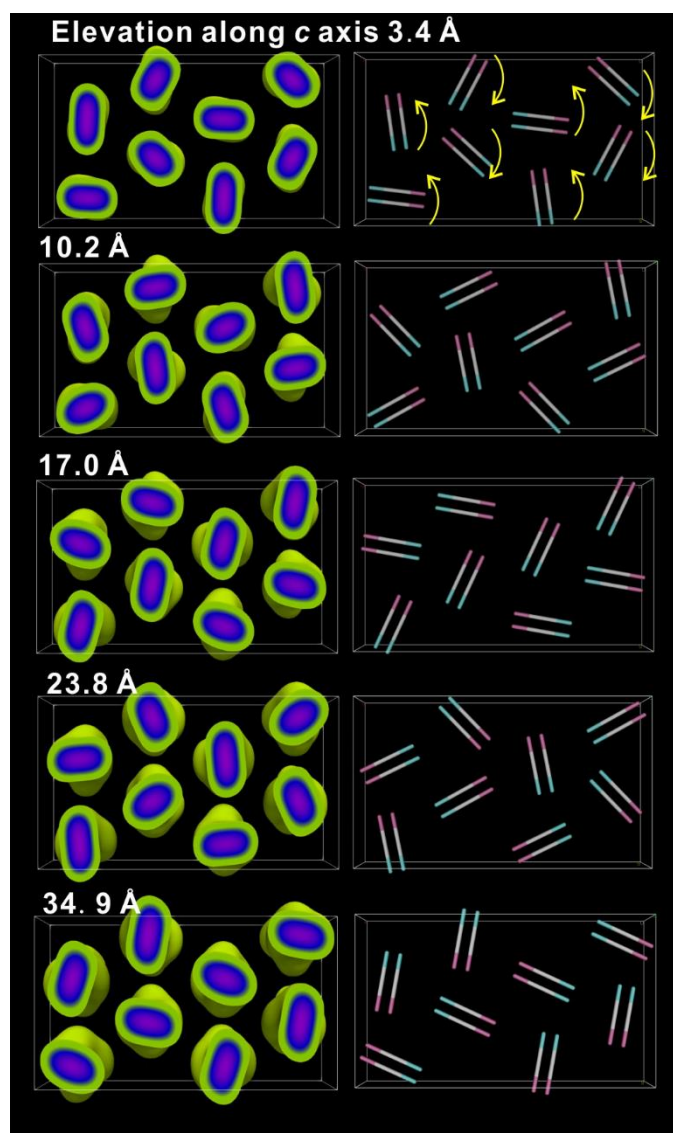


Figure S4.19 Detailed ED maps (high ED region) and sketched models viewing along c -axis with different layers of FCN16.

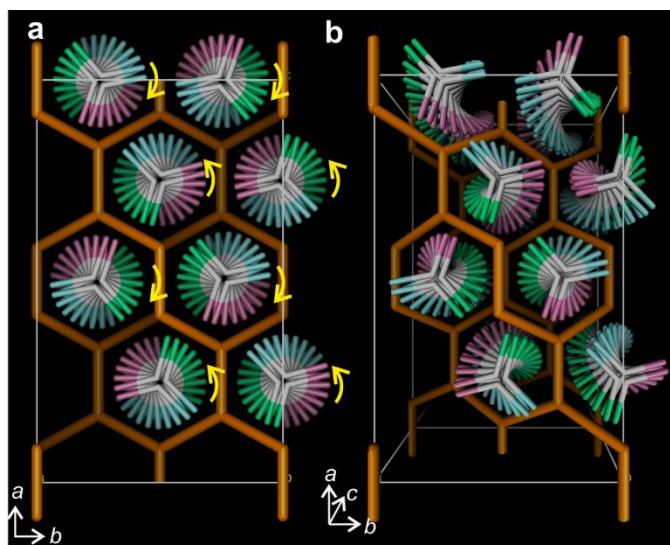


Figure S4.20 Additional sketched $Fddd$ models. The comparison of the single network model formed by copolymers with the model of IC^3/n .

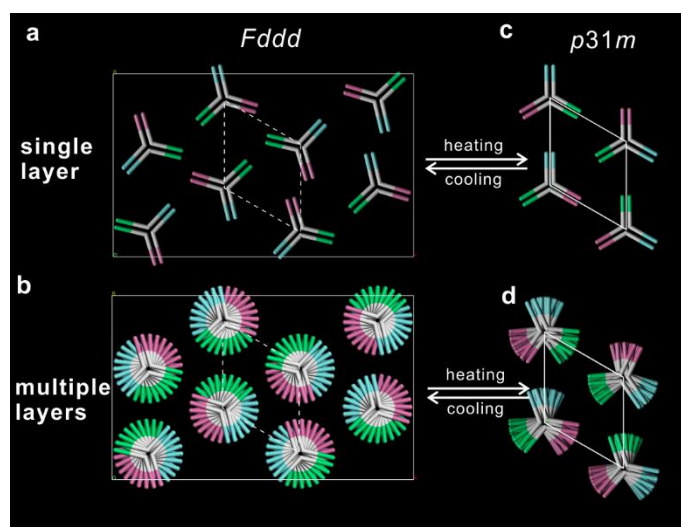


Figure S4.21 The comparison of models at single layer and multiple layers of (a, b) $Fddd$ and (c, d) Col_{tri} phase.

4.5.7 Additional AFM

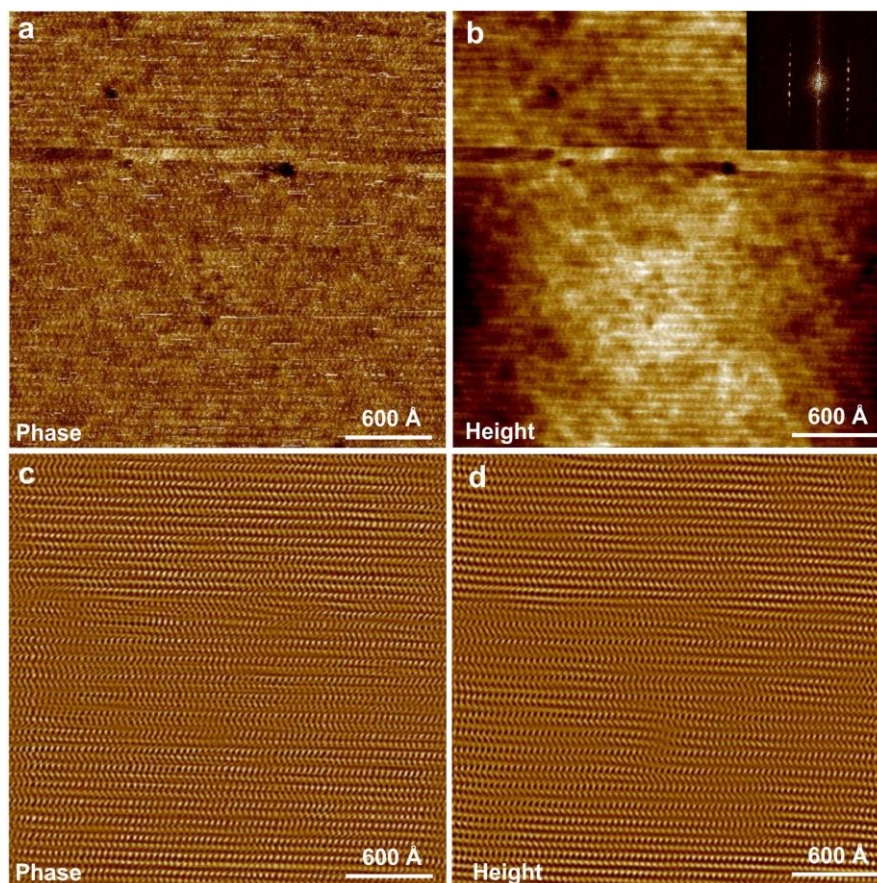


Figure S4.22 AFM of FCN16 (a, b) original figures and (c, d) the inverted FFT.

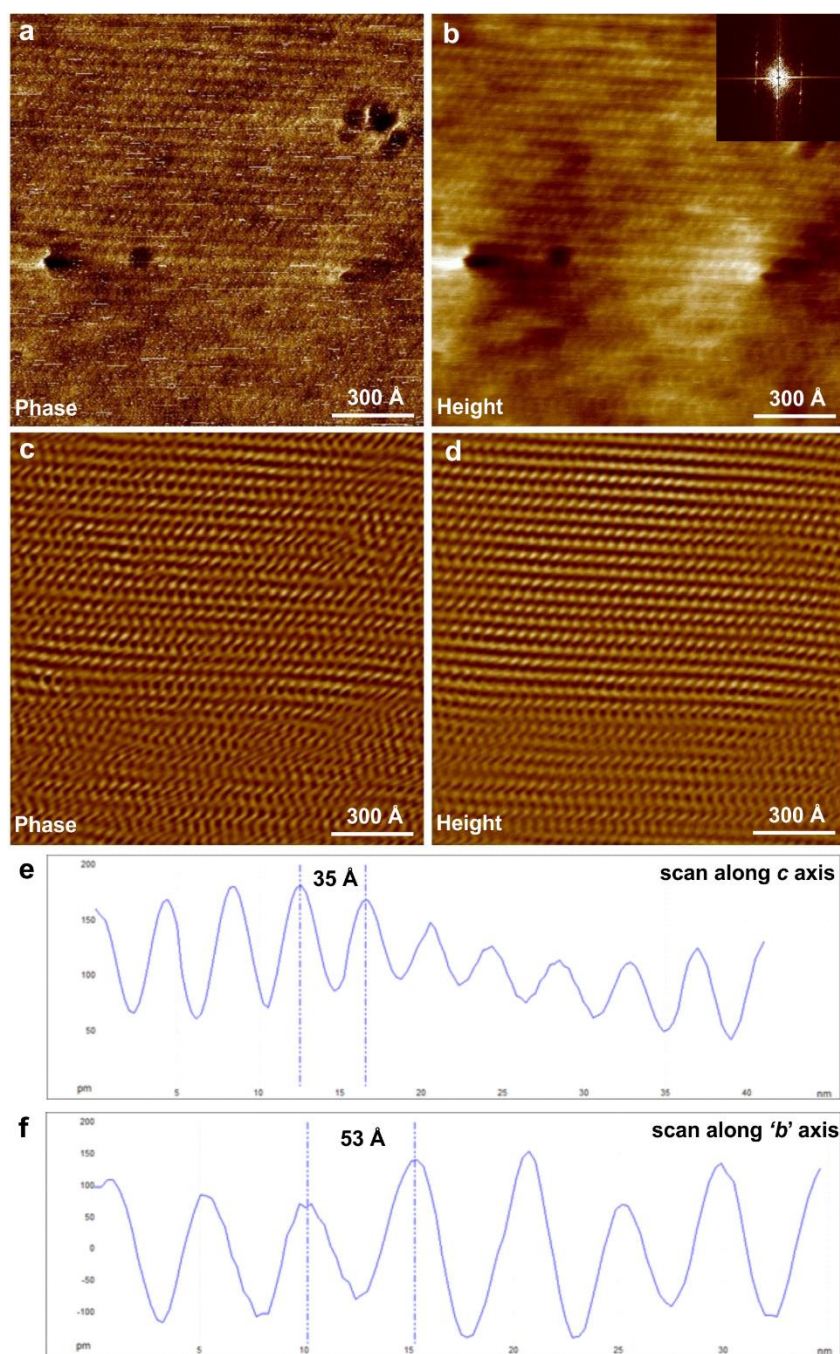


Figure S4.23 AFM of FCN16 (a, b) original figures, (c, d) the inverted FFT and (e, f) scanned spectra along '*b*' and *c* axis.

4.5.8 UV-vis and fluorescence emission spectroscopy

Table S4.11 UV-vis and Fluorescence Emission results

Compound	phase	$\lambda_{\max}/\text{nm}^a$	Band gap/eV ^b	$\lambda_{\max}/\text{nm}^c$	Stokes shift (nm)
FCN16	Col _h	209, 396, 652	1.52 (130 °C)	-	-
FCN16	Fddd	209, 412, 696-714	1.42 (120 °C) 1.35 (30 °C)	-	-
FCO16	Col _h	209, 316, 384, ~512	2.15 (110 °C)	625-633	113-121
FCO16	Fddd	211, 321, 396, 512-517	2.13 (100 °C) 2.10 (40 °C)	642-646	130

a. λ_{\max} in UV-vis spectra. The strong absorption peak at ~400 nm in the two compounds at different temperatures correspond to π - π^* transition of the fluorine derivative. The low absorption peak of FCN at ~690 nm is due to the π - π^* transition of the fluorenedicyanovinylene group. For FCO16, the peak at ~510 nm is the π - π^* transition of the carbonyl group [26].

b. Band gap is calculated by the Tauc plot method. The band gap of FCN16 is smaller than that of FCO16 as the stronger electron-accepting ability and thus the smaller energy gap of the fluorenedicyanovinylene group [26].

c. λ_{\max} in Emission spectra.

4.5.9 HOMO/LUMO energy

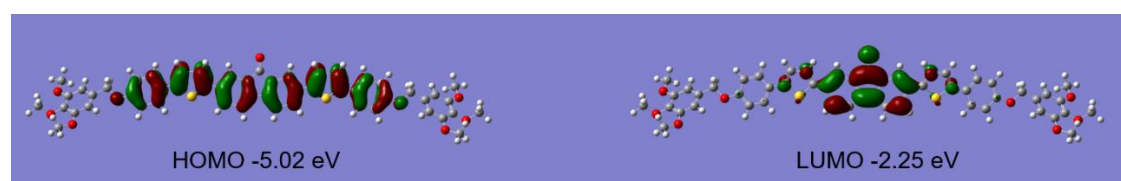


Figure S4.24. (a) HOMO and (b) LUMO of FCO16 by DFT calculation (B3LYP, 6-31G(d)).

4.5.10 Description of the video

The videos show the rotation of ED map and sketched model.

Acknowledgements

For support with experiments at synchrotron radiation sources we are grateful to Drs Olga Shebanova and Nick Terill at station I22, Drs Gareth Nisbet and Steve Collins at station I16, Diamond Light Source, and Drs Oier Bikondoa and Paul Thompson at EPSRC-funded XMaS beam line (BM28) at the ESRF. Financial support is acknowledged from the 111 Project 2.0 of China (BP2018008), from EPSRC (EP-P002250, EP-T003294), and from NSFC (grants 21674099, 21664015, 21865038) and Yunnan Joint Fund Key Project (2018FY001(-012)). Y.X. L. thanks CSC for stipend and UoS for fee waiver.

References

- [1] U. Beginn, L.L. Yan, S.N. Chvalun, M.A. Shcherbina, A. Bakirov, M. Moller, Thermotropic columnar mesophases of wedge-shaped benzenesulfonic acid mesogens, *Liq. Cryst.*, **35** (2008) 1073-1093.
- [2] T. Wohrle, I. Wurzbach, J. Kirres, A. Kostidou, N. Kapernaum, J. Litterscheidt, J.C. Haenle, P. Staffeld, A. Baro, F. Giesselmann, S. Laschat, Discotic Liquid Crystals, *Chem. Rev.*, **116** (2016) 1139-1241.
- [3] Y.X. Li, F.F. Fan, J. Wang, L. Cseh, M. Xue, X.B. Zeng, G. Ungar, New Type of Columnar Liquid Crystal Superlattice in Double-Taper Ionic Minidendrons, *Chem. Eur. J.*, **25** (2019) 13739-13747.
- [4] A. Lehmann, M. Prehm, C.L. Chen, F. Liu, X.B. Zeng, G. Ungar, C. Tschierske, Transition between tangential and co-axial liquid crystalline honeycombs in the self-assembly of Y-shaped bolapolyphiles, *Chem. Commun.*, **54** (2018).
- [5] X. Cheng, M. Prehm, M.K. Das, J. Kain, U. Baumeister, S. Diele, D. Leine, A. Blume, C. Tschierske, Calamitic bolaamphiphiles with (semi) perfluorinated lateral chains: polyphilic block molecules with new liquid crystalline phase structures, *J. Am. Chem. Soc.*, **125** (2003) 10977-10996.
- [6] G. Ungar, C. Tschierske, V. Abetz, R. Holyst, M.A. Bates, F. Liu, M. Prehm, R. Kieffer, X. Zeng, M. Walker, B. Glettner, A. Zywockinski, Self-Assembly at Different

Length Scales: Polyphilic Star-Branched Liquid Crystals and Mikroarm Star Copolymers, *Adv. Funct. Mater.*, **21** (2011) 1296-1323.

[7] C. Destrade, P. Foucher, H. Gasparoux, N.H. Tinh, A.M. Levelut, J. Malthete, Disc-like mesogen polymorphism, *Mol. Cryst. Liq. Cryst.*, **106** (1984) 121-146.

[8] C. Dressel, F. Liu, M. Prehm, X. Zeng, G. Ungar, C. Tschierske, Dynamic mirror-symmetry breaking in bicontinuous cubic phases, *Angew. Chem. Int. Ed.*, **53** (2014) 13115-13120.

[9] H.J. Lu, X.B. Zeng, G. Ungar, C. Dressel, C. Tschierske, The Solution of the Puzzle of Smectic-Q: The Phase Structure and the Origin of Spontaneous Chirality, *Angew. Chem. Int. Ed.*, **57** (2018) 2835-2840.

[10] X. Zeng, G. Ungar, Spontaneously chiral cubic liquid crystal: three interpenetrating networks with a twist, *J. Mater. Chem. C*, (2020).

[11] V. Percec, M. Peterca, T. Tadjiev, X.B. Zeng, G. Ungar, P. Leowanawat, E. Aqad, M.R. Imam, B.M. Rosen, U. Akbey, R. Graf, S. Sekharan, D. Sebastiani, H.W. Spiess, P.A. Heiney, S.D. Hudson, Self-Assembly of Dendronized Perylene Bisimides into Complex Helical Columns, *J. Am. Chem. Soc.*, **133** (2011) 12197-12219.

[12] H.F. Cheng, Y.X. Li, X.B. Zeng, H.F. Gao, X.H. Cheng, G. Ungar, Trigonal columnar self-assembly of bent phasid mesogens, *Chem. Commun.*, **54** (2018) 156-159.

[13] S. Daskeviciute, N. Sakai, M. Franckevicius, M. Daskeviciene, A. Magomedov, V. Jankauskas, H.J. Snaith, V. Getautis, Nonspiro, Fluorene-Based, Amorphous Hole Transporting Materials for Efficient and Stable Perovskite Solar Cells, *Adv. Sci.*, **5** (2018).

[14] J.H. Lee, S.Y. Jeong, G. Kim, B. Park, J. Kim, S. Kee, B. Kim, K. Lee, Reinforcing the Built-In Field for Efficient Charge Collection in Polymer Solar Cells, *Adv. Funct. Mater.*, **28** (2018).

[15] J. Zhang, Q. Sun, Q.Y. Chen, Y.K. Wang, Y. Zhou, B. Song, N.Y. Yuan, J.N. Ding, Y.F. Li, High Efficiency Planar p-i-n Perovskite Solar Cells Using Low-Cost Fluorene-Based Hole Transporting Material, *Adv. Funct. Mater.*, **29** (2019).

[16] S.L. Tao, Z.K. Peng, X.H. Zhang, P.F. Wang, C.S. Lee, S.T. Lee, Highly efficient non-doped blue organic light-emitting diodes based on fluorene derivatives with high thermal stability, *Adv. Funct. Mater.*, **15** (2005) 1716-1721.

[17] X.J. Feng, J.H. Peng, Z. Xu, R.R. Fang, H.R. Zhang, X.J. Xu, L.D. Li, J.H. Gao, M.S. Wong, AIE-Active Fluorene Derivatives for Solution-Processable Nondoped Blue Organic Light-Emitting Devices (OLEDs), *Acs Applied Materials & Interfaces*, **7** (2015) 28156-28165.

- [18] T.S. Bailey, C.M. Hardy, T.H. Epps, F.S. Bates, A noncubic triply periodic network morphology in poly(isoprene-*b*-styrene-*b*-ethylene oxide) triblock copolymers, *Macromolecules*, **35** (2002) 7007-7017.
- [19] M. Takenaka, T. Wakada, S. Akasaka, S. Nishitsuji, K. Saijo, H. Shimizu, M.I. Kim, H. Hasegawa, Orthorhombic Fddd Network in Diblock Copolymer Melts, *Macromolecules*, **40** (2007) 4399-4402.
- [20] A.J. Meuler, M.A. Hillmyer, F.S. Bates, Ordered Network Mesostructures in Block Polymer Materials, *Macromolecules*, **42** (2009) 7221-7250.
- [21] Y.-C. Wang, K. Matsuda, M.I. Kim, A. Miyoshi, S. Akasaka, S. Nishitsuji, K. Saijo, H. Hasegawa, K. Ito, T. Hikima, M. Takenaka, Fddd Phase Boundary of Polystyrene-block-polyisoprene Diblock Copolymer Melts in the Polystyrene-Rich Region, *Macromolecules*, **48** (2015) 2211-2216.
- [22] C.A. Tyler, D.C. Morse, Orthorhombic Fddd network in triblock and diblock copolymer melts, *Phys. Rev. Lett.*, **94** (2005) 208302.
- [23] X.-B. Wang, T.-Y. Lo, H.-Y. Hsueh, R.-M. Ho, Double and Single Network Phases in Polystyrene-block-poly(l-lactide) Diblock Copolymers, *Macromolecules*, **46** (2013) 2997-3004.
- [24] M.I. Kim, T. Wakada, S. Akasaka, S. Nishitsuji, K. Saijo, H. Hasegawa, K. Ito, M. Takenaka, Determination of the Fddd Phase Boundary in Polystyrene-block-polyisoprene Diblock Copolymer Melts, *Macromolecules*, **42** (2009) 5266-5271.
- [25] T.H. Epps, E.W. Cochran, C.M. Hardy, T.S. Bailey, R.S. Waletzko, F.S. Bates, Network phases in ABC triblock copolymers, *Macromolecules*, **37** (2004) 7085-7088.
- [26] D. Kim, M.R. Reddy, K. Cho, D. Ho, C. Kim, S. Seo, Solution-processable fluorene derivative for organic thin-film transistors, *Org. Electron.*, **76** (2020).
- [27] T. Hahn, *International Tables for Crystallography*, Vol. A, Springer, Dordrecht, 5th edition, 2005.
- [28] A. Immirzi, B. Perini, Prediction of density in organic crystals, *Acta Crystallogr. A*, **33** (1977) 216-218.

Chapter 5 Published paper: Tailoring liquid crystal honeycombs by head-group choice in bird-like bent-core mesogens

Journal of Materials Chemistry C, 2020, DOI:10.1039/D0TC01879A

Ya-xin Li^{1,2}, Huifang Cheng³, Xiangbing Zeng², Yuan Tao³, Xiaohong Cheng^{*3,4} and Goran Ungar^{*1,2}

¹ *State Key Laboratory for Mechanical Behaviour of Materials, Shanxi International Research Center for Soft Materials, Xi'an Jiaotong University, Xi'an, PR China.*

² *Department of Materials Sci. and Eng., University of Sheffield, Sheffield, UK*

³ *School of Chemical Science and Technology, Yunnan University, Kunming, PR China*

⁴ *School of Chemistry and Chemical Engineering, Yangtze Normal University, Fuling, PR China*

Keywords: columnar liquid crystals, superlattice, non-centrosymmetric, second harmonic generation, nanopatterning

This Chapter was published as an article in Journal of Materials Chemistry C. I have carried out the experiments and data analysis by POM, X-ray diffraction, SHG, molecular modelling and dynamic simulation and written the corresponding parts in the article. Huifang Cheng, Yuan Tao and Prof. Xiaohong Cheng from Yunnan University synthesized the compounds. They confirmed the chemical structures by NMR, *etc.* and examined the compounds by DSC.

The article is reproduced in its Open Access under a CC BY 3.0 license, with minor adaptations on the figures and section numbering. The details of the synthesis part in the supporting information are not included here and the references in the manuscript and supporting information have been combined for clarity.

5.1 Abstract

We introduce a new class of mesogens that are bird-like in shape and form honeycomb-type supramolecular liquid crystals. They have a bent pi-conjugated aromatic core as wings, a linear or branched chain as the tail and a selection of functional headgroups. Honeycombs of non-centrosymmetric trigonal type ($p3m1$) are obtained, along with two different complex honeycomb superlattices ($p31m$ and $p2gg$) and a randomized hexagonal mesophase ($p6mm$). The key determinant of the self-assembled structure is the nature of interaction of the headgroup with the glycerols at the ends of the wings. The structure depends on whether the sub-columns lying along the edges of the prismatic cells contain pure or mixed headgroups and wing-end hydrogen-bonding groups. Its assembly is further controlled by reducing the tail-chain volume, inducing out-of-plane buckling of the honeycomb. These two modes of symmetry breaking lead to structural polarity both in- and out-of-plane, opening the way to applications in devices relying on properties such as ferroelectricity and second harmonic generation.

5.2 Introduction

Just as there are direct (“oil-in-water”) and inverse (“water-in-oil”) lyotropic liquid crystals (LC) [1], so there are also “direct” and “inverse” thermotropic (solvent-free) LCs. While the columns in the most familiar thermotropic columnar LCs contain an aromatic core surrounded by flexible, typically aliphatic pendant chains [2], there is also a family of “inverse” columnar LCs where the rigid aromatic rods circumscribe polygonal prismatic cells with the pendant flexible chains on the *inside*. Such LC honeycombs are typically formed by aromatic rods (e.g. biphenyl, *p*-terphenyl, bistolane) with different weakly bonding end-groups, and having chains attached laterally [3]. As the circumference of a vertical cell contains an integer number of

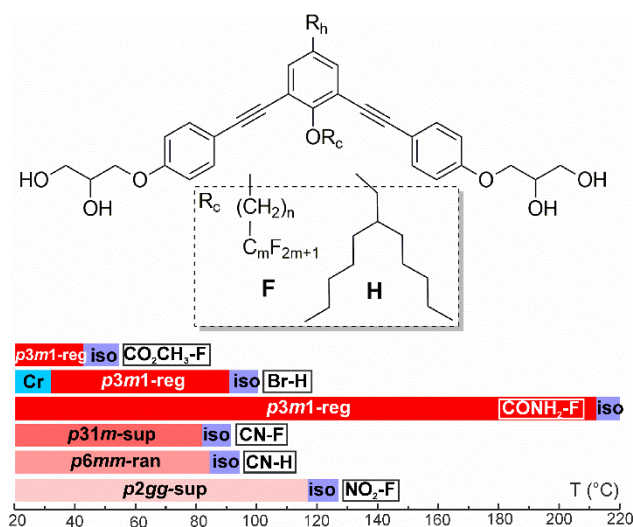
horizontal rods, the cells cross-section (the “tile”) could have a triangular, square, pentagonal, hexagonal, or octagonal shape, and the honeycomb can have a combination of such tiles [4]. If two side-chains are attached and they are different and incompatible, some very complex “multicolour” tiling patterns can be obtained [5]. Such structures provide real-life models for studying physical phenomena in 2-D [6], including phase transitions and criticality, obeying universality classes analogous to those in e.g. magnetism, based on flipping molecules rather than spins [7]. Meanwhile, the choice of regular polygonal nets thus created, including square and rectangular, offers a tool for directed self-assembly of sub-10 nm surface patterns for potential nanoscale electro-optic devices [7b,8].

However, the aromatic cores do not have to be straight, and a few examples of honeycomb-generating bent core polyphiles have been reported. Their cores were bent at the centre, with the attached chain facing inward [9,10] or outward [11] at the bend, the two rigid arms subtending a 120° angle. Mesogens with inward-facing chains are referred to as anchor-shaped. They were found to assemble in hexagonal honeycombs with either 3 or 6 molecules in the cell circumference, depending on whether the pendant chain was small or large [10]. At the time it was actually not clear if the 3-molecule honeycombs had trigonal or hexagonal (randomized) symmetry. Here we introduce a new way of controlling complexity in LC honeycombs; we add a functional headgroup R_h on the outside of the bend in anchor-shaped molecules, turning them into what can be described as bird-shaped. R_h groups interact in different ways between themselves and with the terminal hydrogen-bonding groups, resulting in a variety of new controllable honeycomb structures and superlattices. Furthermore, additional frustration is introduced by reducing the size of the pendant chain (the “tail”), depriving the honeycomb of adequate filler volume and forcing it to “buckle”, thus creating new

opportunities, e.g. for ferroelectric properties. Most structures described are non-centrosymmetric, thus having interesting application potentials.

5.3 Results and Discussion

Table 5.1 The phase transition temperatures of bird-shaped compounds.



Compound R_h -F/H ^a	R_c	a (Å) [A_{col} (Å ²)] ^b	T /°C [ΔH /kJ mol ⁻¹] ^c
CO₂CH₃-F	C ₆ H ₁₂ C ₄ F ₉	29.8 [769]	r.t. \uparrow <i>p3m1</i> -reg 42 Iso ^d
Br-H	CH ₂ CH(C ₅ H ₁₁) ₂	26.9 [627]	\uparrow Cr 113.7[33.3] Iso \downarrow 91.8 [1.9] <i>p3m1</i> -reg 32.2[8.6] Cr
CONH₂-F	C ₄ H ₈ C ₆ F ₁₃	30.1 [785]	\uparrow <i>p3m1</i> -reg 212.5[13.3] Iso \downarrow 206.8[13.2] <i>p3m1</i> -reg
CN-F	C ₆ H ₁₂ C ₄ F ₉	51.7 [772]	\uparrow <i>p31m</i> -sup 82.9[0.1] Iso \downarrow 78 (onset) <i>p31m</i> -sup
CN-H	CH ₂ CH(C ₅ H ₁₁) ₂	24.5 [520]	\uparrow <i>p6mm</i> -ran 84.4[1.6] Iso \downarrow 81.5[1.6] <i>p6mm</i> -ran
NO₂-F	C ₄ H ₈ C ₆ F ₁₃	a 63.3 b 50.6 [801]	\uparrow <i>p2gg</i> -sup 117[2.0] Iso \downarrow 110.3[3.0] <i>p2gg</i> -sup

^aFirst part of compound name is the head group R_h , second part denotes the type of attached chain. ^bLattice parameter [area per column in brackets]. ^cPeak DSC transition temperatures [and enthalpies] on 2nd heating (\uparrow) and cooling (\downarrow), all at 10 K min⁻¹. ^dTransition temperatures of CO₂CH₃-F are determined by XRD, SHG and POM. Phase abbreviations: Cr = crystal, *p6mm*-ran = hexagonal columnar phase with random orientation of the local 3-fold axis with 6-fold *p6mm* overall symmetry; *p3m1*-reg = columnar phase with trigonal symmetry and one column per unit cell; *p31m*-sup = trigonal superlattice with three columns per unit cell; *p2gg*-sup = rectangular superlattice with *p2gg* symmetry and four columns per cell; Iso = isotropic melt. Transition temperatures in the bar chart are from 2nd DSC heating, except for Br-H where they were determined on cooling.

Six compounds were synthesised based on a symmetric bent 1,3-bis(phenylethynyl) benzene “bistolane” core with glycerol end-groups, a chain R_c in 2-position (bay position) that is either a linear semiperfluorinated (denoted F) or a branched “swallow-tail” alkyl (denoted H), and in addition with a functional headgroup R_h in 5-position – see Table 5.1. The compounds are thus named R_h - R_c . Thus the molecules can be said to have a bird-like appearance. For synthesis see the Supporting Information (SI). The compounds were studied by polarized optical microscopy (POM), differential scanning calorimetry (DSC), small- and wide-angle X-ray scattering (SAXS and WAXS), grazing incidence SAXS and WAXS (GISAXS and GIWAXS) on thin films, second harmonic generation (SHG) light emission, and molecular modelling and molecular dynamics (MD) annealing. All compounds form liquid crystal phases that are listed in Table 5.1 together with their transition temperatures, transition enthalpies and lattice parameters. A complete table, including the transitions on heating from a solution-crystallized sample, is given in Table S5.1 of SI. DSC thermograms are shown in Figure S5.1.

POM images of the compounds in the mesophases are shown in Figures 5.1 and S5.2. They are typical of columnar phases, with sizeable fraction of dark area indicating homeotropic alignment, where the optic axis, hence column axis, is normal to the glass substrate. Planar columns, parallel to the substrate, are prevalent in thicker samples. Bright fans are seen in Figures 5.1c, e, where columns form concentric circles or arcs around the focal point. The same are seen as blue or pale-yellow in Figures 5.1d, f recorded with a λ -plate retarder; these confirm that the slow (high-index) axis is radial, hence perpendicular to the column axis. This negative birefringence is also seen in the “tumbling” defects, especially in Figures 5.1a, b, appearing as thin bright streaks, where bundles of vertical columns perform a U-turn. The slow axis is seen to be parallel to the streaks, and since the columns are perpendicular, the slow axis is again confirmed

as normal to the columns. This is consistent with the situation in most honeycomb LCs where the π -conjugated aromatic rods are perpendicular to the axis of the prismatic cells, or columns.

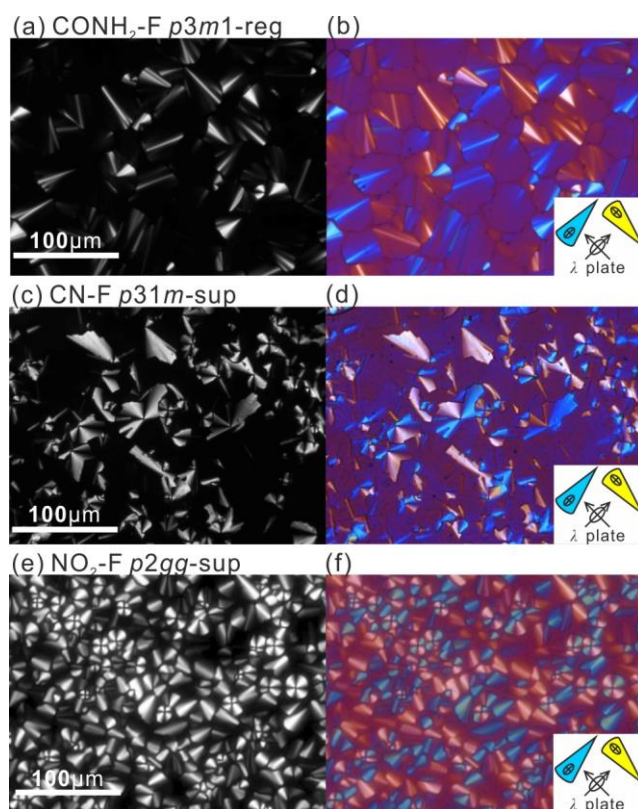


Figure 5.1 Polarized optical microscopy textures of (a, b) CONH₂-F recorded at 190 °C (cooled from 230 °C), (c, d) CN-F at 70 °C (cooled from 90 °C) and (e, f) NO₂-F at 100 °C (cooled from 120 °C); (b, d and f) are recorded with a full-wave (λ) plate.

SAXS patterns of unoriented (“powder”) samples and GISAXS patterns of thin films of the mesophases of all compounds except the nitro-compound NO₂-F give Bragg peaks/spots indexable on a 2D hexagonal lattice with the ratio of squared reciprocal spacings $d^{-2}_{(10)}:d^{-2}_{(11)}:d^{-2}_{(20)}:d^{-2}_{(21)}:d^{-2}_{(30)}\dots = 1:3:4:7:9\dots$ (Figures 5.2a,b, 5.3a, S5.3a, S5.5a). GISAXS patterns of films lying on a horizontal Si substrate confirm this indexing, giving sharp spots or arcs mainly on the equator, consistent with homeotropic alignment (Figures 5.2c, d, 5.3e). Exceptionally, compound NO₂-F displays a

rectangular lattice, plane group $p2gg$ (Figures 5.3b, d, g, i). Its GISAXS pattern in Figure 5.3d, coming from planar domains, shows two orientations, one in which the columns lie with the (010) plane on the substrate (green reciprocal net), the other with the diagonal (210) plane on the substrate (white net). Both (010) and (210) are planes of densely packed columns, supporting the viability of the proposed structural model. The rectangular phase with its $2b/a$ ratio of 1.60 is a distortion of a hexagonal lattice, where the equivalent ratio would be $\sqrt{3}$. WAXS contains only diffuse scatter centred around $2\pi/q=4-5\text{\AA}$, consistent with a true LC phase (Figure S5.3b). No peak around $3.5-4\text{\AA}$ is observed (Figure S5.3b), indicating that the benzene rings do not stack as in a discotic LC with parallel discs. The absence of a $3.5-4\text{\AA}$ peak suggests that the rings are inclined to the xy -plane and to each other.

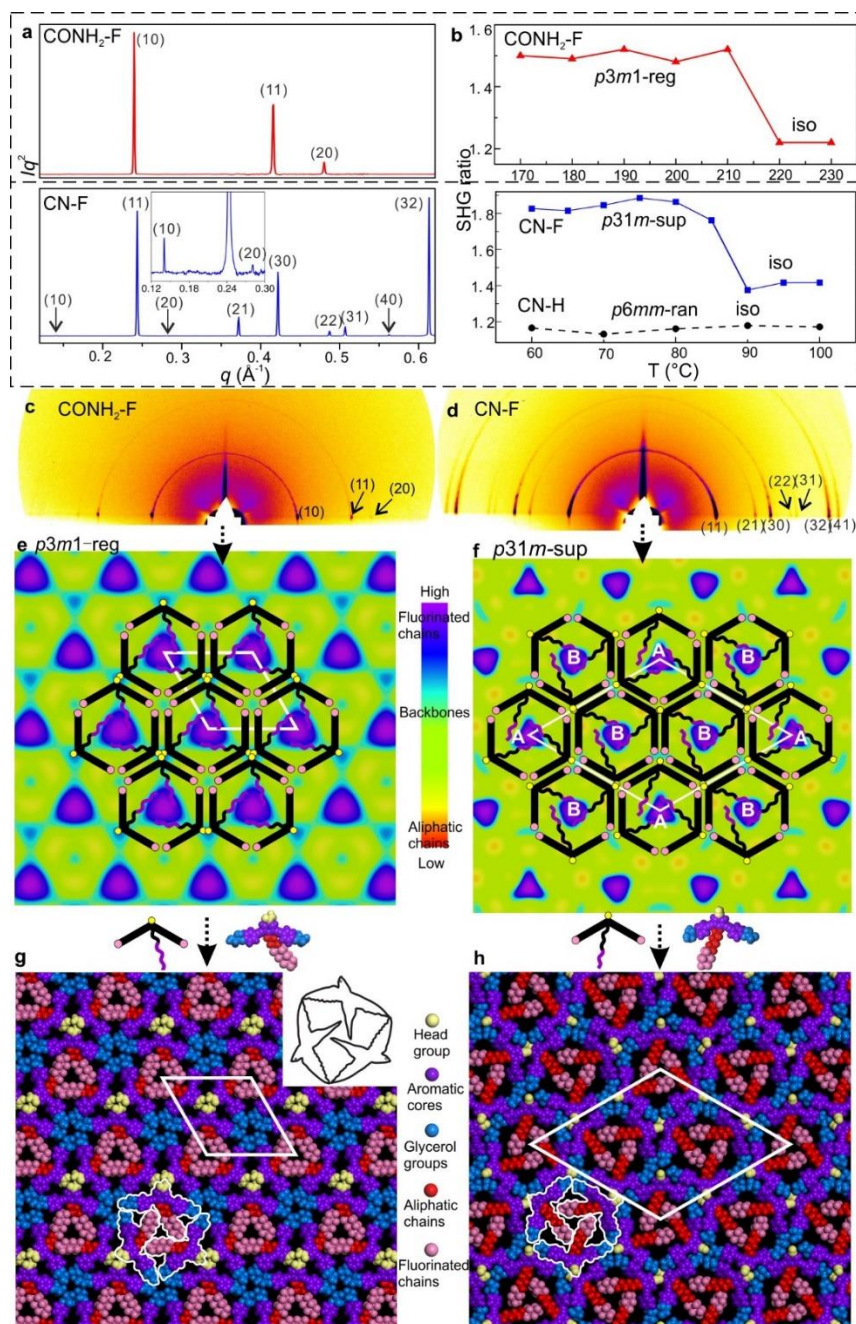


Figure 5.2 (a) Powder SAXS of CONH₂-F and CN-F recorded at 130 and 70°C upon cooling. (b) Temperature dependent intensity of the second harmonic (400 nm) normalized by dividing by the surrounding background level for 800 nm excitation, generated 20 μm above the substrate surface; for measurements at different heights see Figures S5.7 and S5.8. (c, d) GISAXS patterns of CONH₂-F and CN-F recorded at 100 and 60°C upon cooling. (e, f) ED maps with schematic models of CONH₂-F (*p3m1-reg*) and CN-F (*p31m-sup*). (g, h) Snapshot of dynamic simulation of CONH₂-F (*p3m1-reg*) and CN-F (*p31m-sup*).

Based on previous work on anchor-shaped molecules [10], it was reasonable to assume that the structures are based on hexagonal or, in the present case, possibly pseudo-hexagonal prismatic cells. Calculations based on unit cell area, expected average intracolumnar intermolecular distance and molecular volumes (Table S5.8), suggest that in CO₂CH₃-F, Br-H, CONH₂-F and CN-H there are 3 molecules circumscribing a column rather than 6. The fact that the unit cell areas were always close to an integer multiple m of the smallest cell implies that for $m > 1$ we have superlattices with m prismatic columns per unit cell. Specifically, for CO₂CH₃-F, Br-H, CONH₂-F and CN-H $m=1$ (“regular” columnar phase). Meanwhile the unit cell of the superlattice of CN-F contains $m=3$ columns, whereas the rectangular cell in NO₂-F contains $m=4$ columns. Thus the number of molecules per unit cell $3m$ is, respectively, 3, 9 and 12 – Table S5.8. The fact that a column stratum contains only 3 molecules raises the possibility that the structures have 3-fold rather than 6-fold symmetry. As Laue symmetry is hexagonal in both cases, X-ray diffraction alone cannot distinguish between the two. Therefore, we tested the mesophases for the presence of SHG signal. Only CN-H and NO₂-F tested negative, while CO₂CH₃-F, Br-H, CONH₂-F and CN-F all showed clear second harmonic emission above the background level caused by surface effects [12] (Figures 5.2b, S5.4, S5.6, S5.7, S5.8). Hence the columnar phases in these compounds are non-centrosymmetric, i.e. trigonal. In all trigonal compounds SHG intensity drops sharply to the background level near the isotropisation temperature T_i .

While for hexagonal CN-H the plane group is clearly $p6mm$, for trigonal phases the choice was between $p3m1$ and $p31m$ [13]. Since neither imposes any systematic extinctions, the choice was based on the following reasoning. The columns must be centred on the 3-fold axes, all three of which lie on the long diagonal of the rhombic unit cell in both plane groups – Figures 5.4a, b. At the same time two conditions must be fulfilled. (i) To tessellate, the prismatic cells must face each other with their sides

rather than edges. (ii) Since a column stratum contains three identical molecules, the mirror planes must pass through the opposing edges (apices) rather than bisecting the sides of the prisms; otherwise the prisms would acquire hexagonal rather than trigonal symmetry. For the “regular” $m=1$ phase, conditions (i) and (ii) are satisfied only if the symmetry is $p3m1$, with the single column centred at (0,0) (Figure 5.4a). Meanwhile, for the $m=3$ superlattice of CN-F the symmetry must be $p31m$, with the three columns situated at (0,0), (1/3,2/3) and (2/3,1/3) (Figure 5.4b). Accordingly, the regular 1-column trigonal phase is labelled “ $p3m1$ -reg”, and the 3-column superlattice as “ $p31m$ -sup”. In the same vein, the 4-column rectangular superlattice is labelled “ $p2gg$ -sup”.

With the knowledge of mesophase symmetry, electron density (ED) maps of the xy plane were constructed from Lorentz-corrected Bragg reflection intensities (Tables S5.2-5.7), bearing in mind that for trigonal mesophases the phase angles of certain reflections are not limited to 0° or 180° as in the usual centrosymmetric LCs. In choosing the correct map we were guided by the above reasoning and by the ED values calculated for the specific parts of the molecules (Table S5.10). The map for CONH₂-F, representative of the $p3m1$ -reg phase, is shown in Figure 5.2e, and that for the $p31m$ -sup phase of CN-F in Figure 5.2f. The structure factor phase angles are given in Tables S5.4-5.5. While the aromatic and glycerol groups (“backbones”) have similar medium ED (green), the stand-out high-ED features are the three perfluoro chains in the centre of each column (blue-purple triangles). We associate the apices of the high-ED triangles with the positions of attached chains, close to the bay position on the aromatic cores. Schematic molecules at positions compatible with the maps are superimposed. In the $p3m1$ -reg phase the implication is that there are separate glycerol and amide sub-columns at alternative honeycomb nodes, each having, respectively, either 6 glycerols (6Gly) or 3 headgroups (3R_h) in a stratum (Figures 5.2e and 5.4a). As the former sub-columns will be wider than the latter, the hexagonal prisms are likely to be distorted as

shown in an exaggerated way in Figure 5.4a. Meanwhile in the $p31m$ -sup phase of CN-F (Figures 5.2f and 5.4b), the triangles follow an up-down-down sequence along any of the three $\{110\}$ planes (labelled A, B, B in Figures 5.2f and 5.4b). Hence there are again two types of sub-columns, but both are mixed, half of them containing 4Gly+1CN and the other half 2Gly+2CN.

To check the viability of the proposed structures, using experimental lattice parameters molecular models were built and subjected to NVT molecular dynamics annealing. As shown in Figures 5.2g, h, S5.3d and S5.5d, good space-filling is achieved with no overcrowding and no voids. The tessellating bird-like molecules, outlined in black in Figure 5.2g and 3h, are reminiscent of some of the drawings of birds and bats by M.C. Escher [14].

As mentioned, CN-H is the only compound with hexagonal Laue symmetry that shows no SHG signal. This means that, even if it still has only 3 molecules in the unit cell, its honeycomb phase does have an inversion centre and therefore has plane group $p6mm$. Here electron density has a minimum rather than a maximum in the centre of the column (Figure 5.3f), as the pendant chains are low-ED aliphatic (see Table S5.10). Incidentally, a similar situation is seen in Br-H (Figure S5.5c). To explain the high symmetry of the $p6mm$ phase in CN-H, we propose that the honeycomb actually contains small trigonal domains which are, however, randomized in orientation; hence the long-range order, as seen by SAXS, is hexagonal. Accordingly, the mesophase is denoted “ $p6mm$ -ran”. Accordingly, although there may still be some local partial separation of glycerols and cyano-groups, the average composition of all sub-columns is the same, namely $1/2(6\text{Gly}+3\text{CN})$ or $3\text{Gly}+1.5\text{CN}$ (see models in Figures 5.3f and 5.4c, where empty circles and dashed-lined chains indicate half occupancy. Note that the pale-blue ED maxima in Figure 5.3f indicate the positions of chain attachment and branching points. A snapshot of annealed molecular model is shown in Figure 5.3h.

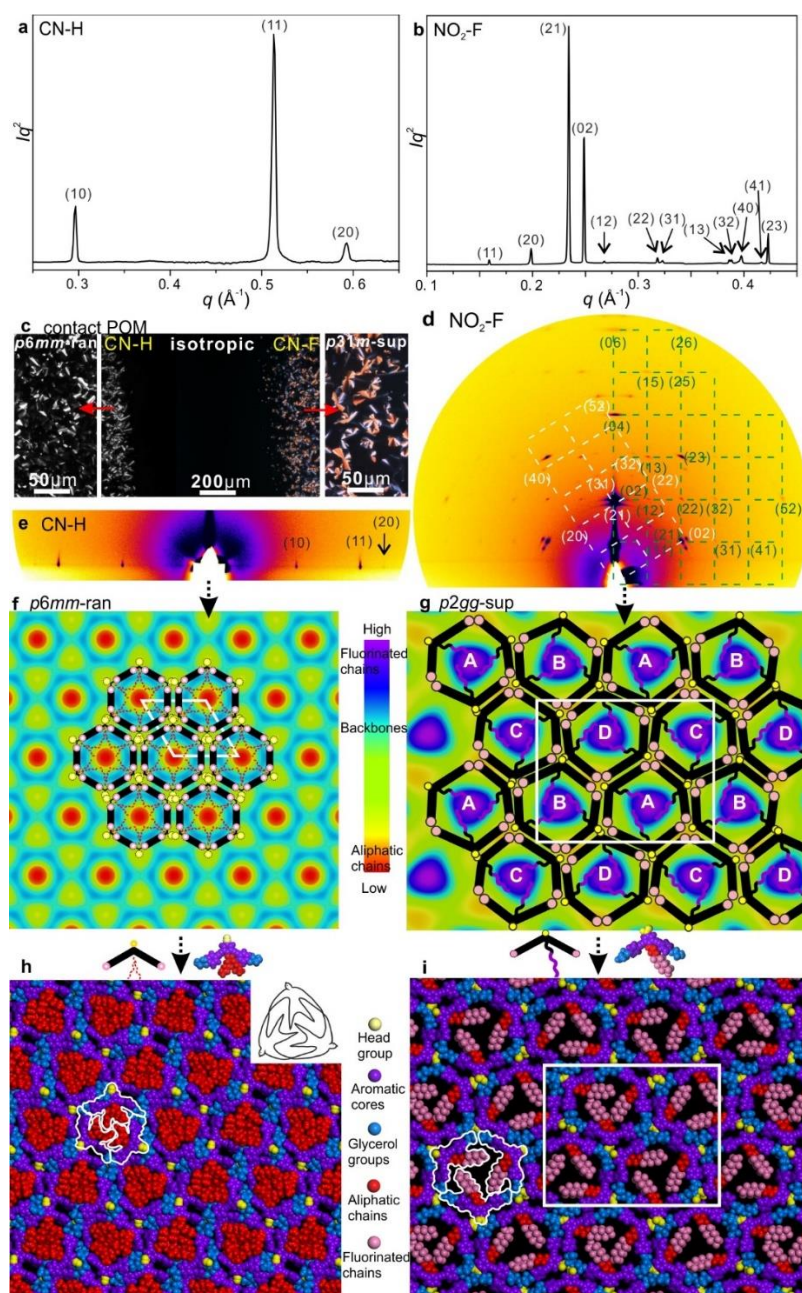


Figure 5.3 (a, b) Powder SAXS of CN-H and NO₂-F recorded at 70 and 100°C upon cooling. (c) POM of a contact preparation of CN-H and CN-F (columnar) with a mixture in the middle (isotropic), recorded at 40 °C; the film is uniform in thickness; zoomed-in insets on left and right. (d, e) GISAXS patterns of CN-H and NO₂-F recorded at 70°C and 100°C, respectively, upon cooling. Green and white reciprocal lattices in (d) show two different orientations of planar columns, with their (010) and (210) plane, respectively, facing the substrate. (f, g) ED maps with schematic models of CN-H (*p6mm-ran*) and NO₂-F (*p2gg-sup*) mesophases. (h, i) Snapshot of dynamically annealed CN-H (*p6mm-ran*) and NO₂-F (*p2gg-sup*).

The only mesophases with the ratio of d^2 values not obeying the hexagonal rule is the rectangular $p2gg$ -sup phase in NO₂-F. The plane group $p2gg$ is determined based on the absence of $(h0)$ and $(0k)$ Bragg reflections with odd h, k (Figure 5.3b, d). The schematic depiction of the xy plane is shown in Figure 5.4d. The apices of the distorted triangular high-ED fluoroalkyl regions in Figure 5.3g again mark the chain attachment points, hence the positions of the centres of molecules. They reveal that there are four different orientations of the distorted hexagonal columns in a unit cell, labelled A, B, C, D in Figures 5.3g and 5.4d. As in the trigonal superlattice of CN-F but replacing the CN headgroup with NO₂, there are two types of sub-columns, one containing 4Gly+1NO₂ and the other 2Gly+2NO₂. If we call the 4Gly+1R_h sub-column “large” (L) and the 2Gly+2R_h sub-column “small” (S), then the difference between the two superlattices is in that going around a distorted hexagon the apex sequence in $p31m$ -sup of CN-F is LSLSLS, while in $p2gg$ -sup of NO₂-F it is LLSSLS.

A further notable feature of the present mesophases is the significantly smaller cross-sectional area of columns filled with branched aliphatic chains compared to those filled with semiperfluoroalkyls – Tables 5.1 and S5.9. The average area of columns in Br-H and CN-H is 573Å², while in fluorinated compounds it is 782Å². At the same time the estimated average intracolumnar spacings (c) between molecules are, respectively, 5.5Å and 4.2Å (Table S5.8). Since the bent core backbones are the same, we conclude that in Br-H and CN-H their long axis is inclined to the xy plane instead of being parallel to it. This conclusion is further supported by the observed lower birefringence of H-compounds compared to that of the F-compounds. This is apparent already by qualitative POM inspection of a contact preparation in Figure 5.3c, showing a film of uniform thickness, with CN-H on the left and CN-F on the right. While CN-F is coloured, CN-H is not. Optical retardation (I) of CN-F and CN-H is also measured

quantitatively by Berek compensator, giving Γ as -436 and -174 nm, respectively. As Γ is proportional to the order parameter S , where

$$S = (3 \langle \cos^2 \theta \rangle - 1)/2$$

we can calculate θ , the angle between the molecular backbone and the columnar (z) axis. Assuming perfect in-plane orientation of backbones in CN-F, i.e. $\theta_{\text{CN-F}}=90^\circ$ and $S_{\text{CN-F}}=-0.5$, and knowing that $\Gamma_{\text{CN-H}} = 0.4 \Gamma_{\text{CN-F}}$, we get $\theta_{\text{CN-H}}=63^\circ$ for CN-H and its complement $90^\circ - \theta_{\text{CN-H}} = \phi_{\text{CN-H}} = 27^\circ$, which is the tilt angle of π -conjugated CN-H backbones to the xy plane. Alternatively, we can calculate $\theta_{\text{CN-H}}$ by using the ratio of column areas $(A_{\text{H}}/A_{\text{F}})^{0.5} = 0.856 = \arccos \phi_{\text{CN-H}}$, wherefrom we get $\phi_{\text{CN-H}} = 31^\circ$. The fact that the two ϕ -values are close suggests that indeed every backbone tilts by angle ϕ , implying that the hexagon in CN-H collapses like an umbrella.

It should be mentioned that this is not the first example of tilted backbones in honeycomb LCs. Examples were reported in a hexagonal facial amphiphile [15] and a square honeycomb of a straight rod-like glycerol-terminated bolaamphiphile [16], both with a laterally attached flexible chain. In both cases θ changed steeply with temperature with S passing through zero causing birefringence inversion. However, in vast majority of honeycombs $\theta=0$, presumably to maximize entropy by allowing transverse self-diffusion. If filler volume is reduced and θ remains 0° , in most cases the system chooses a smaller polygon. Thus hexagonal gives way to pentagonal or square.^{4b} However a change from square to triangle reduces the area to $\sqrt{3}/4=0.43$, evidently too drastic a jump for the system in [16], which chooses the tilt alternative. Other systems have opted for a combination of squares and triangles [5]. However, in the present case what prevents CN-H and Br-H from switching from hexagons to pentagons or squares must be the fixed 120° bend in the aromatic core.

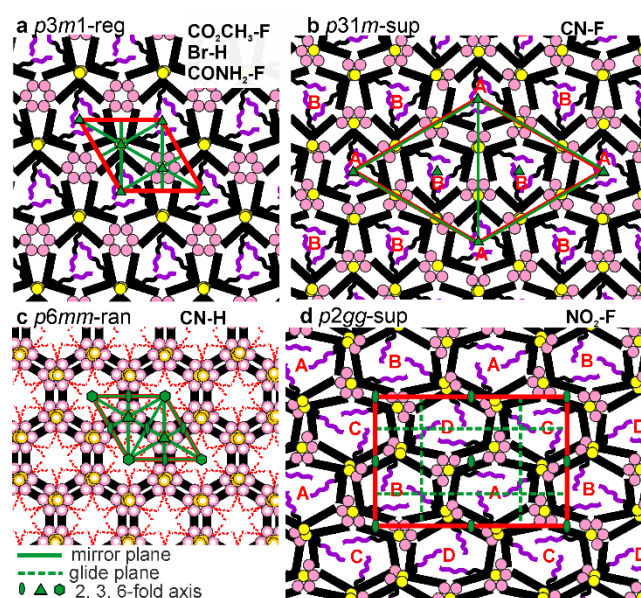


Figure 5.4. Schematics of the four different honeycomb types formed by the bird-shaped molecules. Plane groups and compounds are identified. The bent cores are black, end-glycerols pink and headgroups yellow. The hexagon distortions are exaggerated for clarity. Unit cells are drawn in red, symmetry elements (mirror planes and rotation axes) in green, but glide planes (dashed) are only shown in (d). In (b) some mirror planes coincide with unit cell edges. (c) shows space-time averaged structure with each empty circle dashed line chain indicating half-occupancy; thus each node contains 3 glycerols and 1.5 CN-groups on average.

Finally, we propose an explanation for the key effect of headgroup on phase structure and stability. Compared to compound 2b in ref. 10 with no headgroup ($R_h=H$) and with a $(CH_2)_4C_6F_{13}$ chain, having a T_i of 190°C , all current compounds except the amide have lower T_i . This reflects the packing disturbance caused by the headgroup, also notable by the, on average, 9% larger area per column in F-compounds compared to that in the headless 2b (Table S5.9). The disturbance is partially compensated or even overcompensated by hydrogen bonding and/or dipolar interaction of the headgroups. The lowest T_i , 40°C , is found in the ester, where such interactions are at best weak, while the amide's H-bonds overcompensate lifting T_i to 212°C (Table 5.1).

One would expect the headgroups and glycerols to segregate in separate sub-columns, which is what indeed happens in the $p3m1$ -reg phase of $\text{CO}_2\text{CH}_3\text{-F}$, Br-H and $\text{CONH}_2\text{-F}$. But clustering together all the bulky glycerol endgroups carries an energy penalty of distortion of the hexagons (Figure 5.4a). We propose that avoiding such distortion is responsible for mixed rather than chemically pure sub-columns in CN-F and $\text{NO}_2\text{-F}$. In these two compounds the energies of mutual dipolar interaction between the headgroups and their H-bonding interaction with the glycerols are of the same order of magnitude. The driving force for segregation is thus weaker, so that by mixing and keeping the subcolumn volumes similar, distortion is reduced. This results in the formation of $p31m$ and $p2gg$ superlattices. Data in Table S5.11 indeed suggest that AB cross-interactions of CN and NO_2 groups with glycerol are similar in energy to AA and BB homo-interactions within their own species.

Returning to compounds $\text{CO}_2\text{CH}_3\text{-F}$, Br-H and $\text{CONH}_2\text{-F}$ that do not form a superlattice and where headgroups and glycerols do not mix, we may ask what these three compounds have in common. We propose that since the ester and bromo groups do not interact strongly with hydroxyl groups, mixing them with glycerol would only dilute the H-bonding within the glycerol sub-columns. The resulting energy penalty would outstrip the benefit of reduced lattice and molecular distortion. In sharp contrast, amide groups in $\text{CONH}_2\text{-F}$ H-bond more strongly among themselves than with the glycerols (Table S5.11). So in $\text{CONH}_2\text{-F}$ it is the amide H-bonds that would lose out most by mixing. Again, the accompanying reduction in distortion would not be sufficient to compensate.

Regarding compound CN-H , we refrain from speculating about the situation in its $p6mm$ -ran phase as the detailed short-range configuration in its randomized clusters is not known.

5.4 Conclusion

This work presents a novel approach to designing complex self-assembled nanopatterns in functional materials. Most LC honeycombs so far have had identical, usually H-bonded nodes. By introducing bird-shaped mesogens based on bent π -conjugated cores with attached alkyl or fluoroalkyl tails and an additional functional headgroup of different kinds one can create new 2D lattices and superlattices. The work shows that the nanopatterns thus created can have potentially exploitable ferroelectric, pyroelectric or piezoelectric properties associated with non-centrosymmetric structures. The above results also show how out-of-plane tilt can be enforced upon the honeycombs by reducing side-chain “filler” volume, offering another route to symmetry-breaking normal to the honeycomb plane with interesting consequences for applications. These are currently investigated further.

5.5 Supporting Information

5.5.1 Experimental methods

DSC thermograms were recorded on a DSC 200 F3 Maia calorimeter (NETZSCH) with heating/cooling rates as specified.

Optical micrographs with crossed polarizers (**POM**) were recorded using an Olympus BX50 microscope equipped with a Mettler HS82 hot stage. Optical retardation was measured with a Berek compensator. A λ -plate was used to determine the direction of the optic axis.

Grazing incidence X-ray scattering (**GISAXS**) experiments were carried out on beamline BM28 (XMaS) at European Synchrotron Radiation Facility (ESRF), France and I16 at Diamond Light Source, U.K. The X-ray energy was 12.0 keV, and 2d

diffraction patterns were collected using a MAR165 CCD camera (ESRF) and Pilatus 2M detector (Diamond). Thin film samples were prepared from melt on silicon substrate. *n*-Tetracontane was used to calibrate the sample-to-detector distance. **Powder SAXS and WAXS** experiments were done at station I22 of Diamond Light Source. Powder samples were prepared in 1 mm glass capillaries and held in a modified Linkam hot stage. Pilatus 2M detector at a distance of 2.2 m from the sample was used. The X-ray energy was 12.4 keV.

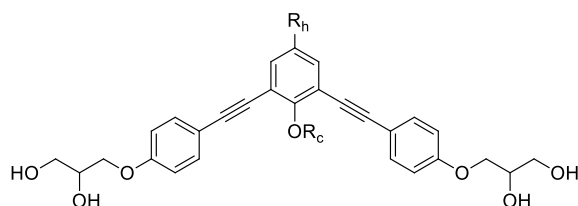
Electron density (ED) maps were calculated by inverse Fourier transformation using the standard procedure as described in International Tables for Crystallography. The structures *p6mm* and *p2gg* are centrosymmetric, thus the phase angle (ϕ) choices of the reflections are either 0 or π . However, this restriction does not apply to reflections (10) and (20) of the *p3m1* phase and (11), (21), (22), (31) and (32) of the *p31m* phase. The selection of the maps is considered based on the physical and chemical information i.e. chemical structure, known electron densities of the molecular fragments, molecular models and simulation.

Samples of ca. 50 μm thickness for **Second harmonic generation (SHG)** measurements were prepared on the rough side of silicon wafer and examined using a Zeiss LSM 510 Meta upright laser-scanning confocal microscope (Oberkochen, Germany) with a 40X/0.75NA objective. Temperature was controlled by a Mettler HS82 hot stage. A Chameleon Ti: Sapphire femtosecond pulsed laser (Coherent, California, USA) tuned to 800 nm, was attached to the microscope and focused onto the sample resulting in a SHG signal detectable at 400 nm. In order to exclude possible surface effects, first the beam was focused at the bottom of the LC film in contact with the Si substrate, then at 10 μm and 20 μm height, respectively. The SHG ratio was calculated by dividing the intensities at 400 nm by the averaged background signals around the peak.

Molecular models were built using Materials Studio (Accelrys). Geometry optimization and molecular dynamic simulation were performed using the Forcite Plus module with Universal Force Field. The experimental value for a -parameter and the value for c from Table S5.7 were used. The convergence tolerances for geometry optimization were 1 cal/mol for energy and 0.5 kcal/mol/Å for force. Constant volume (NVT) annealing dynamics was performed through 30 cycles between 300 and 600 K with a total annealing time of 30 ps.

5.5.2 DSC results

Table S5.1 Phase transition temperatures of the mesogenic compounds.



Compound R _h -F/H ^a	R _c	a (a_{sub}) (Å) ^b	T /°C [ΔH /kJ mol ⁻¹] ^c
CO₂CH₃-F	C ₆ H ₁₂ C ₄ F ₉	29.8	↑ Cr 55 Iso ↓ glass r.t. ↑ $p3m1$ -reg 42 Iso ^d
Br-H	CH ₂ CH(C ₅ H ₁₁) ₂	26.9	↑ Cr ₁ 78.7[8.9] Cr ₂ 118.8[40.1] Iso ↓ 91.9[1.9] $p3m1$ -reg 32.2[8.6] Cr ↑ 113.7[33.3] Iso
CONH₂-F	C ₄ H ₈ C ₆ F ₁₃	30.1	↑ Cr 91.5[1.2] $p3m1$ -reg 213.5[15.2] Iso ↓ 209.2[13.2] $p3m1$ -reg ↑ 212.5[13.3] Iso
CN-F	C ₆ H ₁₂ C ₄ F ₉	51.7 (29.8)	↑ Cr ₁ 63[5.8] Cr ₂ 73.3[4.2] $p31m$ -sup 83.4[0.2] Iso ↓ 77 (onset) $p31m$ -sup ↑ 82.9[0.1] Iso
CN-H	CH ₂ CH(C ₅ H ₁₁) ₂	24.5	↑ Cr 112[16.9] Iso ↓ 81.5[1.6] $p6mm$ -ran ↑ 84.4[1.6] Iso
NO₂-F	C ₄ H ₈ C ₆ F ₁₃	a 63.3 b 50.6 (29.2-31.7)	↑ Cr 85.7[0.7] $p2gg$ 116.3[0.9] Iso ↓ 114[0.09] $p2gg$ 109.9[1.5] ↑ $p2gg$ -sup 117[2.0] Iso

^aFirst part of compound name is the head group R_h, second part denotes the type of the attached chain. ^bLattice parameter (subcell lattice parameter). For superlattice $p31m$, $a_{sub} = \sqrt{3}a/3$. For superlattice $p2gg$, a_{sub} is in the range of $\sqrt{3}b/4$ and $0.5a$. ^cPeak DSC transition temperatures [and enthalpies] on 1st heating (↑), followed by cooling (↓) and 2nd heating (↑), all at 10 K min⁻¹. ^dTransition temperatures of CO₂CH₃-F are determined by XRD, SHG and POM.

Phase abbreviations: Cr = crystal, $p6mm$ -ran = hexagonal columnar phase with random orientation of the local 3-fold axis with 6-fold $p6mm$ overall symmetry; $p3m1$ -reg = columnar phase with trigonal symmetry and one column per unit cell; $p31m$ -sup = trigonal superlattice with three columns per unit cell; $p2gg$ -sup = rectangular superlattice with $p2gg$ symmetry and four columns per cell; Iso = isotropic melt.

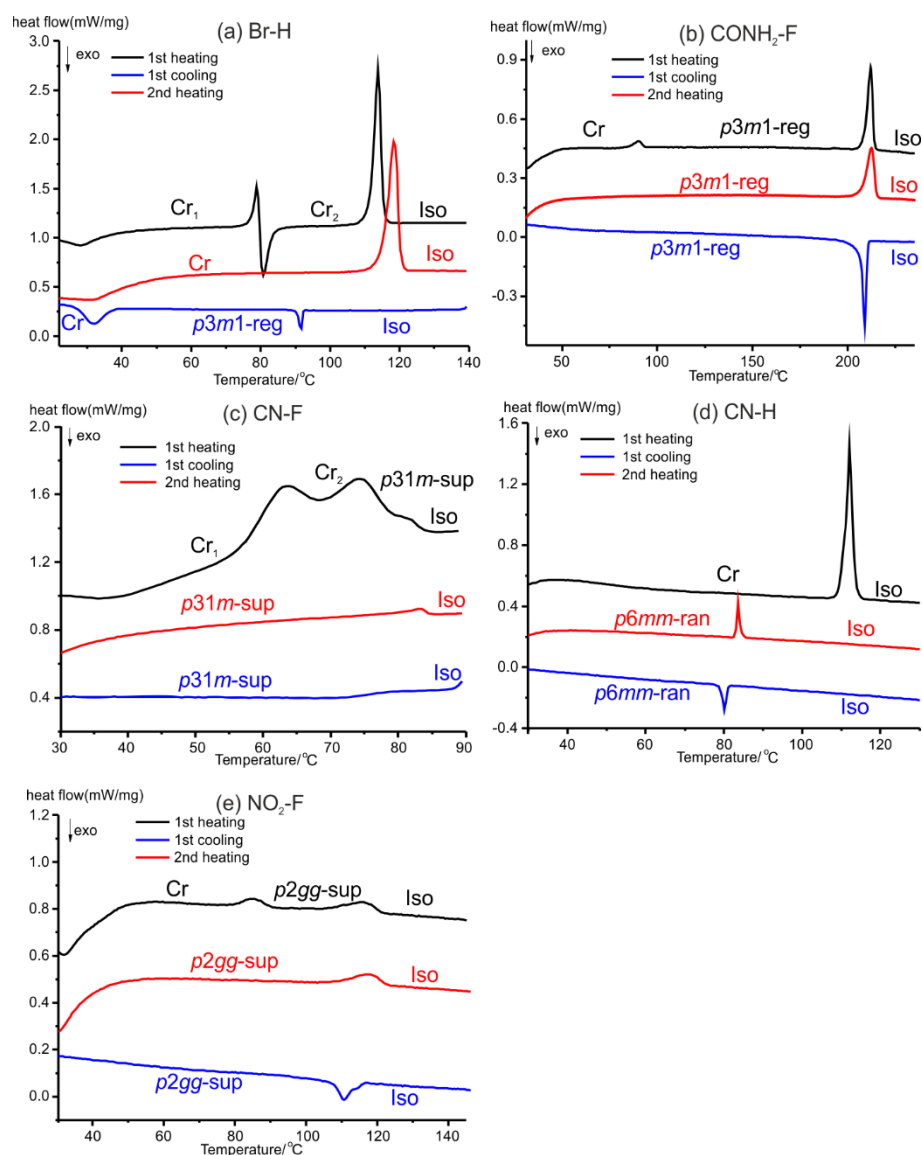


Figure S5.1 DSC thermograms of compounds (a) **Br-H** at heating and cooling scan rate of 10 K min⁻¹; (b) **CONH₂-F** at heating and cooling scan rate of 10 K min⁻¹; (c) **CN-F** at heating and cooling scan rate of 10 K min⁻¹; (d) **CN-H** at heating and cooling scan rate of 10 K min⁻¹; (e) **NO₂-F** at heating and cooling scan rate of 10 K min⁻¹.

5.5.3 Additional POM images

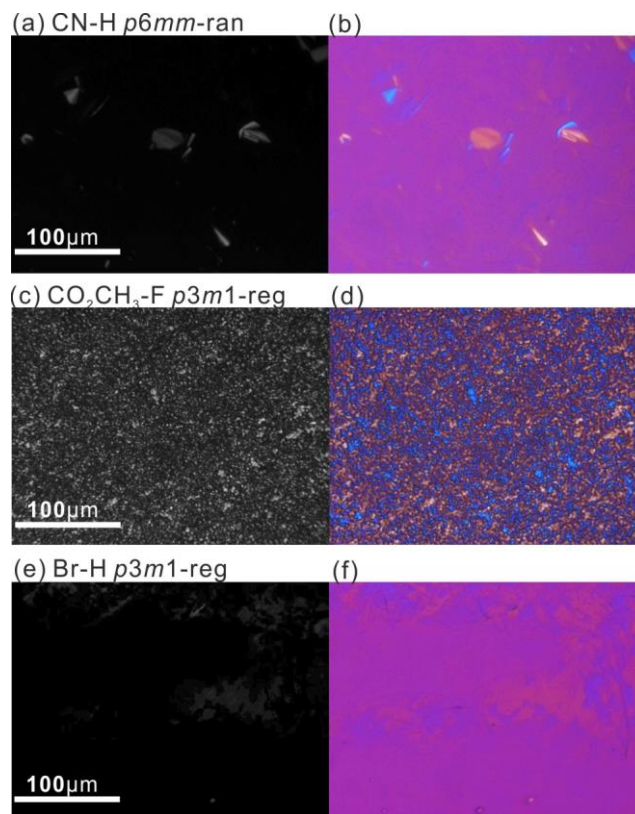


Figure S5.2 Polarized optical microscopy textures of (a, b) CN-H recorded at 70 °C (cooled from 100 °C), $p6mm$ -ran = hexagonal columnar phase with $p6mm$ symmetry and overall random packing; (c, d) $\text{CO}_2\text{CH}_3\text{-F}$ recorded at 25 °C (cooled from 60 °C), $p3m1$ -reg = the hexagonal columnar phase with three-fold symmetry and regular lattice; (e, f) Br-H recorded at 70 °C (cooled from 110 °C); (b, d and f) are recorded with a full-wave (λ) plate.

5.5.4 Additional X-ray diffraction, SHG and molecular modelling/simulation results on individual compounds

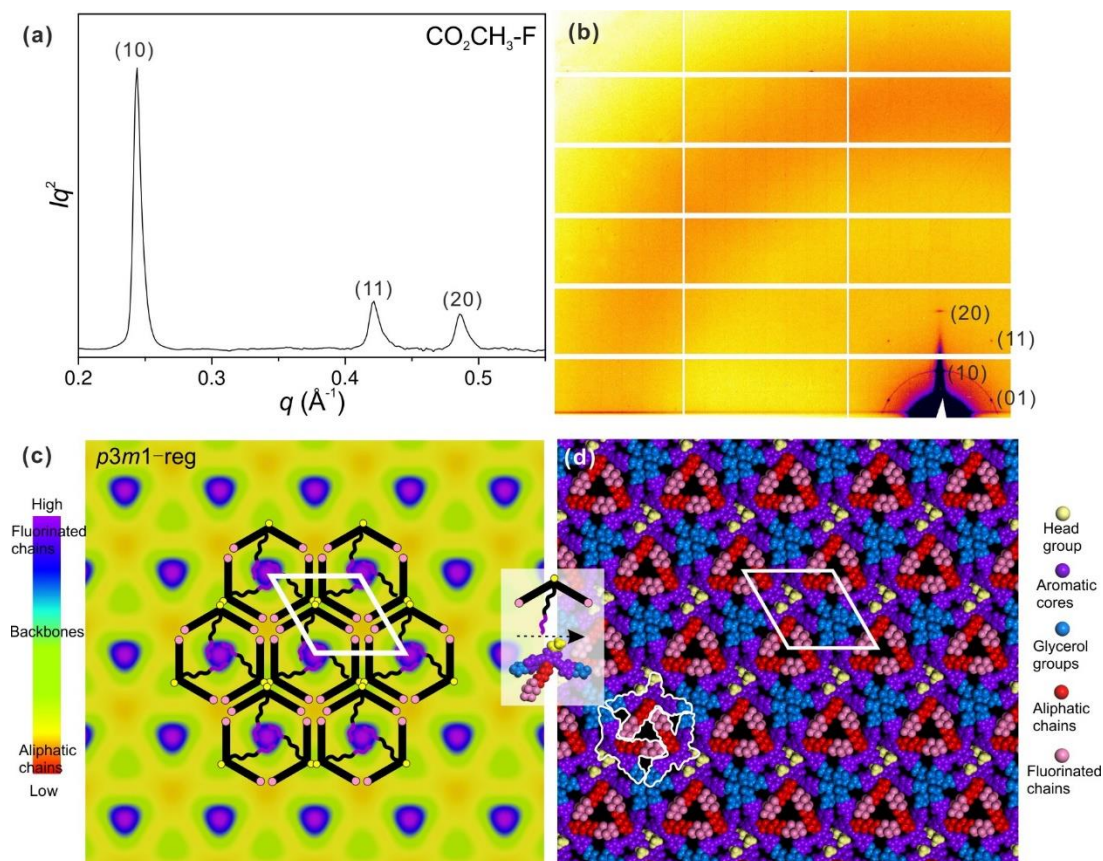
CO₂CH₃-F

Figure S5.3 (a) Powder SAXS curve and (b) GIWAXS/GISAXS pattern of CO₂CH₃-F recorded at 23 °C (cooled from isotropic temperature and kept at room temperature for 12 h to form liquid crystal phase); (c) reconstructed ED map ($\phi(10) = 20^\circ$, $\phi(11) = 0^\circ$ and $\phi(20) = 300^\circ$) with schematic model overlaid; (d) Geometry optimized molecular model.

Table S5.2 The indices, experimental, calculated d -spacings and relative integrated intensities of CO₂CH₃-F obtained from SAXS at 23 °C. All intensity values are Lorentz and multiplicity corrected.

(hk)	d -spacing (Å) experimental	d -spacing (Å) calculated	<i>Intensity</i>	<i>Phase</i> (°)
(10)	25.8	25.8	100.0	20
(11)	14.9	14.9	16.2	0
(20)	12.9	12.9	12.4	300
$a = 29.8 \text{ \AA}$				

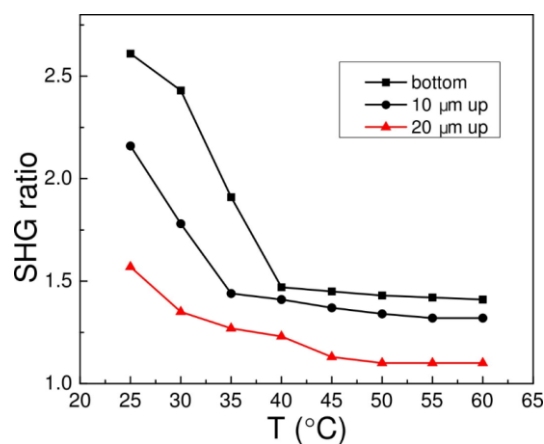


Figure S5.4 Temperature dependent intensity of the second harmonic (400 nm) vs. background for 800 nm excitation of $\text{CO}_2\text{CH}_3\text{-F}$, generated at different heights. (The sample was heated to 60 °C, cooled to room temperature and kept for 12 h to form LC phase. Next, it was heated and examined every 5 °C.)

Br-H

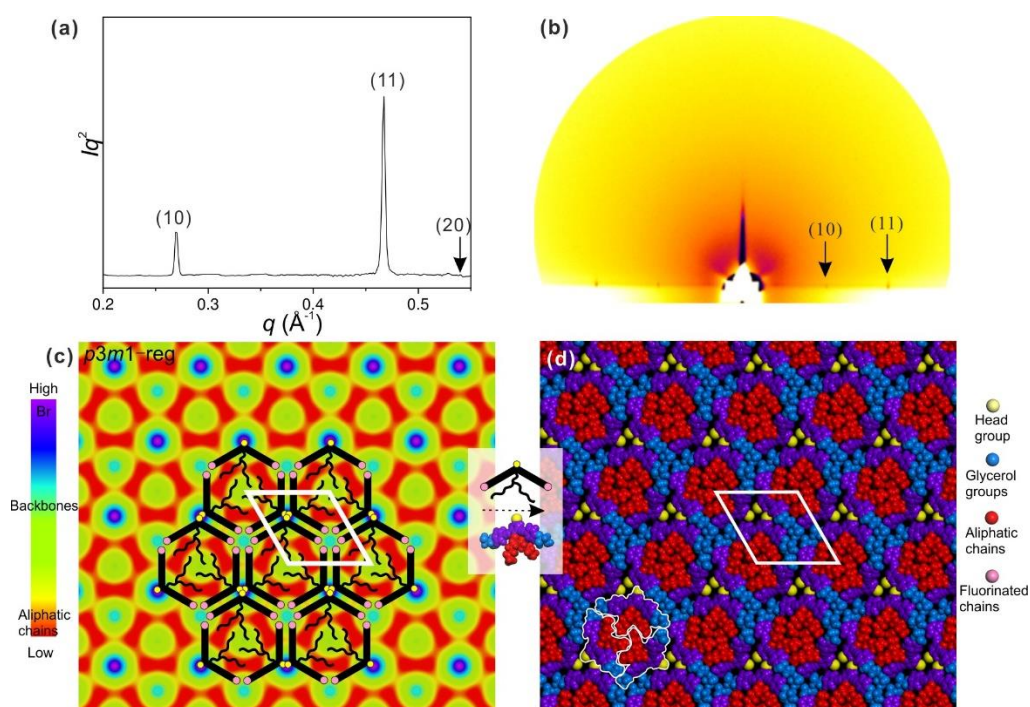


Figure S5.5 (a) Powder SAXS curve and (b) GISAXS diffraction pattern of Br-H recorded at recorded at 70 °C (cooled from 110 °C). The position of the arrow in (a) supposed to show (20), but the intensity of (20) is too weak to be observed; (c) reconstructed electron density

map ($\phi_{(10)} = 20^\circ$ and $\phi_{(11)} = 0^\circ$), with schematic molecules overlaid; (d) snapshot of dynamic simulation.

Table S5.3 The indices, experimental, calculated d -spacings and relative integrated intensities of Br-H obtained from SAXS at 70 °C (cooled from 110 °C). All intensity values are Lorentz and multiplicity corrected.

(hk)	d -spacing (Å) experimental	d -spacing (Å) calculated	<i>Intensity</i>	<i>Phase</i> (°)
(10)	23.3	23.3	26.3	20
(11)	13.5	13.5	100.0	0
$a = 26.9 \text{ \AA}$				

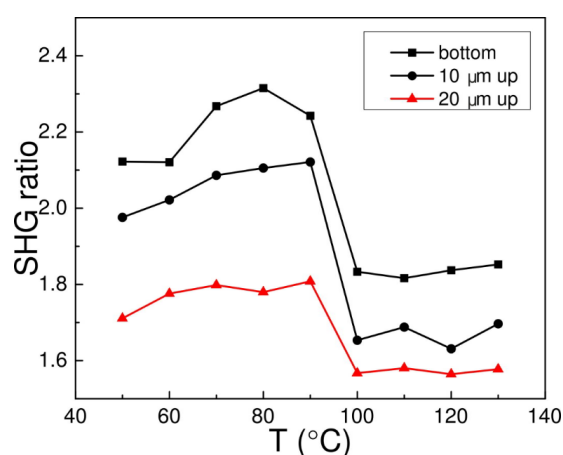


Figure S5.6 Temperature dependent intensity of the second harmonic (400 nm) vs. background for 800 nm excitation of Br-H, generated at different heights (cooled from 130 to 50 °C).

CONH₂-F

Table S5.4 The indices, experimental, calculated d -spacings and relative integrated intensities of of CONH₂-F obtained from SAXS at 130 °C (cooled from 230 °C). All intensity values are Lorentz and multiplicity corrected.

(hk)	d -spacing (Å) experimental	d -spacing (Å) calculated	<i>Intensity</i>	<i>Phase</i> (°)
(10)	26.1	26.1	100.0	20
(11)	15.1	15.1	50.8	0
(20)	13.1	13.1	8.45	140
$a = 30.1 \text{ \AA}$				

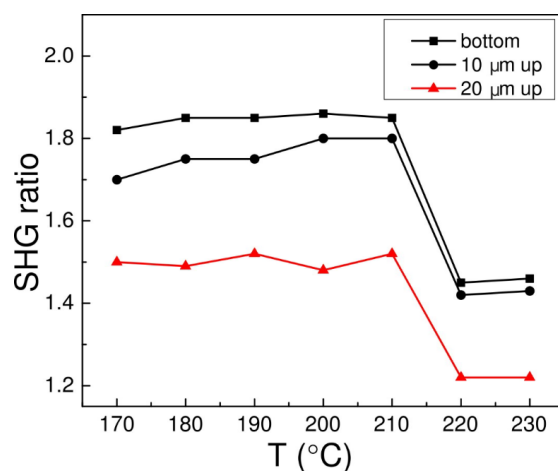


Figure S5.7 Temperature dependent intensity of the second harmonic (400 nm) vs. background for 800 nm excitation of $\text{CONH}_2\text{-F}$, generated at different heights (heated from 170 to 230 °C).

CN-F

Table S5.5 The indices, experimental, calculated d -spacings, relative integrated intensities and phases of CN-F recorded at 70 °C (cooled from 90 °C) from SAXS. All intensities values are Lorentz and multiplicity corrected.

(hk)	d -spacing experimental (Å)	d -spacing calculated (Å)	<i>Intensity</i>	<i>Phase</i> (°)
(10)	44.9	44.8	0.2	0
(11)	25.9	25.9	90.8	20
(20)	22.4	22.4	0.1	0
(21)	16.9	16.9	13.7	240
(30)	14.9	14.9	46.6	0
(22)	12.9	12.9	3.6	20
(31)	12.4	12.4	6.5	220
(40)	11.2	11.2	1.0	180
(32)	10.2	10.3	100.0	60
$a = 51.7 \text{ \AA}$				

CN-H

Table S5.6 The indices, experimental, calculated d -spacings and relative integrated intensities of CN-H obtained from SAXS at 70 °C (cooled from 100 °C). All intensity values are Lorentz and multiplicity corrected.

(hk)	d -spacing (Å) experimental	d -spacing (Å) calculated	<i>Intensity</i>	<i>Phase</i>
(10)	21.2	21.2	25.4	π
(11)	12.2	12.2	100.0	π
(20)	10.6	10.6	8.2	π
$a = 24.5 \text{ \AA}$				

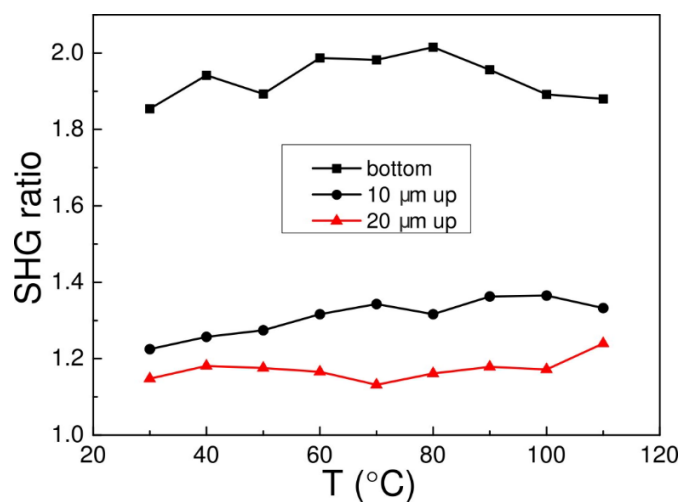


Figure S5.8 Temperature dependent intensity of the second harmonic (400 nm) vs. background for 800 nm excitation of CN-H, generated at different heights (cooling from 110 °C to 30 °C).

NO₂-FTable S5.7 The experimental, calculated d-spacings, intensities, phases and lattice parameters of the Col_{rec}/p2gg phase observed from SAXS at 100 °C. All intensity values are Lorentz and multiplicity corrected.

<i>(hk)</i>	<i>d</i> -spacing (Å) experimental	<i>d</i> -spacing (Å) calculated	<i>Intensity</i>	<i>Phase</i>
(11)	39.5	39.5	1.9	0
(20)	31.6	31.7	11.6	0
(21)	26.9	26.8	86.6	0
(02)	25.2	25.3	100.0	π
(12)	23.4	23.5	0.6	π
(22)	19.8	19.8	2.0	0
(31)	19.5	19.5	0.8	π
(13)	16.3	16.3	1.2	0
(32)	16.2	16.2	1.2	0
(40)	15.8	15.8	5.1	-
(41)	15.1	15.1	0.5	-
(23)	14.9	14.9	11.1	-
$a = 63.3 \text{ \AA}, b = 50.6 \text{ \AA}$				

5.5.5 Estimation of number of molecules per columnar stratum

Table S5.8 Estimation of number of molecules per column stratum

Sample	R _c	Plane group	<i>a</i> (Å)	<i>c</i> (Å) ^a	V _{cell} (Å ³) ^b	V _{mol} (Å ³) ^c	<i>n</i> _{Cr} ^d	<i>n</i> _{liq} ^e	<i>n</i> _{ave} ^f
CO ₂ CH ₃ -F	C ₆ H ₁₂ C ₄ F ₉	<i>p3m1</i> -reg	29.8	4.3	3306.9	980.4	3.4	2.7	3.0
Br-H	CH ₂ CH(C ₅ H ₁₁) ₂	<i>p3m1</i> -reg	26.9	5.0	3133.2	941.3	3.3	2.6	3.0
CONH ₂ -F	C ₄ H ₈ C ₆ F ₁₃	<i>p3m1</i> -reg	30.1	4.2	3318.9	984.1	3.4	2.6	3.0
CN-F	C ₆ H ₁₂ C ₄ F ₉	<i>p31m</i> -reg	51.7	4.1	9490.4	943.1	10.1	7.9	9.0
CN-H	CH ₂ CH(C ₅ H ₁₁) ₂	<i>p6mm</i> -ran	24.5	6.0	3118.9	939.6	3.3	2.6	3.0
NO ₂ -F	C ₄ H ₈ C ₆ F ₁₃	<i>p2gg</i> -sup	<i>a</i> 63.3 <i>b</i> 50.6	4.0	12940.0	961.0	13.5	10.5	12.0

a: Thickness of column stratum, or average spacing between molecules along column axis, *c*, is adjusted to obtain an integer value of *n*_{ave}.

b: Volume of the unit cell for hexagonal phase $V_{\text{cell}} = a^2 \cdot 0.866 \cdot c$, and rectangular phase $V_{\text{cell}} = a \cdot b \cdot c$;

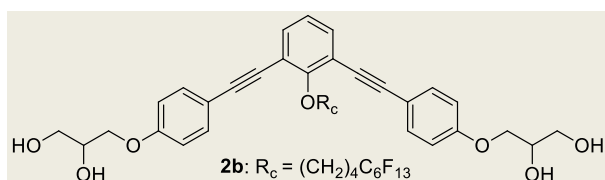
c: Volume of molecule (V_{mol}) = volume of a single molecule as calculated using the crystal volume increments[17];

d: $n_{Cr} = V_{\text{cell}}/V_{\text{mol}}$;

e: $n_{liq} = 0.55/0.7 \cdot n_{Cr}$ (average packing coefficient in the crystal is $k = 0.7$, in isotropic liquid $k = 0.55$) [18];

f: $n_{ave} = (n_{Cr} + n_{liq})/2$.

Table S5.9 Comparison of lattice parameters and column areas of honeycomb phases, including that of the previously reported anchor-shaped molecule 2b with $R_h = H$ [10].



Name	Plane group	Lattice parameters (Å)	Column area A (Å ²)*
CN-H	<i>p6mm</i> -ran	24.5	519.8
Br-H	<i>p3m1</i> -reg	26.9	626.7
CO ₂ CH ₃ -F	<i>p3m1</i> -reg	29.8	769.1
CN-F	<i>p31m</i> -sup	51.7	771.6
CONH ₂ -F	<i>p3m1</i> -reg	30.1	784.6
NO ₂ -F	<i>p2gg</i> -sup	$a = 63.3$ $b = 50.6$	800.7
2b ^[S3]	<i>p3m1</i> -reg	28.8	718.3

*The column area of the regular lattices is calculated by $A = \frac{\sqrt{3}}{2} a^2$. For the superlattices *p31m* (CN-F) and *p2gg* (NO₂-F), there are 3 and 4 columns in each unit cell, respectively. The column area of *p31m*-sup is $\frac{\sqrt{3}}{6} a^2$ and that of *p2gg*-sup is $\frac{ab}{4}$.

5.5.6 Electron densities of functional groups involved, non-bonded interaction energies and dipole moments of headgroups

Table S5.10 Electron densities of different functional groups involved ^a.

Compound	Aromatic core (10 ⁵ electron/Å ³)	glycerol groups (10 ⁵ electron/Å ³)	head group (10 ⁵ electron/Å ³)	Aliphatic chain 1 (10 ⁵ electron/Å ³)	Fluorinated chain (10 ⁵ electron/Å ³)
CONH ₂ -F	4.38	4.50	4.72 (-CONH ₂)	3.69 (-OC ₄ H ₈)	6.58 (-C ₆ F ₁₃)
Br-H			10.60 (-Br)	3.35 (-O-CH ₂ - (C ₅ H ₁₂) ₂)	-
CO ₂ CH ₃ -F			4.52 (-COOCH ₃)	3.54 (-OC ₆ H ₁₂)	6.60 (-C ₄ F ₉)
CN-F			4.15 (-CN)	3.54 (-OC ₆ H ₁₂)	6.60 (-C ₄ F ₉)
CN-H			41.5 (-CN)	3.35 (-O-CH ₂ - (C ₅ H ₁₂) ₂)	-
NO ₂ -F			6.39 (-NO ₂)	3.69 (-OC ₄ H ₈)	6.58 (-C ₆ F ₁₃)

^a Volume of relevant part of molecule is calculated using the method of crystal increments ^[S11].

Table S5.11 Hydrogen bond enthalpies and dipole moments of glycerol and headgroups.

Functional Group	H-bond enthalpy between head group and C _{sp3} -OH (-kcal/mol)	Enthalpy of non-bonded interaction among headgroups (-kcal/mol)	Dipole moment of headgroup (D)
Glycerol	4.8 (single intermolecular H-bond between glycerols) [19]	-	-
Br	0.7 (<i>n</i> -heptyl bromide with <i>n</i> -propanol [20])	1.0 (bromoform, dipolar) [20]	1.72 (bromobenzene [21])
CONH ₂	4.5 (acetamide with isopropanol [20])	7.1 (formamide, H-bond) [22]	-
CN	3.1 (benzonitrile with water, similar to benzonitrile with alcohols [23])	3.1 (Benzonitrile, dipolar) [23]	4.48 (benzonitrile [24])
NO ₂	2.8 (nitromethane with methanol [25])	3.1 (non-bonding between O _{nitro} and π(N) _{nitro} [26])	4.22 (nitrobenzene [27])
COOCH ₃	2.3 (thienylacryloyl methyl ester with ethanol[28]) 2.5 (5-methylthienylacryloyl methyl ester with ethanol [28])	-	1.75 (methyl acetate [29])

Acknowledgements

For support with experiments at synchrotron radiation sources we are grateful to Dr Olga Shebanova and Prof Nick Terill at station I22, Dr Gareth Nisbet and Prof Steve Collins at station I16, Diamond Light Source, and Drs Oier Bikondoa and Paul Thompson at EPSRC-funded XMaS beam line (BM28) at ESRF. Financial support is acknowledged from the 111 Project 2.0 of China (BP2018008), from EPSRC (EP-P002250, EP-T003294), from NSFC (grants 21674099, 21664015, 21865038) and Yunnan Joint Fund Key Project (2018FY001(-012)). Y.X. L. thanks CSC for stipend and UoS for fee waiver.

References

- [1] J. M. Seddon and R. H. Templer, in *Handbook of Biological Physics*, Vol. 1, ed. R. Lipowsky and E. Sackmann, Elsevier, Amsterdam, 1995, chapter 3 Polymorphism of Lipid-Water Systems, pages 97–160.
- [2] (a) C. Destrade, P. Foucher, H. Gasparoux, N.H. Tinh, A.M. Levelut, J. Malthete, Disc-like mesogen polymorphism, *Mol. Cryst. Liq. Cryst.*, **106** (1984) 121-146. (b) F. Vera, J.L. Serrano, T. Sierra, Twists in mesomorphic columnar supramolecular assemblies, *Chem. Soc. Rev.*, **38** (2009) 781-796. (c) M.A. Shcherbina, X.B. Zeng, T. Tadjiev, G. Ungar, S.H. Eichhorn, K.E.S. Phillips, T.J. Katz, Hollow Six-Stranded Helical Columns of a Helicene, *Angew. Chem. Int. Ed.*, **48** (2009) 7837-7840. (d) T. Ghosh, M. Lehmann, Recent advances in heterocycle-based metal-free calamitics, *J. Mater. Chem. C*, **5** (2017) 12308-12337. T. Kato, N. Mizoshita, K. Kishimoto, Functional liquid-crystalline assemblies: Self-organized soft materials, *Angew. Chem. Int. Ed.*, **45** (2006) 38-68. (e) B. Donnio, S. Buathong, I. Bury, D. Guillon, Liquid crystalline dendrimers, *Chem. Soc. Rev.*, **36** (2007) 1495-1513. (f) T. Wöhrle, I. Würzbach, J. Kirres, A. Kostidou, N. Kapernaum, J. Litterscheidt, J.C. Haenle, P. Staffeld, A. Baro, F. Giesselmann, S. Laschat, Discotic Liquid Crystals, *Chem. Rev.*, **116** (2016) 1139-1241. (g) Y.X. Li, F.F. Fan, J. Wang, L. Cseh, M. Xue, X.B. Zeng, G. Ungar, New Type of Columnar Liquid Crystal Superlattice in Double-Taper Ionic Minidendrons, *Chem. Eur. J.*, **25** (2019) 13739-13747.
- [3] (a) C. Tschierske, Development of Structural Complexity by Liquid-Crystal Self-assembly, *Angew. Chem. Int. Ed.*, **52** (2013) 8828-8878. (b) G. Ungar, C. Tschierske,

V. Abetz, R. Holyst, M.A. Bates, F. Liu, M. Prehm, R. Kieffer, X. Zeng, M. Walker, B. Glettner, A. Zywockinski, Self-Assembly at Different Length Scales: Polyphilic Star-Branched Liquid Crystals and Miktoarm Star Copolymers, *Adv. Funct. Mat.*, **21** (2011) 1296-1323. (c) C. Tschierske, C. Nurnberger, H. Ebert, B. Glettner, M. Prehm, F. Liu, X.B. Zeng, G. Ungar, Complex tiling patterns in liquid crystals, *Interface Focus*, **2** (2012) 669-680.

[4] (a) X.H. Cheng, M. Prehm, M.K. Das, J. Kain, U. Baumeister, S. Diele, D. Leine, A. Blume, C. Tschierske, Calamitic bolaamphiphiles with (semi)perfluorinated lateral chains: Polyphilic block molecules with new liquid crystalline phase structures, *J. Am. Chem. Soc.*, **125** (2003) 10977-10996. (b) B. Chen, X.B. Zeng, U. Baumeister, G. Ungar, C. Tschierske, Liquid crystalline networks composed of pentagonal, square, and triangular cylinders, *Science*, **307** (2005) 96-99. (c) S. Poppe, A. Lehmann, A. Scholte, M. Prehm, X. Zeng, G. Ungar, C. Tschierske, Zeolite-like liquid crystals, *Nat. Comm.*, **6** (2015) 8637. (d) A. Scholte, S. Hauche, M. Wagner, M. Prehm, S. Poppe, C.L. Chen, F. Liu, X.B. Zeng, G. Ungar, C. Tschierske, A self-assembled liquid crystal honeycomb of highly stretched (3-1-1)-hexagons, *Chem. Comm.*, **56** (2020) 62-65.

[5] (a) X. Zeng, R. Kieffer, B. Glettner, C. Nurnberger, F. Liu, K. Pelz, M. Prehm, U. Baumeister, H. Hahn, H. Lang, Complex multicolor tilings and critical phenomena in tetraphilic liquid crystals, *Science*, **331** (2011) 1302-1306. (b) F. Liu, R. Kieffer, X. Zeng, K. Pelz, M. Prehm, G. Ungar, C. Tschierske, Arrays of giant octagonal and square cylinders by liquid crystalline self-assembly of X-shaped polyphilic molecules, *Nat. Comm.*, **3** (2012) 1104.

[6] (a) A.J. Crane, F.J. Martinez-Veracoechea, F.A. Escobedo, E.A. Muller, Molecular dynamics simulation of the mesophase behaviour of a model bolaamphiphilic liquid crystal with a lateral flexible chain, *Soft Matter*, **4** (2008) 1820-1829. (b) M.A. Bates, M. Walker, Dissipative particle dynamics simulation of T- and X-shaped polyphilic molecules exhibiting honeycomb columnar phases, *Soft Matter*, **5** (2009) 346-353.

[7] (a) S. George, C. Bentham, X. Zeng, G. Ungar, G.A. Gehring, Monte Carlo study of the ordering in a strongly frustrated liquid crystal, *Phys. Rev. E*, **95** (2017) 062126. (b) W.S. Fall, C. Nurnberger, X.B. Zeng, F. Liu, S.J. Kearney, G.A. Gehring, C. Tschierske, G. Ungar, An Ising transition of chessboard tilings in a honeycomb liquid crystal, *Mol. Syst. Des. Eng.*, **4** (2019) 396-406.

[8] (a) B. Chen, U. Baumeister, S. Diele, M.K. Das, X.B. Zeng, G. Ungar, C. Tschierske, A new type of square columnar liquid crystalline phases formed by facial amphiphilic triblock molecules, *J. Am. Chem. Soc.*, **126** (2004) 8608-8609. (b) M. Prehm, F. Liu, U. Baumeister, X. Zeng, G. Ungar, C. Tschierske, The giant-hexagon cylinder network--a liquid-crystalline organization formed by a T-shaped quaternary amphiphile, *Angew Chem Int Ed Engl*, **46** (2007) 7972-7975. (c) A. Lehmann, A. Scholte, M. Prehm, F. Liu, X.B. Zeng, G. Ungar, C. Tschierske, Soft Rectangular Sub-5 nm Tiling Patterns by Liquid Crystalline Self-Assembly of T-Shaped Bolaamphiphiles,

Adv. Funct. Mater., **28** (2018) 1804162.

[9] H.J. Kim, Y.H. Jeong, E. Lee, M. Lee, Channel Structures from Self-Assembled Hexameric Macrocycles in Laterally Grafted Bent Rod Molecules, *J. Am. Chem. Soc.*, **131** (2009) 17371-17375.

[10] B. Glettner, F. Liu, X. Zeng, M. Prehm, U. Baumeister, G. Ungar, C. Tschierske, Liquid-crystal engineering with anchor-shaped molecules: honeycombs with hexagonal and trigonal symmetries formed by polyphilic bent-core molecules, *Angew Chem Int Ed Engl*, **47** (2008) 6080-6083.

[11] (a) H.J. Kim, S.K. Kang, Y.K. Lee, C. Seok, J.K. Lee, W.C. Zin, M. Lee, Self-Dissociating Tubules from Helical Stacking of Noncovalent Macrocycles, *Angew. Chem. Int. Ed.*, **49** (2010) 8471-8475. (b) H.J. Kim, F. Liu, J.H. Ryu, S.K. Kang, X. Zeng, G. Ungar, J.K. Lee, W.C. Zin, M. Lee, Self-organization of bent rod molecules into hexagonally ordered vesicular columns, *J Am Chem Soc*, **134** (2012) 13871-13880.

[12] G. Hennrich, A. Omenat, I. Asselberghs, S. Foerier, K. Clays, T. Verbiest, J.L. Serrano, Liquid crystals from C-3-symmetric mesogens for second-order nonlinear optics, *Angew. Chem. Int. Ed.*, **45** (2006) 4203-4206.

[13] T. Hahn, *International Tables for Crystallography*, Vol. A, Springer, Dordrecht, 5th edition, 2005, pages 105-106.

[14] J. L. Locher and M. C. Escher, *Escher: The Complete Graphic Work*, Thames and Hudson Ltd: London, 1992.

[15] B. Chen, U. Baumeister, G. Pelzl, M.K. Das, X. Zeng, G. Ungar, C. Tschierske, Carbohydrate Rod Conjugates: Ternary Rod-Coil Molecules Forming Complex Liquid Crystal Structures, *J. Am. Chem. Soc.*, **127** (2005) 16578-16591.

[16] M. Poppe, C.L. Chen, F. Liu, M. Prehm, S. Poppe, C. Tschierske, Emergence of tilt in square honeycomb liquid crystals, *Soft Matter*, **13** (2017) 4676-4680.

[17] A. Immirzi, B. Perini, Prediction of density in organic crystals, *Acta Crystallogr. A*, **33** (1977) 216-218.

[18] A. Kitaigorodsky, *Molecular crystals and molecules*, Vol. 29, Elsevier, 2012.

[19] S.P. Verevkin, D.H. Zaitsau, V.N. Emel'yanenko, A.A. Zhabina, Thermodynamic properties of glycerol: Experimental and theoretical study, *Fluid Phase Equilibria*, **397** (2015) 87-94.

[20] A.S.N. Murthy, C.N.R. Rao, Spectroscopic Studies of the Hydrogen Bond, *Applied Spectroscopy Reviews*, **2** (1968) 69-191.

[21] O. Dorosh, E. Bialkowska-Jaworska, Z. Kislal, L. Pszczolkowski, New measurements and global analysis of rotational spectra of Cl-, Br-, and I-benzene: Spectroscopic constants and electric dipole moments, *J. Mol. Spectrosc.*, **246** (2007) 228-232.

[22] R. Vargas, J. Garza, R.A. Friesner, H. Stern, B.P. Hay, D.A. Dixon, Strength of the N-H center dot center dot center dot O=C and C-H center dot center dot center dot

O=C bonds in formamide and N-methylacetamide dimers, *J. Phys. Chem. A*, **105** (2001) 4963-4968.

[23] J.Y. Le Questel, M. Berthelot, C. Laurence, Hydrogen-bond acceptor properties of nitriles: a combined crystallographic and ab initio theoretical investigation, *J. Phys. Org. Chem.*, **13** (2000) 347-358.

[24] D.R. Borst, T.M. Korter, D.W. Pratt, On the additivity of bond dipole moments. Stark effect studies of the rotationally resolved electronic spectra of aniline, benzonitrile, and aminobenzonitrile, *Chem. Phys. Lett.*, **350** (2001) 485-490.

[25] F.H. Allen, C.A. Baalham, J.P.M. Lommerse, P.R. Raithby, E. Sparr, Hydrogen-bond acceptor properties of nitro-O atoms: A combined crystallographic database and ab initio molecular orbital study, *Acta Crystallogr. B*, **53** (1997) 1017-1024.

[26] M. Daszkiewicz, Importance of O center dot center dot center dot N interaction between nitro groups in crystals, *Crystengcomm*, **15** (2013) 10427-10430.

[27] T. Shikata, Y. Sakai, J. Watanabe, Nitrobenzene anti-parallel dimer formation in non-polar solvents, *AIP Advances*, **4** (2014) 067130.

[28] P.J. Tonge, R. Fausto, P.R. Carey, FTIR studies of hydrogen bonding between alpha,beta-unsaturated esters and alcohols, *J. Mol. Struct.*, **379** (1996) 135-142.

[29] E. Galbiati, M. Delzoppo, G. Tieghi, G. Zerbi, Dipole-dipole interactions in simple esters and in liquid-crystal polyesters, *Polymer*, **34** (1993) 1806-1810.

Chapter 6 Published paper: New Type of Columnar Liquid Crystal Superlattice in Double-Taper Ionic Minidendrons

Chemistry - A European Journal, 2019, 25, 13739-13747

Ya-xin Li,^{a,†} Fang-fang Fan,^{b,†} Jie Wang,^{b,c} Liliana Cseh,^{c,d} Min Xue,^b Xiang-bing Zeng^a and Goran Ungar^{c*}

^a *Department of Materials Science and Engineering, University of Sheffield, Sheffield S1 3JD, U.K.*

^b *Department of Physics, Zhejiang Sci-Tech University, Hangzhou 310018, P.R. China*

^c *State Key Laboratory for Mechanical Behavior of Materials, School of Materials, Xi'an Jiaotong University, Xi'an 710049, P.R. China*

^d *"Coriolan Dragulescu" Institute of Chemistry, Timisoara 300223, Romania*

[†]*These authors contributed equally.*

This Chapter was published as an article in Chemistry - A European Journal. I have carried out the experiments and data analysis by POM, FT-IR, X-ray diffraction, molecular modelling and dynamic simulation, and written the corresponding parts in the article. Fangfang Fan, Jie Wang, and Liliana Cseh synthesized the compounds and confirmed the chemical structures by NMR. I participated in the elemental analysis and Mass spectroscopy experiments and the results analysis for the further confirmation of the structures.

The article is reproduced with permission in its accepted form by the journal, with minor adaptations on the figures and section numbering, and correction of some typos. The details of the synthesis part in the supporting information are not included here and the references in the manuscript and supporting information have been combined for clarity.

6.1 Abstract

Wedge-shaped molecules, such as dendrons, are among the most important building blocks for directed supramolecular self-assembly. Here we present a new approach aimed at widening the range and complexity of potential mesophases by introducing *double-tapered* mesogens. Two series of compounds are presented, both alkali metal salts (Li, Na, Cs) of 3,4,5-*tris*-alkoxybenzoic acid with a second tapered *tris*-alkoxyaryl group attached at the end of an alkoxy chain. The double-tapered compounds all display an unusual hexagonal columnar phase consisting of one ionic and three non-ionic columns per unit cell. The cation size has an unexpectedly drastic effect on unit cell size. Unlike most columnars, the current phases show unusually high dimensional stability on heating, and high stiffness in spite of being 80-85% aliphatic, attributed to their molecular topology. The described approach may lead to co-assemblies of multifunctional materials, e.g. parallel *p*- and *n*-semiconducting nanowires or parallel ionic and electronic conductors.

6.2 Introduction

Columnar liquid crystal phases, having 2D positional order, have come a long way since their first discovery in 1977 in discotic molecules [1]. Subsequent years have seen columnar mesogens increasing in complexity and variety of shapes (star [2,3], bent core [4], bowl [5,6], helicene[7], heterocycle[8], T- and X-shape [9]) and types of non-bonded interactions (H-bonding [10], donor-acceptor[11], ionic [12], coordination[13]).

Wedge-shaped molecules that consist of at least two moderately incompatible parts often exhibit liquid crystal (LC) phases with 2D or 3D periodicity. Typical compounds of this type are dendrons and “minidendrons” (first-generation wedge-shaped dendrons) containing an aromatic core and a functional group at the narrow end, and flexible

terminal alkyl or oligo(ethylene oxide) chains at the wide end. The chains form a soft shell, or corona, that wrap around cylindrical columns or spherical “micelles” [14-19]. Tapered mesogens, including dendrons, are some of the most fundamental and widespread building blocks in supramolecular chemistry. They have been included as assembly-directing moieties in functional materials such as organic semiconductors [20,21], ionic conductors [22-26], crown ethers [27,28], donor-acceptor complexes [29,30], polymers [31-33], peptides [34], nanoparticles [35,36] etc. In this way it is possible to create “dendronized” functional materials that can be used in a variety of potential applications [37]. Columnar organization, often due to the attachment of alkoxyphenyl dendrons,[14] can be usefully exploited, e.g. in forming 1D electronic [20,21] and ionic [22-26] conductors, in encapsulating drugs [38] and light-emitting polymers [39] etc.

The main factor determining whether columnar, spherical, layer-like or bicontinuous self-assembly mode is adopted by such molecules is the actual geometry of the wedge. In a first approximation the cross-section area of the wedge A increases as $A = k x^p$, where x is the distance from the narrow end see Figure 6.1a. For wedges forming cylindrical columns, $k = (2\pi/\mu)$, where μ is the number of wedges in the disk-like section (the “stratum”) of the column. As a rough guide, smectic phases are favoured for $p \approx 0$ (no taper), hexagonal columnar for $p \approx 1$ (“pizza-slice”), spherical for $p \approx 2$ (parabolic wedge, or cone), and bicontinuous cubic for $0 < p < 1$ (shield-like) [40]– see Figure 6.1a. In a further crude approximation, small differences in the value of p close to 2 will determine the packing mode of spherical micelles, with the lowest p giving the Frank-Kasper A15 cubic phase, space-group $Pm\bar{3}n$ [41] and the highest p giving the body-centred cubic (BCC) [42]. BCC seems to be the ultimate structure for wedges of highest divergence (highest p), as shown by benzoate salts with 5 chains emanating from a single phenyl ring [43]. In some cases for $0 < p < 1$ rectangular columnar, or

“ribbon”, phases form instead of bicontinuous cubic [44-46]. It has been shown that a temperature-induced transition between rectangular and hexagonal columnar phase in ionic LCs can be used as a thermal on-off switch for ionic conduction [26].

Except for discotic molecules, the simplest and most common case of column-forming building blocks is that of a pointed wedge, e.g. a dendron tapered down to a small group at the apex, such as carboxylic acid, carboxylate salt, OH or COOCH₃ [14,47]. Such tapered mesogens thus assemble like pizza-slices into a flat disk (Figure 6.1b), or if tilted, into a propeller- or umbrella-like object. The flexible chains form the liquid-like continuum outside the columns. The larger the taper angle, the smaller the μ (Figure 6.1c). There are also numerous examples of wedge-like molecules covalently connected together at their narrow end, forming dimers [48] (Figure 6.1d), as well as oligomers or polymers [14]; the polymer backbone then resides in the column centre. More unusual situations arise when the wedge is “blunt”, as in the case of alkyl-substituted helicene in Figure 6.1e [49]. In that case a hole remains in the centre of the column, the column taking the shape of a helical tube. If the wedge is narrow and blunt, as in the case of biphenyl-based dendrons [50], the number μ of molecules in a disk is large, but the blunt end means that the hole in the column centre also increases. As large voids are not tolerated in liquids or LCs, some molecules reverse their orientation plugging the central hole with their terminal chains (Figure 6.1f) [51]; this results in an array of tightly packed vesicle-like aromatic cylinders, with flexible chains both inside and outside.

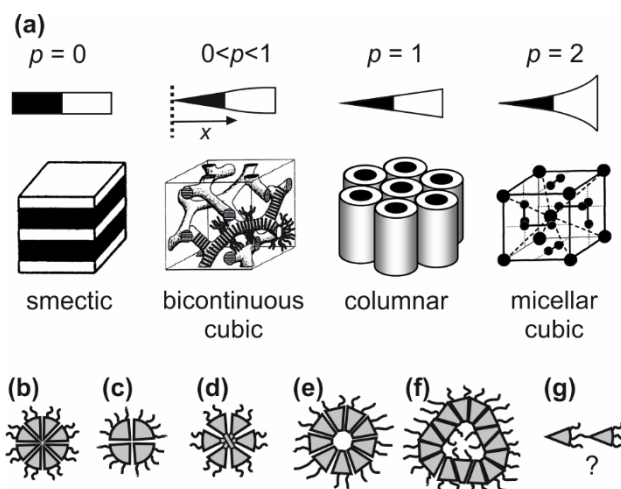
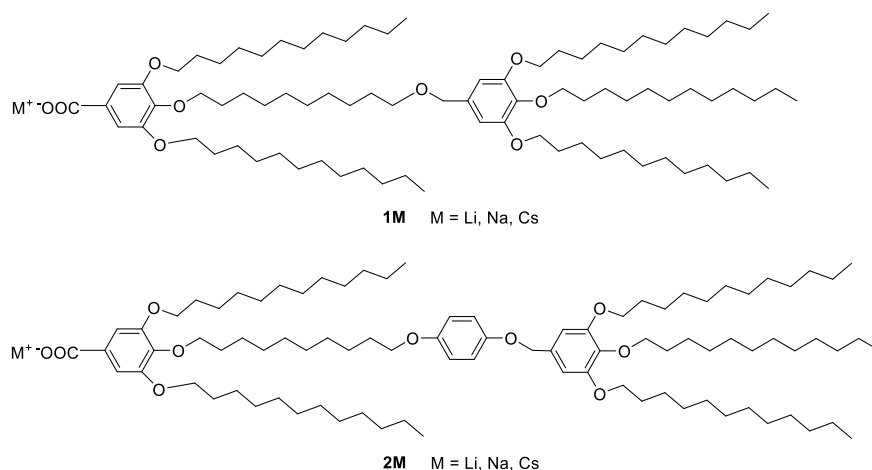
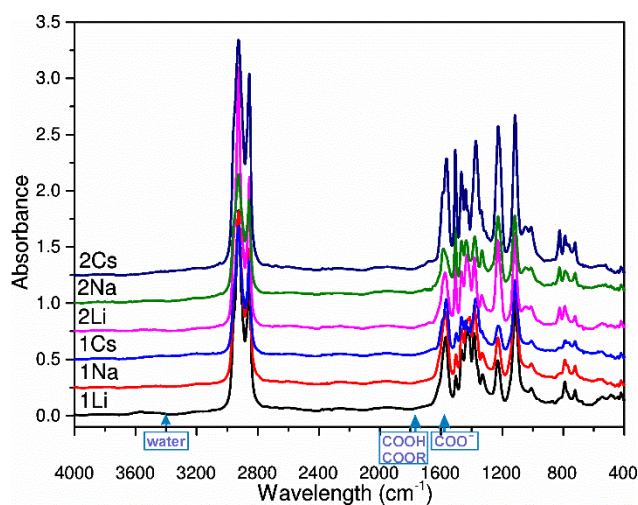


Figure 6.1. (a) Schematic representation of the effect of architecture of a wedge-shaped molecule on the type of their organization in a LC or soft crystal. (b-f) Different modes of arrangement of wedges in a cylindrical column (view along the column axis). (g) Double-tapered molecule.

The exact shape of the wedge can be tailored in a variety of ways, e.g. by changing the branching pattern at each successive generation cascade of a dendron, e.g. 3-way followed by 2-way branching - this often affects the nanostructure [14]. However, restricting the shape to a single wedge, regardless of its shape, still limits the variety of its modes of assembly. In this work we venture outside these limitations by designing molecules of a double wedge shape, where the periphery of the first, inner wedge is the starting point of a second, outer wedge – see (Figure 6.1g and Scheme 6.1). In this way we obtain a new columnar phase of complex superstructure comprising two different coexisting column types. A detailed structural study is presented, exploring the packing principles, morphology and stability of this new self-assembly mode with promising application potential.

6.3 Results

Scheme 6.1. Compounds **1M** and **2M**Figure 6.2. IR spectra of compounds **1M** and **2M** as films between CsI windows

Compounds **1M** and **2M** were prepared as described in Schemes S6.1 and S6.2 in SI. The inner tapered benzoate intermediate was synthesised by benzyl protection of the 4-position, alkylation of 3 and 5 positions and then selective deprotection of the 4-position. The second tapered intermediates contained one (for compounds **1M**) or two (for **2M**) benzene rings and were obtained by etherification of methyl gallate with 1-

bromododecane and subsequent ester group reduction in the presence of LiAlH_4 giving (3,4,5-tris(dodecyloxy)phenyl)methanol. To obtain **2M**, the preparation of the outer tapered intermediate for the synthesis of methyl 3,5-bis(dodecyloxy)-4-((10-(4-((3,4,5-tris(dodecyloxy)benzyl)oxy)phenoxy)decyl)oxy)benzoate (**13**) involved two steps in addition to those for the preparation of methyl 3,5-bis(dodecyloxy)-4-((10-((3,4,5-tris(dodecyloxy)benzyl)oxy)decyl)oxy)benzoate (**9**), i.e. the conversion of hydroxyl group to halide and mono-etherification of 1,4-dihydroxybenzene with a bromo derivative. The inner and outer tapered mesogens were then linked by a *n*-dodecylene chain via two successive Williamson etherifications. The alkali metal salts were prepared by base-assisted hydrolysis of the methyl benzoate with the corresponding alkali metal hydroxides. As in other similar hygroscopic alkali metal salts, it is important to ensure that the material is free of water and that the carboxylic acid is fully ionized. Before analysis compounds **1M** and **2M** were dried *in vacuo* for 24 h at 40 °C. The IR spectra (Figure 6.2) confirm that the compounds were in order on both counts. The absence of water is shown by the absence of a broad O-H stretching peak in the range 3300-2500 cm^{-1} (but exposure to air produced a broad peak around 3300 cm^{-1}). Also, the spectra in Figure 6.2 contain a strong C=O stretching band at 1597 cm^{-1} due to carboxylate anion. Meanwhile C=O bands at 1687 cm^{-1} and 1720 cm^{-1} corresponding, respectively, to acid and ester (Figure S6.29), are completely absent, as is the free acid O-H bending vibration at 932 cm^{-1} .

The compounds were investigated by differential scanning calorimetry (DSC), polarized optical microscopy (POM) and X-ray scattering including powder small- and wide-angle (SAXS and WAXS), grazing incidence SAXS and WAXS (GISAXS and GIWAXS) on thin films, electron density map reconstruction and molecular modelling and molecular dynamics (MD) annealing.

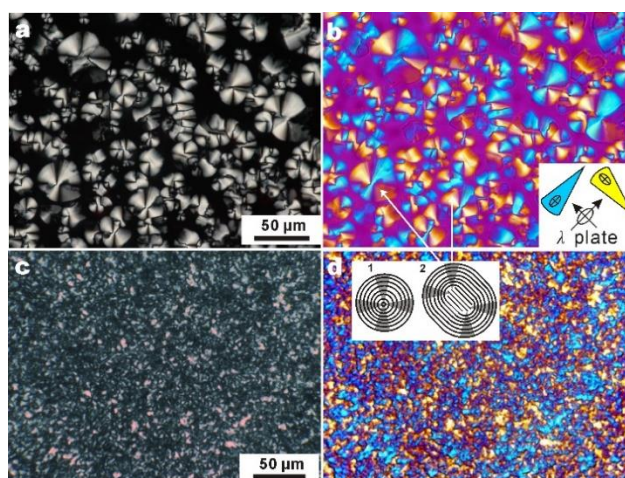


Figure 6.3. POM textures of (a, b) **2Na** at 93 °C and (c, d) Na salt of 3,4,5-tris-dodecyloxybenzoic acid (**12Na**) at 100 °C. (b, d) are recorded with a full-wave (λ) retarder plate. The large ellipse in the inset in (b) shows the indicatrix of the retarder, while the small ellipses are indicatrices in the coloured fans of the sample. Inset 1 in (d) shows schematically the concentric circular column configuration in a developable domain with a single +1 disclination in the centre (not seen in the micrographs), while inset 2 shows the case where the central singularity is split into two remote $+1/2$ disclinations, as seen in several places in (a, b).

Above a low crystal melting point, all compounds display a birefringent mesophase. The POM image in Figure 6.3a shows black regions, meaning that here the optic axis is perpendicular to the glass surface (homeotropic alignment)) and therefore that the material itself is optically uniaxial. The circular or fan-like birefringent regions with a parts of a dark Maltese cross in Figure 6.3a suggest that these are the developable domains [52], or “spherulitic” patterns, characteristic of columnar (Col) LC phases. The uniaxiality suggests that the mesophase is hexagonal. The image taken with the λ -plate (Figure 6.3b) shows that the high-index axis is radial in the developable domains, and since the columns are normally tangential, the high-index direction is perpendicular to the column axis. This is consistent with the columns being negatively birefringent, with the averaged orientation of the benzene rings normal to the column axis.

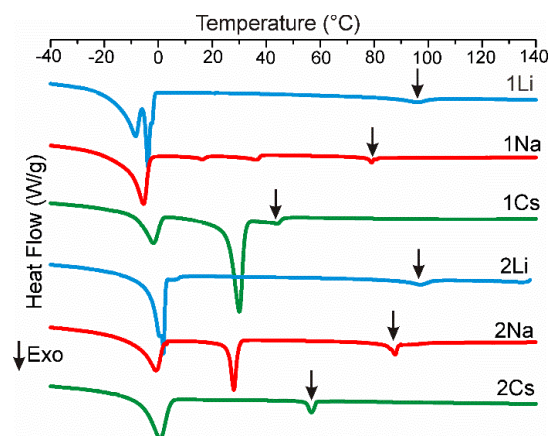


Figure 6.4. DSC thermograms (cooling at 10 K/min) of compounds **1M** and **2M**. The isotropic-columnar transitions are indicated by arrows.

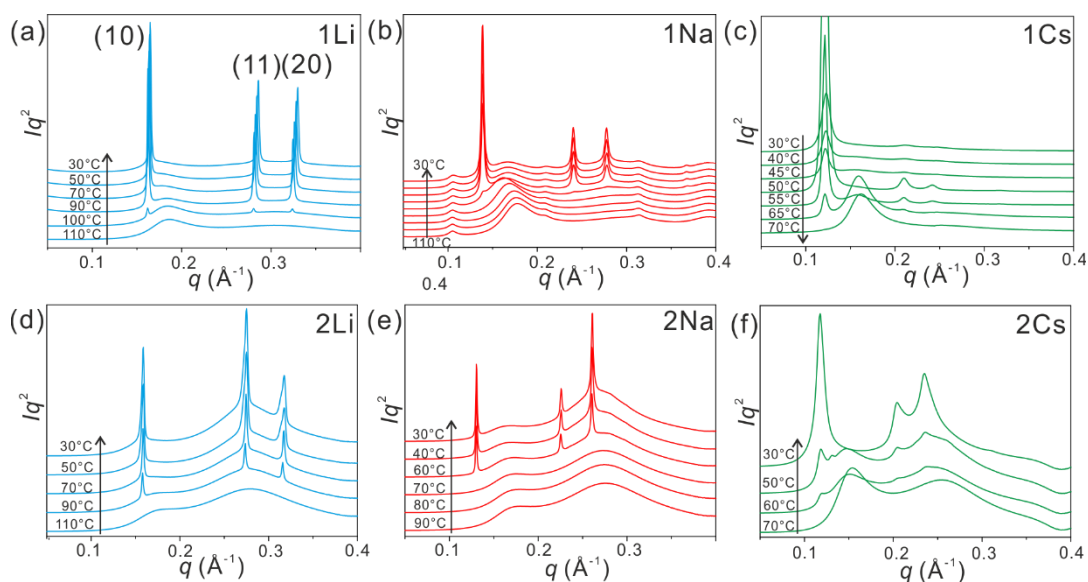


Figure 6.5. Temperature dependence of transmission powder SAXS curves of compounds **1M** and **2M** recorded at beamline I22 of Diamond Light Source. $q = 4\pi (\sin\theta)/\lambda$, where θ is the Bragg angle and λ the X-ray wavelength. Vertical arrow shows the direction of temperature change.

Figure 6.4 shows cooling DSC thermograms of all six compounds, with the isotropic (Iso) to columnar transition exotherm marked by arrow. The Iso-Col transition is highly reversible with low hysteresis as shown by heating thermograms, Table S6.1 in Supporting Information (SI). Transition temperatures and enthalpies are listed in Table

6.1. As can be seen, the isotropization transition temperature T_i decreases with increasing size of the metal cation, from Li to Cs, but is unaffected by the addition of the extra benzylether group in compounds **2M**.

Table 6.1. Phase transition temperatures, lattice parameters and number of molecules in per unit cell of **1M** and **2M**

Compound	$T/ ^\circ\text{C}$ [$\Delta H/\text{J g}^{-1}$]	Lattice parameters		Number of molecules μ^a
		a (\AA)	c (\AA)	
1Li	↓ Iso 96 [2.9] Col -3.9 [7.6] Cr ₁ -8.6 [8.5] Cr ₂ ↑ -2.3 [8.7] Cr ₁ 4.9 [7.3] Col 110 [3.5] Iso	44.0	4.2 ^b	3.0
1Na	↓ Iso 79 [1.5] Col 36 [1.6] Cr ₁ 16 [0.5] Cr ₂ -5.6 [20] Cr ₃ ↑ 2 [22] Cr ₂ 21 [0.2] Cr ₁ 42 [0.4] Col 88 [2.2] Iso	52.2	3.7 ^b	3.8
1Cs	↓ Iso 44 [1.4] Col 30 [24] Cr ₁ -1.8 [8.4] Cr ₂ ↑ 2.2 [8.3] Cr ₁ 49 [17] Col 60/66 [3.7] Iso	59.8	4.5	6.0
2Li	↓ Iso 97 [2.1] Col 1.9 [18] Cr ↑ 5.6 [20] Col 107 [2.9] Iso	46.4	4.0	3.0
2Na	↓ Iso 88 [1.7] Col 28 [7.9] Cr ₁ -1.0 [13] Cr ₂ ↑ 15 [6.8] Cr ₁ 41 [7.1] Col 96 [2.6] Iso	55.6	3.7 ^b	4.0
2Cs	↓ Iso 57 [1.5] Col 0.3 [18] Cr ↑ 4.3 [18] Col 54/69 [3.2] Iso	61.8	4.5	6.0

^a See details in SI.

^b The d -spacings observed in GIWAXS.

Temperature dependent powder SAXS curves are shown in Figure 6.5 and Figures S6.1-6.5 in SI. WAXS patterns were recorded simultaneously with SAXS, as shown in Figures S6.1-6.5. This ensured that LC phases (mesophases) are clearly distinguished from crystal phases. The nature of the mesophase as hexagonal columnar is confirmed in all six compounds by the presence of three Bragg peaks with the reciprocal square spacings d^{-2} in the ratio 1:3:4; the peaks are thus indexed as (10), (11) and (20) of a hexagonal lattice. For all compounds the appearance of the Bragg peaks on cooling

closely matches the temperature of the small sharp exotherm in Figure 6.4, confirming its assignment as Iso-Col transition.

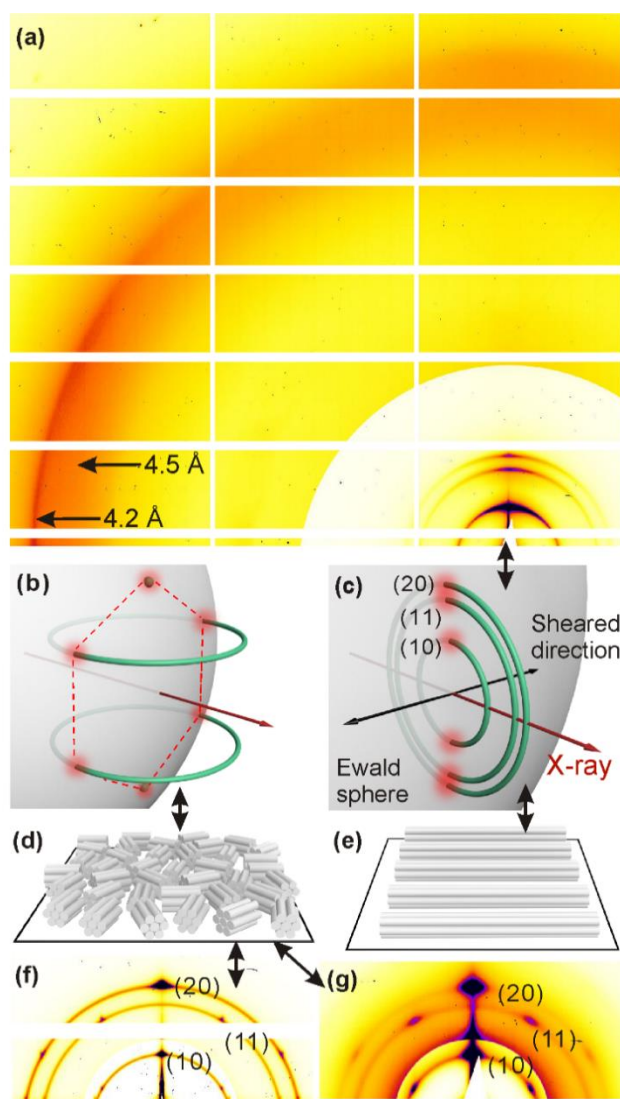


Figure 6.6. (a) GISAXS/GIWAXS pattern of **1Li** sheared at 120°C and quenched to the columnar phase. The shear direction and the columns are in the horizontal plane and perpendicular to the beam, as sketched in panel (e). (f) GISAXS of **2Na** at 60°C (cooled from Iso phase); (g) GISAXS of **1Cs** at 45 °C. Columnar domains, randomized in the plane of the substrate, that give the diffraction patterns in (f) and (g) are depicted in (d). The reciprocal space description of diffraction geometry in pattern (a) is given in (e), and that of patterns in (f) and (g) is given in (b). The intersections of the reciprocal rings with the Ewald sphere, giving rise to the diffraction spots (or arcs), are highlighted in red. All experiments were performed at beamline I16 of Diamond Light Source, with thin LC films on Si substrate. The outer region in

(a), (f) and (g) is enhanced in intensity. The horizontal and vertical white stripes are gaps between detector panels.

To confirm the indexing and find out about column orientation and other features, grazing incidence X-ray diffraction experiments were carried out on **1M** compounds in the form of thin films on silicon substrate – see Figures 6.6, S6.2c and 6.4e. The GISAXS pattern in Figure 6.6f shows (10), (11) and (20) reflections from **2Na**, sharp both radially and azimuthally, superimposed on semicircles coming from unoriented areas, possibly at sample edges. The diffraction spots come from domains of planar alignment (columns parallel to substrate), but with random in-plane orientation – see model in Figure 6.5d and the reciprocal space representation of {10} reflections in Figure 6.6b. We note that reflections from homeotropic areas would be on the equator, but due to the diffraction geometry, these are hidden behind the horizon. In the well-aligned planar domains giving rise to the sharp Bragg spots, the columnar lattice lies on one of its {100} planes, and the same is true for **1Cs** (Figure 6.6g). However, compared to those of **2Na**, the reflections from **1Cs** are radially considerably broader indicating lattice distortion and/or smaller ordered domains. The significant broadening of reflections in **1Cs** and particularly **2Cs** is also evident from powder SAXS in Figure 6.5c,f. Notably T_i values of these two compounds are the lowest (Figure 6.4), suggesting a less stable frustrated structure of the two Cs salts compared with those of Li and Na – see Discussion.

Figure 6.6a shows the full grazing incidence diffraction pattern, including the wide-angle region, from a **1Li** film that had been sheared just above T_i in the direction perpendicular to the beam, i.e. left-to-right, and then quenched into the Col phase at 30°C. The fact that all three SAXS peaks are now on the vertical axis means that columns are aligned along the shear direction (Figure 6.6e) and, moreover, that the orientation of the hexagonal lattice is randomized around the shear direction, rather than

the $\{100\}$ planes lying on the substrate. The geometry in reciprocal space is depicted in Figure 6.6c. The lack of preferential $\{100\}$ surface anchoring is attributed to the rapid growth of Col phase on quenching and limited low-temperature mobility hindering the attainment of optimal anchoring. However the shearing experiment has achieved its goal of aligning the columns in a way that condenses the “(001)” reciprocal lattice point in diffraction position on the Ewald sphere (see the arc labelled “4.2 Å” near the horizon in Figure 6.6a). This scattering maximum is not a true Bragg peak as there is no true long-range order along the column axis. Nevertheless it reflects the average intermolecular distance along the column, allowing the estimation of the volume of the “3-D unit cell” and thus the number of molecules μ in it. The intra-columnar “001” spacings for other compounds were also determined from GIWAXS and these, along with the μ -values, are listed in Tables 6.1 and Figure S6.7. As can be seen, there are 3 molecules per cell in Li salts, 4 in Na salts, and 6 in Cs salts.

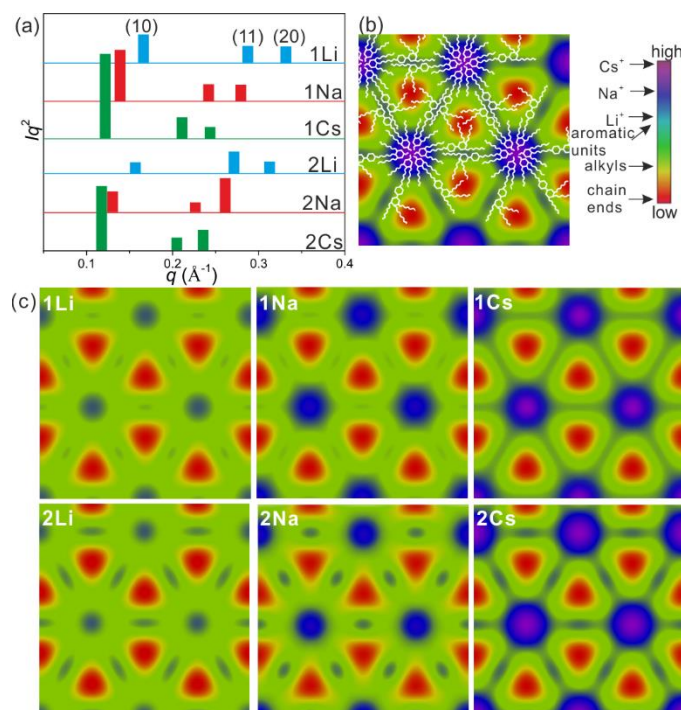


Figure 6.7. (a) Integrated intensities of the hk Bragg peaks (Lorentz corrected) of the Col₁₊₃ phase of compounds **1M** and **2M**. (b) Electron density map of the Col₁₊₃ phase of **2Cs** with overlaid schematic molecular model. (c) ED maps of Col₁₊₃ phase of all compounds.

In order to determine the molecular arrangement, we first consider the integrated diffraction peak intensities. For easy comparison, these are plotted in Figure 6.7a. What is unusual is the high intensity of the (11) and (20) peaks, which is normally much lower than that of the (10) peak in most Col phases. This immediately suggests that the structure is not the simple hexagonal arrangement of aromatic columns embedded in an aliphatic continuum. Yet the fact that the relative intensity of the (10) peak increases profoundly with the number of electrons in the metal, i.e. from Li to Cs, suggests that these cations congregate in a single cluster in the unit cell, the site of maximum amplitude of the first term of the Fourier representation of electron density (ED). The full ED maps reconstructed from the powder diffraction intensities in Figure 6.6a indeed confirm this, as shown in Figure 6.7b,c. The species most likely to be found in areas of a particular colour are indicated on the colour scale in panel b. Thus the metal-containing columns are found to be arranged on a hexagonal lattice, one per unit cell, with the lowest ED level (blue) in the maps of **1Li** and **2Li**, and the highest (purple) in those of **1Cs** and **2Cs**. The green continuum represent the alkyl chains, which make up 84.7% and 80.2% of the volume of compounds **1M** and **2M**, respectively. The interesting features are the small blobs of elevated ED half way between the main ionic columns. They are more pronounced in **2M** than in **1M** compounds. As shown in the schematic model of the molecular arrangement of **2Cs** in panel (b), these are the locations of the “outer” benzene rings, one per molecule in compounds **1M** and two in compounds **2M**. Not unexpectedly, the points furthest away from benzene rings, i.e. the points where alkyl chains must stretch to reach, have the lowest density, as shown by the red triangles. Since the unit cell contains 1 major and 3 minor columns, henceforth we denote this phase as Col₁₊₃.

To test the viability of our structures we have built molecular models of each compound on a hexagonal lattice with experimentally determined lattice parameters a and c , and

the number of molecules μ . These were subjected to 30 cycles of molecular dynamics annealing between 300 and 600 K using the Forcite module of Materials Studio (Accelrys). Snapshots of annealed geometry are shown in Figure 6.8 for **2Li**, **12-12-12Cs**, **1Cs** and **2Cs** (see also Figure S6.6 for **1Li**). **12-12-12Cs** is the simple single-tapered Cs 3,4,5-*tris*-dodecyloxybenzoate minidendron, reported previously [53] and shown here for comparison (see Discussion). As can be seen, efficient space-filling is achieved in all cases. In compounds **1M** and **2M** the spacer chains, coloured green, are just about long enough in their all-*trans* conformation for the outer benzene rings from neighbouring columns to aggregate together forming separate minor non-ionic aromatic columns half way between the major ionic columns.

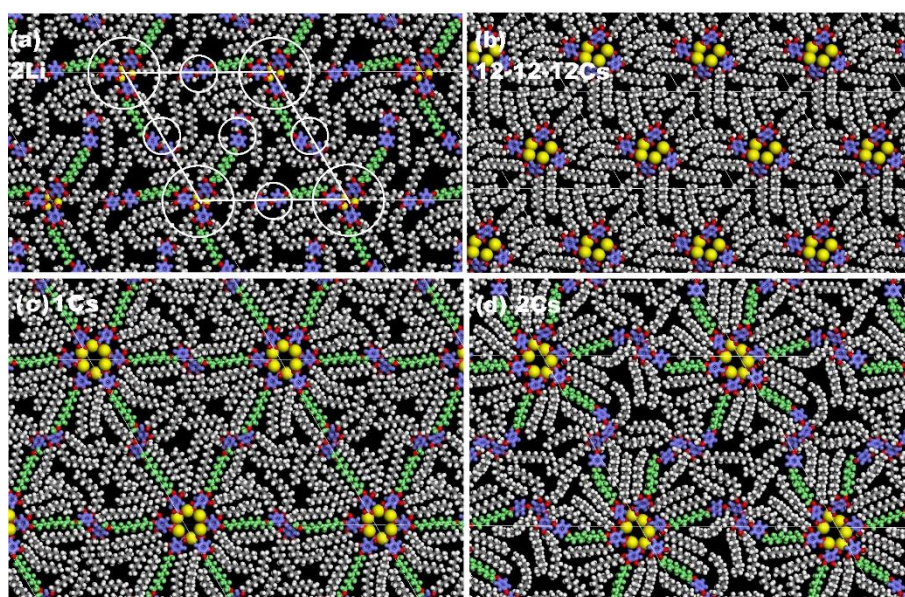


Figure 6.8. Snapshots of molecular models of compounds (a) **2Li**, (b) **12-12-12Cs**, (c) **1Cs** and (d) **2Cs** after NVT molecular dynamics heat-cool annealing cycles with a total duration of 30 ps. For clarity benzoate and benzyloxy groups are purple, cations are yellow, and the linker chains are green. All atoms are ball-and-stick except cations which are CPK with true ionic radii. The unit cell as well as the major (ionic) and minor (non-ionic) columns are indicated in (a).

Since in **1Li** and **2Li** there are only 3 molecules assembling around an ionic column, there can be only one benzene ring, on average, in the cross-section of each of the 6

surrounding minor non-polar columns in **1Li**, and two in **2Li**; these are attached alternately to the reference ionic column and to three of the six neighbouring ones. Except in **1Li**, the non-ionic columns are clearly discernible as distinct ED maxima in the maps in Figure 6.7, and with an intensity consistent with the model, i.e. increasing from Li to Cs, and from **1M** to **2M**. As there are six molecules of **1Cs** and **2Cs** in a cell there are, respectively, 2 and 4 benzene rings in each non-ionic column, half of them attached to the central ionic column and half to its six ionic neighbours. In the case of **1Na** and **2Na** $\mu = 4$ in an ionic column, hence there must be $4/3$ benzene rings, on average, in each minor column in **1Na**, and $8/3$ in that of **2Na**. Since the system preserves hexagonal symmetry, non-ionic column strata with 1 and 2 rings in **1Na**, and 2 and 3 rings in **2Na**, must be distributed randomly in the ratio 2:1 and 1:2, respectively.

6.4 Discussion

The above results show how redesigning tapered mesogens in a relatively simple way can lead to a novel and complex type of self-assembled “columnar alloy”. Learning from these results should help obtain other new complex 2D and, possibly also 3D mesostructures. Keeping within 2D, in principle it is possible to vary the chemical nature of the focal points of the inner and outer fan, one forming e.g. a *p*-semiconducting and the other a *n*-semiconducting π -stacked column type. This would result in a self-assembled columnar mini bulk heterojunction. Similarly, one could construct a complex array comprising ionically and electronically conducting nanowires.

Regarding self-assembly of compounds **1M** and **2M**, there are several further features worth commenting on. First we note the remarkable effect of the size of the alkali metal cation. As the ionic radius increases by no more than 1 Å between Li^+ and Cs^+ , and as the benzoate groups are pushed away from the column centre by that small amount, the

number of molecules that can fit around the cationic core doubles from 3 to 6, doubling the area of the unit cell. This amplification effect of small differences in the focal group of tapered mesogens can be compared with the similarly striking effect of “bluntness” of the tip of the wedge described in Figure 6.1.

Another notable difference between the behaviour of single and double-tapered minidendrons is the fact that while in the former the column area decreases steeply with increasing temperature due to widening taper angle and consequent ejection of surplus molecules from the column, [43,46,54,55] in the current double-taper compounds the cell area remains constant (Figure 6.5). It has been found previously that in the simple single-tapered Li 3,4,5-*tris*-dodecyloxybenzoate minidendron (**12-12-12Li**) there are also, as in **1Li** and **2Li**, only $\mu = 3$ molecules in a column stratum.[53,55] The MD-annealed model of **12-12-12Li** is shown in Figure S6.6 alongside that of **1Li** for easy comparison. In fact **12-12-12Li** is the only **12-12-12M** salt whose columns do not thin down on heating, as the loss of one of its three molecules in a disk would create an unsustainable void. It was shown, however, that the void could be easily filled, and thus column thinning enabled, if free alkane is added to the minidendron [53]. As in **1Na** and **2Na**, in the simple **12-12-12Na** compound $\mu = 4$ above the crystal melting point. But on further heating there is an unusual first-order $\text{Col}_{\text{hex}}\text{-Col}_{\text{hex}}$ phase transition with an abrupt drop in column diameter, due to a cooperative ejection of the fourth minidendron [55].

As in most other single-taper dendrons, in **12-12-12Cs** column diameter was found to decrease significantly but continuously on heating [54]. At 100 °C $\mu \approx 4$, compared to $\mu = 6$ in **1Cs** and **2Cs**. The MD annealed model of **12-12-12Cs** is shown in Figure 6.8b. It can be seen that, as adjacent columns in **12-12-12Cs** are closer together than in **1Cs** or **2Cs**, there is more interdigitation of alkyl chains effectively increasing the taper angle of the molecules. In contrast, the exclusion of the outer fans from the inner column

corona in **1Cs** and **2Cs** increases the distance between the ionic columns to the point where intercolumnar interdigitation ceases to be an option. Some interdigitation does occur, but this is between the chains of the major and the minor columns. As most of the chains of the outer fans are now engaged in filling the depleted interstitial zones (red triangles in Figure 6.7b, c), the degree of interdigitation is considerably reduced. This reduces the effective taper angle of the inner fans, allowing μ of **1Cs** and **2Cs** to increase from ~ 4 to 6, and staying at 6 up to the clearing temperature. The same reasoning explains why in double-tapered Na salts μ is constant at 4, while in **12-12-12Na** it decreases sharply from 4 to nearly 3 on heating [55].

From the low T_i (Figure 6.4) and poor order in the Col₁₊₃ phase of **1Cs** and **2Cs** (broad Bragg peaks in Figure 6.5c, f) it is clear that the Col₁₊₃ structure in double-tapered Cs minidendrons is a highly frustrated one, compared to those in Li and Na compounds. We attribute this to the low conformational entropy of this structure, with only a low *gauche/trans* ratio allowed by the need to keep the outer fans outside the inner column shell of exceptionally large diameter.

In this context we also comment on the shape of the SAXS curves of the Iso liquid above T_i (Figure 6.5, bottom curves in all panels). Normally above the clearing temperature of a columnar LC a diffuse scattering maximum remains close to the position of the (10) Bragg peak of the Col phase; this reflects the persistence of short-range columnar order in the Iso liquid. However in the present compounds there are two diffuse maxima in the Iso phase, the second one particularly pronounced in **2M** compounds. The q -values of the two peaks are roughly in the ratio $1:\sqrt{3}$, suggesting short-range hexagonal order. The first peak intensifies in the order of cations Li⁺ - Na⁺ - Cs⁺, indicating that it is dominated by the correlation between persisting ionic columns. The peak is clearly shifted to higher q away from that of the (10) Bragg peak, particularly in Na and Cs compounds. This suggests that, upon isotropization, the

column diameter shrinks substantially, but only after the steric constraints of the Col₁₊₃ phase had been relaxed. In fact in the Iso phase of all six compounds the first maximum is almost at the same position of $0.17 \pm 0.1 \text{ \AA}^{-1}$, which corresponds to a spacing of $2\pi/q \approx 37 \text{ \AA}$. This would suggest a significant reduction in the number of dendrons per column, probably to no more than 3, upon Col₁₊₃-Iso transition. It is also notable that the second diffuse peak is much stronger in **2M** than in **1M** compounds, reflecting correlation between all columns, non-ionic as well as ionic, with the additional benzene ring in **2M** making the two column types more similar in electron numbers. However, the persistence of the low- q peak in the Iso phase of all compounds confirms that fragments of the basic Col₁₊₃ pattern remain in the Iso liquid.

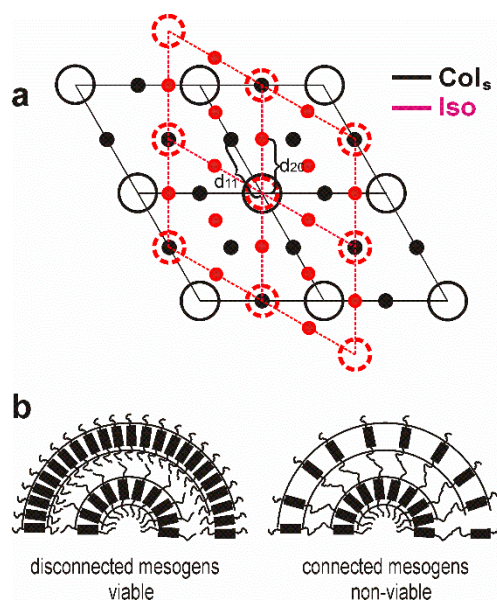


Figure 6.9. (a) Schematic model showing the relationship between the 1+3 type columnar arrangements in the Col (black) and Iso (red) phases. Empty circles are ionic and small full circles non-ionic columns. The arrangement in Iso phase is only short-range. Four unit cells are shown for each structure. d_{11} and d_{20} are lattice spacings in the Col phase. (b) Qualitative explanation of the high bending modulus of covalently linked columns in the “topologically stiff” Col₁₊₃ phase (right), compared to the low modulus of non-linked columns in an ordinary Col phase (left). The black rectangles represent discotic molecules or supramolecular self-assembled discs.

The fact that the second diffuse Iso peak, the “(11)_{Iso}”, coincides with the (20) Bragg peak of the Col₁₊₃ phase in **2Na** and **2Cs** can be represented schematically as in Figure 6.9a. The relationship between the two arrays, the Col₁₊₃ (black) and the Iso “lattice” (red) is obtained by rotating the unit cell by 30°, whereby the distance between the major (ionic) and minor (non-ionic) columns drops from d_{11} to d_{20} , i.e. by a factor $\sqrt{3}/2$. However, in spite of the unit cell shrinking, the inter-chain distance increases on isotropization, as indicated by the shift to lower q of the diffuse WAXS peak (Figure S6.5b).

Finally a comment on the optical textures. In areas of planar alignment Col₁₊₃ phase of compounds **1M** and **2M** grows large developable domains with fan-like appearance (Figure 6.3a,b). These are very different from the fine and irregular textures displayed by most single taper minidendrons (Figure 6.3c,d and ref. [56]). Even where larger domains were observed in single-taper compounds, most were marked by a clear central disclination of strength $s = +1$, evidenced by a Maltese cross with four dark brushes meeting in the centre, as depicted in Inset 1 in Figure 6.3d [57]. Such textures are indicative of a low bending modulus (low Frank constant K_3), [58] as is expected from highly flexible columns containing a high aliphatic fraction and no large rigid mesogens. However, in the “spherulites” of compounds **1M** and **2M**, the central disclination is always split in two clearly separated $s = +1/2$ disclinations – see Figure 6.2a,b and Inset 2 in panel d. This means that the columns are stiff (high K_3) and cannot withstand high curvature. So what is the origin of the stiffness of the Col₁₊₃ phase, of which 80-85% consists of molten alkyl chains and the rest are flexibly connected single benzene rings?

We explain this puzzling observation with the help of the sketch in Figure 6.9b. The figure on the left shows half of the centre of a +1 disclination in the Col phase of single-tapered mesogens or of an ordinary small discotic mesogen. Such columns can be highly bendable, and circles of radius r down to the size of a single molecule have been

observed by high-resolution atomic force microscopy [59]. But in the case of Col₁₊₃ where neighbouring columns, in this case the major and minor columns, are connected by covalent linkers, the outer circle with larger circumference is still restricted to containing the same number of mesogens as the inner circle. Consequently the relative distortion in intermolecular spacing in two successive circular columns is $\Delta c/c = d/r$, where d is the width of the column. Only for sufficiently large r will the relative distortion be small enough for the cumulative energy of all distortions along the innermost loop of the $s = 1/2$ disclination to drop below the end energy of the bundle of straight but truncated columns in the middle (Inset 2 of Figure 6.3d).

This origin of column stiffness is distinct from the usual case of inflexible columns of large discotic mesogens, and it can be regarded as topological in nature; the Col₁₊₃ structure can thus be regarded as “topologically stiff”. One can draw a parallel with a similarly topological nature of high splay elastic constant K_1 in main-chain nematic polymers, which is primarily due not to the intrinsic rigidity of the chains, but to the scarcity of chain ends needed for insertion between diverging chains [60].

6.5 Conclusion

We have synthesised the first examples of double-tapered mesogens and obtained a new type of hexagonal columnar LC superlattice consisting of two kinds of columns, major and minor, in the ratio 1:3. The double-tapered anionic minidendrons are held together by Li, Na or Cs cations, the size of which strongly affects the number of molecules in the unit cell. Optical textures indicate surprisingly high columnar bending modulus, attributed here to topological resistance to curvature. Based on the structural model presented, we can propose ways to increase the stability of specific structures; e.g. an increase in linker length will further stabilize the Col₁₊₃ phase of Cs compounds. The

coexistence of ionic and non-ionic columns in an ordered superlattice points the way to creating novel materials with double functionality. Moreover, unlike other columnar LCs, this structure has zero lateral thermal expansivity, which is highly desirable in nanopatterning applications. We note that high dimensional stability has recently also been achieved in a honeycomb-type columnar LC, but this was based on a framework of in-plane lying rigid rod-like mesogens [61]. The present work is expected to lead to the design of further novel complex 2D columnar and 3D micellar soft alloy-like mesophases.

6.6 Supporting Information

6.6.1 Materials

Methyl 3,4,5-trihydroxybenzoate (methyl gallate, 98%), palladium on activated charcoal (10%) (all from Aldrich), benzyl bromide (98%), hydroquinone (99%), 1-bromododecane (98.5%), 1,10-dibromodecane (98%), phosphorus tribromide (99%), lithium aluminium hydride (97%), sodium hydride (60% dispersion in mineral oil) (all from Energy Chemical), all other chemicals or solvents were of analytical grade and were used as received. Silica gel (Sorbent Technology) was used as received. Dry DCM and dry THF were thoroughly washed with distilled water and freshly distilled from Na.

Abbreviations: DCM – dichloromethane; DMF – dimethylformamide; EtOAc – ethyl acetate; PE – petroleum ether (fraction 60-90); THF – tetrahydrofurane.

6.6.2 Analytical Techniques

^1H -NMR spectra and ^{13}C -NMR spectra were recorded on a Bruker Advance II DMX 400 spectrometer using CDCl_3 and $\text{d}_6\text{-DMSO}$ as solvents and TMS as internal standard.

Chemical shifts are reported as ppm. The purity of products was determined by a combination of techniques including thin-layer chromatography (TLC) on silica gel-coated aluminum plates and elemental analysis (Vario Micro cube from Elemental Analyses System). Mass spectrometry was done using a Bruker Reflex III MALDI-TOF instrument. The ICP optical emission spectrometer was a Spectro Ciros Vision with radial argon plasma and a circular optical detection system. IR spectra were recorded with a Perkin-Elmer Frontier FTIR instrument. The samples were melted on a CsI window and dried under vacuum at 40°C for 1 day. A second CsI window was placed over the sample as cover. The sandwich was then heated into the mesophase (50 - 60 °C) under vacuum to ensure uniform film thickness.

Optical micrographs with crossed polarizers were recorded using an Olympus BX-53 microscope equipped with Mettler HS82 hot stage.

6.6.3 DSC

Table S6.1. Phase transition temperatures of **1M** and **2M**

Compound	$T/ ^\circ\text{C}$ [$\Delta H/J \text{ g}^{-1}$]
1Li	↑ Cr ₁ -0.5 [2.2] Cr ₂ 44 [41] Col 107 [5.5] Iso ↓ 96 [2.9] Col -3.9 [7.6] Cr ₂ -8.6 [8.5] Cr ₁ ↑ -2.3 [8.7] Cr ₁ 4.9 [7.3] Col 110 [3.5] Iso
1Na	↑ Cr 45 [36] Col 87 [18] Iso ↓ 79 [1.5] Col 36 [1.6] Cr ₁ 16 [0.5] Cr ₂ -5.6 [20] Cr ₃ ↑ 2 [22] Cr ₂ 21 [0.2] Cr ₁ 42 [0.4] Col 88 [2.2] Iso
1Cs	↑ Cr 49 [34] Col 68 [12] Iso ↓ 44 [1.4] Col 30 [24] Cr ₁ -1.8 [8.4] Cr ₂ ↑ 2.2 [8.3] Cr ₁ 49 [17] Col 60/66 [3.7] Iso
2Li	↑ Cr ₁ 4.9 [16] Cr ₂ 58 [7.3] Col 98 [5.6] Iso ↓ 97 [2.1] Col 1.9 [18] Cr ↑ 5.6 [20] Col 107 [2.9] Iso
2Na	↑ Cr 44 [33] Col 96 [11] Iso ↓ 88 [1.7] Col 28 [7.9] Cr ₁ -1.0 [13] Cr ₂ ↑ 15 [6.8] Cr ₁ 41 [7.1] Col 96 [2.6] Iso
2Cs	↑ Cr ₁ 4.9 [16] Cr ₂ 58 [7.3] Col 98 [5.6] Iso ↓ 57 [1.5] Col 0.3 [18] Cr ↑ 4.3 [18] Col 54/69 [3.2] Iso

Thermal transitions of samples were measured on a TA Instruments Q2000 and Mettler Toledo differential scanning calorimeter. The samples were dried *in vacuo* at room temperature for 1-2 days prior to the scan, and the DSC cell was flushed with dry nitrogen. First order transition temperatures were reported as the maxima and minima of their endothermic and exothermic peaks, corrected for thermal lag determined from the ascending slope of indium melting endotherm at the appropriate heating rate. Indium was also used for calibration of heat flow.

6.6.4 X-ray Diffraction

Powder small/wide-angle X-ray Scattering (SAXS/WAXS) experiments were carried out at station I22 of Diamond Light Source with 12.4 keV X-rays using a Pilatus 2M detector (Dectris). The samples were kept in 1 mm capillaries held in a modified Linkam hot stage. As with the DSC measurements, the samples for X-rays were also dried *in vacuo* at room temperature for 1-2 days prior to the experiment. Immediately on transferring them to the capillaries, the capillaries were evacuated on a vacuum line and sealed. Electron density maps were calculated by inverse Fourier transformation using the standard procedure as described in International Tables for Crystallography. Grazing incidence SAXS/WAXS (GISAXS/GIWAXS) experiments were carried out at station I16 of Diamond Light Source, equipped with a multi-circle Huber goniometer and also using a Pilatus 2M detector. Thin films were prepared from the melt on a silicon wafer.

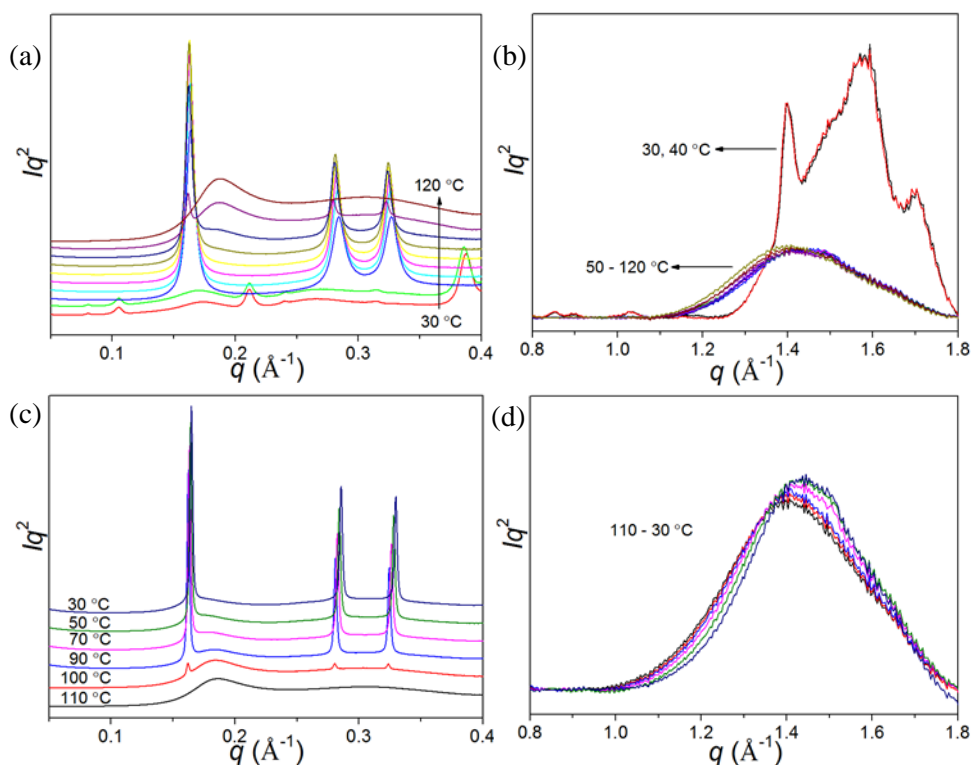


Figure S6.1. SAXS and WAXS (a, b) 1st heating (every 10 °C) and (c, d) cooling scans of **1Li**. In the 1st heating, the sample transformed from crystal to hexagonal columnar phase and then to isotropic liquid. On cooling, the sample transformed from Iso liquid to the hexagonal columnar phase.

Table S6.2. *d*-spacings of **1Li** at different temperatures.

1 st heating	<i>d</i> (Å)			cooling	<i>d</i> (Å)		
T (°C)	(10)	(11)	(20)	T (°C)	(10)	(11)	(20)
50	38.3	22.1	19.2	90	38.8	22.4	19.4
60	38.5	22.2	19.3	70	38.8	22.4	19.4
70	38.5	22.2	19.3	50	38.5	22.2	19.3
80	38.5	22.3	19.3	30	38.3	22.1	19.2
90	38.5	22.3	19.4				
80	38.8	22.4	19.5				

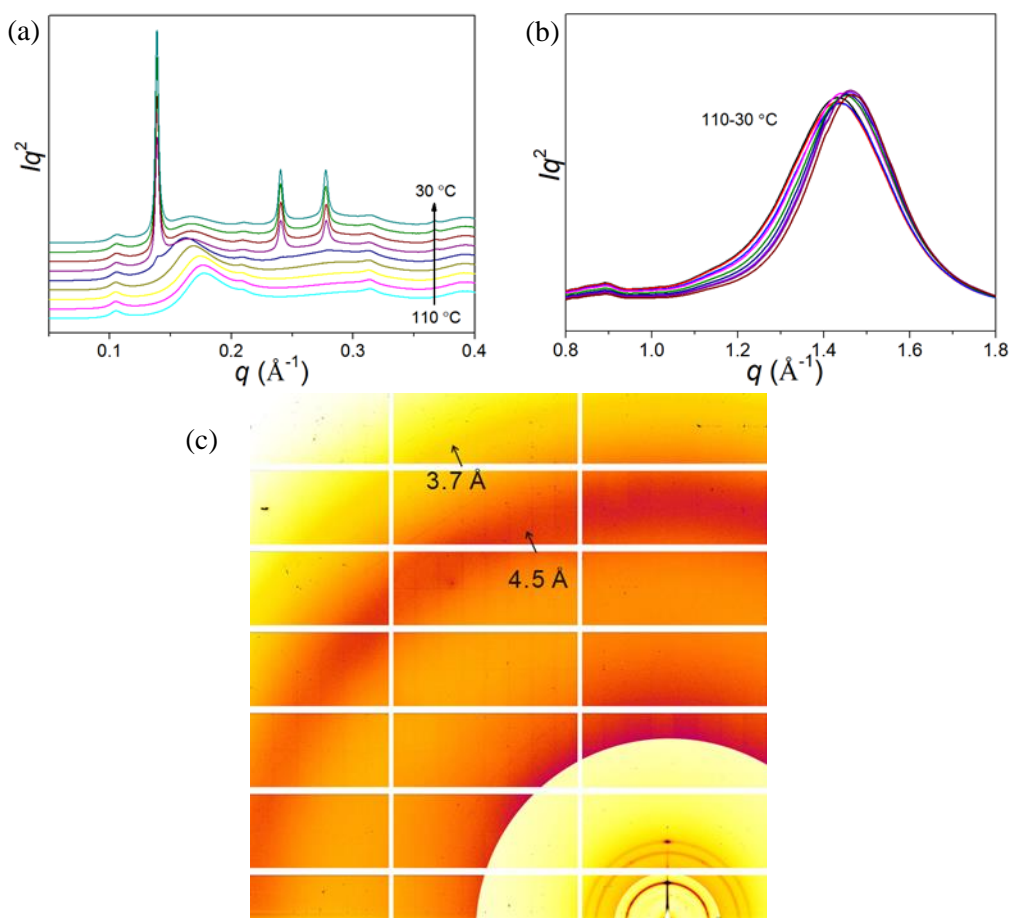
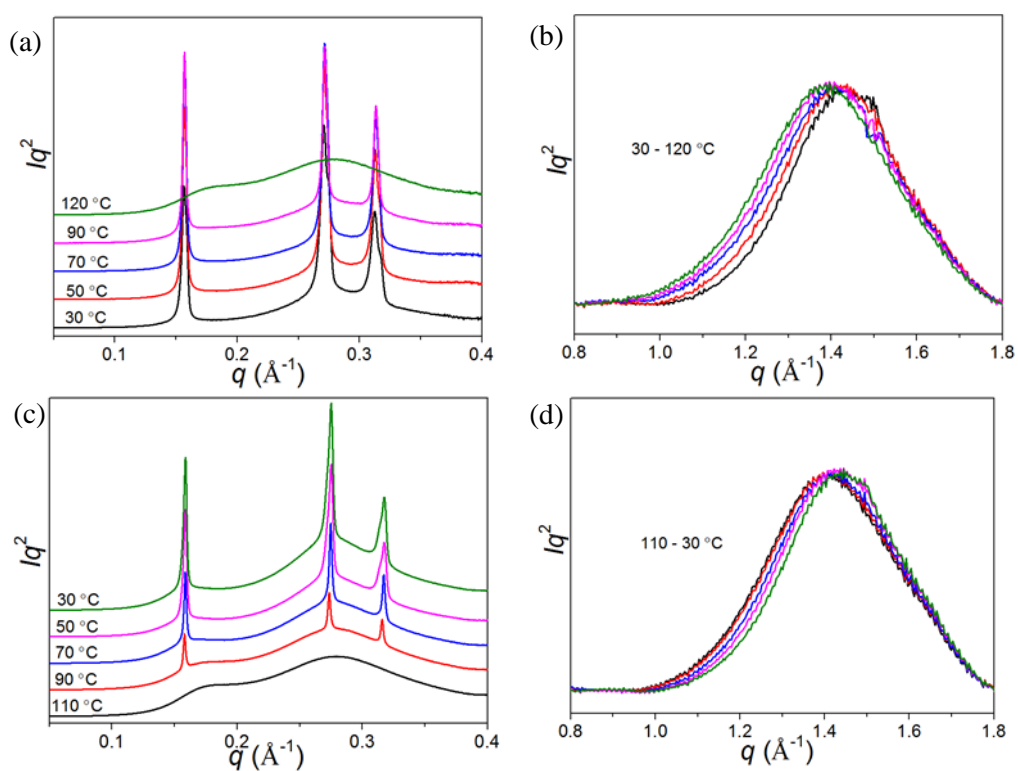


Figure S6.2. (a) SAXS and (b) WAXS 1st cooling scans of **1Na**; (c) GISAXS/GIWAXS pattern of **1Na** examined at 50 °C (sample cooled from isotropic phase)

Table S6.3. *d*-spacings of **1Na** at different temperatures

cooling	<i>d</i> (Å)		
T (°C)	(10)	(11)	(20)
60	45.2	26.2	22.6
50	45.2	26.2	22.6
40	45.2	26.2	22.6
30	45.2	26.2	22.6

Figure S6.3. Powder SAXS and WAXS (a, b) 2nd heating and (c, d) cooling scans of **2Li**.Table S6.4. *d*-spacings of **2Li** at different temperatures

2 nd heating		<i>d</i> (Å)			cooling		<i>d</i> (Å)		
T (°C)		(10)	(11)	(20)	T (°C)	(10)	(11)	(20)	
30		40.1	23.2	20.1	90	39.8	23.0	19.9	
50		40.1	23.1	20.1	70	39.6	22.9	19.8	
70		40.0	23.2	20.0	50	39.6	22.8	19.8	
90		40.0	23.1	20.1	30	39.6	22.8	19.8	

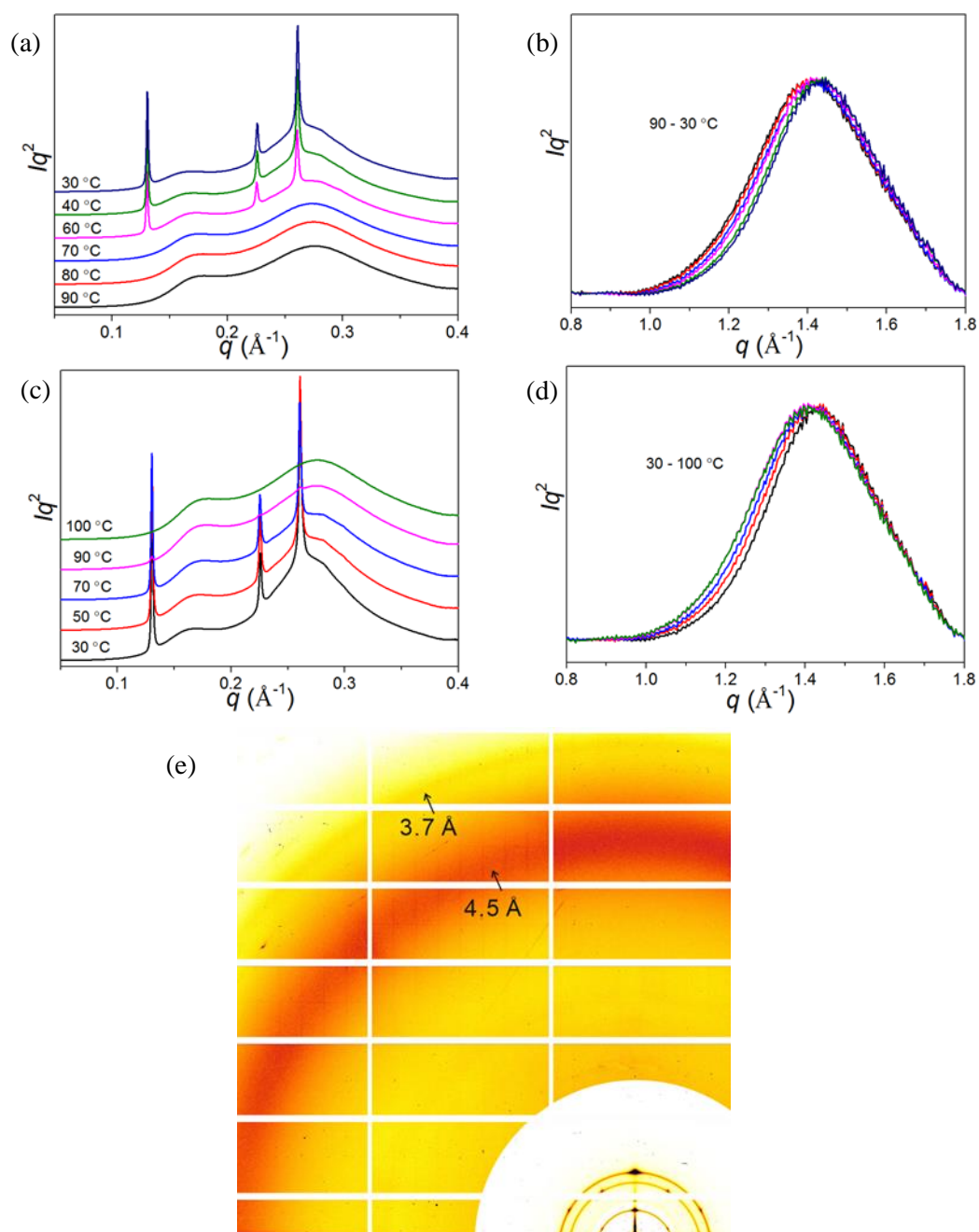


Figure S6.4. Powder SAXS and WAXS 1st cooling (a, b) and 2nd heating (c, d) scans of **2Na**; (e) GISAXS/GIWAXS pattern of **2Na** recorded at 60 °C (cooled from isotropic temperature).

Table S6.5. d -spacings of **2Na** at different temperatures

cooling		d (Å)			2 nd heating		d (Å)		
T (°C)		(10)	(11)	(20)	T (°C)	(10)	(11)	(20)	
60		48.3	27.9	24.2	30	48.1	27.8	24.1	
40		48.3	27.8	24.1	50	48.3	27.8	24.2	
30		48.1	27.8	24.1	70	48.3	27.9	24.2	

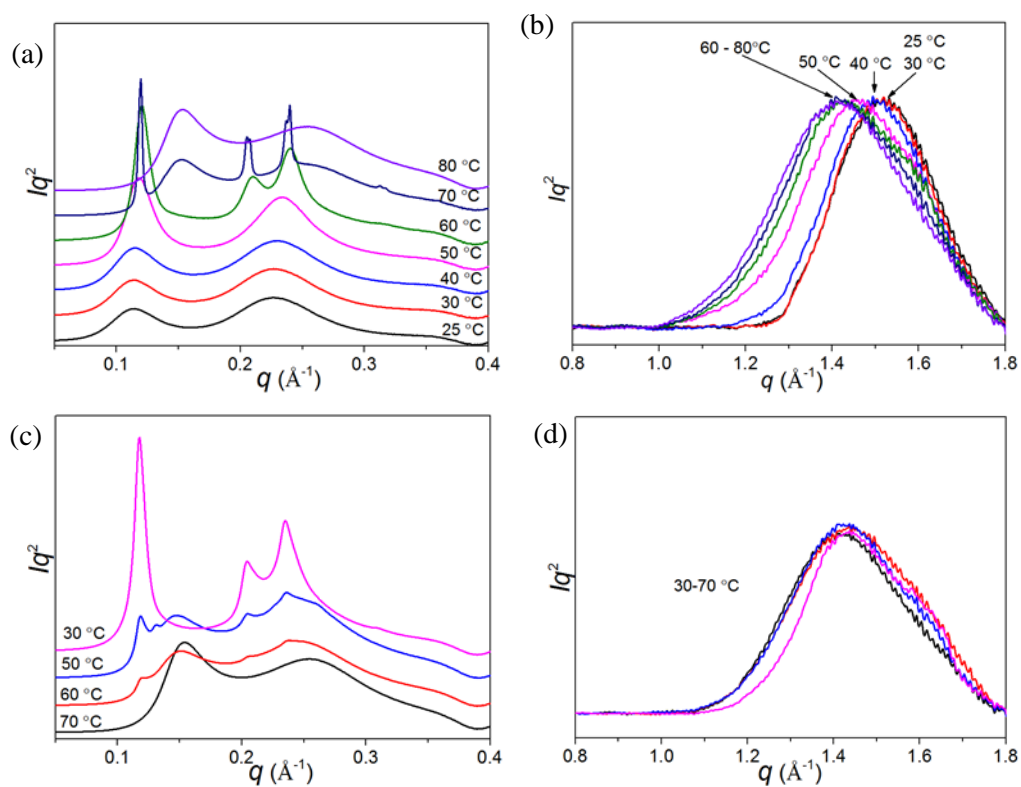
Figure S6.5. SAXS and WAXS 1st heating (a, b) and cooling (c, d) scans of **2Cs**.

Table S6.6. Miller indices, experimental and calculated d -spacings, intensities, phases and lattice parameter of **1M** and **2M**. All intensity values are Lorentz and multiplicity corrected.

Compound (temperature)	(hk)	d -spacing (Å) experimental	d -spacing (Å) calculated	Intensity	Phase
1Li (30 °C)	(10)	381	38.1	44.4	0
	(11)	22.0	22.0	29.2	π
	(20)	19.1	19.1	26.3	0
	$a = 44.0 \text{ \AA}$				
1Na (30 °C)	(10)	45.2	45.2	58.8	0
	(11)	26.1	26.1	19.6	π
	(20)	22.6	22.6	18.6	0
	$a = 52.2 \text{ \AA}$				
1Cs (50 °C)	(10)	51.9	51.8	71.7	0
	(11)	29.9	29.9	18.2	π
	(20)	25.9	25.9	10.0	0
	$a = 59.8 \text{ \AA}$				
2Li (30 °C)	(10)	4.01	4.01	24.9	0
	(11)	2.32	2.32	48.9	π
	(20)	2.01	2.01	26.3	0
	$a = 46.4 \text{ \AA}$				
2Na (30 °C)	(10)	48.1	48.1	31.9	0
	(11)	27.8	27.8	15.0	π
	(20)	24.1	24.1	53.0	0
	$a = 55.6 \text{ \AA}$				
2Cs (30 °C)	(10)	53.5	53.5	65.9	0
	(11)	30.8	30.8	11.7	π
	(20)	26.8	26.8	20.3	0
	$a = 61.8 \text{ \AA}$				

Table S6.7. Calculation of number of molecules in a unit cell

Compound	a (Å)	c (Å)	V_{cell} (Å ³ ·10 ²) ^a	V_{mol} (Å ³ ·10 ²) ^b	n_{Cr}^c	n_{liq}^d	μ^e
1Li	44.0	4.2 ^f	70.4	20.86	3.4	2.6	3.0
1Na	52.2	3.7 ^f	87.3	20.87	4.2	3.3	3.8
1Cs	59.8	4.5 ^f	139.4	20.92	6.7	5.2	6.0
2Li	46.4	4.0	74.2	22.05	3.4	2.6	3.0
2Na	55.6	3.7 ^f	99.1	22.06	4.5	3.5	4.0
2Cs	61.8	4.5	148.8	22.11	6.7	5.3	6.0

- a: $V_{\text{cell}} = a^2 c \sin 60^\circ$;
- b: Volume of molecule (V_{mol}) = volume for a single molecule as calculated using the crystal volume increments [62]^{Error! Reference source not found.} and the volume of Na^+ , Li^+ and Cs^+ is calculated by the cube of ionic radius;
- c: Number of molecules in crystal $n_{\text{Cr}} = V_{\text{cell}} / V_{\text{mol}}$;
- d: $n_{\text{liq}} = 0.55/0.7 * n_{\text{Cr}}$ (average packing coefficient in the crystal and liquid is 0.7 and 0.55, respectively);
- e: $\mu = (n_{\text{Cr}} + n_{\text{liq}})/2$.
- f: d -spacings determined from GIWAXS.

6.6.5 Molecular Simulation

Molecular models were built using Materials Studio (Accelrys). Geometry optimization and molecular dynamic simulation were performed using the Forcite Plus module with Universal Force Field. The experimental value for the a -parameter and the value for c from Table S6.7 were used. The convergence tolerances for geometry optimization were 0.001 kcal/mol for energy and 0.5 kcal/mol/Å for force. NVT annealing dynamics was performed through 30 cycles between 300 and 600 K with a total annealing time of 30 ps.

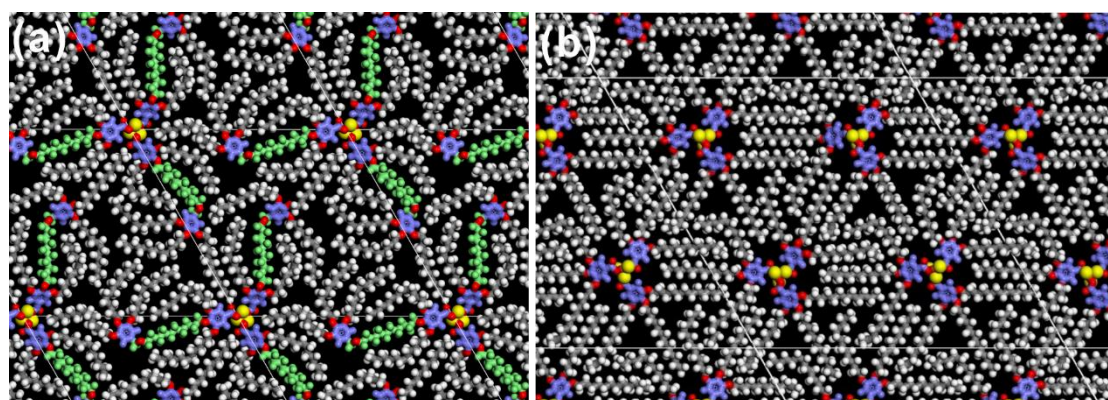


Figure S6.6. Snapshots of molecular models of compounds (a) **1Li** and (b) **12-12-12Li** in 2*2 supercell after NVT molecular dynamics heat-cool annealing cycles with a total duration of 30 ps. For clarity benzoate and benzylether groups are purple, cations are yellow, and the linker chains are green. All atoms are ball-and-stick except cations which are CPK with true ionic radii.

Acknowledgements

This work was supported by the National Natural Science Foundation of China, Grants 21772178 and 21674099, by EPSRC (UK), grant EP_P002250, and by CNCS - UEFISCDI (Romania), project PN-III-P4-ID-PCE-20160720 within PNCDI-III. Y.X. L. thanks CSC for stipend and University of Sheffield for waiving tuition fees. For help with synchrotron experiments we thank Prof. N. Terrill and Dr. O. Shebanova, beamline I22, and Dr. Gareth Nisbet, beamline I16 at Diamond Light Source.

References

- [1] S. Chandrasekhar, B. K. Sadashiva, K. A. Suresh, Liquid crystals of disc-like molecules, *Pramana*, **9** (1977) 471–480.
- [2] F. Vera, J. L. Serrano, T. Sierra, Twists in mesomorphic columnar supramolecular assemblies, *Chem. Soc. Rev.*, **38** (2009) 781-796.
- [3] H. Detert, M. Lehmann, H. Meier, *Materials*, **3** (2010) 3218-3330.
- [4] K. V. Le, H. Takezoe, F. Araoka, Chiral Superstructure Mesophases of Achiral Bent-Shaped Molecules–Hierarchical Chirality Amplification and Physical Properties, *Adv. Mater.*, **29** (2017) 1602737.
- [5] Malthéte, J.; Collet, A., Inversion of the cyclotribenzylene cone in a columnar mesophase: a potential way to ferroelectric materials, *J. Am. Chem. Soc.*, **109** (1987) 7544-7545.
- [6] C. Roche, H.-J. Sun, M. Prendergast, P. Leowanawat, B. Partridge, P. A. Heiney, F. Araoka, R. Graf, H. W. Spiess, X.B. Zeng, G. Ungar, V. Percec, Homochiral columns constructed by chiral self-sorting during supramolecular helical organization of hat-shaped molecules, *J. Am. Chem. Soc.*, **136** (2014) 7169–7185.
- [7] M. A. Shcherbina, X.Zeng, T. Tadjiev, G.Ungar, S.H.Eichhorn, K. E. S.Phillips, T.J. Katz, Hollow Six-Stranded Helical Columns of a Helicene, *Angew. Chem. Int. Ed.*, **48** (2009) 7837-7840.
- [8] T. Ghosh, M. Lehmann, Recent advances in heterocycle-based metal-free calamitics, *J. Mater. Chem. C*, **5** (2017) 12308-12337.
- [9] C. Tschierske, C. Nürnberger, H. Ebert, B. Glettner, M. Prehm, F. Liu, X. B. Zeng and G. Ungar, Complex tiling patterns in liquid crystals, *Interface Focus*, **2** (2011) 669–680.
- [10] J. Barbera, L. Puig, P. Romero J. L. Serrano, T. Sierra, Propeller-like hydrogen-

bonded Banana– Melamine complexes inducing helical supramolecular organizations, *J. Am. Chem. Soc.*, **128** (2006) 4487–4492.

[11] A. Das, S. Ghosh, Supramolecular assemblies by charge-transfer interactions between donor and acceptor chromophores, *Angew. Chem. Int. Ed.*, **53** (2014) 2038 – 2054.

[12] K. Tanabe, Y. Suzui, M. Hasegawa, T. Kato, Full-color tunable photoluminescent ionic liquid crystals based on tripodal pyridinium, pyrimidinium, and quinolinium salts, *J. Am. Chem. Soc.*, **134** (2012) 5652–5661.

[13] F. Morale, R. L. Finn, S. R. Collinson, A. J. Blake, C. Wilson, D. W. Bruce, D. Guillon, B. Donnio, M. Schroder, Metal-directed columnar phase formation in tetrahedral zinc (II) and manganese (II) metallomesogens, *J. Chem.*, **32** (2008) 297-305.

[14] B. M. Rosen, C. J. Wilson, D. A. Wilson, M. Peterca, M. R. Imam, V. Percec, Dendron-Mediated Self-Assembly, Disassembly, and Self-Organization of Complex Systems, *Chem. Rev.*, **109** (2009) 6275-6540.

[15] S. Hecht, J. M. Frechet, Dendritic Encapsulation of Function: Applying Nature's Site Isolation Principle from Biomimetics to Materials Science, *Angew. Chem. Int. Ed.* **40** (2001) 74–91.

[16] B. Donnio, S. Buathong, I. Bury, D. Guillon, Liquid crystalline dendrimers, *Chem. Soc. Rev.* **36** (2007) 1495–1513.

[17] C. Tschierske, Complexity by Liquid-Crystal Self-assembly, *Angew. Chem. Int. Ed.* **52** (2013) 8828-8878.

[18] T. Kato, N. Mizoshita, K. Kishimoto, Functional liquid-crystalline assemblies: Self-organized soft materials, *Angew. Chem., Int. Ed.*, **45** (2006) 38–68.

[19] H. J. Sun, S. D. Zhang, V. Percec, From structure to function via complex supramolecular dendrimer systems, *Chem. Soc. Rev.*, **44** (2015) 3900-3923.

[20] F. Würthner, C. Thalacker, S. Diele, C. Tschierske, Fluorescent J-type aggregates and thermotropic columnar mesophases of perylene bisimide dyes, *Chem. Eur. J.*, **7** (2001) 2245-2253.

[21] Z. Z. An, J. S. Yu, B. Domercq, S. C. Jones, S. Barlow, B. Kippelen, S. R. Marder, Marder, S. R. Room-temperature discotic liquid-crystalline coronene diimides exhibiting high charge-carrier mobility in air, *J. Mater. Chem.* **19** (2009) 6688-6698.

[22] G. Ungar, S.V. Batty, V. Percec, J. Heck, G. Johansson, Structure and conductivity of liquid crystal channel-like linic complexes of taper-shaped compounds, *Adv. Mater. Opt. Electro.* **4** (1994) 303–313.

[23] T. Ichikawa, M. Yoshio, A. Hamasaki, T. Mukai, H. Ohno, T. Kato, Self-organization of room-temperature ionic liquids exhibiting liquid-crystalline bicontinuous cubic phases: Formation of nano-ion channel networks, *J. Am. Chem. Soc.*, **129** (2007), 10662–10663.

- [24] M. Peterca, V. Percec, A. E. Dulcey, S. Nummelin, S. Korey, M. Ilies, P. A. Heiney, Self-assembly, structural, and retrostructural analysis of dendritic dipeptide pores undergoing reversible circular to elliptical shape change, *J. Am. Chem. Soc.*, **128** (2006) 6713–6720.
- [25] C. S. Pecinovsky, E. S. Hatakeyama, D. L. Gin, Polymerizable Photochromic Macrocyclic Metallomesogens: Design of Supramolecular Polymers with Responsive Nanopores, *Adv. Mater.*, **20** (2008) 174–178.
- [26] B. Soberats, M. Yoshio, T. Ichikawa, X. B. Zeng, S. Taguchi, H. Ohno, F. Liu, G. Ungar, T. Kato, Ionic Switch Induced by a Rectangular–Hexagonal Phase Transition in Benzenammonium Columnar Liquid Crystals, *J. Am. Chem. Soc.*, **137** (2015) 13212–13215.
- [27] G. Johansson, V. Percec, G. Ungar, D. Abramic, Molecular recognition directed self-assembly of tubular liquid crystalline and crystalline supramolecular architectures from taper shaped (15-crown-5)methyl 3,4,5-tris(p-alkyloxybenzyloxy)benzoates and (15-crown-5)methyl 3,4,5-tris(p-dodecyloxy)benzoate, *J. Chem. Soc., Perkin Trans. 1*, (1994) 447-459.
- [28] A. Schultz, S. Laschat, A. Saipa, F. Gießelmann, M. Nimtz, J. L. Schulte, A. Baro, B. Miehl, Columnar Liquid Crystals with a Central Crown Ether Unit, *Adv. Funct. Mater.*, **14** (2004) 163-168.
- [29] V. Percec, M. Glodde, T. K. Bera, Y. Miura, I. Shiyanovskaya, K. D. Singer, V. S. K. Balagurusamy, P. A. Heiney, I. Schnell, A. Rapp, H.-W. Spiess, S. D. Hudson, H. Duan, Self-organization of supramolecular helical dendrimers into complex electronic materials, *Nature*, **419** (2002) 384-387.
- [30] T. T. Steckler, X. Zhang, J. Hwang, R. Honeyager, S. Ohira, X. H. Zhang, A. Grant, S. Ellinger, S. A. Odom, D. Sweat, D. B. Tanner, A. G. Rinzler, S. Barlow, J. L. Bredas, B. Kippelen, S. R. Marder, J. R. Reynolds, Spray-Processable, Low Bandgap, and Ambipolar Donor–Acceptor Conjugated Polymer, *J. Am. Chem. Soc.*, **131** (2009) 2824-2826.
- [31] D. J. P. Yeardley, G. Ungar, V. Percec, N. M. Holerca, G. Johansson, Supramolecular Minidendrimers Self-Organized in an “Inverse Micellar”-like Thermotropic Body-Centered Cubic Liquid Crystalline Phase, *J. Am. Chem. Soc.*, **122** (2000) 1684-1689.
- [32] Y. Tsuda, R. Kuwahara, J. -M. Oh, Polyimides having dendron side chains, *Trans. Mater. Res. Soc. Jpn.*, **29** (2004), 267-271.
- [33] A. Grotzky, E. Atamura, J. Adamcik, P. Carrara, P. Stano, F. Mavelli, T. Nauser, R. Mezzenga, A. D. Schluter, Structure and Enzymatic Properties of Molecular Dendronized Polymer–Enzyme Conjugates and Their Entrapment inside Giant Vesicles, *Langmuir*, **29** (2013) 10831-10840.
- [34] V. Percec, A. E. Dulcey, M. Peterca, P. Adelman, R. Samant, V. S. K. Balagurusamy, P. A. Heiney, Helical Pores Self-Assembled from Homochiral

Dendritic Dipeptides Based on l-Tyr and Nonpolar α -Amino Acids, *J. Am. Chem. Soc.*, **129** (2007) 5992-6002.

[35] B. Donnio, P. Garcia-Vazquez, J. -L. Gallani, D. Guillon, E. Terazzi, Dendronized Ferromagnetic Gold Nanoparticles Self-Organized in a Thermotropic Cubic Phase, *Adv. Mater.*, **19** (2007) 3534-3539.

[36] K. Kanie, M. Matsubara, X. B. Zeng, F. Liu, G. Ungar, H. Nakamura, A. Muramatsu, A. Simple Cubic Packing of Gold Nanoparticles through Rational Design of Their Dendrimeric Corona, *J. Am. Chem. Soc.*, **134** (2012) 808-811.

[37] X. Feng, M. E. Tousley, M. G. Cowan, B. R. Wiesenauer, S. Nejati, Y. Choo, R. D. Noble, M. Elimelech, D. L. Gin, C. O. Osuji, Scalable Fabrication of Polymer Membranes with Vertically Aligned 1 nm Pores by Magnetic Field Directed Self-Assembly, *ACS Nano*, **8** (2014) 11977–11986.

[38] S. Zhang, H. -J. Sun, A. D. Hughes, R. O. Moussodia, A. Bertin, Y. Chen, D. J. Pochan, P. A. Heiney, M. L. Klein, V. Percec, Self-assembly of amphiphilic Janus dendrimers into uniform onion-like dendrimersomes with predictable size and number of bilayers, *Proc. Natl. Acad. Sci. U. S. A.*, **111** (2014) 9058–9063.

[39] B. P. Hoag, D. L. Gin, Polymerizable hexacatenar liquid crystals containing a luminescent oligo(p-phenylenevinylene) core, *Liq. Cryst.*, **31** (2004) 185-199.

[40] G. Ungar, F. Liu, X. B. Zeng, *Handbook of Liquid Crystals*, Vol. 5 (Eds.: J. W. Goodby, P. J. Collings, T. Kato, C. Tschierske, H. F. Gleeson, P. Raynes), VCH_Wiley, Weinheim, 2nd Ed., 2014, pp. 363-436.

[41] D. R. Dukeson, G. Ungar, V. S. K. Balagurusamy, V. Percec, G. Johansson, M. Glodde, Application of Isomorphous Replacement in Structure Determination of a Cubic Liquid Crystal Phase and Location of Counterions, *J. Am. Chem. Soc.*, **125** (2003) 15974-15980.

[42] D. J. P. Yeardley, G. Ungar, V. Percec, N. M. Holerca, G. Johansson, Spherical supramolecular minidendrons self-organised in an “inverse micellar”-like thermotropic body centred cubic liquid crystal phase, *J. Am. Chem. Soc.*, **122** (2000), 1684-1689.

[43] X. H. Yao, L. Cseh, X. B. Zeng, M. Xue, Y. S. Liu, G. Ungar, Body-centred cubic packing of spheres – the ultimate thermotropic assembly mode for highly divergent dendrons, *Nanoscale Horiz.*, **2** (2017) 43-49.

[44] A. C. Ribeiro, B. Heinrich, C. Cruz, H. T. Nguyen, S. Diele, M. W. Schroeder, D. Guillon, Rectangular to hexagonal columnar phase transition exhibited by a biforked mesogen, *Eur. Phys. J. E*, **10** (2003) 143–151.

[45] V. Percec, C. M. Mitchell, W. -D. Cho, S. Uchida, M. Glodde, G. Ungar, X. B. Zeng, Y. Liu, V. S. K. Balagurusamy, P. A. Heiney, Designing Libraries of First Generation AB₃ and AB₂ Self-Assembling Dendrons via the Primary Structure Generated from Combinations of (AB)_y-AB₃ and (AB)_y-AB₂ Building Blocks, *J. Am. Chem. Soc.*, **126** (2004) 6078-6094.

[46] V. Percec, M. N. Holerca, S. Uchida, W. D. Cho, G. Ungar, Y. S. Liu, D. J. P.

Yeardeley, Exploring and Expanding the Three-Dimensional Structural Diversity of Supramolecular Dendrimers with the Aid of Libraries of Alkali Metals of Their AB₃ Minidendritic Carboxylates, *Chem. Eur. J.*, **8** (2002) 1106-1117.

[47] T. Woehrle, I. Wurzbach, J. Kirres, A. Kostidou, N. Kapernaum, J. Litterscheidt, J. C. Haenle, P. Staffeld, A. Baro, F. Giesselmann, S. Laschat, Discotic Liquid Crystals, *Chem. Rev.*, **116** (2016) 1139–1241.

[48] G. Ungar, D. Abramic, V. Percec, J. Heck, Self-assembly of twin tapered bisamides into supramolecular columns exhibiting hexagonal columnar mesophases. Structural evidence for a microsegregated model of the supramolecular column, *Liq. Cryst.* **21** (1996) 73-86.

[49] M. A. Shcherbina, X. B. Zeng, T. Tadjiev, G. Ungar, S. H. Eichhorn, K. E. S. Phillips, T. J. Katz, Six-Stranded Hollow Helical Supramolecular Structure of a Columnar Heterohelicene, *Angew. Chem. Int. Ed.*, **48** (2009) 7837-7840.

[50] B. M. Rosen, D. A. Wilson, C. J. Wilson, M. Peterca, B. C. Won, C. -H. Huang, L. R. Lipski, X. B. Zeng, G. Ungar, P. A. Heiney, V. Percec, Predicting the Structure of Supramolecular Dendrimers via the Analysis of Libraries of AB₃ and Constitutional Isomeric AB₂ Biphenylpropyl Ether Self-Assembling Dendrons, *J. Am. Chem. Soc.*, **131** (2009) 17500–17521.

[51] M. Peterca, M. R. Imam, P. Leowanawat, B. M. Rosen, D. A. Wilson, C. J. Wilson, X. B. Zeng, G. Ungar, P. A. Heiney, V. Percec, Self-Assembly of Hybrid Dendrons into Doubly-Segregated Supramolecular Polyhedral Columns and Vesicles, *J. Am. Chem. Soc.*, **132** (2010) 11288–11305.

[52] M. Kleman, Developable domains in hexagonal liquid crystals, *J. Physique*, **41**(1980) 737-745.

[53] M.-H. Yen, J. Chairapa, X. B. Zeng, Y. Liu, L. Cseh, G. H. Mehl, G. Ungar, Added Alkane Allows Thermal Thinning of Supramolecular Columns by Forming Superlattice - An X-ray and Neutron Study, *J. Am. Chem. Soc.*, **138** (2016) 5757–5760.

[54] G. Ungar, V. Percec, M. N. Holerca, G. Johansson, J. A. Heck, Heat-shrinking spherical and columnar self-assemblies, their interconversion and dependence on molecular taper angle, *Chem. Eur. J.*, **6** (2000) 1258-1266.

[55] W. S. Fall, M. H. Yen, X. B. Zeng, L. Cseh, Y. S. Liu, G. A. Gehring, G. Ungar, Quantised Molecular Ejection Transition in Liquid Crystal Columns Self-Assembled from Wedge-Shaped Minidendrons, *Soft Matter*, **15** (2019) 22 – 29.

[56] X. Feng, S. Nejati, M. G. Cowan, M. E. Tousley, B. R. Wiesenauer, R. D. Noble, M. Elimelech, D. L. Gin, C. O. Osuji, Thin Polymer Films with Continuous Vertically Aligned 1 nm Pores Fabricated by Soft Confinement, *ACS Nano*, **10** (2016) 150–158.

[57] U. Beginn, L. Yan, S. N. Chvalun, M. Shcherbina, A. V. Bakirov, M. Möller, Thermotropic columnar mesophases of wedge-shaped benzenesulfonic acid mesogens, *Liq. Cryst.*, **35** (2008) 1073–1093.

[58] P. G. de Gennes, J. Prost, *Physics of Liquid Crystals*. 2nd Ed., Clarendon Press,

Oxford, 1993, pp: 98-155.

[59] (a) R. B. Zhang, X. B. Zeng, B. -S. Kim, R. Bushby, K. -S. Shin, P. Baker, V. Percec, G. Ungar, Columnar Liquid Crystals in Cylindrical Nano-Confinement, *ACS Nano.*, **9** (2015) 1759-1766; (b) R. B. Zhang, X. B. Zeng, C. Y. Wu, Q. Jin, Y. S. Liu, G. Ungar, Square and hexagonal columnar liquid crystals confined in square and triangular pores, *Adv. Funct. Mater.*, **29** (2019) 1806078.

[60] A. Popadić, D. Svenšek, R. Podgornik, K. C. Daoulas, M. Praprotnik, Splay–density coupling in semiflexible main-chain nematic polymers with hairpins, *Soft Matter.*, **14** (2018) 5898-5905.

[61] W. S. Fall, C. Nürnberger, X.B. Zeng, F. Liu, S. J. Kearney, G. A. Gehring, C. Tschierske, G. Ungar, An Ising transition of chessboard tilings in a honeycomb liquid crystal, *Mol. Syst. Des. Eng.*, **4** (2019) 396-406.

[62] A. Immirzi, B. Perini, Prediction of density in organic crystals, *Acta Crystallogr. A*, **33** (1977) 216-218.

Chapter 7 Published paper: Gyroid structured aqua-sheets with sub-nanometer thickness enabling 3D fast proton relay conduction

Chemical Science, 2019, 10, 6245-6253

Tsubasa Kobayashi,^a Ya-xin Li,^b Ayaka Ono,^a Xiang-bing Zeng,^b and Takahiro Ichikawa*

^a*Department of Biotechnology, Tokyo University of Agriculture and Technology, Nakacho, Koganei, Tokyo, 184-8588, Japan. E-mail: t-ichi@cc.tuat.ac.jp*

^b*Department of Materials Science and Engineering, University of Sheffield, Sheffield S1 3JD, UK*

^c*JST, PRESTO, 4-1-8 Honcho, Kawaguchi, Saitama, 332-0012, Japan*

This Chapter was published as an article in Chemical Science. I have carried out the experiments and data analysis by synchrotron X-ray diffraction experiments at Diamond Light Source, reconstruction of ED maps and the calculation of the densities, and written the corresponding parts in the article.

The article is reproduced in its Open Access under a CC BY-NC 3.0 license, with minor adaptations on the figures and section numbering. The details of the synthesis part in the supporting information are not included here and the references in the manuscript and supporting information have been combined for clarity.

7.1 Abstract

A polymerizable amphiphile having two zwitterionic head-groups has been designed. This compound coorganizes with an acid, bis(trifluoromethanesulfonyl)imide (HTf₂N), into a gyroid bicontinuous cubic liquid-crystalline phase. *In situ* polymerization of this phase has been successfully achieved by UV irradiation in the presence of a photoinitiator, yielding a self-standing gyroid-nanostructured polymer film. When the polymer film is placed under different relative humidity conditions or in water, it absorbs water owing to the strong hydration ability of the zwitterionic parts. It has been found that the polymer film preserves the gyroid nanostructure after the water absorption. Based on reconstructed electron density maps, it is assumed that the absorbed water molecules form a 3D continuous network along the gyroid minimal surface, which satisfies several key conditions for inducing fast proton conduction. As expected, such hydrated films show high ionic conductivities in the order of 10⁻¹ S cm⁻¹ when the water content of the film reaches 15.6 wt% at RH = 90%. The high conductivity is attributed to the induction of the Grotthuss mechanism, that is, proton conduction *via* the hydrogen-bonding network of the incorporated water molecules

7.2 Introduction

Proton conductive membranes are key materials that play a crucial role in developing a sustainable world because of their versatile utilities in fuel cells, bio-devices, sensors, catalysis, so robotics, and so on. Following the discovery of proton-conductive uoropolymers, e.g., Naflon,[1,2] a variety of proton-conductive membranes have been designed using aromatic polymers,[3-6] block-copolymers,[7] gels,[8] liquid crystals,[9-14] metal-organic frameworks,[15] and some hybrid materials.[16] It is

considered that an ideal proton-conductive membrane should have properties such as high ionic conductivity, high mechanical strength, extremely low fuel (H_2 gas or MeOH) permeability, and surface morphology forming effective interfaces with catalysts. For the realization of such ideal membranes, there have been intensive demands for the development of an innovative membrane design strategy. We expect that the construction of polymer membranes with 3D-continuous proton conductive pathways should be a promising approach and therefore focus on the matrix design based on a gyroid surface,[17] a type of infinite periodic minimal surface.

A gyroid bicontinuous cubic (Cub_{bi}) phase, consisting of two interpenetrating networks separated by a 3D infinite periodic minimal surface with the space group $Ia\bar{3}d$, is typically found in liquid crystals with a lattice parameter of several nanometers. [18-24] Despite its 3D continuous and periodic structure and hence potential for application, the number of studies on the application of Cub_{bi} liquid crystals is still limited.[25–39] There has been recent progress on our original molecular design principle for creating Cub_{bi} liquid crystals. In a representative system, we have employed amphiphilic zwitterions consisting of an organic cation and a sulfonate anion.[12,40–43] Owing to the ability of zwitterions to form adducts with suitably selected acids, it is possible to tune their self-organization behavior in order to form $Ia\bar{3}d$ -type (gyroid-type) Cub_{bi} liquid-crystalline (LC) assemblies by controlling the addition of acids. Since the Cub_{bi} structures formed by the combination of amphiphilic zwitter- ions and acids possess a hydrophilic gyroid minimal surface where their sulfonic acid groups align densely, they have been expected to be a potential matrix for proton conductive materials.

For the realization of fast proton conduction, one of the most general but advantageous approaches is to create hydrogen- bonding networks of water molecules in the matrices because water molecule networks enable fast transport of protons based on a bucket brigade conduction mechanism. This approach is effective for our Cub_{bi} LC systems to

some extent. [12] However, since the Cub_{bi} LC materials have fluidity, it is impossible to introduce a sufficient amount of water molecules into them while maintaining the LC nanostructures.[12,40,41] In general, conversion of fluidic LC materials to solid ones can be achieved by introducing polymerizable groups into LC molecules and subsequent *in situ* polymerization.[44-54] In the present study, we report the development of self-standing polymer films with a hydrophilic gyroid minimal surface *via in situ* polymerization of amphiphilic zwitterions. These polymer films can incorporate water molecules onto the gyroid minimal surface, forming a 3D continuous water network, which leads to the induction of high ionic conductivities in the order of $10^{-1} \text{ S cm}^{-1}$.

7.3 Results and discussion

We have designed a new gemini-type polymerizable amphiphile, **Diene-GZI** (Fig. 7.1a). Several unique features are incorporated into the molecular design which was inspired by several previous studies on amphiphilic liquid crystals.[12,40,47,55-59] One is that the new gemini monomer has zwitterionic head groups consisting of pyridinium cations and sulfonate anions.[12,40] A second is that two single-head/single-tail halves of this monomer are connected via a linker to create a gemini-type amphiphile. [55–59] A third is that polymerizable diene groups are introduced in between the zwitterionic head groups and the long alkyl chains.[47] The detailed synthesis steps are shown in the SI (Scheme S7.1†). The thermal behavior of pristine **Diene-GZI** was examined by polarized optical microscopy (POM), differential scanning calorimetry, and X-ray diffraction (XRD) measurements (see the SI†). It has been found that pristine **Diene-GZI** shows thermotropic LC behavior. Although it is difficult to identify the mesophase behavior because thermal polymerization of **Diene-**

GZI starts before isotropization on heating, it is assumed that **Diene-GZI** forms a layered smectic (Sm) phase through nanosegregation of the zwitterionic and ionophobic parts.

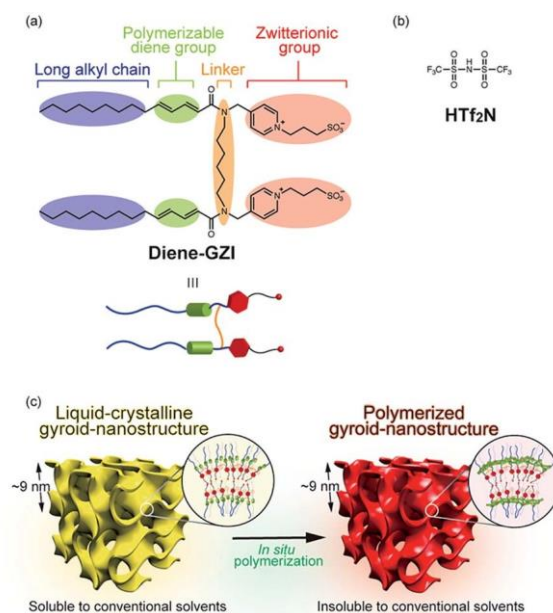


Fig. 7.1 Design strategy for creating a gyroid-nanostructured matrix. (a) Molecular structure of the polymerizable gemini-type amphiphile (**Diene-GZI**). (b) Molecular structure of HTf₂N. (c) Schematic illustration of our strategy for the preparation of a gyroid-nanostructured matrix. The gyroid-nanostructure formed by the self-organization of **Diene-GZI** has been fixed by *in situ* radical cross-linking polymerization.

It is of importance that the isotropization temperature and mesophase behavior of **Diene-GZI** can be tuned by adding some acid and water. By examining the amphotropic (lyotropic and thermotropic) LC behavior of the mixtures of **Diene-GZI**, acid and water, we have found that **Diene-GZI** self-organizes into Cub_{bi} phases in the presence of suitable amounts of an acid, bis(trifluoromethanesulfonyl)imide (HTf₂N, Fig. 7.1b), and water. For example, the mixture of **Diene-GZI**/HTf₂N/water (1.0/0.5/14 by mol) (**MX**) exhibits a Cub_{bi} phase at room temperature (Fig. 7.1c, left). The formation of the Cub_{bi} phase has been characterized by powder XRD measurement and

POM observation. The XRD pattern of **MX** shows two intense diffraction peaks in the small angle region and the reciprocal d -spacing ratio of the two peaks is $\sqrt{6} : \sqrt{8}$, which can be indexed as (211) and (220) reflections of an $Ia\bar{3}d$ -type (gyroid-type) Cub_{bi} structure having a lattice parameter a of 94.4 Å (Fig. 7.2a). No birefringence is observed for **MX** under POM observation (Fig. 7.2a, inset), which is also indicative of the formation of the Cub_{bi} nanostructure. Based on the insights into the molecular assemblies of the previously designed amphiphilic LC zwitterions, [12,40-43] it is most plausible to assume that the sulfonic acid groups of **Diene-GZI** align regularly on the gyroid minimal surface.

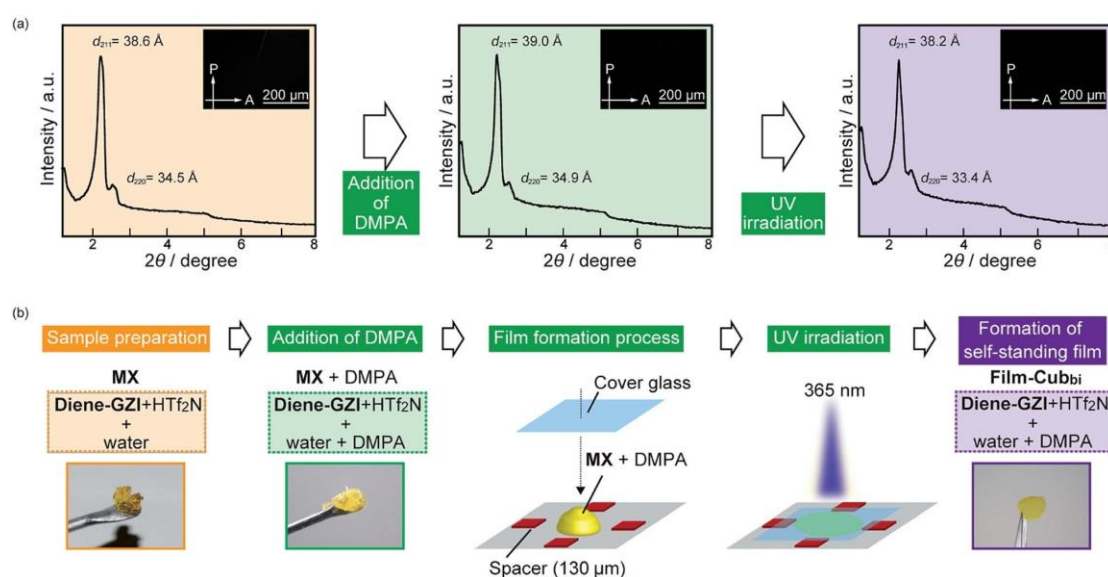


Fig. 7.2 Preparation procedure for **Film-Cub_{bi}** having a gyroid-nanostructure. (a) X-ray diffraction (XRD) patterns and polarized optical microscope (POM) textures of **MX** (background: yellow), **MX + DMPA** (background: green) and **Film-Cub_{bi}** (background: purple). There is little difference among the XRD patterns and POM textures, suggesting that **MX** changes into **Film-Cub_{bi}** while preserving the gyroid-nanostructure. (b) Key steps for converting **MX** to **Film-Cub_{bi}**. Photographs of **MX** and **MX + DMPA** are shown. They are viscous LC phases. After the film formation and UV irradiation steps, **MX + DMPA** turns into a self-standing polymer film (**Film-Cub_{bi}**).

We performed *in situ* polymerization of **MX** in the Cub_{bi} state. The detailed procedure is classified into 5 steps and is shown in Fig. 7.2b: step (I) preparation of **MX**; step (II) addition of 1 wt% of 2,2-dimethoxy-2-phenylacetophenone (DMPA) as a radical photopolymerization initiator; step (III) film formation of the fluidic LC sample on a Teflon substrate; step (IV) UV irradiation; step (V) removal of the film from the substrate. These 5 steps produced a self-standing polymer film (**Film-Cub_{bi}**). It is noteworthy that the polymerization has progressed while preserving the gyroid-nanostructure. This was confirmed by X-ray measurement and POM observation (Fig. 7.2a). By performing gravimetric analysis before and after the polymerization process, it was found that **Film-Cub_{bi}** contains less than 10 wt% water, while the water content in **MX** was 18.7 wt%. The difference in the water content before and after polymerization is attributed to water evaporation during the polymerization process.

To obtain further insight into the nanostructure in **Film-Cub_{bi}**, synchrotron XRD measurements were performed. By transforming the obtained diffraction patterns into scattered electron waves, we reconstructed the electron density map for **Film-Cub_{bi}** (Fig. S7.11 in the SI†). It was confirmed that the high electron density region forms a 3D-continuous domain along the gyroid minimal surface, which is occupied by the zwitterionic part, HTf_2N and water. On the other hand, the electron lower domains formed by the alkyl chains are observed in the center of 3D-branched nanochannels. The microscopic structure in **Film-Cub_{bi}** was investigated by scanning electron microscopy (SEM). Floor and cross-sectional views are shown in Fig. S7.8 in the SI.† It can be seen that **Film-Cub_{bi}** is a homogeneous polymer film with no micro-scale pores, suggesting that the polymerization proceeds homogeneously in the film.

Our aim in the present study is to develop a 3D continuous proton conducting pathway in the film by installing water molecules densely on the gyroid minimal surface. For the realization of this aim, we have examined the structure preserving ability of **Film-**

Cub_{bi} under various conditions. To examine the temperature dependence of the gyroid-nanostructure of **Film-Cub_{bi}**, we have carried out XRD measurements with varying temperatures from 30 to 180 °C on heating and 180 to 30 °C on cooling (Fig. 7.3a). It can be seen that little change of the XRD patterns occurs upon heating and cooling, indicating that **Film-Cub_{bi}** maintains the gyroid-nanostructure in the temperature range whereas the unpolymerized **MX** monomer mixture starts to lose the **Cub_{bi}** structure at around 35 °C (see Fig. S7.6 in the SI†). Focusing on the peak positions, we have found a slight shift of the positions with the increase/decrease of the temperature. For example, the (211) peak gradually shifts to the wide-angle region upon heating from $2\theta = 2.31^\circ$ at 30 °C to $2\theta = 2.36^\circ$ at 180 °C. From these values, the cubic lattice parameter “a” in **Film-Cub_{bi}** was calculated to be 93.5 Å at 30 °C and 91.7 Å at 180 °C (Fig. 7.3a), indicating a shrinkage of the lattice upon heating. This behavior is opposite to what would be expected due to thermal expansion. We assume that the shrinkage of the gyroid structure in **Film-Cub_{bi}** results from water drying out of the sample.

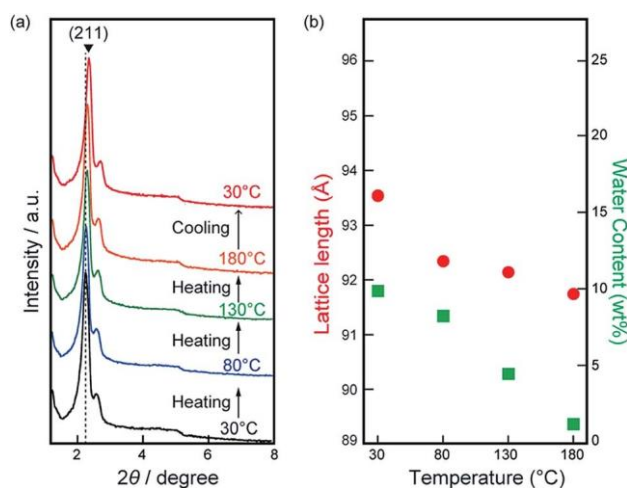


Fig. 7.3 Stability of the gyroid-nanostructure of **Film-Cub_{bi}** at various temperatures. (a) XRD patterns of **Film-Cub_{bi}** at various temperatures. (b) The cubic lattice lengths and water contents at each temperature are plotted.

To confirm this assumption, gravimetric analysis was performed on **Film-Cub_{bi}** before and after the heating process. A weight decrease in **Film-Cub_{bi}** was clearly observed as a function of the increasing temperature. Assuming that the weight decrease results from water drying out of the sample, we calculated the change of water content in **Film-Cub_{bi}**, and these values are plotted in Fig. 7.3b. It can be seen that the water content decreases from 9.9 wt% in the initial state to 1.2 wt% at 180 °C. We conclude that water evaporates from **Film-Cub_{bi}** on heating, which leads to weight loss accompanied by the slight shrinkage of the gyroid-nanostructure. On cooling, further shrinkage of the lattice from 91.7 to 89.6 Å was found when the sample was cooled from 180 to 30 °C, due to thermal contraction. The most notable point is that the gyroid-nanostructure in **Film-Cub_{bi}** is maintained in the water-drying process, suggesting that the mean positions of the zwitterionic amphiphiles are strongly fixed by cross-linking polymerization while they still have molecular fluctuations. We assume that the creation of the well-stabilized gyroid-nanostructure is attributed to the progress of many more cross-linking reactions that are attainable for gemini-type molecular structures but unattainable for single-head + single-tail ones. [48]

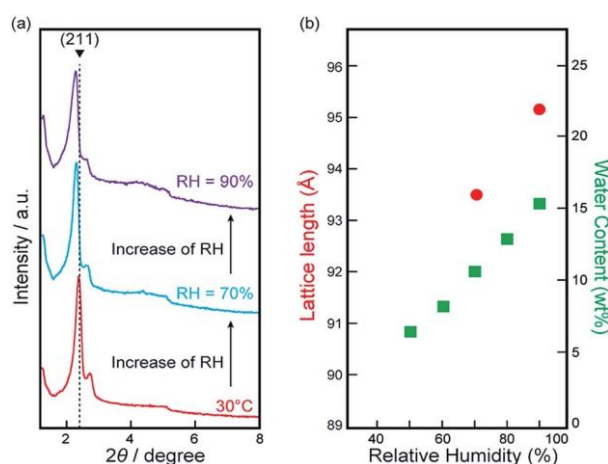


Fig. 7.4 Stability of the gyroid-nanostructure of **Film-Cub_{bi}** at various relative humidity (RH) values. (a) XRD patterns of **Film-Cub_{bi}** at various RH values. (b) The cubic lattice lengths and water contents at each RH are plotted.

The next question we addressed is whether it is possible to incorporate a sufficient amount of water molecules into **Film-Cub_{bi}** to form a 3D continuous hydrogen-bonding network of water molecules along a gyroid minimal surface. To help answer this question, we have prepared **Film-Cub_{bi}** and placed it under RH controlled conditions (RH = 50 to 90%) for 12 h in order to reach an equilibrium state where water absorption and evaporation proceed at the same speed. The water contents (X wt%) in the treated films were evaluated from the weight change and henceforth they are denoted as **Film-Cub_{bi}(X)**. It was found that the water content X increases from 6.7 wt% at RH = 50% to 15.6 wt% at RH = 90% (Fig. 7.4b). To confirm whether **Film-Cub_{bi}** maintains the gyroid structure or not during the water absorption and evaporation processes, XRD measurements have been performed for **Film-Cub_{bi}(X)**. Little difference in the shape of the XRD patterns was found for **Film-Cub_{bi}(X)** while a slight shift of the peak positions was observed (Fig. 7.4a). These results indicate that it is possible to introduce/remove water molecules into/from **Film-Cub_{bi}(X)** by controlling the RH without distorting the gyroid-nanostructure. In addition, there was no splitting of the (211) reflection peak upon water absorption, suggesting that the incorporated water molecules are homogeneously dispersed around the hydrophilic gyroid minimal surface in **Film-Cub_{bi}**.

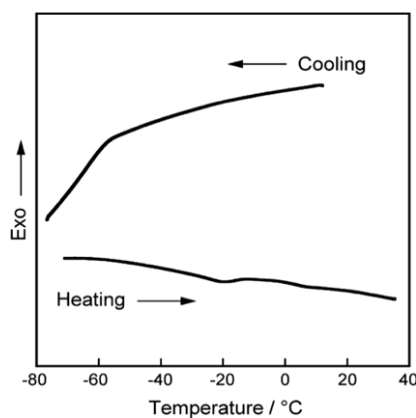


Fig. 7.5 DSC thermograms of **Film-Cub_{bi}(15.6)** on cooling and heating.

To obtain further insight into the position and state of the incorporated water molecules in the gyroid-nanostructures of **Film-Cub_{bi}(X)**, DSC measurement was performed for **Film-Cub_{bi}(15.6)**. No exothermic and endothermic peak is observed for **Film-Cub_{bi}(15.6)** at around 0 °C on cooling, indicating that almost all the water molecules in the film exist not as free water but as bound water (Fig. 7.5). The number of water molecules per sulfonate group in **Film-Cub_{bi}(15.6)** is calculated to be about 5.6. Taking into account the general knowledge that one sulfonic acid group has the ability to strongly interact with up to [8-14] water molecules, [60-62] it is plausible that the absorbed water molecules are placed exclusively on the gyroid minimal surface where the sulfonate/sulfonic-acid groups of **Diene-GZI** are aligned densely.

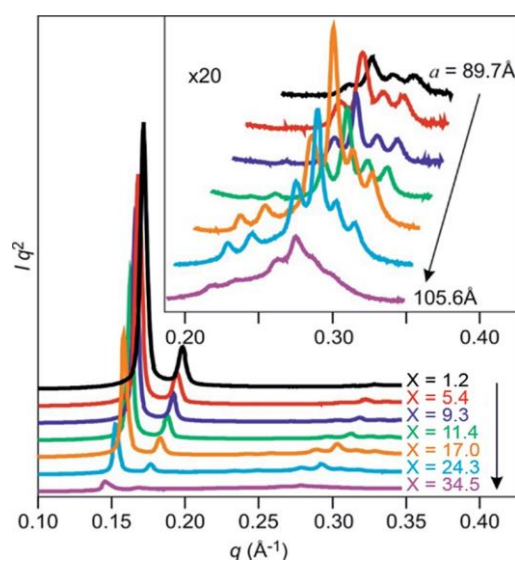


Fig. 7.6 X-ray diffraction patterns of **Film-Cub_{bi}(X)** with various water contents at 25 °C.

In order to obtain critical information on the positions of the incorporated water molecules, we performed synchrotron XRD measurements on samples of **Film-Cub_{bi}** containing various amounts of water. The driest sample was obtained by drying at 110 °C and the wettest sample was prepared by immersing into water. Samples with a whole range of water contents were prepared by tuning these processes. The XRD

patterns obtained for these samples clearly show that **Film-Cub_{bi}(X)** can maintain the **Cub_{bi}** periodic structure with the same $Ia\bar{3}d$ with combining macron]d space group while increasing the water amount leads to expansion of the lattice (Fig. 7.6). In particular, the lattice parameter increases by 18% from the driest to the wettest conditions, which corresponds to an increase in the unit cell volume of 63%. Such an increase in the unit cell volume is attributed to the increase in the water content in **Film-Cub_{bi}(X)**. The density of the driest sample is measured to be 1.27 g cm^{-3} by means of flotation analysis (Fig. S7.12 in the SI†). Using the measured lattice parameters and water content of the as-prepared, dried **Film-Cub_{bi}(X)** samples, and assuming that the water density in the film is 1.00 g cm^{-3} , we have derived a relationship between the lattice parameter and the amount of absorbed water by weight (Table S7.9 in the SI†). It was thus estimated that the water content X in the prepared samples ranged from 1.2 to 34.5 wt%. The derived relationship suggests that the wettest sample has a density of 1.16 g cm^{-3} , which is consistent with the experimentally obtained value (1.17 g cm^{-3}).

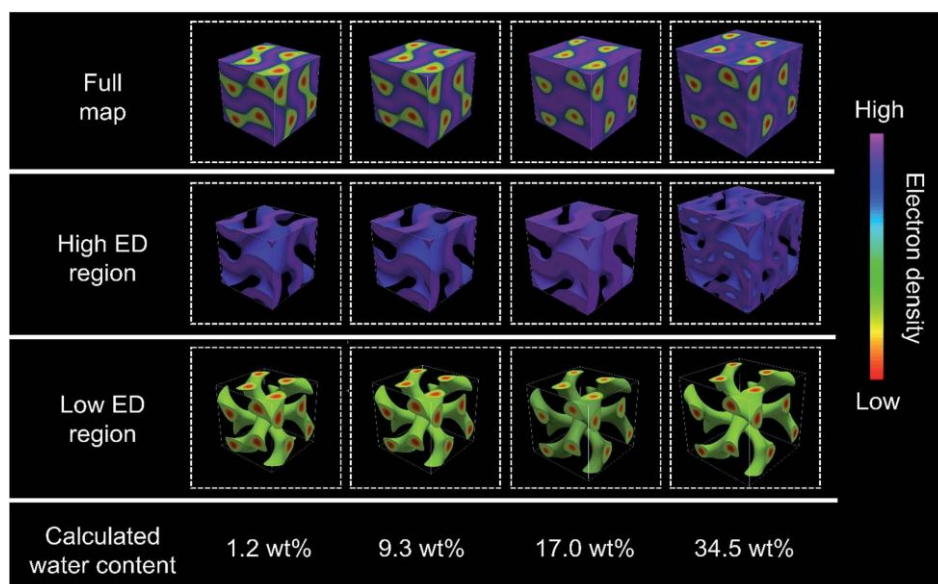


Fig. 7.7 Reconstructed electron density maps of **Film-Cub_{bi}(X)** with various water contents. The highest electron density region is coloured with purple. The lowest electron density region is coloured with red.

Another noteworthy feature in the XRD patterns is that the relative intensities of the first two diffraction peaks, (211) and (220), decrease dramatically with increasing water content in the **Film-Cub_{bi}(X)** samples. It is expected that the increase in water content would expand the volume of high electron density regions (ionic + water) and reduce the relative volume of the lower electron density regions (alkyl chain); therefore the overall contrast in the structure is reduced leading to weaker diffraction peaks. This assumption is clearly confirmed from reconstructed electron density maps (Fig. 7.7 and S13 in the SI†). The changes of the electron density are visualized with colour changes from red, yellow, green, aqua, and blue to purple as the electron density increases. Focusing on the gyroid minimal surface, it can be seen that, while it is coloured only purple when the water content is low ($X = 1.2, 5.4,$ and 9.3), scattered blue domains appear when the water content is 17.0 wt%, and the blue domains gain 3D continuity when the water contents are 24.3 and 34.5 wt%. In other words, a blue coloured gyroid minimal surface appears upon water absorption between the purple domains with the highest electron density. This can be explained by assuming that the blue gyroid surface between the purple regions is formed by localization of some water molecules, and the purple domains are composed mostly of the ionic segments with high electron density. We attribute this local segregation between water and the ionic domains to two effects. One is the strong hydrophobicity of the Tf₂N anion. The other is the strong hydrophilicity of the sulfonate anion of the zwitterionic parts. The number of water molecules per zwitterionic headgroup on the monomer in the films with 17.0, 24.3, and 34.5 wt% water can be calculated to be 6.2, 9.8, and 16.0. Recently, there have been several studies on the relationship between the ion structure of various ionic liquids and their water sorption ability.[63] Considering this general insight, the maximum number of water molecules that form strong interactions with a pyridinium-cation is expected to be lower than 5. This led us to assume that there is an excess number of water

molecules beyond the hydration limitation of the pyridinium cation when the water content X is ≥ 21 wt%. Consequently, the excess water molecules, being bound to the sulfonate groups and/or being shed by the Tf₂N anions, form an extremely thin water sheet domain along the gyroid minimal surface. It is worth noting that the blue domain along the gyroid minimal surface can be named a “3D continuous aqua sub-nanosheet”.

It is well-known that proton conduction is induced by the combination of two mechanisms, the vehicle and the Grotthuss mechanisms. [64,65] The former mechanism is proton migration based on the molecular diffusion of protonated water clusters. The latter mechanism is instantaneous transmittance of protons through water molecule networks as a result of breaking/forming of hydrogen-bonding, which provides exceptionally high-speed ion conduction. This mechanism can be recognized as a kind of Newton's cradle (NC) phenomenon where water molecules act as “balls”. Taking into account the geometrical character of a gyroid structure which is composed of patching of saddle-shaped plates, we expect that the present polymer film should act as a novel platform for water molecules to exhibit a 3D NC phenomenon and then show high proton conductivity in the order of 10^{-1} S cm⁻¹, which is comparable to the limit value of the Grotthuss mechanism. Generally, it is essential for inducing effective NC phenomena to align “balls” one- or two-dimensionally without any space between them. With this in mind, it is considered that successive proton conduction via the Grotthuss mechanism along the gyroid minimal surface can be induced when water molecules are installed all over the surface (Fig. S7.14 in the SI†). Roughly estimating the number of water molecules that is required to fulfill a gyroid minimal surface in a cubic lattice with a lattice length of 95 Å (see the SI†), it is calculated to be about 4000. By converting the number of water molecules per unit cell into the weight ratio, it is expected that over 12 wt% of the water content is needed at least in the case of **Film-Cubi(X)** to cover the gyroid minimal surface.

In order to examine the relationship between the ball filling rate (namely water content) and proton conductivity, impedance measurements were performed for **Film-Cub_{bi}(X)** with various water contents. The ionic conductivity (σ) values are plotted against the water content X in Fig. 7.8a. It can be seen that the σ values depend largely on the water content. For example, the σ of **Film-Cub_{bi}(X)** is $3.3 \times 10^{-5} \text{ S cm}^{-1}$ when $X = 6.7 \text{ wt\%}$, which is far lower than $10^{-1} \text{ S cm}^{-1}$. The conduction mechanism in **Film-Cub_{bi}(6.7)** is thus probably dominated by the vehicle mechanism because the gyroid minimal surface is not fully covered by water molecules enough to induce the Grotthuss mechanism. On the other hand, the σ of **Film-Cub_{bi}(13.1)** is $1.5 \times 10^{-2} \text{ S cm}^{-1}$ and that of **Film-Cub_{bi}(15.6)** is close to $10^{-1} \text{ S cm}^{-1}$, which is an achievable value only when protons can be transported based on the Grotthuss mechanism over a long distance. These results led us to conclude that it is possible to induce a NC phenomenon along a gyroid minimal surface by adding an adequate amount of balls to fully cover the surface. We assume that, owing to the 2D nature of the gyroid structure, protons can show 2D NC-type fast transport in local ranges, which develops into 3D transport in larger ranges as a result of the 3D patching manner of the 2D plates.

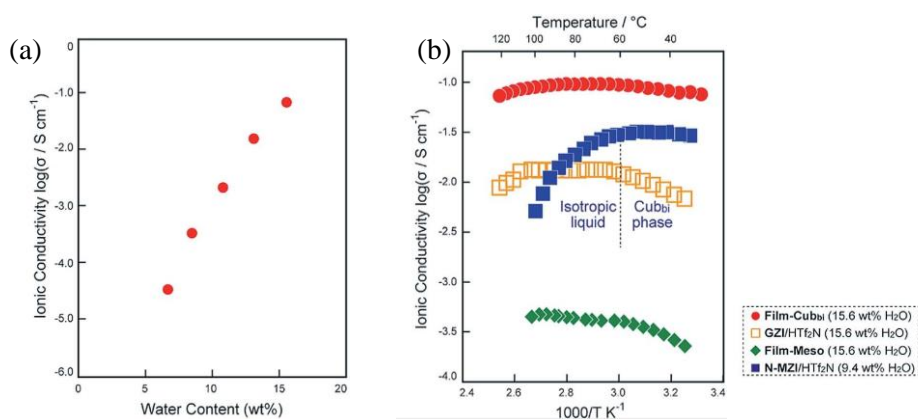


Fig. 7.8 (a) Ionic conductivity of **Film-Cub_{bi}(X)** against the water content X. (b) Arrhenius plot of the ionic conductivity of **Film-Cub_{bi}(15.6)** (●). As comparisons, that of **N-MZI/HTf₂N** (1.0/1.0 by mol) containing 9.4 wt% of water (■), that of **Film-Meso** (◆), and that of the **GZI/HTf₂N** mixture containing 15.6 wt% of water (□) are also plotted.

To date, a variety of materials design methods have been employed for improving proton-conductive polymer electrolytes for fuel cell applications. [66–68] The present materials design should be a new advantageous method for providing a new electrolyte design. Below, we compare the present materials and conventional polymer electrolytes, such as Nafion, from the viewpoint of ion conductive materials. The temperature dependence of σ of **Film-Cub_{bi}(15.6)** was investigated under measurement conditions of a heating rate of 2 °C min⁻¹ and RH = 40%. The σ linearly increases as temperature increases from ambient temperature to around 70 °C (Fig. 7.8b) and it reaches 9.9×10^{-2} S cm⁻¹ at 70 °C, which is comparable to that of highly hydrated Nafion.⁶⁹ The activation energy in this temperature range is calculated to be 2.2 kJ mol⁻¹. This low activation energy strongly supports our conclusion that the proton conduction in **Film-Cub_{bi}(15.6)** mostly depends on the Grotthuss mechanism. The activation energy of highly hydrated Nafion has been reported to be 10–15 kJ mol⁻¹. [68] Recently, there have been some reports that hydrogen-bonding networks of water molecules confined under specific conditions, such as in carbon nanotubes and in between mineral layers, exhibit exceptionally high ionic conductivity and low activation energy due to the formation of specifically coordinated structures of water molecules. [70,71] Considering these examples, there is a possibility that a specific proton conduction mechanism is induced in the present materials in which water molecules are confined exclusively on a gyroid minimal surface.

In order to further discuss the effects of the polymerization on the ion conduction behavior, the σ of **Film-Cub_{bi}(15.6)** was compared with that of an analogous non-polymerizable LC system. For such a non-polymerizable LC control sample, a mixture of a mono-type amphiphilic zwitterion with a normal alkyl chain (**N-MZI**) [72] and HTf₂N with a small amount of water was selected. The σ of the **N-MZI/HTf₂N** mixture (1.0/1.0 by mol) with 9.4 wt% water (reported in our previous paper [12]) is also plotted

in Fig. 7.8b. Comparing the σ of **Film-Cub_{bi}(15.6)** and that of the **N-MZI/HTf₂N** mixture, we found some significant differences. For example, **Film-Cub_{bi}(15.6)** shows a σ of $8.4 \times 10^{-2} \text{ S cm}^{-1}$ at 35 °C, which is about 3 times higher than that of the **N-MZI/HTf₂N** mixture. The large difference in σ mostly results from the difference in water content. The water content in **Film-Cub_{bi}(15.6)** is about twice that in the **N-MZI/HTf₂N** mixture. Here it should be noted that, while the **N-MZI/HTf₂N** mixture forms gyroid-nanostructures when the water content is <10 wt%, it is impossible to increase the water content above 10 wt% for the **N-MZI/HTf₂N** mixture while maintaining its molecular assembled gyroid-nanostructures because the increase of the water content results in phase changes and significant lowering of the isotropization temperature. Another noteworthy point is that the σ of the **N-MZI/HTf₂N** mixture abruptly decreases at around 60 °C, which can be explained in two ways. One is the collapse of hydrogen-bonding networks of the water molecules, followed by phase transition to the isotropic phase. The other is decrease of the water content through evaporation. Compared to the ion conduction behaviour of the **N-MZI/HTf₂N** mixture, **Film-Cub_{bi}(15.6)** shows a gradual decrease of σ at temperatures higher than 70 °C. First, it is concluded that the polymerization of the amphiphilic zwitterions results in overcoming the disadvantage of the LC materials that they lose structural benefits in the temperature region higher than their isotropization temperature. Not only does it enhance the structural-benefits, it also contributes to the enhancement of the water-binding ability as a result of the preservation of a unique situation where the sulfonate/sulfonic-acid groups are densely aligned on a continuous surface. As another control sample, we prepared a polymeric sample by polymerizing the **Diene-GZI/HTf₂N** mixture in a molar ratio of 1 : 0.5 with 1 wt% of DMPA at 130 °C in a disordered state under UV irradiation for 1 h. The obtained polymeric sample was mixed with water to obtain a water content of 15.6 wt% (**Film-Meso(15.6)**). The

absence of a well-ordered nanostructure in **Film-Meso(15.6)** was confirmed by XRD measurement (see Fig. S7.15 in the SI†). Comparing the σ of **Film-Cub_{bi}(15.6)** and **Film-Meso(15.6)**, it is notable that **Film-Cub_{bi}(15.6)** shows higher σ than **Film-Meso(15.6)**. For example, the σ of **Film-Cub_{bi}(15.6)** is $9.7 \times 10^{-2} \text{ S cm}^{-1}$, which is 240 times larger than that of **Film-Meso(15.6)**. These results suggest that the presence of the gyroid nanostructure is a critical factor that enhances the contribution of the Grotthuss mechanism in the polymerized amphiphilic zwitterionic systems.

To further confirm the importance of the polymerization for high proton conduction, we prepared a gemini-type amphiphilic zwitterion with normal alkyl chains (**GZI**, see the SI†). By mixing **GZI** and HTf₂N in a 1 : 0.5 molar ratio and adding 15.6 wt% of water, a control sample forming a fluidic LC state was prepared. The σ of the **GZI/HTf₂N** mixture is also plotted in Fig. 8b. It can be seen that the σ of **Film-Cub_{bi}(15.6)** is about an order of magnitude higher than that of the **GZI/HTf₂N** mixture. These results lead us to assume that the polymerization of the gemini-amphiphilic zwitterion has an effect on limiting the position of water molecules in the system at the hydrophilic gyroid minimal surface. Consequently, it enhances the macroscopic continuity of hydrogen-bonding networks of water molecules, which enables a more efficient Grotthuss proton conduction mechanism over a long distance.

In addition to these physicochemical properties, the present materials have great potential for exhibiting new advantageous aspects as polymer electrolytes for fuel cells. For example, since the proton conduction pathways in **Film-Cub_{bi}(X)** have 3D continuity, this film is independent of the formation of “dead-ends” in proton conduction pathways. Another aspect is that the nanosegregated structure in **Film-Cub_{bi}(X)** should contribute to the formation of an effective interface between catalysts and electrolytes. It is also expected that, by substituting the Tf₂N anion with non-fluorinated anions after polymerization, **Film-Cub_{bi}(X)** can be converted to fluorine-

free polymer electrolytes, which may endow **Film-Cub_{bi}(X)** with more bio-compatibility.

7.4 Conclusion

We have succeeded in creating a self-standing polymer film having a hydrophilic gyroid minimal surface by cross-linking polymerization of an amphiphilic zwitterionic gemini monomer in a bicontinuous cubic liquid-crystalline assembly. This polymer film has the ability to absorb water molecules while maintaining the gyroid nanostructure until the gyroid minimal surface is fully covered by water molecules. Under these water-fulfilled conditions, the film shows high ionic conductivity in the order of $10^{-1} \text{ S cm}^{-1}$ at room temperature, suggesting that the Grotthuss mechanism, a type of Newton's cradle phenomenon, occurs successively along the 3D continuous gyroid minimal surface over a long distance.

7.5 Experimental section

Materials

All the reagents were purchased from Sigma Aldrich and Tokyo Kasei corporation. The synthetic scheme for **Diene-GZI** is shown in the SI.† The obtained compounds are characterized by ¹H NMR, ¹³C NMR, and elemental analysis (see the SI†).

Polymerization

1 wt% of DMPA is added as a photo-polymerization initiator. **MX** was sandwiched by a Teflon sheet and a cover glass with 130 μm thickness spacers. UV irradiation was performed for DMPA-added **MX** for 2 h at 30 °C using a xenon lamp as a light source.

Thermogravimetric analysis

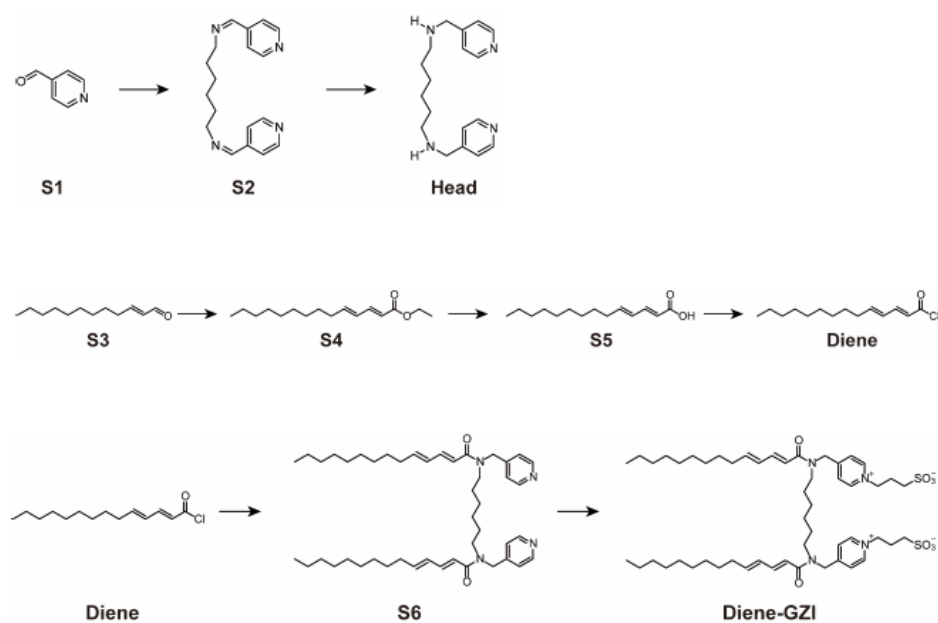
The samples of **Film-Cub_{bi}** were heated at 30, 80, 130, and 180 °C for 15 minutes, respectively. After that, their weights were measured immediately.

Impedance measurement

Alternating current impedance measurements were performed using a Schlumberger Solartron 1260 impedance analyzer (frequency range = 10 Hz to 10 MHz, applied voltage = 0.1 V). Comb-shaped gold electrodes with a glass substrate were used as a cell for the measurements of ionic conductivity. To determine the cell constant of the cell, a 0.01 mol L⁻¹ KCl aqueous solution was employed as a calibration standard.

7.6 Supporting Information

7.6.1 Synthesis of Diene-GZI



Scheme S7.1. Synthetic scheme for **Diene-GZI**.

7.6.2 Thermal behavior of Diene-GZI

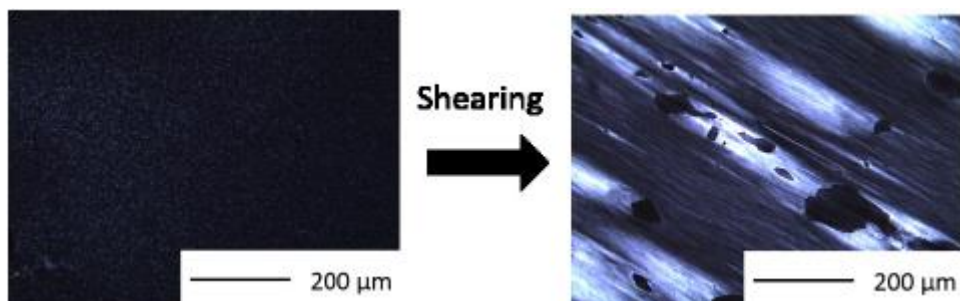


Fig. S7.3. Polarizing optical microphotographs of **Diene-GZI** in the LC state at 100 °C before and after shearing.

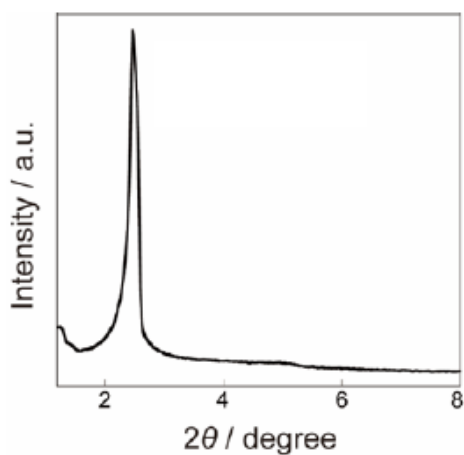


Fig. S7.4. Wide-angle X-ray diffraction pattern of **Diene-GZI** in the LC state at 25 °C.

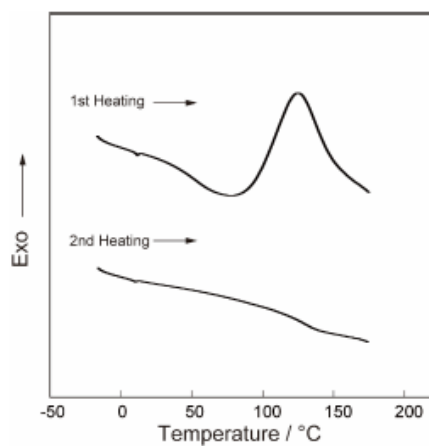


Fig. S7.5. Differential scanning calorimetry thermograms of **Diene-GZI**.

7.6.3 Thermal behavior of MX

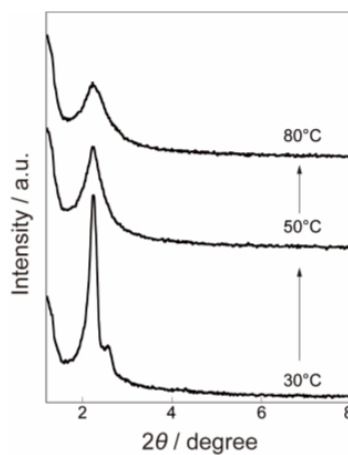


Fig. S7.6. Wide-angle X-ray diffraction patterns of **MX** at various temperatures.

7.6.4 A molecular structure of N-MZI and its liquid-crystalline behaviour

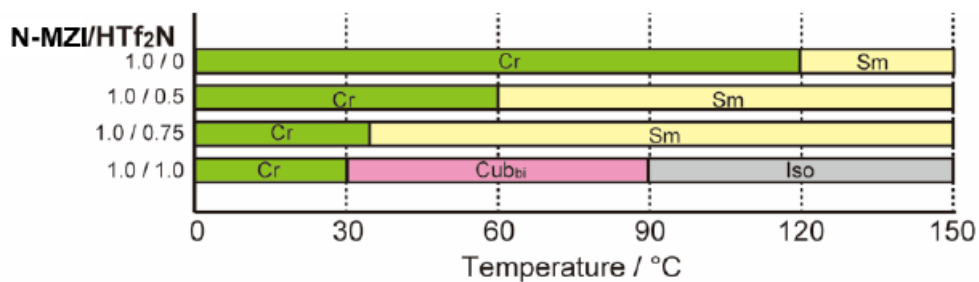
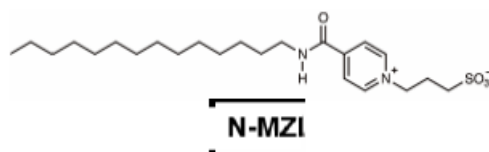


Fig. S7.7. Thermotropic liquid-crystalline behavior of the mixtures of the **N-MZI** and HTf₂N in various molar ratios. (Cr; crystalline, Sm; smectic, Cub_{bi}; bicontinuous cubic, Iso; isotropic liquid.)

7.6.5 Microscopic structure in **Film-Cub_{bi}**

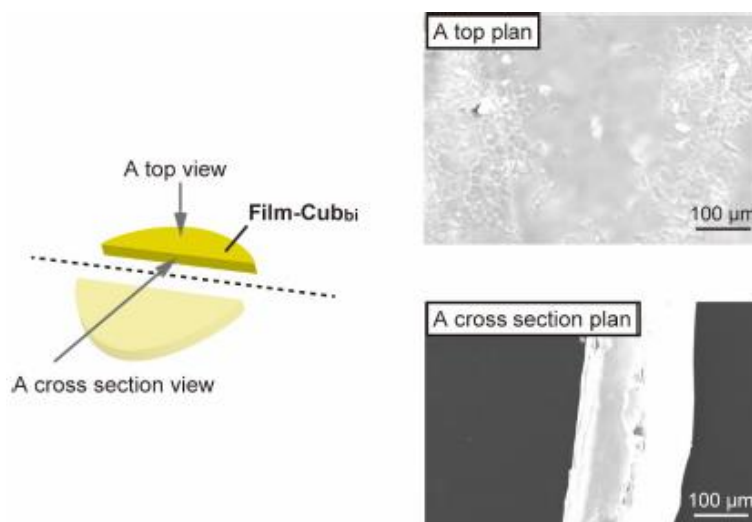


Fig. S7.8. Macroscopic structure in **Film-Cub_{bi}** and its surface. Scanning electron microscope (SEM) images of **Film-Cub_{bi}**. A floor and cross section plans are shown.

7.6.6 IR spectra of **Film-Cub_{bi}**

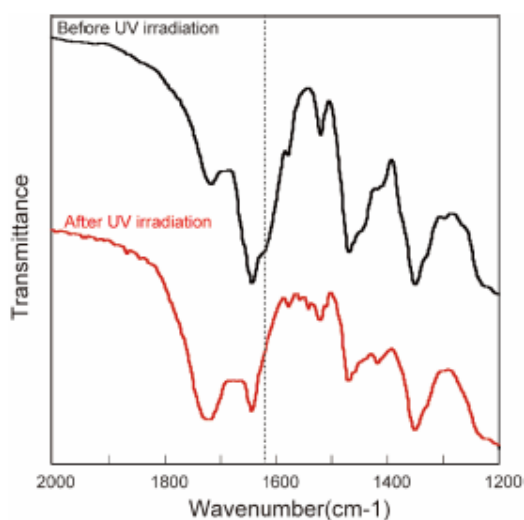


Fig. S7.9. IR spectra of **MX** (before UV irradiation) and **Film-Cub_{bi}** (after UV irradiation).

7.6.7 Relative humidity dependence of the cubic lattice length in Film-Cub_{bi}

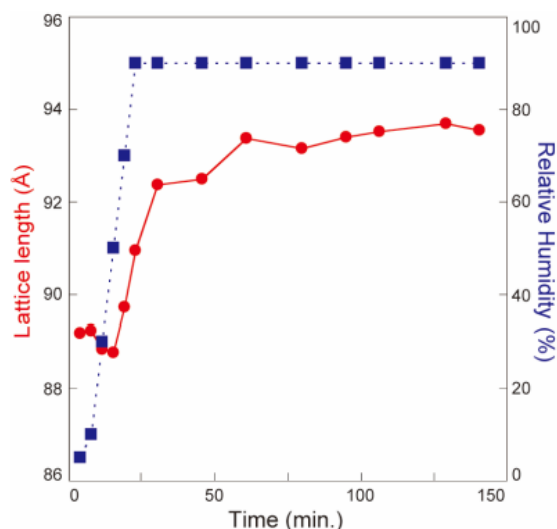


Fig. S7.10. XRD measurements were performed for **Film-Cub_{bi}** with varying relative humidity (RH) at 30 °C. RH was controlled by RIGAKU Corporation. Increase speed of the cubic lattice length gradually becomes slow at around 50 minutes, suggesting that **Film-Cub_{bi}** reaches an equilibrium state where water absorption and evaporation into/from **Film-Cub_{bi}** occur in the same speed.

7.6.8 Gravimetric analysis for Film-Cub_{bi} under humidity-controlled condition

Table S7.1. Weights of **Film-Cub_{bi}** before and after polymerization are shown. In addition, the weights of **Film-Cub_{bi}** after being placed under various RH conditions (RH = 50, 60, 70, 80, and 90) are also measured. By using these values, the water weights (mg) and water contents (wt %) in **Film-Cub_{bi}** were estimated.

	Weight (mg)	Δ weight (mg)	Water weight (mg)	Water content (wt%)
Before Polymerization	38.58	0.00	7.21	18.7
After Polymerization	34.11	-4.47	2.74	8.05
Film-Cubbi (RH=50%)	33.61	-4.97	2.24	6.68
Film-Cubbi (RH=60%)	34.27	-4.31	2.90	8.48
Film-Cubbi (RH=70%)	35.18	-3.40	3.81	10.84
Film-Cubbi (RH=80%)	36.09	-2.49	4.72	13.09
Film-Cubbi (RH=90%)	37.14	-1.44	5.77	15.55

7.6.9 Synchrotron X-ray diffraction patterns of Film-Cub_{bi}

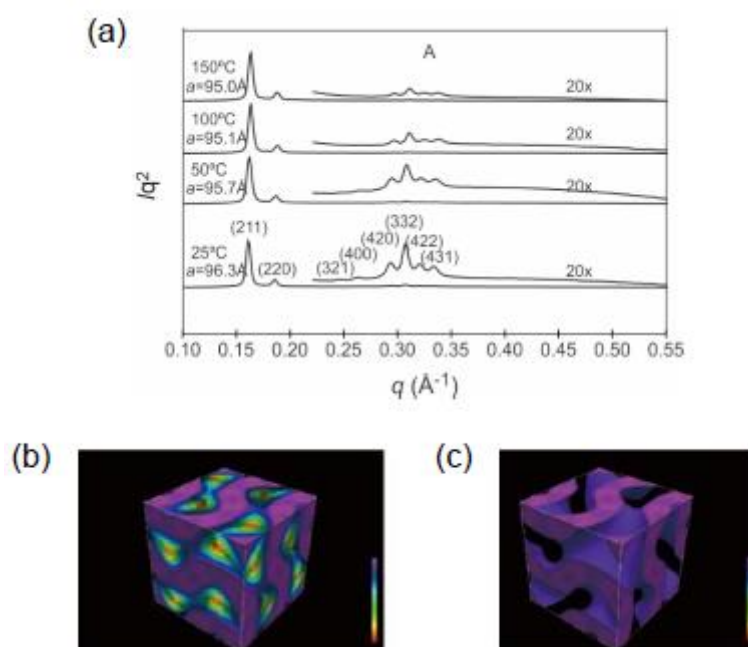


Fig. S7.11. (a) XRD patterns of **Film-Cub_{bi}** measured by synchrotron X-ray diffraction measurement. (b) Reconstructed electron density map. (c) Reconstructed electron density map of highest region.

Synchrotron X-ray diffraction experiments were carried out at station I22, Diamond Light Source. A monochromatic wavelength of 1.0 Å was used and sample to detector distance was calibrated using AgBeh. A Pilatus 2M detector was used to collect the SAXS diffractograms which is then converted to 1D curves by radial integration. The samples were held in glassy capillaries (diameter: 1.0mm), with or without water, and for dried samples sealed to avoid effect of humidity in the air.

In the experiments, two intense peaks and six weak peaks are observed. Their reciprocal d -spacing ratio of these peak is $\sqrt{6} : \sqrt{8} : \sqrt{14} : \sqrt{16} : \sqrt{20} : \sqrt{22} : \sqrt{24} : \sqrt{26}$. The observed diffraction peaks can only be indexed by a body centered cubic lattice with indices (211), (220), (321), (400), (420), (332), (422) and (431). An alternative indexing

to a primitive lattice is not possible. If you index the first two peaks as (111) and (200) instead, the 3rd peak should have $h^2+k^2+l^2$ equal to 7 which is impossible. The (hkl) indices conforms strictly to the $Ia\bar{3}d$ space group symmetry: $h+k+l$ is always even, for $(hk0)$ peaks both h and k are even, for (hhl) peaks $2h+l=4n$, and for $(h00)$ peak $h=4n$. All unobserved peaks (100), (110), (111), (200), (210), (300), (310), (311), (222), (320), (410), (411), (330), (331), (421), and so on are expected to be extinct by the $Ia\bar{3}d$ space group symmetry.

7.6.10 Material density measurement for Film-Cub_{bi}

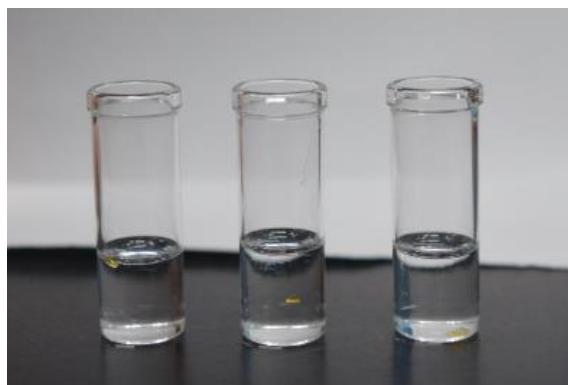
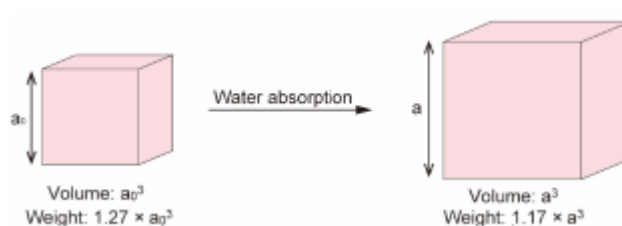


Fig. S7.12. Driest Film-Cub_{bi} in chloroform (left), chloroform/hexane mixture (3/1 by volume) (middle), chloroform/hexane mixture (1/1 by volume) (right).

Material densities of the driest Film-Cub_{bi} and the wettest Film-Cub_{bi} are determined by floating the films into mixed solvents of chloroform ($d = 1.49 \text{ g cm}^{-3}$) and hexane ($d = 0.66 \text{ g cm}^{-3}$) in various ratios. It has been found that the driest film starts to float when the density of the solvent reach 1.27 g cm^{-3} whereas wettest film starts to float when the density of the solvent reach 1.17 g cm^{-3} .

The cubic lattice length of the driest **Film-Cub_{bi}(1.2)** was found to be 89.6 \AA (a_0) while that of the wettest **Film-Cub_{bi}(X_{wettest})** was found to be 105.6 \AA (a). The amount of the absorbed water weight in a cubic lattice is calculated from $1.17a^3 - 1.27a_0^3$ ($\text{H}_2\text{O}_{\text{abs}}$).

The initial water content of the driest **Film-Cub_{bi}(1.2)** in a cubic lattice is $1.27a_0^3 \times 0.012$ (H_2O_{init}). We estimated the water content X_{wetest} from $(H_2O_{abs} + H_2O_{init}) / 1.17a^3 \times 100$ to be 34.5 wt%.



7.6.11 Preparation of samples with various water contents for synchrotron X-ray diffraction measurements

For the Synchrotron X-ray measurement for **Film-Cub_{bi}(X)** with various X values, we prepared various **Film-Cub_{bi}(X)** by putting it under various conditions, such as dried at 110 °C, dried at 80 °C, vacuum dried at room temperature, no treatment, wet, after soaked in water for 3 h, and immersed in water. Since it was impossible to perform gravimetric analysis for these films, we made an assumption below to estimate the water content X .

Assuming that the cubic lattice length in **Film-Cub_{bi}(X)** increase linearly against the water content X , we obtained an equation $Y = 0.4805X + 89.0$ by using these data of the driest **Film-Cub_{bi}** and the wettest **Film-Cub_{bi}**.

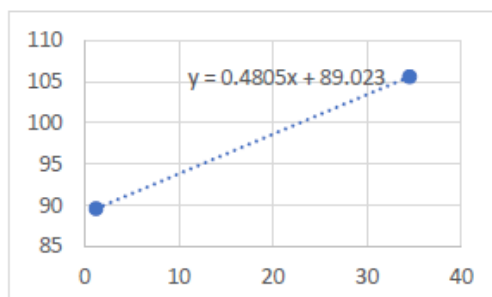


Table S7.2. Water contents calculated from the lattice parameter.

Lattice parameter Y (Å)	Water content (wt%) from experiment	Water content (wt%) from calculation
89.7	1.2	1.2
91.6	-	5.4
93.5	-	9.3
94.5	-	11.4
97.2	-	17.0
100.7	-	24.3
105.6	-	34.5

7.6.12 Reconstruction of electron density maps

The intensities and phases used to reconstruct the electron density maps are listed in the tables below.

Table S7.3. The indices, experimental, calculated d-spacings, intensities, phases and lattice parameter of **Film-Cub_{bi}** with 1.2 wt% **H₂O** obtained from SAXS. All intensity values are Lorentz corrected.

(<i>hk</i>)	<i>d</i> -spacing (nm) experimental	<i>d</i> -spacing (nm) calculated	<i>Intensity</i>	<i>Phase</i>
(211)	3.66	3.66	100.00	0
(220)	3.17	3.17	13.62	0
(321)	-	2.40	-	-
(400)	-	2.24	-	-
(420)	2.01	2.01	0.19	0
(332)	1.91	1.91	0.67	π
(432)	1.83	1.83	0.34	π
(431)	1.76	1.76	0.30	π
$a = 8.97$ nm				

Table S7.4. The indices, experimental, calculated d-spacings, intensities, phases and lattice parameter of **Film-Cub_{bi}** with 5.4 wt% **H₂O** obtained from SAXS. All intensity values are Lorentz corrected.

<i>(hk)</i>	<i>d</i> -spacing (nm) experimental	<i>d</i> -spacing (nm) calculated	<i>Intensity</i>	<i>Phase</i>
(211)	3.74	3.74	100.00	0
(220)	3.24	3.24	12.43	0
(321)	-	2.45	-	-
(400)	-	2.29	-	-
(420)	2.04	2.05	0.53	0
(332)	1.95	1.95	1.60	π
(432)	1.87	1.87	0.69	π
(431)	1.80	1.80	0.59	π
$a = 9.16 \text{ nm}$				

Table S7.5. The indices, experimental, calculated d-spacings, intensities, phases and lattice parameter of **Film-Cub_{bi}** with 9.3 wt% **H₂O** obtained from SAXS. All intensity values are Lorentz corrected.

<i>(hk)</i>	<i>d</i> -spacing (nm) experimental	<i>d</i> -spacing (nm) calculated	<i>Intensity</i>	<i>Phase</i>
(211)	3.78	3.78	100.00	0
(220)	3.27	3.27	12.22	0
(321)	-	2.47	-	-
(400)	2.32	2.32	0.07	0
(420)	2.07	2.07	0.56	0
(332)	1.97	1.97	1.66	π
(432)	1.89	1.89	0.61	π
(431)	1.82	1.82	0.54	π
$a = 9.26 \text{ nm}$				

Table S7.6. The indices, experimental, calculated d-spacings, intensities, phases and lattice parameter of **Film-Cub_{bi}** with 11.4 wt% **H₂O** obtained from SAXS. All intensity values are Lorentz corrected.

<i>(hk)</i>	<i>d</i> -spacing (nm) experimental	<i>d</i> -spacing (nm) calculated	<i>Intensity</i>	<i>Phase</i>
(211)	3.86	3.86	100.00	0
(220)	3.34	3.34	12.58	0
(321)	2.53	2.53	0.07	0
(400)	2.36	2.36	0.14	0
(420)	2.11	2.11	1.01	0
(332)	2.01	2.01	2.69	π
(432)	1.93	1.93	1.06	π
(431)	1.85	1.85	0.85	π
$a = 9.45 \text{ nm}$				

Table S7.7. The indices, experimental, calculated d-spacings, intensities, phases and lattice parameter of **Film-Cub_{bi}** with 17.0 wt% **H₂O** obtained from SAXS. All intensity values are Lorentz corrected.

<i>(hk)</i>	<i>d</i> -spacing (nm) experimental	<i>d</i> -spacing (nm) calculated	<i>Intensity</i>	<i>Phase</i>
(211)	3.97	3.97	100.00	0
(220)	3.44	3.44	12.73	0
(321)	2.60	2.60	0.48	0
(400)	2.43	2.43	0.67	0
(420)	2.17	2.17	2.98	0
(332)	2.07	2.07	7.33	π
(432)	1.98	1.98	2.52	π
(431)	1.91	1.91	1.72	π
$a = 9.72 \text{ nm}$				

Table S7.8. The indices, experimental, calculated d-spacings, intensities, phases and lattice parameter of **Film-Cub_{bi}** with 24.3 wt% **H₂O** obtained from SAXS. All intensity values are Lorentz corrected.

<i>(hk)</i>	<i>d</i> -spacing (nm) experimental	<i>d</i> -spacing (nm) calculated	<i>Intensity</i>	<i>Phase</i>
(211)	4.11	4.11	100.00	0
(220)	3.56	3.56	14.97	0
(321)	2.69	2.69	1.36	0
(400)	2.52	2.52	1.47	0
(420)	2.25	2.25	5.39	0
(332)	2.15	2.15	13.23	π
(432)	2.06	2.06	4.24	π
(431)	1.98	1.97	2.68	π
<i>a</i> = 10.07 nm				

Table S7.9. The indices, experimental, calculated d-spacings, intensities, phases and lattice parameter of **Film-Cub_{bi}** with 34.5 wt% **H₂O** obtained from SAXS. All intensity values are Lorentz corrected.

<i>(hk)</i>	<i>d</i> -spacing (nm) experimental	<i>d</i> -spacing (nm) calculated	<i>Intensity</i>	<i>Phase</i>
(211)	4.31	4.31	100.0	0
(220)	3.73	3.73	16.91	0
(321)	2.82	2.82	2.15	0
(400)	2.64	2.64	1.12	0
(420)	2.36	2.36	11.24	0
(332)	2.25	2.25	26.91	π
(432)	2.16	2.16	14.79	π
(431)	2.07	2.07	5.84	π
<i>a</i> = 10.56 nm				

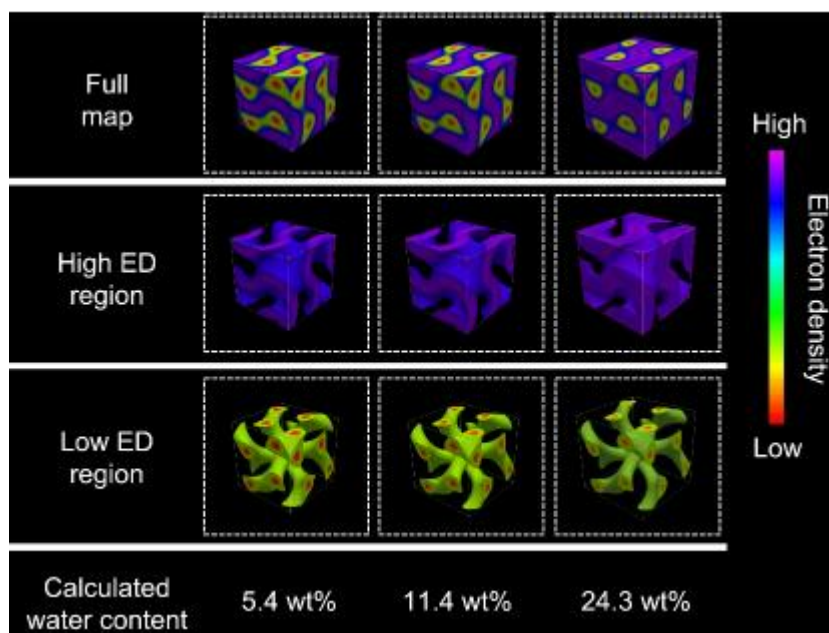


Fig. S7.13. Reconstructed electron density maps of **Film-Cub_{bi}(X)** with various water contents. The highest electron density region is coloured with purple. The lowest electron density region is coloured with red.

7.6.13 Calculation of the surface area of a gyroid minimal surface

Torquato and co-workers simulated total surface area of gyroid surfaces with various mean curvature.[74] When a mean curvature equals to zero, that surface is defined as a gyroid minimal surface in a cubic lattice. Assuming the length of the cubic lattice as L , the surface area of the gyroid minimal surface is about 3.10 times as large as $L \times L$. With this, we calculated the surface area of the gyroid minimal surface in a cubic lattice in Film-Cub_{bi} with a cubic lattice length of 95 \AA (A_G).

$$A_G = 95 (\text{\AA}) \times 95 (\text{\AA}) \times 3.10$$

Roughly assuming a water molecule as a sphere with 1.5 \AA radius, the number of water molecules required for fulfilling the gyroid minimal surface is estimated as below.

$$A_G / 1.5 (\text{\AA}) \times 1.5 (\text{\AA}) \times \pi = 3960$$

Assuming that the density of **Film-Cub_{bi}** is 1.17 g/cm³, the water content (wt%) in **Film-Cub_{bi}** containing 3960 water molecules can be calculated as follow.

$$100 \times (3960 \times 18 / 6.02 \times 10^{23}) / \{(9.5 \times 10^{-7})^3 \times 1.0\} = 11.8 \text{ (wt \%)}$$

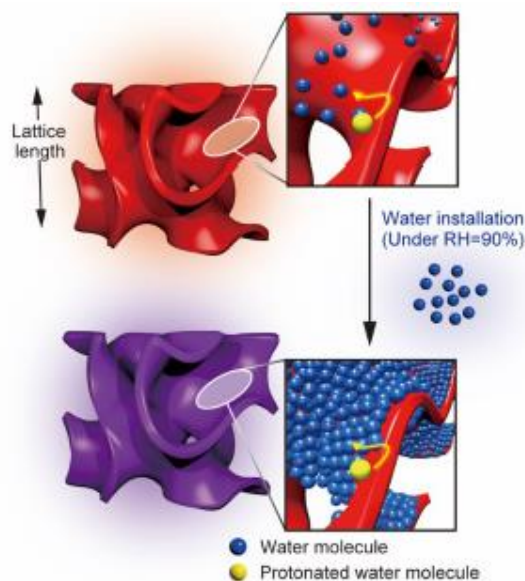


Fig. S7.14. Schematic image of the installation of water molecules on a gyroid minimal surface. Considering that **Film-Cub_{bi}** contains water content of 15.6 wt% at RH = 90%, it is expected that the gyroid minimal surface is fully covered with water molecules.

7.6.14 Characterization of **Film-Meso**

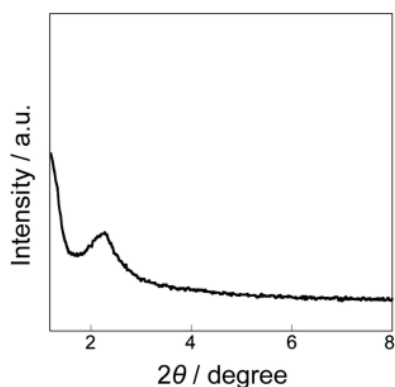


Fig. S7.15. Wide-angle X-ray diffraction pattern of **Film-Meso** at 30 °C.

7.6.15 Synthetic scheme for GZI

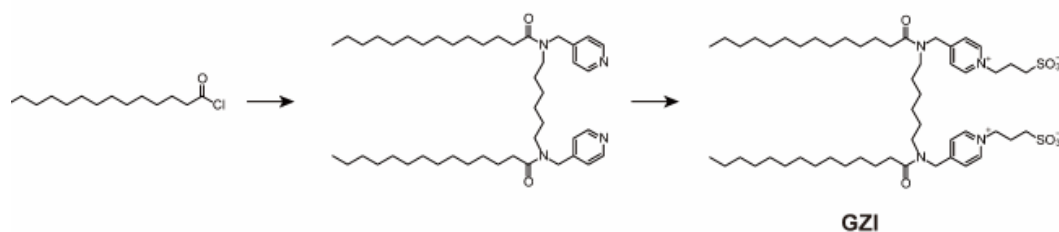
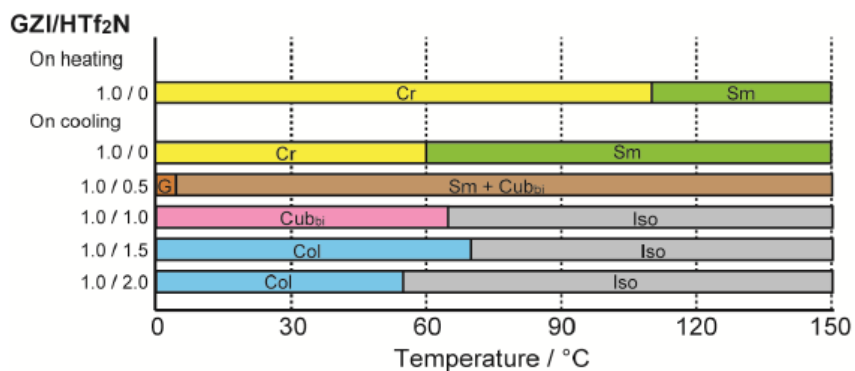
7.6.16 Self-organization behavior of GZI and the GZI/HTf₂N mixtures

Fig. S7.17. Thermotropic liquid-crystalline behavior of the mixtures of **GZI** and HTf₂N in various molar ratios. Cr; crystalline, Sm; smectic, G; glassy, Cub_{bi}; bicontinuous cubic, Iso; isotropic liquid, Col; columnar.

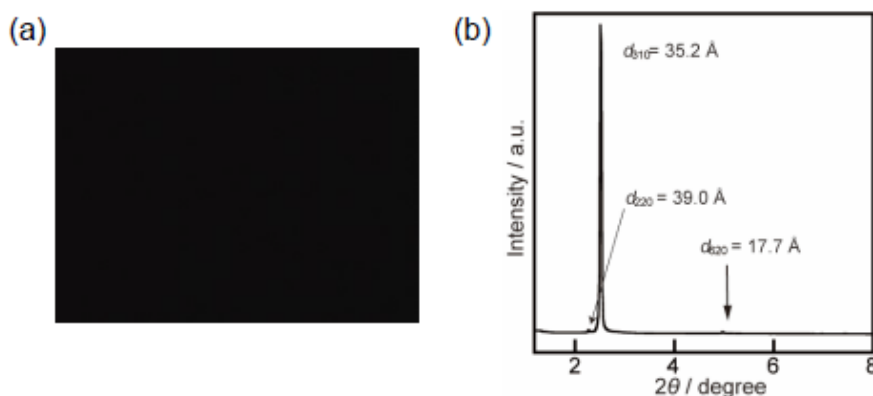


Fig. S7.18. (a) POM image of **GZI/HTf₂N** (1.0/1.0 by mol) at 30 °C in the Cub_{bi} phase. (b) XRD pattern of **GZI/HTf₂N** (1.0/1.0 by mol) at 30 °C in the Cub_{bi} phase.

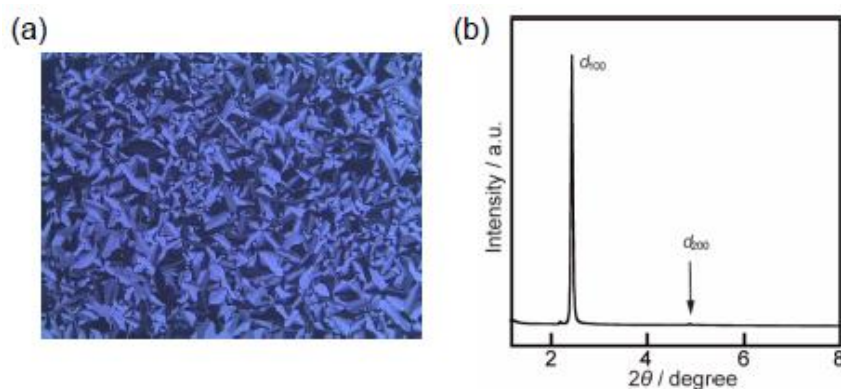


Fig. S7.19. (a) POM image of **GZI/HTf₂N** (1.0/2.0 by mol) at 30 °C in the columnar phase. (b) XRD pattern of **GZI/HTf₂N** (1.0/2.0 by mol) at 30 °C in the columnar phase.

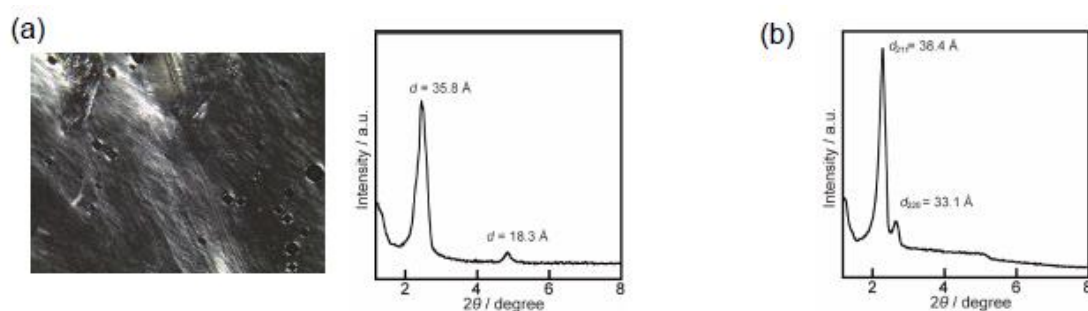


Fig. S7.20. (a) POM image and XRD pattern of **GZI/HTf₂N** (1.0/0.5 by mol) containing 15.6 wt% H₂O at 30 °C. (b) XRD pattern of **GZI/HTf₂N** (1.0/0.5 by mol) containing 20.0 wt% H₂O at 30 °C in the Cub_{bi} phase. Taking into account these LC behavior of **GZI/HTf₂N** (1.0/0.5 by mol) with various water contents, it is assumed that **GZI/HTf₂N** (1.0/0.5 by mol) containing 15.6 wt% H₂O (a non-polymerizable control sample) forms a LC phase in which smectic and Cub_{bi} phase domains are co-existing.

Acknowledgements

T. I. is grateful for financial support from the Precursory Research for Embryonic Science and Technology (PRESTO) from the Japan Science and Technology Agency (JST) (no. JPMJPR1413). This work was also partially supported by the Foundation for the Promotion of Ion Engineering. T. K. is grateful for financial support from the JSPS Research Fellowships for Young Scientists (no. JP 18J21088). The authors thank

Takahiro Kuzumaki in RIGAKU Corporation for the XRD measurements under various relative humidities. We are grateful to Dr N. Terill and O. Shebanova at I22, Diamond Light Source for help with SAXS experiments. The authors acknowledge funding for this work from the EPSRC (EP-K034308, EP-P002250). Y.X. L. thanks the CSC for the stipend and the UoS for waiving the tuition fee.

References

- [1] K. D. Kreuer, On the development of proton conducting polymer membranes for hydrogen and methanol fuel cells, *J. Membr. Sci.*, **185** (2001) 29.
- [2] K. A. Mauritz and R. B. Moore, State of Understanding of Nafion, *Chem. Rev.*, **104** (2004) 4535.
- [3] M. A. Hickner, H. Ghassemi, Y. S. Kim, B. R. Einsla and J. E. McGrath, Alternative Polymer Systems for Proton Exchange Membranes (PEMs), *Chem. Rev.*, **104** (2004) 4587.
- [4] B. Lafitte and P. Jannasch, Proton - Conducting Aromatic Polymers Carrying Hypersulfonated Side Chains for Fuel Cell Applications, *Adv. Funct. Mater.*, (2007), 17, 2823.
- [5] B. Bae, T. Yoda, K. Miyatake, H. Uchida and M. Watanabe, Proton - Conductive Aromatic Ionomers Containing Highly Sulfonated Blocks for High - Temperature - Operable Fuel Cells, *Angew. Chem., Int. Ed.*, **49** (2010) 317.
- [6] P. Nimmanpipug, K. Kodchakorn, V. S. Lee, J. Yana, C. Jarumaneeroj, S. Phongtamrug and S. Chirachanchai, Structural and transport phenomena of urocanate - based proton carrier in sulfonated poly(ether ether ketone) membrane composite, *J. Polym. Sci., Part B: Polym. Phys.*, **56** (2018) 1625.
- [7] M. J. Park and N. P. Balsara, Anisotropic Proton Conduction in Aligned Block Copolymer Electrolyte Membranes at Equilibrium with Humid Air, *Macromolecules*, **43** (2010) 292.
- [8] M. Michau and M. Barboiu, Self-organized proton conductive layers in hybrid proton exchange membranes, exhibiting high ionic conductivity, *J. Mater. Chem.*, **19** (2009) 6124.

- [9] C.-F. Chow, V. A. L. Roy, Z. Ye, M. H. W. Lam, C. S. Lee and K. C. Lau, Novel high proton conductive material from liquid crystalline 4-(octadecyloxy)phenylsulfonic acid, *J. Mater. Chem.*, **20** (2010) 6245.
- [10] Y. Chen, M. Thorn, S. Christensen, C. Versek, A. Poe, R. C. Hayward, M. T. Tuominen and S. Thayumanavan, Enhancement of anhydrous proton transport by supramolecular nanochannels in comb polymers, *Nat. Chem.*, **2** (2010) 503.
- [11] S. Ueda, J. Kagimoto, T. Ichikawa, T. Kato and H. Ohno, Anisotropic Proton - Conductive Materials Formed by the Self - Organization of Phosphonium - Type Zwitterions, *Adv. Mater.*, **23** (2011) 3071.
- [12] T. Ichikawa, T. Kato and H. Ohno, Anisotropic Proton - Conductive Materials Formed by the Self - Organization of Phosphonium - Type Zwitterions, *J. Am. Chem. Soc.*, **134** (2012) 11354.
- [13] E. Tunkara, C. Albayrak, E. O. Polat, C. Kocabas and O. Dag, Highly Proton Conductive Phosphoric Acid–Nonionic Surfactant Lyotropic Liquid Crystalline Mesophases and Application in Graphene Optical Modulators, *ACS Nano*, **8**, (2014) 11007.
- [14] Y. Nagao, Proton-Conductivity Enhancement in Polymer Thin Films, *Langmuir*, **33** (2017) 12547.
- [15] J. A. Hurd, R. Vaidhyanathan, V. Thangadurai, C. I. Ratcliffe, I. L. Moudrakovski and G. K. H. Shimizu, Anhydrous proton conduction at 150 °C in a crystalline metal–organic framework, *Nat. Chem.*, **1** (2009) 705.
- [16] L. Cao, H. Wu, P. Yang, X. He, J. Li, Y. Li, M. Xu, M. Qiu and Z. Jiang, Graphene Oxide - Based Solid Electrolytes with 3D Prepercolating Pathways for Efficient Proton Transport, *Adv. Funct. Mater.*, **28** (2018) 1804944.
- [17] P. Garstecki and R. Holyst, Periodic surfaces of simple and complex topology: Comparison of scattering patterns, *Phys. Rev. E: Stat., Nonlinear, Soft Matter Phys.*, **64** (2001) 021501.
- [18] S. Diele, On thermotropic cubic mesophases, *Curr. Opin. Colloid Interface Sci.*, **7** (2002) 333.
- [19] M. Imp´eror-Clerc, Thermotropic cubic mesophases, *Curr. Opin. Colloid Interface Sci.*, **9** (2005) 370.
- [20] D. W. Bruce, Calamitics, Cubics, and ColumnarsLiquid-Crystalline Complexes of Silver(I), *Acc. Chem. Res.*, **33** (2000) 831.
- [21] C. Tschierske, Development of Structural Complexity by Liquid - Crystal Self - assembly, *Angew. Chem., Int. Ed.*, **52** (2013) 8828.

- [22] C. Tschierske and G. Ungar, Mirror Symmetry Breaking by Chirality Synchronisation in Liquids and Liquid Crystals of Achiral Molecules, *ChemPhysChem*, **17** (2016) 9.
- [23] S. Kutsumizu, Recent Progress in the Synthesis and Structural Clarification of Thermotropic Cubic Phases, *Isr. J. Chem.*, **52** (2012) 844.
- [24] X. Zeng, G. Ungar and M. Imp´eror-Clerc, A triple-network tricontinuous cubic liquid crystal, *Nat. Mater.*, **4** (2005) 562.
- [25] T. Kato, M. Yoshio, T. Ichikawa, B. Soberats, H. Ohno and M. Funahashi, Transport of ions and electrons in nanostructured liquid crystals, *Nat. Rev. Mater.*, **2** (2017) 17001.
- [26] D. L. Gin, W. Gu, B. A. Pindzola and W.-J. Zhou, Polymerized Lyotropic Liquid Crystal Assemblies for Materials Applications, *Acc. Chem. Res.*, **34** (2001) 973.
- [27] B.-K. Cho, Nanostructured organic electrolytes, *RSC Adv.*, **4** (2014) 395.
- [28] B.-K. Cho, A. Jain, S. M. Gruner and U. Wiesner, Mesophase Structure-Mechanical and Ionic Transport Correlations in Extended Amphiphilic Dendrons, *Science*, **305** (2004) 1598.
- [29] T. Ichikawa, M. Yoshio, A. Hamasaki, T. Mukai, H. Ohno and T. Kato, Self-Organization of Room-Temperature Ionic Liquids Exhibiting Liquid-Crystalline Bicontinuous Cubic Phases: Formation of Nano-Ion Channel Networks, *J. Am. Chem. Soc.*, **129** (2007) 10662.
- [30] D. L. Gin, X. Lu, P. R. Nemade, C. S. Pecinovsky, Y. Xu and M. Zhou, Recent Advances in the Design of Polymerizable Lyotropic Liquid - Crystal Assemblies for Heterogeneous Catalysis and Selective Separations, *Adv. Funct. Mater.*, **16** (2006) 865.
- [31] A. J. Boydston, C. S. Pecinovsky, S. T. Chao and C. W. Bielawski, Phase-Tunable Fluorophores Based upon Benzobis(imidazolium) Salts, *J. Am. Chem. Soc.*, **129** (2007) 14550.
- [32] R. L. Kerr, S. A. Miller, R. K. Shoemaker, B. J. Elliott and D. L. Gin, New Type of Li Ion Conductor with 3D Interconnected Nanopores via Polymerization of a Liquid Organic Electrolyte-Filled Lyotropic Liquid-Crystal Assembly, *J. Am. Chem. Soc.*, **131** (2009) 15972.
- [33] H. Zhang, L. Li, M. Moller, X. Zhu, J. J. Hernandez Rueda, M. Rosenthal and D. A. Ivanov, From Channel - Forming Ionic Liquid Crystals Exhibiting Humidity - Induced Phase Transitions to Nanostructured Ion - Conducting Polymer Membranes, *Adv. Mater.*, **25** (2013) 3543.

- [34] J. C. Shah, Y. Sadhale and D. M. Chilukuri, Cubic phase gels as drug delivery systems, *Adv. Drug Delivery Rev.*, **47** (2001) 229.
- [35] T. Kato, J. Uchida, T. Ichikawa and T. Sakamoto, Functional Liquid Crystals towards the Next Generation of Materials, *Angew. Chem., Int. Ed.*, **57** (2018) 4355.
- [36] J. W. Goodby, I. M. Saez, S. J. Cowling, V. Gortz, M. Draper, A. W. Hall, S. Sia, G. Cosquer, S.-E. Lee and E. P. Raynes, Transmission and Amplification of Information and Properties in Nanostructured Liquid Crystals, *Angew. Chem., Int. Ed.*, **47** (2008), 2754.
- [37] K. V. Axenov and S. Laschat, Thermotropic Ionic Liquid Crystals, *Materials*, **4** (2011) 206.
- [38] K. Goossens, K. Lava, C. W. Bielawski and K. Binnemans, Ionic Liquid Crystals: Versatile Materials *Chem. Rev.*, **116** (2016) 4643.
- [39] T. Ichikawa, K. Fujimura, M. Yoshio, T. Kato and H. Ohno, Designer lyotropic liquid-crystalline systems containing amino acid ionic liquids as self-organisation media of amphiphiles, *Chem. Commun.*, **49** (2013) 11746.
- [40] T. Kobayashi, T. Ichikawa, T. Kato and H. Ohno, Development of Glassy Bicontinuous Cubic Liquid Crystals for Solid Proton - Conductive Materials, *Adv. Mater.*, **29** (2017) 1604429.
- [41] T. Ichikawa, A. Okafuji, T. Kato and H. Ohno, Induction of an Infinite Periodic Minimal Surface by Endowing An Amphiphilic Zwitterion with Halogen - Bond Ability, *ChemistryOpen*, **5** (2016) 439.
- [42] T. Matsumoto, A. Ono, T. Ichikawa, T. Kato and H. Ohno, Construction of gyroid-structured matrices through the design of geminized amphiphilic zwitterions and their self-organization, *Chem. Commun.*, **52** (2016) 12167.
- [43] A. Ono, H. Ohno, T. Kato and T. Ichikawa, Design of 3D continuous proton conduction pathway by controlling co-organization behavior of gemini amphiphilic zwitterions and acids, *Solid State Ionics*, **317** (2018) 39.
- [44] D. J. Broer, C. M. W. Bastiaansen, M. G. Debije and A. P. H. J. Schenning, Functional Organic Materials Based on Polymerized Liquid - Crystal Monomers: Supramolecular Hydrogen - Bonded Systems, *Angew. Chem., Int. Ed.*, **51**, (2012), 7102.
- [45] U. Beginn, G. Zipp and M. Moller, Functional Membranes Containing Ion - Selective Matrix - Fixed Supramolecular Channels, *Adv. Mater.*, **12** (2000) 510.

- [46] H.-K. Lee, H. Lee, Y. H. Ko, Y. J. Chang, N.-K. Oh, W.-C. Zin and K. Kim, Synthesis of a Nanoporous Polymer with Hexagonal Channels from Supramolecular Discotic Liquid Crystals, *Angew. Chem., Int. Ed.*, **40** (2001) 2669.
- [47] D. Yang, D. F. O'Brien and S. R. Marder, Polymerized Bicontinuous Cubic Nanoparticles (Cubosomes) from a Reactive Monoacylglycerol, *J. Am. Chem. Soc.*, **124** (2002) 13388.
- [48] B. A. Pindzola, J. Jin and D. L. Gin, Cross-Linked Normal Hexagonal and Bicontinuous Cubic Assemblies via Polymerizable Gemini Amphiphiles, *J. Am. Chem. Soc.*, **125** (2003) 2940.
- [49] L. Y. Jin, J. Bae, J.-H. Ryu and M. Lee, Ordered Nanostructures from the Self - Assembly of Reactive Coil - Rod - Coil Molecules, *Angew. Chem., Int. Ed.*, **45** (2006) 650.
- [50] M. Yoshio, T. Kagata, K. Hoshino, T. Mukai, H. Ohno and T. Kato, One-Dimensional Ion-Conductive Polymer Films: Alignment and Fixation of Ionic Channels Formed by Self-Organization of Polymerizable Columnar Liquid Crystals, *J. Am. Chem. Soc.*, **128** (2006) 5570.
- [51] D. Batra, D. N. T. Hay and M. A. Firestone, Formation of a Biomimetic, Liquid-Crystalline Hydrogel by Self-Assembly and Polymerization of an Ionic Liquid, *Chem. Mater.*, **19** (2007) 4423.
- [52] T. Ichikawa, M. Yoshio, A. Hamasaki, J. Kagimoto, H. Ohno and T. Kato, 3D Interconnected Ionic Nano-Channels Formed in Polymer Films: Self-Organization and Polymerization of Thermotropic Bicontinuous Cubic Liquid Crystals, *J. Am. Chem. Soc.*, **133** (2011) 2163.
- [53] H. Takeuchi, T. Ichikawa, M. Yoshio, T. Kato and H. Ohno, Induction of bicontinuous cubic liquid-crystalline assemblies for polymerizable amphiphiles via tailor-made design of ionic liquids, *Chem. Commun.*, **52** (2016) 13861.
- [54] M. Henmi, K. Nakatsuji, T. Ichikawa, H. Tomioka, T. Sakamoto, M. Yoshio and T. Kato, Self - Organized Liquid - Crystalline Nanostructured Membranes for Water Treatment: Selective Permeation of Ions, *Adv. Mater.*, **24** (2012) 2238.
- [55] F. M. Menger and C. A. Littau, Gemini surfactants: a new class of self-assembling molecules, *J. Am. Chem. Soc.*, **115** (1993) 10083.
- [56] M. Zhou, P. R. Nemade, X. Lu, X. Zeng, E. S. Hatakeyama, R. D. Noble and D. L. Gin, New Type of Membrane Material for Water Desalination Based on a Cross-Linked Bicontinuous Cubic Lyotropic Liquid Crystal Assembly, *J. Am. Chem. Soc.*, **129** (2007) 9574.

- [57] E. S. Hatakeyama, B. R. Wiesenauer, C. J. Gabriel, R. D. Noble and D. L. Gin, Nanoporous, Bicontinuous Cubic Lyotropic Liquid Crystal Networks via Polymerizable Gemini Ammonium Surfactants, *Chem. Mater.*, **22** (2010) 4525.
- [58] G. P. Sorenson, K. L. Coppage and M. K. Mahanthappa, Unusually Stable Aqueous Lyotropic Gyroid Phases from Gemini Dicarboxylate Surfactants, *J. Am. Chem. Soc.*, **133** (2011) 14928.
- [59] G. P. Sorenson and M. K. Mahanthappa, Unexpected role of linker position on ammonium gemini surfactant lyotropic gyroid phase stability, *Soft Mater.*, **12** (2016) 2408.
- [60] B. Guo, S. W. Tay, Z. Liu and L. Hong, Embedding of Hollow Polymer Microspheres with Hydrophilic Shell in Nafion Matrix as Proton and Water Micro-Reservoir, *Polymers*, **4** (2012) 1499.
- [61] I. Nicotera, L. Coppola, C. O. Rossi, M. Youssry and G. A. Ranieri, NMR Investigation of the Dynamics of Confined Water in Nafion-Based Electrolyte Membranes at Subfreezing Temperatures, *J. Phys. Chem. B*, **113** (2009) 13935.
- [62] A. Siu, J. Schmeisser and S. Holdcroft, Effect of Water on the Low Temperature Conductivity of Polymer Electrolytes, *J. Phys. Chem. B*, **110** (2006) 6072.
- [63] H. Ohno, K. Fujita and Y. Kohno, Is seven the minimum number of water molecules per ion pair for assured biological activity in ionic liquid–water mixtures?, *Phys. Chem. Chem. Phys.*, **17** (2015) 14454.
- [64] T. Ueki and M. Watanabe, Macromolecules in Ionic Liquids: Progress, Challenges, and Opportunities, *Macromolecules*, **41** (2008) 3739.
- [65] K. D. Kreuer, S. J. Paddison, E. Spohr and M. Schuster, Transport in Proton Conductors for Fuel-Cell Applications: Simulations, Elementary Reactions, and Phenomenology, *Chem. Rev.*, **104** (2004) 4637.
- [66] M. Armand and J. M. Tarascon, Building better batteries, *Nature*, **451** (2008) 652.
- [67] A. J. Kim, M. S. Kaucher, K. P. Davis, M. Peterca, M. R. Imam, N. A. Christian, D. H. Levine, F. S. Bates, V. Percec and D. A. Hammer, Proton Transport from Dendritic Helical - Pore - Incorporated Polymersomes, *Adv. Funct. Mater.*, **19** (2009) 2930.
- [68] E. B. Trigg, T. W. Gaines, M. Maréchal, D. E. Moed, P. Rannou, K. B. Wagener, M. J. Stevens and K. I. Winey, Self-assembled highly ordered acid layers in precisely sulfonated polyethylene produce efficient proton transport, *Nat. Mater.*, **17** (2018) 725.
- [69] A. Kusoglu and A. Z. Weber, New Insights into Perfluorinated Sulfonic-Acid Ionomers, *Chem. Rev.*, **117** (2017) 987.

- [70] Z. Cao, Y. Peng, T. Yan, S. Li, A. Li and G. A. Voth, Mechanism of Fast Proton Transport along One-Dimensional Water Chains Confined in Carbon Nanotubes, *J. Am. Chem. Soc.*, **132** (2010) 11395.
- [71] D. Muonz-Santiburcio, C. Wittekindt and D. Marx, Nanoconfinement effects on hydrated excess protons in layered materials, *Nat. Commun.*, **4** (2013) 2349.
- [72] The molecular structure of N-MZI is shown in the SI.†
- [73] Y. Jung, K. T. Chu, S. Torquato, *J. Comput. Phys.*, **223** (2007), 711.

Summary and future work

In this thesis, a series of LC compounds, straight polycatenars, bent-core polycatenars, simple bent-core bolaamphiphiles, double-tapered ionic molecules and polymerizable gemini-type amphiphile, have been studied. The results indicate that a variety of self-assembled 2D and 3D lower symmetry LC structures, which consist of for example noncentrosymmetrical or chiral nanoobjects, could be controlled by the modifications of classic LC compounds. These include the trigonal columnar lattice formed by bent-core polycatenars, the new class of trigonal, hexagonal lattices and superlattices formed by simple bent-core bolaamphiphiles, and the new type of hexagonal ionic and non-ionic superlattices formed by double-tapered ionic molecules. These lead the way to manipulate structures by controlled modification of LC molecules. The 3D orthorhombic *Fddd* phase formed by straight polycatenars and bent-core polycatenars consisting of helical columns, and double gyroid phase formed by polymerizable gemini-type amphiphile that can be swelled by water 50% in volume, have also been studied. The main results are summarized in below.

- The lower symmetry trigonal columnar phases formed by bent-core polycatenars are studied in Chapter 3. The non-centrosymmetric structures are confirmed by second harmonic generation, and the work leads to the new path to creating non-centrosymmetric self-assemblies with application potentials in e.g. frequency-doubling optical devices.
- The first thermotropic *Fddd* phase is confirmed in bent- and straight-core molecules in Chapter 4. This 3D phase is found to be formed by self-assembled helical columns, both left- and right-handed columns with equal numbers in the unit cell. This is also the first case of a liquid crystalline structure where each

individual column is confirmed to be homochiral, leading the way to manipulate 3D helical self-assembled structures.

- A new class of trigonal, hexagonal lattices and superlattices formed by bent-core bolaamphiphiles is studied in Chapter 5. We have investigated how the functional groups outside of the bend and inner chains can be used to control the formation of different types of honeycomb lattices. Again, second harmonic generation is used to confirm non-centrosymmetric trigonal structures.
- A new type of hexagonal superlattices, consisting of both ionic and non-ionic columns, formed by double-tapered ionic compounds is discussed in Chapter 6. This has widened the range and complexity of liquid crystal columnar phases with promising applications as semiconducting nanowires and electronic-ionic conductors.
- The polymerized self-standing film with the 3D double gyroid cubic structure is studied in Chapter 7. The film retains its structure and its good ionic conductivity, while at the same time it can absorb a lot of water from 6.7 to 15.6 wt% at various relative humidity, with potential applications in fuel cells.

The work in this thesis provides more possibilities of the complexity of LC phases, structures and phase sequences. In addition to these, some further work on polycatenars and bent-core molecules is still in progress to build a further understanding of self-assembly and mirror symmetry breaking processes and the application potentials, as listed below.

- Study of FCN and FCO polycatenars with different chain length and chiral aliphatic chains.

This would help to understand the formation of the helical columns, which are the basic arrangements in Cub_{bi} and $Fddd$ phases. It could also point to the possibility

of even more complex 3D columnar structures in similar compounds with potential spontaneous formation of macroscopic chirality. As for the long fluorescent core of the compounds and the high-level conjugation in the *Fddd* phase, the measurement of charge carrier mobilities is being performed. This could help to understand compounds' potential applications in displays and electronics.

- Study of 3-1-taper-shaped polycatenars.

The work helps to understand the effect of the number of attached chains and the chain length on the phase behaviours. Circularly polarized luminescence is being studied on the compounds to search for potential applications on the display, such as OLEDs that emit circularly polarized light.

- The study on the chiral polycatenars and the racemic mixture.

The enantiomers form a triple network cubic phase and their single crystal diffraction patterns are good choices to confirm the *I23* space group. Furthermore, the understanding of the phase behaviours of enantiomers, racemic mixtures and mixtures with different contents could guide the way to manipulate the bicontinuous cubic phases.

- Study of possible ferroelectric behaviours on the bent-core molecules with different lengths of branched chains.

The compound CN-H ($n = 5$) in Chapter 5 forms the trigonal honeycombs that are out-of-plane. More compounds with different branched-chain lengths and polar head-groups are designed according to the previous work. The study on the possible ferroelectric behaviours of columnar phases is in progress.